# Solitons and nonlinear optics in silicon-on-insulator photonic wires

Benton, Charlotte

*Award date:*
2009

*Awarding institution:*
University of Bath

# SOLITONS AND NONLINEAR OPTICS IN SILICON-ON-INSULATOR PHOTONIC WIRES

Christopher James Benton
A thesis submitted for the degree of Doctor of Philosophy
University of Bath
Department of Physics
April 2009

# Abstract

A theoretical study of silicon-on-insulator (SOI) photonic wires was conducted. These nanoscale optical waveguides can have transverse dimensions substantially smaller than the wavelength of the infrared light they carry. This extreme confinement provides very strong dispersion, which can be greatly controlled by specifying the waveguide geometry. The confinement also enhances silicon's already considerable Kerr nonlinearity (whereby refractive index increases with optical intensity), allowing for nonlinear optical phenomena with record-breakingly small powers.

The most notable of these phenomena (and the prime subject of this report) is the soliton, which is a self-sustaining localised pulse held together by a balance between dispersion and nonlinearity. A variety of other phenomena are also considered, including continuum generation, in which the spectral width of a pulse is greatly increased, and modulational instability, in which deviations from an optical waveform are reinforced by nonlinearity.

Light propagation through a single wire is modelled numerically, and the results compared to third-party experimental data. The analysis reveals that the experimental results are consistent with soliton evolution, thus strengthening the base of evidence for the existence of solitons in silicon wires.

Light propagation through arrays of multiple waveguides is also modelled. It is shown that inter-wire diffraction is intimately linked to dispersion, and that by exploiting this it is possible to realise both solitons and modulational instability in arrays of wires that individually would not be able to support these phenomena. It is also shown that silicon nanowires are an excellent medium for realising "optical bullets" in which a pulse of light is self-localised both in and transverse to the direction of propagation. A distinctive pattern of radiation emitted by these bullets is predicted.

Solitons supported by the Raman effect (rather than the Kerr effect) are also considered. A novel class of soliton solutions are derived, which have the novel property of existing even when the frequency components comprising the soliton are not phase matched.

## Acknowledgements

I would like to thank my supervisor Dmitry Skryabin for his considerable support and guidance. I would like to thank Andrey Gorbach and Alexey Yulin for patiently answering a great many questions. I would also like to thank my experimental collaborators Richard De-La-Rue, Charles De Nobriga, Wei Ding, Marco Gnan, Jonathan Knight, Marco Sorel and William Wadsworth for the opportunity to turn theory into experimental reality.

## Declaration of work previously published and work done in conjuction with others

- Figures 1.2, 3.15, 3.16 and 3.17 incorporate third-party experimental data as credited.
- Figures 3.16, 3.17, 3.18 and 3.19 of which I am the creator (excepting the inclusion of third-party experimental data as credited) have been published elsewhere. (Optics Express, 16:3310, 2008.)
- Figures 4.2, 4.3, 4.4, 4.9, 4.13, 4.16, 4.18 and 4.19, of which I am the creator, have been published in whole or in part elsewhere. (Optics Express 17:5879, 2009.)
- Figures 5.2, 5.3, 5.5, 5.6, 5.7, 5.8, 5.9, 5.10, 5.11, 5.12, 5.17, 5.18, 5.21, 5.22 and 5.23, of which I am the creator, have been published in whole or in part elsewhere. (Physical Review A, 78:033818, 2008.)

# List of abbreviations

| | |
|---|---|
| **2PA** | 2 Photon Absorption |
| **3PA** | 3 Photon Absorption |
| **AlGaAs** | Aluminium Gallium Arsenide |
| **CW** | Continuous Wave |
| **FCC** | Free Charge Carrier |
| **FFT** | Fast Fourier Transform |
| **FROG** | Frequency Resolved Optical Gating |
| **FWHM** | Full Width at Half Maximum |
| **GVD** | Group Velocity Dispersion |
| **HOD** | Higher Order Dispersion |
| **HSQ** | Hydrogen Silsesquioxane |
| **MI** | Modulational Instability |
| **NLS** | Nonlinear Schrödinger (equation) |
| **OPA** | Optical Parametric Amplifier |
| **SOI** | Silicon on Insulator |
| **SPM** | Self Phase Modulation |
| **SRS** | Stimulated Raman Scattering |
| **ZDW** | Zero dispersion wavelength |

# Contents

# Chapter 1

# Introduction

This report is fundamentally about *Nonlinear Optics*. This is the study of how light behaves at high intensities, and how to exploit this behaviour to gain extreme control over light. Nonlinearity is important because it allows light to interact with light. In a system where electric polarisation is simply proportional to the electric field, waveforms can be superposed without any change to the dynamics of the individual components; if two waveforms meet, they will simply pass through one another. Consequently, if you pass light with a given set of frequency components through a linear medium, you can only ever get those frequencies out. When optical nonlinearity is present, however, waveforms can mix or self-interact to produce an entirely new waveform.

Examples of nonlinear phenomena include *second harmonic generation* [1], in which photons are essentially combined to give photons with twice the energy; *four wave mixing* in which three frequency components interact to produce [2] or amplify [3] a fourth; *supercontinuum generation* [4, 5], in which light with a very broad frequency spectrum can be generated from a narrow-spectrum pulse; *electromagnetically induced transparency* [6] in which absorption at a particular frequency is eliminated by optically inducing destructive interference between the corresponding quantum states; *stimulated Raman scattering* [7] in which photons are swapped for photons with shifted energy, with attendant excitation or relaxation of the medium; and *modulational instability* [8] in which small deviations from a waveform are reinforced by nonlinearity, causing it to break up into a chain of pulses. Nonlinearity can also be used to create an environment for exotic linear phenomena. These include "slow light" in which light can be drastically slowed, or even halted and "fast light" in which the group velocity of light exceeds the speed of light in vacuum, or even becomes negative, causing a pulse to move *towards* the source [9].

An extremely important nonlinear phenomenon—and the subject of this report—is the soliton.

## 1.1 Solitons

A *soliton* is a localised and self-sustaining wave motion that can arise in many non-linear systems. They contain a range of frequency components, and are bound together by the balance between the dispersion of these frequency components and the nonlinearity of the system.

The archetypal example of a soliton is the "Wave of Translation" observed by John Scott Russell in 1834. When a boat moving along a canal suddenly stopped, the surge of water at its bow continued to move, and "assum[ed] the form of a large solitary elevation, a rounded, smooth and well-defined heap of water, which continued its course along the channel apparently without change of form or diminution of speed" [10]. This description highlights an extremely important feature of solitons, namely their ability to retain their shape as they propagate, despite the inevitable presence of noise and damping. This feature is one of the principal reasons for interest in solitons. In fact, the very name "soliton" (as opposed to the more general term, "solitary wave") reflects the fact that solitons can be regarded as discrete particles, rather than waves.

Russell's wave of translation is more specifically a *temporal soliton*. That is, at any point in time, the soliton only occupies a finite region of space along the direction of propagation. The name derives from the fact that an observer at a given point along the direction of propagation will only see the soliton for a limited time duration. Temporal solitons are also seen in magnetostatic waves [11], sound waves [12] and optical fibres [13]. They have also been proposed as a mechanism for many natural phenomena, including tsunamis [14] and signal propagation through neurons [15].

In contrast to the temporal soliton is the *spatial soliton*, in which the wave motion is confined in one or more directions transverse to the direction of propagation. (As with temporal solitons, the separation of frequency components is being nonlinearly suppressed, but this frequency is spatial rather than temporal.) A prime example of this is the optical self trapping described below, whereby diffractive spreading of a beam of light is cancelled by nonlinearity. Spatial solitons have also been observed in magnetic materials [16]. A relative of the spatial soliton is the *edge soliton*, in which the wave is self-confined against the edge of the propagation medium [17]. Solitons can fulfil the requirements for both spatial and temporal solitons [18], in which case they are called *spatiotemporal solitons*.

A concept related to the soliton is the *topological soliton* or *topological defect*. This has particle like properties which result from the medium being twisted or distorted in such a way as for it to be impossible to deform the defect into a non-defect through a continuous series of intermediate states. Instead, the solutions are split into topologically distinct families, which can only be switched between by the intervention of another physical effect. Examples include structural defects in liquid crystals [19], Falaco cells (vortex pairs that can occur on the surface of liquids) [20] and vortices in liquid helium [21]. Of particular interest is the possibility that spacetime itself may contain topological defects known as cosmic strings [22]. Topological solitons can be said to carry a *topological charge* which is a conserved number, describing the exact form of the

defect. Solitons carrying such a charge are considered in chapter 6.

In some systems, it is possible for an absence of energy to behave as a soliton. These *dark solitons* or *antisolitons* consist of a region of reduced amplitude set against a continuous wave background. (In this context, a non-dark soliton is known as a *bright soliton*.) Like bright solitons, dark solitons can be both temporal and spatial in nature [23].

The resemblance of solitons to particles suggests that the converse may be true, and that elementary particles such as electrons are themselves solitons [24]. (There is as yet no experimental evidence to support this theory, and so it remains highly speculative.)

### 1.1.1 Optical solitons

In the field of optics, temporal solitons were first observed in silica fibres by Linn Mollenauer and Roger Stolen in 1980 [13]. These solitons are sustained by the Kerr effect, whereby the refractive index increases in proportion to optical intensity. This causes *self phase modulation* in which the leading edge of the pulse is red-shifted, whilst the trailing edge is blueshifted. In the presence of *anomalous group velocity dispersion* (in which blue light has a higher group velocity than red light, as opposed to the *normal group velocity dispersion* which is more commonly encountered) the dispersion and the nonlinearity can balance to form a soliton. Temporal solitons in single waveguides are studied in chapter 3, whilst temporal solitons in coupled waveguide arrays are considered in chapter 4.

Spatial solitons are seen in the form of *self trapping* of optical beams [25]. This occurs when beam spreading due to diffraction is counteracted by *self focussing*, in which optically-induced refractive index increase causes the beam to converge. This effect can also be thought of as the light creating its own waveguide. Spatial solitons are not studied directly in this report, but attention is given to a related phenomenon known as the *spatial discrete soliton*. These occur in arrays of coupled waveguides, whereby the natural inter-waveguide coupling is suppressed by nonlinearity. Spatial discrete solitons were first proposed by Demetrios Christodoulides and Richard Joseph in 1988 [26] and were first realised experimentally in 1998 [27].

Optical spatiotemporal solitons are known as *light bullets* [18], where the light is both localised in the direction of propagation, and self trapped in the transverse direction. Edge bullets are also possible, whereby the light is trapped against the edge of the medium [17, 28]. In chapter 5 *spatiotemporal discrete solitons*, in which the properties of the temporal soliton and spatial discrete solitons are combined [17, 29, 30] are considered. Light bullets (and spatiotemporal solitons in general) have proved highly elusive, with only a few examples (e.g. [31, 32, 33]) seen to date. Difficulties include the need to balance the intrinsic length scales of dispersion and diffraction [34] (so that the powers needed to balance the two are equivalent), and the need for sufficiently strong nonlinearity [35] to reduce the power requirements to practical levels.

**Non-Kerr solitons**

The Kerr effect is not the only form of optical nonlinearity capable of producing optical solitons. In materials lacking inversion symmetry (such as lithium niobate or $\beta$-barium-borate) electric polarisation as a function of electric field can have a quadratic component (as opposed to the cubic nonlinearity of the Kerr effect), and this can also be used to support solitons [36, 37]. Raman-effect solitons have been observed in a variety of forms; these include hybrid bright-dark temporal solitons in which a bright-soliton of Stokes-shifted light co-moves with a dark-soliton in the optical pump [38], and more conventional bright solitons [39] (which are considered in chapter 6). Solitons have also been observed in systems where stimulated Brillouin scattering (the result of photon-phonon interactions [40]) is the source of the nonlinearity [41]. It has even been suggested that spatial solitons supported by the fundamental nonlinearity of the vacuum may exist [42, 43]. (These, however, require intensities beyond currently available laser technology.)

### 1.1.2 Solitons versus non-solitons

Determining if a waveform is or isn't a soliton is a non-trivial problem. It becomes more complicated still in light of the fact that the mathematical models yielding exact soliton solutions are only approximations to physical reality. As such, the solitons that occur in nature are sometimes referred to as *quasi-solitons*. These, however, must retain several important characteristics. Firstly, although deviations from an exact model will generally cause a quasi-soliton's shape to change as it propagates, there must still be strong supression of this shape change. For example, a temporal quasi-soliton in a optical fibre may lengthen slightly as it propagates, but this increase should be far smaller than that seen without nonlinearity. Throughout this report, the difference between propagation with and without nonlinearity is used to demonstrate quasi-soliton formation.

Another crucial feature of any soliton (or quasi soliton) is that the localisation must be intrinsic to the bulk properties of the propagation medium, and not imposed by any artificial constraints. Mathematically speaking, the soliton should be a intrinsic property of the equations of motion of the propagation medium, rather than something that is forced by boundary conditions. For example, a pulse of monochromatic light being fired through a linear medium would not constitute a temporal soliton, as the localisation would be purely a result of the initial pulse being finite in time. Similarly, light travelling through an optical fibre would not – under ordinary circumstances – constitute a spatial soliton, as the localisation would be simply a result of the light undergoing total internal reflection at the fibre's boundaries. (For a topological defect, this distinction is more complicated, as the separation between the topological families is generally the result of boundary conditions. However, these conditions do not push the solution into one particular family and so they don't force a soliton to be present.) In chapter 5 this distinction between self-localisation and boundary condition localisation will become important, as spatial localisation in finite arrays of waveguides is considered.

Some sources (e.g. [44]) draw an explicit distinction between the terms "soliton" and "solitary wave", by stating that in addition to the requirement of self-sustaining localisation, a soliton must also be able to pass through another soliton with no ultimate effect other than a phase shift. However, in the context of nonlinear optics this requirement is often inappropriate. For example, optical phenomena which otherwise resemble solitons are widely observed to fuse, split or annihilate on collision [45]. (This is related to the above distinction between solitons and quasisolitons, as whilst the nonlinear Schrödinger equation derived in chapter 2 supports solitons with the phase-shift-only property, this is broken by the modifications that must be made in order to accurately describe a real system [23].) As the particle-like behaviour remains, it is unhelpful to exclude these objects as being solitons. Therefore, the phase-shift-only requirement is commonly disregarded by many sources. There does, however, remain an informal requirement that something interesting should happen on collision. In section 3.3.3 pulse fusion is used as a test to see if quasi-solitons are present.

Another test arises from the fact that many soliton solutions possess non-trivial conservation laws, in which a particular combination of variables should remain constant. In sections 3.3.3 and 5.2.3 such laws are used to gauge quasi-soliton formation.

For clarity, the term "quasi-soliton" will be dropped throughout the rest of this report.

## 1.2 Semiconductor waveguides

Silicon on insulator (SOI) devices consist of nanoscale silicon waveguides sitting on top of an insulator base (which is almost always silica). These waveguides are commonly referred to as *photonic nanowires* (or just "wires"), where "photonics" is a general term used to describe the emission, manipulation and detection of photons. They typically operate at wavelengths in the vicinity of the $1.55\mu$m infrared telecom band (which corresponds to the maximum transparency of silica fibre). A schematic of the type of SOI device considered in this report is given in figure 1.1, whilst an electron micrograph is given in figure 1.2.

Silicon has an extremely high refractive index (approximately 3.5 in the band of interest [46]), allowing for tight-confinement of light. This confinement can be spectacular, with light having a wavelength greater than a micron being confined to waveguides with transverse dimensions of only a few hundred nanometres. The strong dielectric boundary effects resulting from this confinement allows for *dispersion tailoring*, in which the dispersion relation can be modified by altering the geometry of the waveguide. In particular, the group velocity dispersion (GVD) can be made anomalous [47, 48]. This allows for solitons, despite silicon's strongly normal GVD at these wavelengths. This dispersion can be enormous, with values three orders of magnitude greater than that in silica fibres attainable [49]. Silicon's high refractive index can also be used to trap light in a gap between wires by total internal reflection, in an arrangement known as a slot waveguide [50, 51, 52, 53].

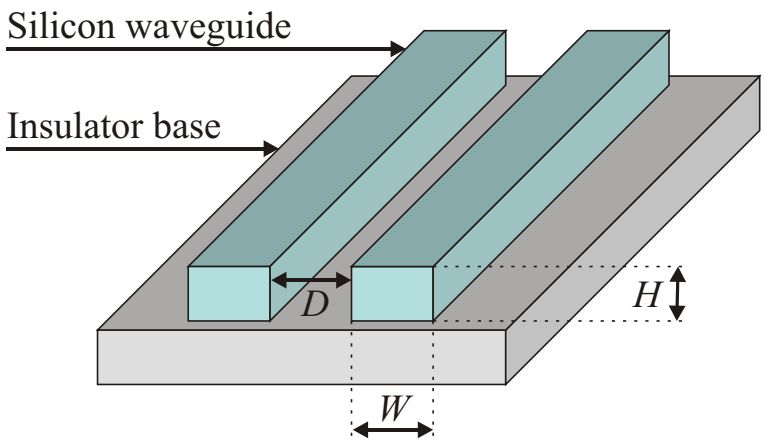


Figure 1.1: Schematic of two silicon on insulator waveguides. The width $W$, height $H$ and separation distance $D$ are all variable. (In chapter 3, single waveguides with a variety of dimensions are considered. In chapter 4, arrays with $H = 220$nm, $W = 330$nm and $D = 330$nm are considered. In chapter 5, arrays with $H = 220$nm, $W = 380$nm or 420nm and $D = 700$nm are considered.)

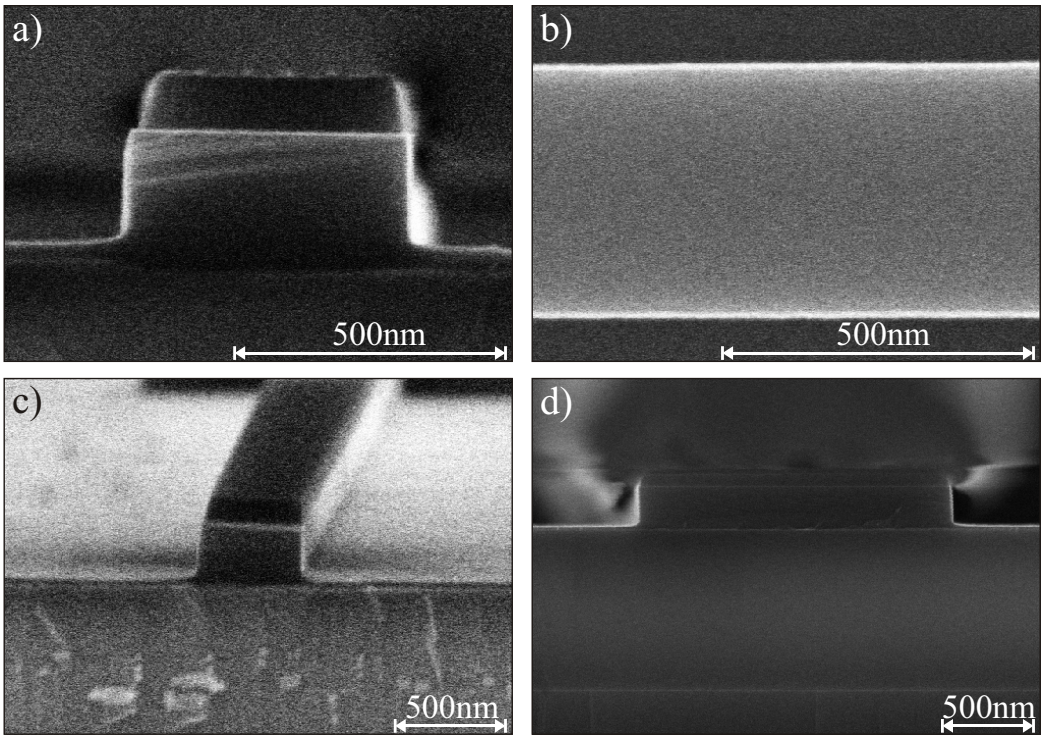


Figure 1.2: Scanning electron micrographs of an SOI waveguide, fabricated by Marco Gnan, Marc Sorel and Richard De la Rue [54]. (This device is modelled in section 3.3.) a) Cross-section view of waveguide. (The slightly darker material on top of the waveguide is the etching mask.) b) Top-down view of waveguide. c) Perspective view of waveguide. d) Cross-section view of taper used to couple light into waveguide. (Images taken by Marco Gnan.)

Silicon has a large Kerr nonlinearity [55, 56], which is greatly enhanced by the tight confinement

that silicon nanowires give [57]. As with dispersion, the nonlinear coefficient can exceed that of silica fibres by three orders of magnitude [58]. Furthermore, this nonlinearity is ultrafast [58], so that in comparison to the frequency of the light, it responds effectively instantaneously to the changing electric field. These effects allow for temporal solitons [48, 59, 60, 61] with record-breakingly small peak powers (for sub-picosecond optical pulses) of only a few watts. [54, 62, 63, 64].

Silicon on insulator devices have a wide range of applications [59, 65, 66, 67]. One such example is the ring resonator [68, 69] which can be used as an optical delay line in optical signal processing [70, 71]. On-chip supercontinuum source are also possible [62, 64, 72]. Raman amplifiers are another application [73, 74, 75], with demonstration devices having been constructed [76, 77, 78, 79]. Raman lasers have been fabricated [80, 81], as have wavelength converters [82]. Devices utilising four wave mixing are also of interest [83, 84], with both amplifiers [85] and wavelength converters [86] having been demonstrated. Signal modulation is another area of importance [87, 88, 89, 90], as is signal switching [65, 91] and signal detection [92].

Ultimately, silicon on insulator promises to have a major impact upon future technology. A primary example is the realisation of optical data lines within microchips [93], which would greatly improve the performance of complex integrated circuits by allowing different regions to communicate at greater speed [94]. The ability to place optical components on a silicon chip would also greatly benefit the construction of optical signal transceivers, as all the functions could be performed by a single chip, rather than multiple components [95]. Another potential application is all-optical signal routing, in which data packets in telecommunication networks are directly switched in optical form (rather than being detected, processed in electrical form, and then reemitted).

## 1.3 Synopsis

In this report, silicon on insulator devices are considered as on-chip laboratories with which to investigate a wide range of nonlinear optical phenomena. A theoretical approach is used, but close links to experimental reality are maintained throughout.

In chapter 2 a model of optical propagation through SOI waveguides is derived, taking into account a range of physical effects, and (so far as possible) using physical parameters based upon experimental data. This includes the material dispersion of the silicon and silica, waveguide dispersion, linear absorption due to light escaping the waveguide, nonlinear absorption, and the effect of free charge carriers on optical transmission.

In chapter 3, light propagation through a single wire is modelled, revealing a variety of physical effects. A comparison to third-party experimental data is made, providing strong evidence for the existence of solitons in silicon wires.

In chapters 4 and 5 multiwire arrays are modelled. In chapter 4 it is shown that inter-wire

diffraction is intimately linked to dispersion, and that by exploiting this it is possible to see temporal solitons in arrays of normally dispersive wires. In chapter 5, silicon on insulator is shown to be an excellent medium for realising spatiotemporal solitons. A distinctive pattern of radiation emitted by these "optical bullets" is predicted.

In chapter 6, solitons supported by the Raman effect (rather than Kerr nonlinearity) are considered. A new class of soliton solutions are derived, which have the novel property of existing even when the set of frequency components comprising the soliton are phase-mismatched.

A summary of original findings and published works is given in chapter 7.

# Chapter 2

# Modelling SOI waveguides

The propagation of light through silicon waveguides involves the complex interplay between a variety of physical effects. In this chapter, a model for this propagation is developed.

Whilst Maxwell's equations can be integrated directly [96], such an approach is time consuming and requires vast amounts of memory. A 3D array of volume elements must be stored in its entirety, with each being represented by a set of twelve numbers (the vector components of both the electric and magnetic fields, plus back-values) [96]. For a dispersive nonlinear system, further vectors representing the dielectric polarisation must be added [96]. The simulation must also use a very large number of time steps, as there must be sufficient resolution to accurately describe the form of each wavecycle, and yet up to 10,000 such cycles may be present over the full length of propagation.

The system can be greatly simplified by reformulating it into a *Nonlinear Schrödinger Equation* [8, 23, 97, 98]. This is scalar and one dimensional, in that the waveguide is represented by an amplitude factor, which is a function of the distance along the waveguide. This reduction, however, does not amount to ignoring the vectorial nature of the fields, or their variation perpendicular to the direction of propagation. Instead, it uses the *effective index approximation*, in which the amplitude is a scaling factor for the vector mode.

The Nonlinear Schrödinger (NLS) equation has another great advantage in that instead of describing the electric field itself, it describes a *slowly varying envelope* which modulates a fixed frequency carrier signal. This allows the step size in any integration scheme to be greatly increased, as the rapid oscillation of the carrier wave has been removed. More importantly, the second derivative of this envelope function with respect to distance of propagation is negligible, allowing it to be removed. This *slowly varying envelope approximation* reduces what would be a second order equation (in distance) into a first order equation.

The equation itself is given by [8]

$$\frac{\partial A}{\partial z} + i\beta_2 \frac{\partial^2 A}{\partial t^2} = i\gamma |A|^2 A \tag{2.1}$$

where $A$ is the amplitude of the envelope, $z$ is distance along the waveguide, and $t$ is time. The group velocity dispersion (GVD) of the waveguide is specified by the constant $\beta_2$ (which is described in section 2.1.2) whilst the Kerr nonlinearity is specified by the constant $\gamma$ (which is described in section 2.2.2).

In order accurately represent an SOI waveguide, the ideal NLS equation must be substantially modified. Firstly, the NLS equation assumes a simplified model of dispersion, in which the relation between frequency and wavenumber is fitted with a parabola (where $\beta_2$ is the quadratic coefficient). This approximation is sometimes acceptable for optical fibre [8], but in SOI it becomes inadequate [57, 99, 100, 101]. Therefore, the NLS must be extended into a *Generalised Nonlinear Schrödinger equation*, which includes higher order derivatives. The other main deviation from the ideal NLS model is caused by damping. Both linear damping (due to light escaping from the waveguide) and nonlinear damping (due to two-photon effects) will be present. Furthermore, the light will excite free charge carriers, which themselves will absorb and scatter light.

In the following sections, the generalised NLS equation is both derived and extended to encompass the effects of damping and free charge carrier interactions.

## 2.1 Light in a waveguide

Maxwell's equations in a dispersive and nonlinear optical material (for electric field $\vec{E}$, displacement field $\vec{D}$ and magnetic field $\vec{H}$) are given by

$$\nabla \times \vec{E} = -\frac{1}{\epsilon_0 c^2} \frac{\partial \vec{H}}{\partial t} \tag{2.2}$$

$$\nabla \times \vec{H} = \frac{\partial \vec{D}}{\partial t} \tag{2.3}$$

where $\nabla \cdot \vec{D} = 0$ and $\nabla \cdot \vec{H} = 0$. We have assumed that there are no free charge carriers or currents, a fact which is actually false for silicon; however, we will explicitly reintroduce the role of free charge carriers in section 2.3.2. We have also ignored the effect of magnetisation, which is justified, as silicon's relative permeability differs from unity by less than $10^{-5}$. We can eliminate the magnetic part of these equations entirely to give a second-order wave equation of the form

$$\nabla^2 \vec{E} = \frac{1}{\epsilon_0 c^2} \frac{\partial^2 \vec{D}}{\partial t^2} + \nabla \left( \nabla \cdot \vec{E} \right) \tag{2.4}$$

When considering wave propagation in a single direction $\hat{z}$, it is convenient to rewrite equation 2.4 as

$$\frac{\partial^2 \vec{E}}{\partial z^2} + \nabla_\perp^2 \vec{E} = \frac{1}{\epsilon_0 c^2} \frac{\partial^2 \vec{D}}{\partial t^2} + \nabla \left( \nabla \cdot \vec{E} \right) \tag{2.5}$$

in which the Laplacian operator has been split up as $\nabla^2 \equiv \partial^2/\partial z^2 + \nabla_\perp^2$, where $\nabla_\perp^2$ is the *transverse Laplacian*. This is a 2-dimensional Laplacian operator which acts of the plane perpendicular to $\hat{z}$. The $\partial^2/\partial z^2$ operator corresponds to wave propagation along the $\hat{z}$ axis, whilst the $\nabla_\perp^2$ operator gives diffraction.

### 2.1.1 Material dispersion

The displacement field is related to the electric field by

$$\vec{D} = \epsilon_0 \vec{E} + \vec{P} \tag{2.6}$$

where $\vec{P}$ is the polarisation induced by the electric field. This polarisation is not instantaneous, and at optical frequencies the delay becomes highly significant. (Neither is the relation truly linear, a phenomenon of fundamental importance that we will introduce in section 2.2.) The polarisation at each point in space can be modelled as a sum of driven harmonic oscillators, each corresponding to a particular excitation in the material, which at resonance will cause absorption. (This connection between absorption and dispersion is highly notable. The two are inextricably linked by the need for causality, as is mathematically formalised by the Kramers-Krönig relations [102].) The equation of motion of the $n$th oscillator (in terms of $\vec{P}_n$, its contribution to the total polarisation) is given by

$$\omega_n^2 \vec{P}_n + \frac{\partial^2 \vec{P}_n}{\partial t^2} = \epsilon_0 \Delta\epsilon_n \omega_n^2 \vec{E} \tag{2.7}$$

where $\omega_n$ is the resonant frequency, and $\Delta\epsilon_n$ is the extent to which the oscillator couples to the electric field (and thus its contribution to the relative permittivity). The $\Delta\epsilon_n$ term is actually a second-order tensor (where deviation from isotropy is known as birefringence). However the birefringence of silicon corresponds to a refractive index difference of less than $10^{-5}$ [103], and so $\Delta\epsilon_n$ is to a good approximation a scalar. The lack of any damping term means that these equations are only physically valid when the optical spectrum does not overlap with the fundamental resonant frequency $\omega_n$. Summing over these polarisations gives a displacement field of the form

$$\vec{D} = \epsilon_0 \epsilon_\infty \vec{E} + \sum_n \vec{P}_n + \epsilon_0 \chi_0^{(3)} \tag{2.8}$$

where we have also added a quasi-instantaneous term, with polarisation $\epsilon_0 \left(\epsilon_\infty - 1\right) \vec{E}$, where $\epsilon_\infty$ is the instantaneous susceptibility. This is formally the susceptibility at infinite frequency, but in reality it corresponds to the low-frequency tail of a much faster resonance. In silicon, it has a value (in the infrared) of $\epsilon_\infty = 11.6858$ [46], but in some formulations this is replaced by the usual oscillator term [104, 105]. Physically, this term results from the sum of several high energy direct-gap transitions [106].

In response to an electric field of the form $a\cos(\beta z - \omega t)\,\hat{x}$, these oscillators reach a steady state (with Lorentzian frequency dependence) of the form

$$\vec{P}_n = a\frac{\epsilon_0 \Delta\epsilon_n \omega_n^2}{\omega_n^2 - \omega^2}\cos(\beta z - \omega t)\,\hat{x} \tag{2.9}$$

which implies a frequency dependent dielectric permittivity

$$\epsilon(\omega) = \epsilon_\infty + \sum_n \frac{\Delta\epsilon_n \omega_n^2}{\omega_n^2 - \omega^2} \tag{2.10}$$

which in terms of free space wavelength $\lambda = 2\pi c/\omega$ and refractive index $n = \sqrt{\epsilon}$ gives

$$n(\omega) = \sqrt{\epsilon_\infty + \sum_n \frac{\Delta\epsilon_n \lambda^2}{\lambda^2 - \lambda_n^2}} \tag{2.11}$$

Equations of this type are known as Sellmeier equations. The physical coefficients are well documented for both silica and silicon [46, 107], and are given in figure 2.1. It is, however, more accurate to say that these coefficients are curve-fitting parameters to experimental data, rather than the precise physical parameters of the polarisation oscillators. In silicon, the Sellmeier equation is often tweaked to improve this fitting [46], giving a modified formula of

$$n_{\mathrm{Si}}(\omega) = \sqrt{\epsilon_\infty + \frac{\Delta\epsilon_1 \lambda_1^2}{\lambda_1^2 - \lambda^2} + \frac{\Delta\epsilon_2 \lambda_2^2}{\lambda^2}} \tag{2.12}$$

For silicon at the wavelengths of interest, $\Delta\epsilon_1$ is the dominant cause of dispersion, and is due to silicon's 1.1 eV indirect band-gap [75]. The $\Delta\epsilon_2$ term provides a small correction, which is highly detuned from any resonance. In silica, the $\Delta\epsilon_1$ and $\Delta\epsilon_2$ terms correspond to absorptions in the ultraviolet, whilst the $\Delta\epsilon_3$ term corresponds to an infrared absorption (as can be seen from the corresponding values of $\lambda_n$).

| | **Silicon** | **Silica** |
|---|---|---|
| $\epsilon_\infty$ | 11.6858 | 1 |
| $\Delta\epsilon_1$ | 0.00810461 | 0.6961663 |
| $\Delta\epsilon_2$ | 0.939816 | 0.4079426 |
| $\Delta\epsilon_3$ | – | 0.8974794 |
| $\lambda_1$ ($\mu$m) | 1.1071 | 0.0684043 |
| $\lambda_2$ ($\mu$m) | 1 | 0.1162414 |
| $\lambda_3$ ($\mu$m) | – | 9.896161 |

Figure 2.1: Sellmeier coefficients for both silicon [46] and silica [107]. For silica for conventional Sellmeier formula (equation 2.11) is used, whilst for silicon a modified formula (equation 2.12) is used.

We can therefore write the (low power) dispersion relation as

$$\vec{D} = \epsilon_0 \epsilon(\omega)\,\vec{E} \tag{2.13}$$

where the frequency dependent permittivity is given by equation 2.10. This approach of replacing the oscillators with a frequency dependent function is not, however, universally applicable. If we wish to directly solve Maxwell's equations for a nonlinear system (rather than using the envelope approach described below), then the oscillators must be explicitly integrated [96].

### Dispersion parameter

At this point we need to provide a rigorous definition of what we mean by group velocity dispersion. We start by noting that the phase velocity of light is given by $v_\mathrm{p} = \omega/k$, where $k$ is (by definition) the wavenumber. A pulse, however, will not travel at this speed, but at the group velocity $v_\mathrm{g} = d\omega/dk$. We can use the group velocity to define a *group refractive index* $n_\mathrm{g} \equiv c/v_\mathrm{g} = n - \lambda\,(dn/d\lambda)$. The gradient of group index is an obvious choice for specifying GVD, and so we define the *dispersion parameter* $\mathcal{D}$ as [8]

$$\mathcal{D}\,(\lambda) \equiv \frac{1}{c}\frac{dn_\mathrm{g}}{d\lambda} \tag{2.14}$$

This is constructed so that a pulse with spectral width $\Delta\lambda$ (about a central frequency $\lambda$) will temporally broaden by $\Delta\lambda\,\mathcal{D}\,(\lambda)$ per unit propagation length. The GVD is conventionally measured in units of $\mathrm{ps\,nm^{-1}\,km^{-1}}$, which is a consequence of its use in fibre optic communication, where the pulse duration is typically measured in picoseconds, the wavelength in nanometres and the distance in kilometers. The dispersion parameter can also be written in terms of (ordinary) refractive index $n$ as

$$\mathcal{D} \equiv -\frac{\lambda}{c}\frac{d^2n}{d\lambda^2} \tag{2.15}$$

A positive value of $\mathcal{D}$ corresponds to *anomalous GVD* in which blue pulses move faster than red pulses, whilst a negative value corresponds to *normal GVD*, in which the converse is true.

### Material dispersion of silicon and silica

Dispersion parameters calculated from the coefficients in figure 2.1 are shown in figure 2.2. In the range of interest (around 1.5$\mu$m), the GVD of silicon is strongly normal, whilst the much weaker GVD of silica is anomalous.

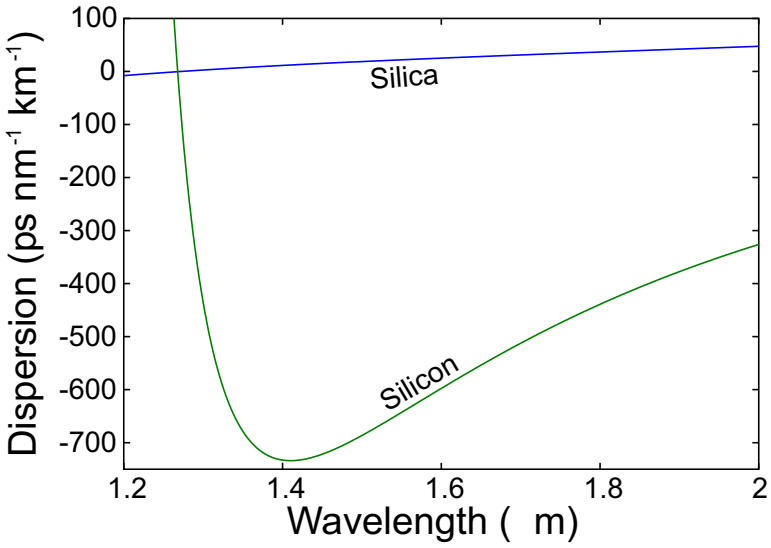


Figure 2.2: Dispersion parameters of silicon and silica, calculated from [46] and [107]. Positive values correspond to anomalous GVD, and negative values to normal GVD.

### 2.1.2 Waveguide dispersion

A waveguide introduces a dispersion of its own, due to the dielectric effects at material boundaries. This can be used to achieve strong anomalous GVD, despite the strongly normal material GVD of silicon [47, 48]. Assuming monochromatic light and a lossless waveguide mode, we can write the electric field $\vec{E}$ as

$$\vec{E} = \vec{F}_{\omega,\epsilon(\vec{x}_\perp,\omega)}\left(\vec{x}_\perp\right)\cos\left(\beta_{\omega,\epsilon(\vec{x}_\perp,\omega)}z - \omega t\right) \tag{2.16}$$

where $\vec{F}$ is the modal profile (as a function of position on the transverse plane $\vec{x}_\perp$), and $\beta$ is its corresponding *propagation constant*. Both $\vec{F}$ and $\beta$ depend on the frequency $\omega$, and the cross-sectional dielectric profile of the waveguide $\epsilon\left(\vec{x}_\perp,\omega\right)$. This profile varies with position over the transverse plane (depending on what material is present at that point in space) and is also dependent on frequency, as specified by equation 2.10 for the particular material. (This approach is not universal, as some sources recommend finding the modes in $\vec{H}$ rather than $\vec{E}$ for mathematical convenience [108].)

At given $\omega$, values of $\vec{F}$ and corresponding $\beta$ satisfying Maxwell's equations can be found using readily available software packages. The FemSIM module of the RSoft package [109] was used. For the configurations used, the principal mode was a quasi-$TE_0$ mode. (TE stands for *transverse electric*, meaning that the electric field has no component along the direction of propagation. By quasi-TE, we mean a mode in which the electric field component along the direction of propagation is small but non-zero. The subscript zero denotes the lack of any nodes within the mode.) A quasi-$TM_0$ (transverse magnetic) mode also exists, but it is less confining, and is more difficult to excite. The two modes have different values of $\beta$, and so any coupling between them will not be phase matched, making the interaction between them negligible. The

coupling is reduced further still by the fact that the modes are roughly orthogonal and so will have minimal projection on to one another. Due to its tighter confinement (and hence higher nonlinearity) we will concentrate on the quasi-$TE_0$ mode throughout this report.

A variety of SOI waveguides are considered in this report, with dispersions tailored for a large range of applications. Their dispersions are given in figure 2.3. An example of the mode profiles used to calculate these dispersion relations is given in figure 2.4.

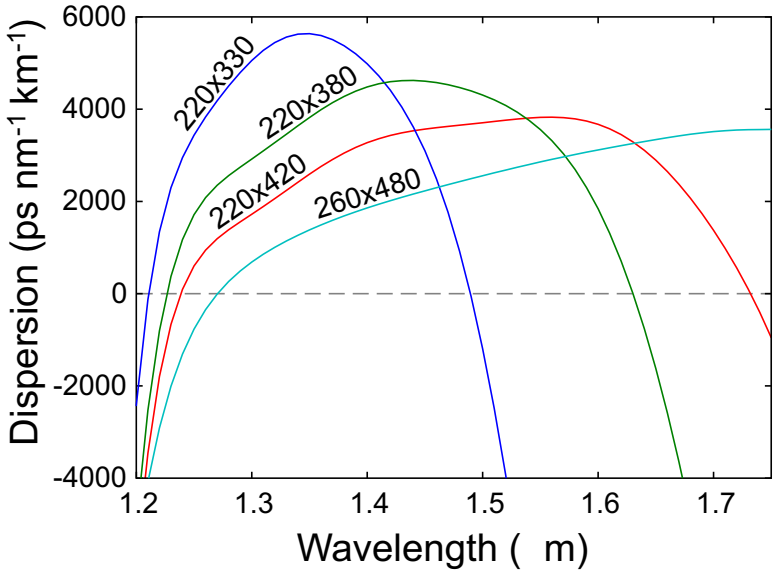


Figure 2.3: A selection of dispersion curves for silicon on insulator waveguides with rectangular cross-section. Dimensions are given in nanometres. Positive values correspond to anomalous GVD, whilst negative values correspond to normal GVD.

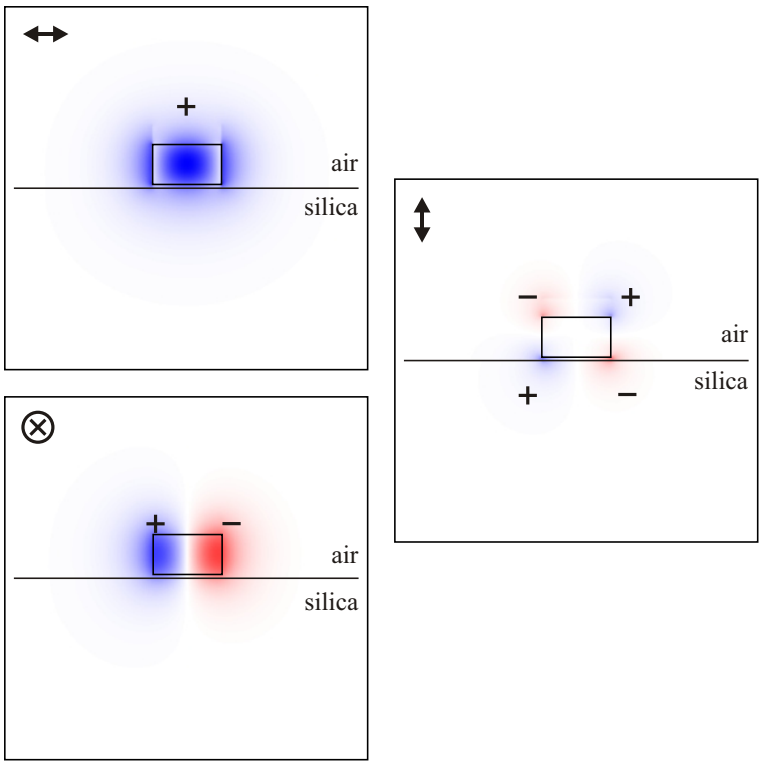


Figure 2.4: Principal quasi-$TE_0$ mode of a 220nm × 380nm SOI waveguide. Shown over a 1$\mu$m × 1$\mu$m cross section. The electric field vector is split into Cartesian components, with transverse components parallel to the silica-air interface shown top, transverse perpendicular components shown middle, and longitudinal components shown bottom. The horizontal lines denote the silica-air interface, whilst the rectangles show the cross section of the silicon wire. It has been assumed that the wire lies 20nm above the silica-air plane due to over-etching, and that the wire is covered with a 100nm thick etching mask of refractive index 1.35. Colour saturation gives absolute value. The + and − signs denote relative phase.

### Extracting dispersion coefficients

Values of $\beta$ at various $\omega$ were fitted to a polynomial

$$\beta = \beta_0 + \frac{\beta_1}{1!}(\omega - \omega_0) + \frac{\beta_2}{2!}(\omega - \omega_0)^2 + \frac{\beta_3}{3!}(\omega - \omega_0)^3 + \cdots \tag{2.17}$$

where $\beta_m$ are the *dispersion coefficients*. The core frequency $\omega_0$ is chosen to be the *pump frequency*. This is the principal frequency of the light fired into the waveguide. Through most of this report we use a pump wavelength of $\lambda_0 = 1.5$ $\mu$m, giving a pump frequency of $\omega_0/2\pi =$ 1256 THz.

An important issue with polynomial fitting is the order of polynomial used. Whilst a sufficiently high order is required to accurately fit the underlying function, the use of too high an order (in which the number of polynomial coefficients starts to approach the number of datapoints) will cause pathological behaviour in which the datapoints themselves are well fitted, but the curve of

the polynomial lurches wildly between them. (In the extreme case of an $N$th order polynomial being used to interpolate $N+1$ datapoints, this is known as Runge's phenomenon [110].) This problem was avoided by calculating a large number of data points (typically between 60 to 100). Using an 11th order polynomial gave fitting errors in the region of 1 part in $10^5$, whilst maintaining a high ratio between the number of data points and the number of free parameters in the polynomial. Even so, it is possible that slight fitting pathologies have crept into the analysis. In figure 2.3, for example, the plots for the 220nm × 380nm and 220nm × 420nm wires show an unusually flat region between about 1.25$\mu$m and 1.35$\mu$m. This feature, however, is relatively slight, and is unlikely to affect further analysis.

The constant parameter $\beta_0$ is an unimportant phase-factor. The first-order parameter $\beta_1$ is the reciprocal of the group velocity. Again, this is of relatively little importance, as it merely describes the time taken for a pulse to leave a waveguide, rather than how it evolves whilst in the waveguide. Indeed, in the nonlinear Schrödinger formulation derived in section 2.2.2, $\beta_1$ is explicitly removed, by switching to a moving frame of reference. (It should be noted, however, that these coefficients cannot be neglected for the coupled waveguides considered in section 4.1.)

The most important coefficient is $\beta_2$, which gives the group velocity dispersion at the pump frequency. This is related to the pump-wavelength dispersion parameter by

$$\mathcal{D}(\lambda_0) = -\frac{2\pi c}{\lambda_0^2}\beta_2 \tag{2.18}$$

where the change in sign means that positive values will give normal GVD, and negative values will give anomalous GVD.

The coefficients $\beta_3$ and above comprise what is known as the *higher order dispersion* (HOD). These provide corrections to the parabolic dispersion model that results from considering $\beta_2$ only. In many systems, the impact of HOD is negligible, except at wavelengths very close to the zero-dispersion wavelengths [8]. For SOI however, HOD is very important [57, 99, 100, 101], and so it must be considered fully.

## 2.2 Optical nonlinearity

By optical nonlinearity, what we specifically mean is that the dielectric polarisation induced by an electric field is not directly proportional to that field. The general form of the polarisation (up to third order) is given by [97]

$$\begin{aligned} P_j \quad = \quad & \epsilon_0 \int_{-\infty}^{\infty} \hat{\chi}_{jk}^{(1)}(t-\tau_1)\, E_k(\tau_1)\, d\tau_1 \\ & + \epsilon_0 \int_{-\infty}^{\infty} \hat{\chi}_{jkl}^{(2)}(t-\tau_1, t-\tau_2)\, E_k(\tau_1)\, E_l(\tau_2)\, d\tau_1 d\tau_2 \\ & + \epsilon_0 \int_{-\infty}^{\infty} \hat{\chi}_{jklm}^{(3)}(t-\tau_1, t-\tau_2, t-\tau_3)\, E_k(\tau_1)\, E_l(\tau_2)\, E_m(\tau_3)\, d\tau_1 d\tau_2 d\tau_3 \end{aligned} \tag{2.19}$$

(which is written using Einstein notation, so that index duplication implies summation). The first of these terms corresponds to the linear dispersion considered above, the second term corresponds to quadratic nonlinearity (the Pockel's effect), and the third term corresponds to the Kerr effect.

This equation is extremely unwieldy, as the second-order tensor $\hat{\chi}^{(1)}$ contains 9 functions, the third-order tensor $\hat{\chi}^{(2)}$ contains 27 functions and the fourth order tensor $\hat{\chi}^{(3)}$ contains 81 functions. However, we assume silicon to be isotropic, which reduces equation 2.19 to

$$\begin{aligned} P_j &= \epsilon_0 \int_{-\infty}^{\infty} \hat{\chi}_0^{(1)} (t-\tau_1) E_j (\tau_1) d\tau_1 \\ &\quad + \epsilon_0 \int_{-\infty}^{\infty} \hat{\chi}_0^{(3)} (t-\tau_1, t-\tau_2, t-\tau_3) E_k (\tau_1) E_k (\tau_2) E_j (\tau_3) d\tau_1 d\tau_2 d\tau_3 \end{aligned} \tag{2.20}$$

where $\hat{\chi}_0^{(1)}$ and $\hat{\chi}_0^{(3)}$ are scalars, and the inherently anisotropic quadratic term has vanished completely. Secondly, we note that the nonlinearity of silicon is ultrafast [58] in that $\vec{P}$ responds effectively instantaneously to $\vec{E}$. Therefore, the cubic susceptibility becomes

$$\hat{\chi}_0^{(3)} = \chi_0^{(3)} \delta (t-\tau_1) \delta (t-\tau_2) \delta (t-\tau_3) \tag{2.21}$$

where $\chi_0^{(3)}$ is a scalar constant which defines the strength of the nonlinearity. The $\hat{\chi}_0^{(1)}$ term remains time-dependent, but this simply corresponds to linear dispersion considered in section 2.1.1.

Therefore, in bulk silicon, we have a displacement field of the form

$$\vec{D} = \epsilon_0 \epsilon (\omega) \vec{E} + \epsilon_0 \chi_0^{(3)} \left( \vec{E} \cdot \vec{E} \right) \vec{E} \tag{2.22}$$

In silicon (and in the majority of materials), $\chi_0^{(3)}$ is positive, meaning that refractive index increases with intensity. This is referred to as a *focusing nonlinearity*, as it enables the self-focusing effects that give spatial solitons.

We can generalise this to a waveguide by making the *effective index approximation*. We assume that the nonlinear propagation through a waveguide is the same as plane wave propagation through a bulk material with the same dispersion relation. We therefore rewrite equation 2.22 as

$$\vec{D} = \epsilon_0 n_{\text{eff}}^2 (\omega) \vec{E} + \epsilon_0 \chi_0^{(3)} \left( \vec{E} \cdot \vec{E} \right) \vec{E} \tag{2.23}$$

where the *effective refractive index* $n_{\text{eff}}$ is defined in terms of the modal propagation constant $\beta$ as $n_{\text{eff}} (\omega) = \beta c / \omega$.

### 2.2.1 Nonlinear continuous wave propagation

Before proceeding with a full dispersive treatment of nonlinear propagation, it is instructive to consider the propagation of continuous wave (CW) radiation through a nonlinear waveguide. We assume a sinusoidal wave of the form

$$\vec{E} = a\cos\left(\tilde{\beta}z - \omega t\right)\vec{F}' \tag{2.24}$$

where $a$ is an amplitude parameter, which we will shortly relate to the optical power. We have also replaced the linear propagation constant $\beta$ with a modified quantity $\tilde{\beta}$, which is to be determined. The field profile $\vec{F}'$ is normalised as

$$\vec{F}' = \frac{\vec{F}}{\sqrt{\int\int |\vec{F}|^2 dxdy}} \tag{2.25}$$

which is done so that $\int\int |\vec{F}'|^2 dxdy = 1$, thus allowing $a$ to uniquely control the optical power. Substituting this into equation 2.23 gives a displacement field of the form

$$\begin{aligned}\vec{D} &= \epsilon_0 n_{\text{eff}}^2(\omega)\, a\cos(kz-\omega t)\,\vec{F}' \\ &+ \epsilon_0\frac{3\chi_0^{(3)}}{4}|a|^2 a\cos(kz-\omega t)\left(\vec{F}'\cdot\vec{F}'\right)\vec{F}' \\ &+ \epsilon_0\frac{\chi_0^{(3)}}{4}|a|^2 a\cos(3kz-3\omega t)\left(\vec{F}'\cdot\vec{F}'\right)\vec{F}'\end{aligned} \tag{2.26}$$

where we have used the identity $\cos^3(\theta) \equiv \frac{3}{4}\cos(\theta) + \frac{1}{4}\cos(3\theta)$ to split the nonlinear term into its frequency components. The $\cos(3kz - 3\omega t)$ harmonic is not particularly important, as it isn't phase matched to the driving field, and will thus integrate to zero over successive wavecycles. Therefore, we can approximate this as zero.

Substituting the expressions for $\vec{E}$ and $\vec{D}$ (without the third-order harmonic term) into equation 2.5 gives

$$\tilde{\beta}^2 a\vec{F}' = \frac{\omega^2}{c^2}\left(n_{\text{eff}}^2(\omega)\, a\vec{F}' + \frac{3\chi_0^{(3)}}{4}|a|^2 a\left(\vec{F}'\cdot\vec{F}'\right)\vec{F}'\right) \tag{2.27}$$

where we have assumed $\vec{E}$ to have zero divergence, and have removed the diffractive $\nabla^2\vec{F}'$ term. We can eliminate the field profile from our equations by taking the scalar product with $\vec{F}'$ and integrating over the transverse plane. This gives the dispersion relation

$$\tilde{\beta}(\omega, a) = \sqrt{\frac{\omega^2}{c^2}\left(n_{\text{eff}}^2(\omega) + \frac{3\chi_0^{(3)}}{4S_{\text{eff}}}|a|^2\right)} \tag{2.28}$$

where the effective area $S_{\text{eff}}$ is given by

$$S_{\text{eff}} = \frac{\left(\int\int |\vec{F}|^2 dxdy\right)^2}{\int\int |\vec{F}|^4 dxdy} \tag{2.29}$$

If the intensity was uniform within the waveguide, and zero outside, then this quantity would correspond to the waveguide's cross-sectional area. In reality, this is not the case, and so $S_{\text{eff}}$ has a value which is similar but not identical to the real area.

We can rewrite equation 2.28 as

$$\tilde{n}\left(\omega, a\right) = \frac{\tilde{\beta}\left(\omega, a\right) c}{\omega} = \sqrt{n_{\text{eff}}^2\left(\omega\right) + \frac{3\chi_0^{(3)}}{4S_{\text{eff}}}|a|^2} \tag{2.30}$$

where $\tilde{n}$ is a modified refractive index. (As expected, this expression reduces to $n_{\text{eff}}$ in the lower-power limit.)

**Intensity and nonlinear refractive index**

The Poynting vector $\vec{S}$ is given by

$$\vec{S} = \vec{E} \times \vec{H} = c\epsilon_0\, n_{\text{eff}}\left(\omega\right)\left(\vec{E} \cdot \vec{E}\right)\hat{z} \tag{2.31}$$

where $\hat{z}$ is the direction of propagation. The total power vector can then be found by integrating over the transverse plane to give

$$\int\int \vec{S} dxdy = c\epsilon_0\, n_{\text{eff}}\left(\omega\right) a^2 \cos^2\left(\tilde{\beta}\left(\omega, a\right) z - \omega t\right)\hat{z} \tag{2.32}$$

Taking the mean of the $\hat{z}$ component over time gives the power $P$ as

$$P = \frac{c\epsilon_0\, n_{\text{eff}}\left(\omega\right)}{2}|a|^2 \tag{2.33}$$

It is convenient to treat the amplitude as being the square root of the optical power. Therefore, we define a new measure of amplitude

$$A \equiv a\sqrt{\frac{c\epsilon_0\, n_0}{2}} \tag{2.34}$$

which gives $P = |A|^2$ as required. In order to remove the explicit frequency dependence, we have replaced $n_{\text{eff}}\left(\omega\right)$ with a typical value $n_0$ which is representative of the frequency range of interest. Rewriting equation 2.30 using $A$ gives

$$\tilde{n}\left(\omega, A\right) = \sqrt{n_{\text{eff}}^2\left(\omega\right) + \frac{3\chi_0^{(3)}}{2c\epsilon_0\, n_0 S_{\text{eff}}}|A|^2} \tag{2.35}$$

The nonlinearity of silicon and silica are more conventionally described using their *nonlinear refractive indices*, rather than their $\chi_0^{(3)}$ values. The coefficient $n_2$ is defined as that fitting the approximation

$$\tilde{n}\left(\omega, I\right) = n\left(\omega\right) + I n_2 \tag{2.36}$$

where the intensity $I$ is given by $P/S_{\text{eff}}$. For silicon, this constant has a value between about $10^{-18}\,\text{m}^2\,\text{W}^{-1}$ and $10^{-17}\,\text{m}^2\,\text{W}^{-1}$ [55, 56], whilst for silica it is much smaller at about $3 \times 10^{-20}\,\text{m}^2\,\text{W}^{-1}$ [111]. We can relate $\chi_0^{(3)}$ with $n_2$ by assuming a weak nonlinearity and thus approximating equation 2.35 with a first-order binomial expansion

$$\tilde{n}\left(\omega, A\right) = n_{\text{eff}}\left(\omega\right) + \frac{3\chi_0^{(3)}}{4\epsilon_0 c\, n_0^2}\frac{|A|^2}{S_{\text{eff}}} \tag{2.37}$$

where in accordance with the effective index approximation, we have replaced the bulk index $n$ with the effective index. This conforms to equation 2.36, with $n_2$ given by

$$n_2 = \frac{3\chi_0^{(3)}}{4\epsilon_0 c\, n_0^2} \tag{2.38}$$

Using this conversion, we can rewrite equation 2.35 as

$$\tilde{n}\left(\omega, A\right) = \sqrt{n_{\text{eff}}^2\left(\omega\right) + \frac{2n_0 n_2}{S_{\text{eff}}}|A|^2} \tag{2.39}$$

### 2.2.2 Derivation of the Nonlinear Schrödinger Equation

We are now ready to derive a dispersive and nonlinear model of waveguide propagation. We proceed by making $A$ a function of time and position.

$$\vec{E} = \vec{F}'\left(\vec{x}\right) A\left(z, t\right) e^{i\beta_0 z - i\omega_0 t} \tag{2.40}$$

where the $e^{i\beta_0 z - i\omega_0 t}$ factor represents a carrier wave with frequency $\omega_0$ and wavenumber $\beta_0$. The variable $A$ is now a *slowly varying envelope*, which controls amplitude (via its absolute value), phase (via its complex argument) and spectral composition relative to the carrier wave (via temporal variation of its complex argument). We will see shortly that this envelope formulation allows us to reduce the second-order Maxwell equations into a first-order equation (in $z$). In the frequency domain, the field is given by

$$\tilde{\vec{E}} = \vec{F}'\tilde{A}\left(z, \omega - \omega_0\right) e^{i\beta_0 z} \tag{2.41}$$

In section 2.2.1 we showed how an electric field with frequency $\omega$ propagates with a wavenumber $\tilde{\beta}$. This implies a wave-equation of the form

$$\nabla^2 \vec{E} = \frac{\tilde{\beta}^2}{\omega^2}\frac{\partial^2 \vec{E}}{\partial t^2} \tag{2.42}$$

Taking the Fourier transform of equation 2.42 gives the Helmholtz equation

$$\nabla^2 \tilde{\vec{E}} = -\tilde{\beta}^2 \tilde{\vec{E}} \tag{2.43}$$

We wish to remove diffraction, and so we remove the transverse Laplacian from equation 2.43 to give

$$\frac{\partial^2 \tilde{\vec{E}}}{\partial z^2} = -\tilde{\beta}^2 \tilde{\vec{E}} \tag{2.44}$$

Substituting equation 2.41 into equation 2.44 gives

$$\frac{\partial^2 \tilde{A}}{\partial z^2} + 2i\beta_0 \frac{\partial \tilde{A}}{\partial z} - \beta_0^2 \tilde{A} = -\tilde{\beta}^2 \tilde{A} \tag{2.45}$$

It follows from equation 2.39 that the wavenumber is given by

$$\tilde{\beta}^2 = \beta^2 + \frac{2\beta_0 \omega_0 n_2}{S_{\text{eff}} c} |A|^2 \tag{2.46}$$

where the representative refractive index $n_0$ has been specified to be that at the carrier frequency, so that $n_0 = \beta_0 c/\omega_0$. Substituting this into equation 2.45 and rearranging gives

$$\frac{\partial \tilde{A}}{\partial z} + \frac{1}{2i\beta_0} \frac{\partial^2 \tilde{A}}{\partial z^2} + i \left( \frac{\beta_0^2 - \beta^2}{2\beta_0} \right) \tilde{A} = i \frac{\omega_0 n_2}{S_{\text{eff}} c} |A|^2 \tilde{A} \tag{2.47}$$

This can be rewritten as

$$\frac{\partial \tilde{A}}{\partial z} + \frac{1}{2i\beta_0} \frac{\partial^2 \tilde{A}}{\partial z^2} + i \left( \frac{\beta_0^2 - \beta^2}{2\beta_0} \right) \tilde{A} = i\gamma |A|^2 \tilde{A} \tag{2.48}$$

where we have replaced the constants in the nonlinear term with a single coefficient given by

$$\gamma \equiv n_2 \omega_0 / S_{\text{eff}} c \tag{2.49}$$

**Slowly varying envelope approximation**

If we assume that the light is spectrally narrow (i.e. $|\omega - \omega_0| \ll \omega_0$) then it follows that the same applies to wavenumber (i.e. $|\beta - \beta_0| \ll \beta_0$). This justifies the approximation $\beta_0^2 - \beta^2 \approx 2\beta_0(\beta_0 - \beta)$, giving

$$\frac{\partial \tilde{A}}{\partial z} + \frac{1}{2i\beta_0} \frac{\partial^2 \tilde{A}}{\partial z^2} + i \left( \beta_0 - \beta \right) \tilde{A} = i\gamma |A|^2 \tilde{A} \tag{2.50}$$

We are now readily to make our most important approximation: We drop the $\partial^2 \tilde{A}/\partial z^2$ term. The justification for this can be seen by taking the spatial Fourier transform of the derivative terms

$$\frac{1}{2i\beta_0} \frac{\partial^2 \tilde{A}}{\partial z^2} \quad \Rightarrow \quad \frac{(\beta - \beta_0)^2}{2i\beta_0} A \tag{2.51}$$

$$\frac{\partial \tilde{A}}{\partial z} \quad \Rightarrow \quad -i \left( \beta - \beta_0 \right) A \tag{2.52}$$

The coefficient in front of the second derivative is extremely small (being a small value squared), and so the whole term can be removed to give

$$\frac{\partial \tilde{A}}{\partial z} + i\left(\beta_0 - \beta\right)\tilde{A} = i\gamma|A|^2\tilde{A} \tag{2.53}$$

This simplification is known as the *slowly varying envelope approximation*. The envelope $A$ is spectrally narrow (both in terms of frequency and wavenumber), and hence it is broad both temporally and spatially. Therefore, the approximation amounts to requiring that the envelope must vary over a time scale that is much longer than the time period, and over a length scale that is much longer than the wavelength.

By using this approximation, we have reduced a second-order equation (in distance) to a first-order equation, which is extremely useful for finding both analytical and numerical solutions.

We can then replace $\beta$ with the Taylor expansion denoted by equation 2.17, and so specify the waveguide dispersion by using the coefficients described in section 2.1.2. This gives

$$\frac{\partial \tilde{A}}{\partial z} - i\left(\left(\omega - \omega_0\right)\beta_1 + \frac{1}{2}\left(\omega - \omega_0\right)^2\beta_2 + \cdots\right)\tilde{A} = i\gamma|A|^2\tilde{A} \tag{2.54}$$

Finally, we switch back to the time domain (noting both that $\tilde{A}$ is a function of $\omega - \omega_0$ and not just $\omega$, and that $|A|^2$ is a function of $t$ and not $\omega$), to give the Generalised Nonlinear Schrödinger Equation

$$\frac{\partial A}{\partial z} - i\sum_{m=2}^{M} i^m \frac{\beta_m}{m!}\frac{\partial^m A}{\partial t^m} = i\gamma|A|^2 A \tag{2.55}$$

where $M$ is the total number of $\beta_m$ coefficients used to fit the dispersion relation. We have removed the $\beta_1$ term (the reciprocal of the group velocity) which amounts to switching to a moving frame of reference. The reason for this is simply because the group velocity is largely irrelevant. We are interested in how light interacts with light, and the velocity at which these interactions takes place is a needless distraction from the fundamental physics of the situation. (Additionally, the removal of group velocity can be useful when finding numerical solutions, as the entire simulation can be confined to a relatively small time window.)

In the simplest possible dispersive case, we can truncate the expansion of $\beta$ to second order. This gives the Nonlinear Schrödinger Equation as

$$\frac{\partial A}{\partial z} + i\beta_2\frac{\partial^2 A}{\partial t^2} = i\gamma|A|^2 A \tag{2.56}$$

### 2.2.3 Generalised nonlinearity

Equation 2.55 is in fact only one example of a Generalised Nonlinear Schrödinger Equation. We can in principle replace the cubic term with any nonlinear function of $A$.

If we consider a more general nonlinear polarisation $\vec{P}_{\mathrm{NL}}$, such that the displacement field is

given by

$$\vec{D} \equiv \epsilon_0 \, \epsilon \left( \omega \right) \vec{E} + \vec{P}_{\mathrm{NL}} \tag{2.57}$$

we can derive an equation of the form

$$\frac{\partial A}{\partial z} - i \sum_{m=2}^{M} i^m \frac{\beta_m}{m!} \frac{\partial^m A}{\partial t^m} = i \frac{\omega_0}{2 \epsilon_0 n_0 c} \Lambda_{\mathrm{NL}} \tag{2.58}$$

where $\vec{P}_{\mathrm{NL}}$ has been represented by a slowly varying envelope $\Lambda_{\mathrm{NL}} \left( z, t \right)$, such that

$$\vec{P}_{\mathrm{NL}} = \frac{1}{2} \vec{F}' \left( \Lambda_{\mathrm{NL}} e^{i \beta_0 z - i \omega_0 t} + \Lambda^*_{\mathrm{NL}} e^{-i \beta_0 z + i \omega_0 t} \right) \tag{2.59}$$

If there are multiple sources of nonlinearity, then we can generalise this to

$$\vec{P}_{\mathrm{NL}} = \frac{1}{2} \vec{F}' \sum_{n=1}^{N} \left( \Lambda_{\mathrm{NL}n} e^{i \beta_{0n} z - i \omega_{0n} t} + \Lambda^*_{\mathrm{NL}n} e^{-i \beta_{0n} z + i \omega_{0n} t} \right) \tag{2.60}$$

where $\Lambda_{\mathrm{NL}n}$ is the envelope for a nonlinear term with carrier frequency $\omega_{0n}$ and wavenumber $\beta_{0n}$. We will return to this formulation in chapter 6, where the evolution of solitons sustained by the Raman effect (rather than Kerr nonlinearity) is considered.

### 2.2.4 Elementary solutions and dimensionless units

As we are interested in finding solitons, it is convenient to switch to a system of dimensionless units that reflects this fact. For negative $\beta_2$ (i.e. anomalous GVD) a soliton solution to equation 2.56 of the form

$$A \left( z, t \right) = \frac{1}{T_0} \sqrt{\frac{|\beta_2|}{\gamma}} \exp \left( i \frac{|\beta_2|}{2 T_0^2} z \right) \mathrm{sech} \left( \frac{t}{T_0} \right) \tag{2.61}$$

exists, where $T_0$ defines its temporal width. We will consider this solution in detail in section 3.1, but at present will merely use it as a basis for intrinsic units. The power profile of this solution is given by

$$P = |A|^2 = \frac{|\beta_2|}{T_0^2 \gamma} \mathrm{sech}^2 \left( \frac{t}{T_0} \right) \tag{2.62}$$

and so the peak power is given by

$$P_0 = \frac{|\beta_2|}{T_0^2 \gamma} \tag{2.63}$$

This is the soliton threshold power, above which solitons can (for a given pulse duration) form. It can be written as

$$P_0 = \frac{1}{L_{\mathrm{D}} \gamma} \tag{2.64}$$

where we have defined the *dispersion length* to be $L_{\mathrm{D}} \equiv T_0^2 / |\beta_2|$. Roughly speaking, this is the "typical" length scale over which dispersion becomes significant. A more specific definition is that a Gaussian pulse (of the form $e^{-\tau^2 / 2 T_0^2}$) will increase in width by a factor of $\sqrt{2}$ after one dispersion length [8].

**Dimensionless units**

The NLS can be converted into dimensionless form by setting $T_0$, $P_0$ and $L_\mathrm{D}$ to unity, which reduces the soliton solution to an unscaled sech function (multiplied by an appropriate phase factor). The conversion is achieved by making the substitutions

$$t = T_0\tau \tag{2.65}$$

$$z = L_\mathrm{D}\zeta \tag{2.66}$$

$$|A|^2 = P_0|E|^2 \tag{2.67}$$

This gives

$$\frac{\partial E}{\partial \zeta} + \sum_{m=2}^{M} i^{m-1} p_m \frac{\partial^m E}{\partial \tau^m} = i|E|^2 E \tag{2.68}$$

where higher order dispersion has been reintroduced, with the corresponding coefficients being

$$p_m = \frac{\beta_m L_\mathrm{D}}{m! T_0^m} = \frac{\beta_m T_0^{2-m}}{m!|\beta_2|} \tag{2.69}$$

It follows from its definition that $p_2 = \pm\frac{1}{2}$, with the sign depending on whether the GVD is normal or anomalous.

These intrinsic units depend on the system, but it is instructive to consider typical values. The value of $T_0$ is defined by the temporal power profile of the input pulse, which we assume to be from a mode-locked laser. These devices are widely used as sources of ultrashort pulses, including experiments with silicon (e.g. [57, 76, 72]). Notably, their pulse shape is the same as the above soliton, having a power profile of the form $P \propto \mathrm{sech}^2\,(t/T_0)$ [112, 113]. It is conventional to define pulse width using full width at half maximum (FWHM), which is related to $T_0$ by the relation $T_\mathrm{FWHM} \equiv 2\ln\left(1+\sqrt{2}\right) T_0$. Throughout most of this report we assume a 100fs FWHM, giving a value of $T_0 \approx 56.730$fs.

The value of $L_\mathrm{D}$ is dependent on the waveguide geometry and the operational wavelength. For the systems considered, it ranges from about 0.5mm to 2mm. It should be noted that these values are exceptionally small; in fibre optics, values of metres or even kilometres are more typical.

The value of $P_0$ is usually of the order a few watts, which again is exceptionally low. It can in principal be derived from other physical parameters using equation 2.49, but this is problematic due to the accuracy with which these coefficients are known. In section 3.3.2 we analyse this problem in more detail, and attempt to derive a value from (third party) experimental data. This ambiguity in $P_0$ is not particularly important from a mathematical point of view, as it merely corresponds to a scaling of the necessary input power.

**Dispersion Operator**

It is convenient to combine all the time derivative terms into a single operator. This enables us to write the NLS equation in the more compact form of

$$\frac{\partial E}{\partial \zeta} - i\hat{D}E = i|E|^2 E \tag{2.70}$$

where the operator $\hat{D}$ is defined as

$$\hat{D} \equiv \sum_{m=2}^{M} p_m \left( i\frac{\partial}{\partial \tau} \right)^m \tag{2.71}$$

## 2.3 Optical loss

Optical loss can be accounted for by noting that—mathematically speaking—attenuation is the same as wave propagation, but with an imaginary propagation constant. For linear attenuation, we replace the linear propagation constant with a complex number of the form

$$\beta \rightarrow \beta + \frac{i}{2}\alpha \tag{2.72}$$

where $\alpha$ is the attenuation coefficient. (The factor of $\frac{1}{2}$ results from the fact that we have specified the absorption in terms of amplitude, whereas the attenuation coefficient is conventionally defined in terms of power.)

This loss primarily results from leakage to the waveguides having rough edges, and from optical coupling to the substrate on which the waveguide is fabricated [114]. Material absorption has been tentatively suggested as an additional loss mechanism [115]. Absorption typically ranges from about 2 $\mathrm{dB\,cm^{-1}}$[116] to 5 $\mathrm{dB\,cm^{-1}}$ [63], but values as low as $\sim$ 1$\mathrm{dB\,cm^{-1}}$ have been achieved [117, 118].

Making this replacement gives

$$\frac{\partial E}{\partial \zeta} - i\hat{D}E = i|E|^2 E - \epsilon_{\mathrm{l}} E \tag{2.73}$$

where we have represented $\alpha_{\mathrm{l}}$ in dimensionless units as $\epsilon_{\mathrm{l}} \equiv L_{\mathrm{D}}\alpha_{\mathrm{l}}/2$.

### 2.3.1 Multi photon absorption

Another important effect is two photon absorption. This occurs when two or more photons combine to overcome silicon's $\sim$ 1.1eV indirect bandgap, and generate free charge carriers [119]. (For silica, with its very large $\sim$ 9eV bangap [120], this effect is insignificant.) Just

as linear dispersion and absorption are interlinked, so are their nonlinear counterparts. The optical nonlinearity is an inevitable consequence (again mathematically formalised by a Kramers Krönig transformation) of these nonlinear absorptions [121, 122].

Two photon absorption can be represented by changing the nonlinear refractive index as

$$n_2 \rightarrow n_2 + i\frac{c\alpha_{2\mathrm{pa}}}{2\omega_0} \tag{2.74}$$

where $\alpha_{2\mathrm{pa}}$ is the two-photon-absorption coefficient. This has a value between about $0.3 \times 10^{-11}\,\mathrm{mW}^{-1}$ and $1.1 \times 10^{-11}\,\mathrm{mW}^{-1}$ [55, 56].

Making this substitution yields

$$\frac{\partial E}{\partial \zeta} - i\hat{D}E = i|E|^2E - \epsilon_1 E - \epsilon_{2\mathrm{pa}}|E|^2E \tag{2.75}$$

where the dimensionless 2PA coefficient is given by $\epsilon_{2\mathrm{pa}} \equiv (\alpha_{2\mathrm{pa}}P_0L_\mathrm{D}) \,/\, (2S_\mathrm{eff})$. This coefficient is the ratio between the real and imaginary parts of the refractive index (such that the complex index is given by $(1 + \epsilon_{2\mathrm{pa}}i)\, n_2$). It is this ratio (rather than the absolute values) which is of particular importance for soliton dynamics [123], and so it is useful to specify $\epsilon_{2\mathrm{pa}}$ directly, rather than deriving it from $\alpha_{2\mathrm{pa}}$. In section 3.3.2 this coefficient is determined from (third-party) experimental data [54], yielding a value of $\epsilon_{2\mathrm{pa}} = 0.1$. This is consistent with other estimates, which range from 0.1 [124] to 0.14 [64].

#### Three photon absorption

In section 3.3.2 we propose the existence of three photon absorption. This is known to exist at much longer wavelengths where the photon energy is less than half the 1.1 eV bandgap making 2PA impossible [117], but we propose that it is also present when 2PA is possible. This can be modelled by adding a quintic absorption term to 2.75, giving

$$\frac{\partial E}{\partial \zeta} - i\hat{D}E = i|E|^2E - \epsilon_1 E - \epsilon_{2\mathrm{pa}}|E|^2E - \epsilon_{3\mathrm{pa}}|E|^4E \tag{2.76}$$

where $\epsilon_{3\mathrm{pa}}$ gives the magnitude of the absorption. In section 3.3.2 we estimate it to have a value of 0.05.

### 2.3.2 Free charge carrier interactions

Another important effect is the impact of the free charge carriers (FCCs) excited by the multiphoton absorption. These can both absorb photons [74], and change the refractive index of the material [125].

The absorption is proportional to the number of free carriers, and so can represented by ex-

tending the modification to $\beta$ given by transformation 2.72 to

$$\beta \rightarrow \beta + \frac{i}{2}\alpha + \frac{i}{2}\sigma N \tag{2.77}$$

where $N$ is the volumetric density of free carriers, and $\sigma$ is the cross section of the absorption. [78].

The change in refractive index $\Delta n$ caused by an increase in carrier density $\Delta N$ can be expressed as

$$\Delta n = -N_{\mathrm{fc}} k \Delta N \tag{2.78}$$

where the constant $N_{\mathrm{fc}}$ is defined by this relation, and has a value of approximately $1.35 \times 10^{-27}\,\mathrm{m}^3$ [69, 126, 127]. In this expression, the free space wavenumber is given by $k$. If the FCC density starts from a low value, this can be approximated as $\Delta n = N_{\mathrm{fc}} N$.

We can directly subtract this from $\beta$, but it is more conventional [124] to instead add an imaginary component to the cross section, such that

$$\sigma_{\mathrm{fc}} = \sigma_{\mathrm{abs}} + i\sigma_{\mathrm{ind}} \tag{2.79}$$

where the real component $\sigma_{\mathrm{abs}}$ is the absorption, and the imaginary component $\sigma_{\mathrm{ind}} = 2N_{\mathrm{fc}}k$ represents the index change. In the wavelength region of interest, $\sigma_{\mathrm{abs}}$ has a value of approximately $1.45 \times 10^{-21}\,\mathrm{m}^2$, whilst $\sigma_{\mathrm{ind}}$ is approximately $1.09 \times 10^{-20}\,\mathrm{m}^2$, giving a combined value of $\sigma_{\mathrm{fc}} = 1.45 \times 10^{-21}\,(1 + 7.5i)\ \mathrm{m}^2$ [124]. Making the replacement gives

$$\frac{\partial E}{\partial \zeta} - \hat{D}E = i|E|^2E - \epsilon_1 E - \epsilon_{2\mathrm{pa}}|E|^2E - \epsilon_{3\mathrm{pa}}|E|^4E - \epsilon_{\mathrm{fc}}E\nu \tag{2.80}$$

where we have converted $\sigma_{\mathrm{fc}}$ into dimensionless units as $\epsilon_{\mathrm{fc}} \equiv L_{\mathrm{D}}\sigma_{\mathrm{fc}}N_0/2$. The scaled carrier density $\nu$, and the conversion factor $N_0$ are described below.

### Evolution of free charge carriers

To fully account for free charge carrier effects, the NLS must be coupled to another equation describing the carrier evolution. The volumetric density of charge carriers is given by [78]

$$\frac{\partial N}{\partial t} = \frac{\alpha_{2\mathrm{pa}}}{2\hbar\omega_0 S_{\mathrm{eff}}^2}|A|^4 - \frac{1}{t_{\mathrm{c}}}N \tag{2.81}$$

where $\hbar$ is the reduced Planck's constant. The first term corresponds to the excitation of charge carriers by two-photon-absorption, whilst the second term corresponds to carrier decay, with a mean lifetime of $t_{\mathrm{c}}$. This can range from 10ns to 200ns [128], and is dependent on the waveguide geometry [129]. The exact value of the lifetime is not particularly important for the purpose of this report, as it is both much larger than the pulse durations used, and much smaller than the pulse repetition time (a value of $4\mu$s is used in section 3.3). Therefore we can assume decay to be negligible within pulses, but total between pulses, removing the need for a precise figure.

The equation for free-charge-carrier evolution can be converted into the same system of units as that used for the NLS by making the further substitution $N \equiv \nu N_0$, where $N_0$ is a typical free-charge-carrier density, which is given by

$$N_0 \equiv \frac{\alpha_{2\mathrm{pa}} T_0 P_0^2}{2\hbar\omega_0 S_{\mathrm{eff}}^2} \tag{2.82}$$

This gives

$$\frac{\partial \nu}{\partial \tau} = |E|^4 - \frac{\nu}{\tau_{\mathrm{c}}} \tag{2.83}$$

where the recombination time has been scaled as $\tau_{\mathrm{c}} \equiv t_{\mathrm{c}}/T_0$. At a given point in distance, this equation is readily converted to integral form, giving

$$\nu = e^{-\tau/\tau_{\mathrm{c}}} \int_{\tau'=0}^{\tau} |E|^4 e^{\tau'/\tau_{\mathrm{c}}} d\tau' + \nu_{\tau=0} e^{-\tau/\tau_{\mathrm{c}}} \tag{2.84}$$

where the integration constant $\nu_{\tau=0}$ gives the carrier density at $\tau = 0$.

## 2.4 Summary of the model

The propagation of light through a silicon on insulator photonic wire is described by

$$\boxed{\frac{\partial E}{\partial \zeta} - i\hat{D}E = i|E|^2 E - \epsilon_{\mathrm{l}} E - \epsilon_{2\mathrm{pa}}|E|^2 E - \epsilon_{3\mathrm{pa}}|E|^4 E - \epsilon_{\mathrm{fc}} E\nu} \tag{2.85}$$

where the dispersion operator $\hat{D}$ is defined as

$$\hat{D} \equiv \sum_{m=2}^{M} p_m \left( i\frac{\partial}{\partial \tau} \right)^m \tag{2.86}$$

and where the evolution of the free charge carriers is described by

$$\frac{\partial \nu}{\partial \tau} = |E|^4 - \frac{\nu}{\tau_{\mathrm{c}}} \tag{2.87}$$

**Using the model**

We now have a model capable of describing the evolution of SOI waveguides. The next chapter is devoted to finding solutions of equation 2.85, and to understanding the physical phenomena that they represent.

# Chapter 3

# Nonlinear propagation in SOI waveguides

## 3.1 Temporal solitons

Temporal optical solitons were first predicted by Akira Hasegawa in 1973 [130], and first observed experimentally by Linn Mollenauer and Roger Stolen in 1980 [13]. Since then, solitons have become fundamental to modern optics. They have been applied in pulsed laser systems [131], optical logic gates [132], and optical data lines. It is possible to transmit solitons over thousands of km [133]; this has not only been achieved in loops of fibre in a laboratory, but in a 2872 km communication line between the Australian cities of Perth and Adelaide [134].

Optical solitons were originally observed in conventional fibre [13]. More recently, the need for dispersion tailoring has seen photonic crystal fibre (PCF) used as a medium for soliton propagation. [135]. These fibres have an intricate transverse structure of glass and air-gaps which run through their entire length. By selecting the geometry of this structure, the group velocity dispersion (GVD) can be greatly altered, thus allowing for anomalous GVD in materials with a normal bulk GVD.

Interest in solitons has naturally carried over into silicon on insulator, which is an ideal medium as it provides both strong ultrafast nonlinearity [55, 56, 58], and (like PCF) the capability for substantial dispersion tailoring [47, 48, 49]. Solitons in silicon on insulator have been observed by groups at Columbia University [57] and Rochester University [63]. In section 3.3, the results of a collaboration with experimentalists at the University of Bath are presented, further strengthening the base of evidence for the existence of solitons in silicon waveguides.

These solitons can be analysed using the model derived in the previous chapter. In the absence of damping and higher order dispersion, the NLS equation (equation 2.85) admits an extremely

well known bright soliton solution of the form [23, 8, 97, 98]

$$E(\zeta,\tau) = \sqrt{2q}\,\mathrm{sech}\left(\sqrt{2q}\,\tau\right) e^{iq\zeta} \tag{3.1}$$

where $q$ (which must be positive) is the wavenumber. This solution (plotted in figure 3.1) requires anomalous GVD, such that $p_2 = -\frac{1}{2}$.

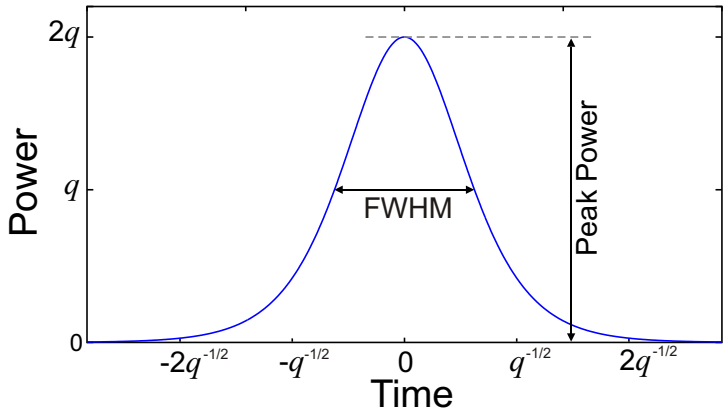


Figure 3.1: The sech-like soliton solution, displayed as function of power against time. The peak power is given by $2q$, whilst the FWHM duration is given by $2\ln\left(1+\sqrt{2}\right)/\sqrt{2q}$

This is not an exact solution when damping or higher order dispersion is reintroduced. In fact, for the general case, no exact soliton solution can exist. Although solitons can never retain their shape perfectly in a real system, they can certainly exist, as is shown in section 3.1.1. The loss of exactitude also corresponds to the absence of the phase-shift on collision property described in section 1.1.2. Whilst solutions to the ideal NLS equation can pass through one another with only a phase shift, this effect is broken for the more realistic model, as is shown in section 3.3.3 [23].

The special case of $q = \frac{1}{2}$, gives $E(\zeta,\tau) = \mathrm{sech}\,(\tau)\,e^{i\zeta/2}$, namely a pulse of unit duration and unit amplitude in the dimensionless units defined in section 2.2.4. In equation 3.1, the duration and the amplitude are both linked to $q$, and so by specifying one, the other will also be specified. For a given pulse duration, the corresponding power is known as the *soliton threshold*. It follows from the choice of dimensionless units that a pulse with unit duration has a unit soliton threshold. In real units, the soliton threshold is $P_0$, as defined in equation 2.64.

In the spectral domain, equation 3.1 has the power profile

$$P(\omega) \propto \mathrm{sech}^2\left(\frac{\pi}{\sqrt{8q}}\,\omega\right) \tag{3.2}$$

where the spreading about the carrier frequency (which is given by $\omega = 0$ due to the moving frame of reference) is a consequence of the pulse having a finite duration. The solution is in fact *transform limited* in that the bandwidth is as small as it possibly can be, and is limited only by this fundamental effect. For a 100fs second pulse at 1.5$\mu$m, this gives a FWHM spectral

bandwidth of 24nm.

Physically, the sech-like soliton corresponds to a balance between self phase modulation (SPM) and dispersive pulse broadening. SPM is a nonlinear effect that occurs in optical pulses, and is the temporal analogue of spatial self-focussing [8]. At the leading edge of the pulse, the refractive index increases with time, due to the rising intensity. This gives the phase of the optical wave an extra time dependence, which retards the fundamental temporal oscillation of the electromagnetic wave, thus redshifting it. Conversely, at the trailing edge of the pulse, the reverse happens, causing a blueshift. In an anomalously dispersive medium, blue light (by definition) has a higher group-velocity than red light, and so without nonlinearity, the pulse would lengthen. (The terms red and blue are used figuratively, to describe longer and shorter wavelengths.) This, however, is counteracted by the SPM. The strength of SPM is power dependent, and at the soliton threshold, the two effects precisely cancel to give a soliton.

With normal GVD, the SPM acts to reinforce dispersive pulse broadening, and so a soliton will not be formed. Dark solitons *are* possible however [136], as the leading edge of the soliton corresponds to decreasing (rather than increasing) amplitude, and so SPM acts in the opposite direction. Bright solitons can also be seen in the normal regime, by using materials with a defocussing nonlinearity such as aluminium gallium arsenide (AlGaAs) [137], again reversing the direction of SPM.

This soliton in equation 3.1 is not the only one that exists for the ideal system. (It is, however, the most common, and is known as the *fundamental soliton*.) There exist so-called *higher order solitons*, which can be excited with an initial condition of $E(\tau) = N\,\mathrm{sech}\,(\tau)$, where $N$ is an integer. These solutions change shape as they propagate (but return to their original state at periodic intervals) and are known as *breathers* [23]. They are, however, unlikely to be seen in silicon on insulator, as they break up in the presense of linear absorption [138], nonlinear absorption [123] and other deviations [23]. A breather can be thought of as a superposition of solitons, and perturbations will cause these to separate. This pulse fission is considered in section 3.2.1.

It should be noted that these soliton solutions can be formally derived from the NLS equation by a procedure known as the *inverse scattering transform* [139]. This is an extremely powerful method of solving nonlinear partial differential equations, which can also be used to extract solutions from other soliton-yielding equations such as the Sine-Gordon equation and Korteweg-de Vries equation [44]. For the purpose of this report, however, such a formal approach is unnecessary, and will not be considered further.

### 3.1.1 Soliton formation

Pulse evolution in a lossless waveguide was modelled numerically for a range of input powers, as is shown in figure 3.2. (The temporal pulse profile at $\zeta = 0$ was specified, and this was advanced in $\zeta$ to the desired output value. The computational algorithm is described in appendix A.1.)

The input consisted of transform limited pulses with a 1.5$\mu$m carrier frequency and a FWHM duration of 100fs. A waveguide 220nm in height and 420nm in width was chosen. The waveguide was also assumed to be topped with a 100nm thick layer of a material with refractive index 1.35, in order to simulate an etching mask. The dispersion relation of this geometry is given in figure 2.3.

This waveguide provides a strong anomalous GVD (at the chosen 1.5$\mu$m pump wavelength) of 3934 $\mathrm{ps\,nm^{-1}\,km^{-1}}$. The zero dispersion wavelengths (ZDWs) are well removed from the pump, having values of 1.243$\mu$m and 1.736$\mu$m. This provides low higher order dispersion (with $\beta_3 = 0.00615$). The waveguide geometry is therefore well suited for observing straightforward soliton evolution, without the complication of other effects.

When the wire is pumped with pulses having a peak power below the soliton threshold, the SPM is unable to fully compensate for the dispersive pulse broadening, and so the pulse duration increases. At the soliton threshold, a soliton is formed. Above the soliton threshold power, the focussing effect of SPM exceeds the dispersive pulse broadening, and we see pulse compression.

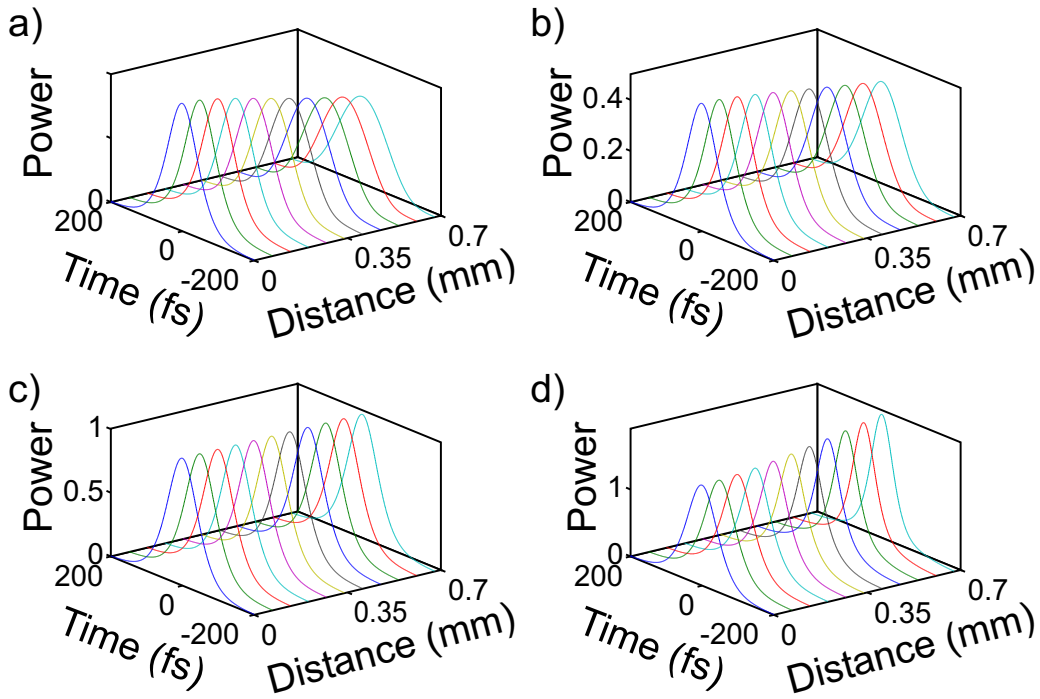


Figure 3.2: Propagation of 100fs sech-like pulses through a 220nm × 420nm SOI waveguide in the absence of damping. Shown over a 0.7mm (1 dispersion length) propagation distance. a) At low power $\epsilon P_0$ (where $\epsilon \ll 1$, giving quasi-linear evolution), the pulse disperses. b) At $0.5P_0$ dispersion is suppressed but not eliminated. c) At $P_0$ pulse broadening is precisely counteracted by SPM, forming a soliton. d) At $1.5P_0$ SPM starts to overcompensate for dispersive broadening, causing pulse compression.

**Damped solitons**

In a real SOI wire, the effect of damping significantly affects soliton evolution. We therefore assume a 2PA coefficient of $\epsilon_{2\text{pa}} = 0.1$. This value has been reported in the literature [124], and is that which will be extracted from experimental data in section 3.3.2. We also assume a linear damping of $\epsilon_{\text{l}} = 0.01$, giving a real-unit attenuation of 1.3 dB cm$^{-1}$, which is low but perfectly realisable [117, 118]. On the other hand, the effect of free charge carriers is negligible at these relatively low energies, and will only become important when we consider more energetic pulses in the following sections.

When we introduce this damping (figure 3.3), we no longer see a soliton at the threshold energy. Instead, we must increase the energy slightly to compensate for the energy loss.

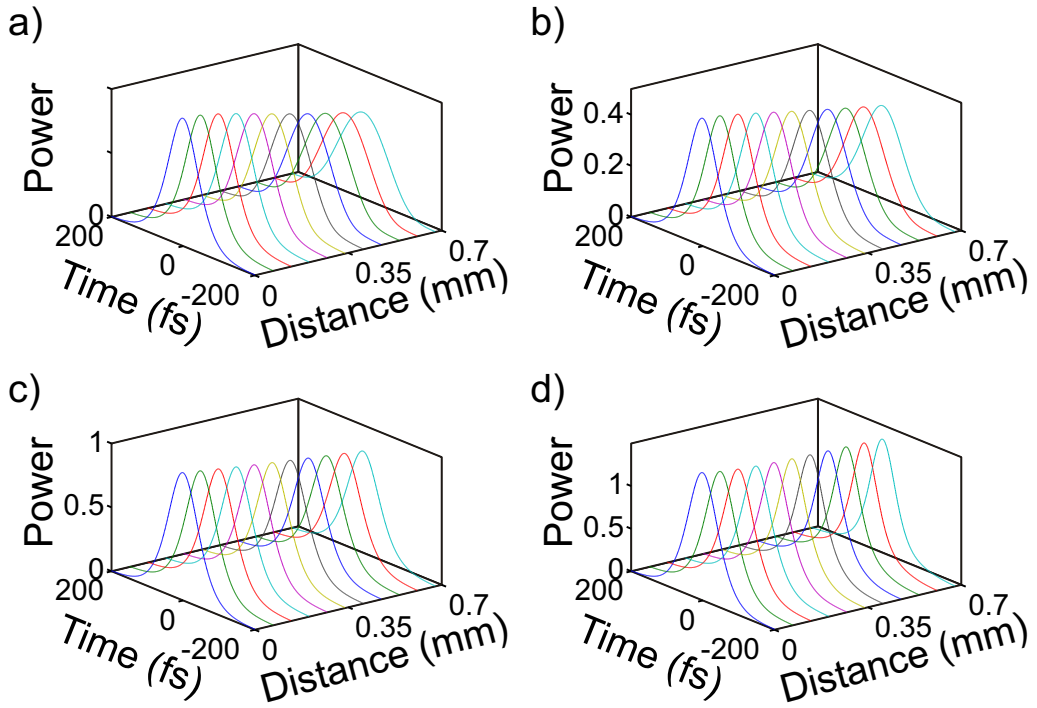


Figure 3.3: Propagation of 100fs sech-like pulses through a 220nm × 420nm SOI waveguide with both linear and nonlinear damping included. Shown over a 0.7mm (1 dispersion length) propagation distance propagation distance. a) At low power $\epsilon P_0$ (where $\epsilon \ll 1$), the pulse broadens. b) At $0.5P_0$ dispersive pulse broadening is suppressed but not eliminated. c) At $P_0$ there is (unlike with the undamped case) still some pulse broadening. d) At $1.5P_0$ the best approximation to a soliton is formed, as the increased power compensates for the energy loss. (Note that after a slight change in pulse shape, it settles down into an unchanging waveform.)

### 3.1.2 Soliton compression

Pulse compression happens at powers above the soliton threshold, due to nonlinearity over-compensating for the dispersive pulse broadening [8]. This has been observed in PCF [39] and

glass nanowires [140]. The soliton pulse compression effect is demonstrated in figure 3.4 for a 220nm × 420nm wire, showing that a 100fs pulse (with power $3.5P_0$) is nonlinearly compressed to 34fs. This effect is put to use in section 5.2, where a spatiotemporal soliton requiring an upper pulse duration of 80fs is generated from a 100fs pulse.

The $3.5P_0$ pulse gives a roughly optimal compression ratio, as it occurs at a power slightly below that of the first higher order soliton (which having twice the amplitude of the fundamental soliton, occurs at $4P_0$). Therefore the pulse isn't a superposition of multiple solitons, and so a relatively clean compression effect can be seen. At higher powers (at $7P_0$ for instance, as is shown in figure 3.4) the pulse *is* a higher order soliton, which under perturbation will break up. This soliton fission is considered in more detail in section 3.2.1. (It is in fact possible to compress pulses further, by using tapered waveguides in which the GVD gradually decreases along the propagation length. As a soliton moves, the soliton threshold gradually drops, providing a gentle but sustained compression effect, allowing for compression ratios of over ten to one [141].)

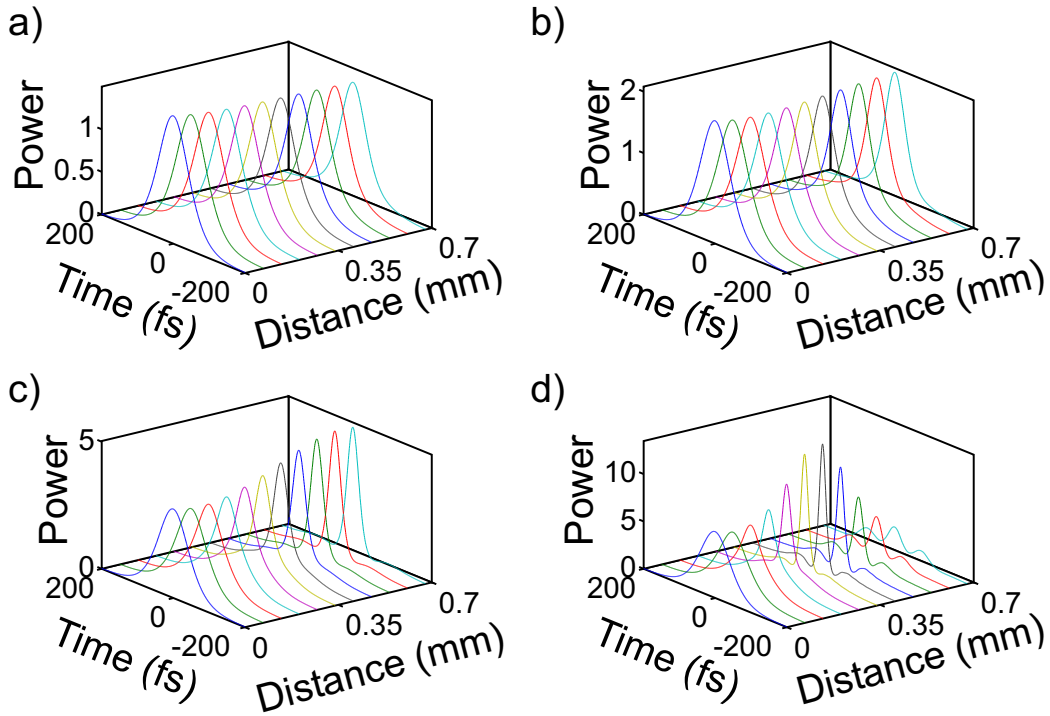


Figure 3.4: Compression of a 100fs pulse in a 220nm × 420nm SOI waveguide. Shown over a 0.7mm (1 dispersion length) propagation distance. The model includes both linear and nonlinear damping. a) At $1.5P_0$ a soliton exists. b) At $2P_0$ pulse compression occurs. c) At $3.5P_0$ maximal pulse compression occurs, with the pulse being reduced to 34fs. d) At $7P_0$ the pulse splits.

### 3.1.3 Čerenkov radiation

The sech-like soliton is extremely robust, in that it can retain its basic shape in the presence of a range of perturbations [130]. This stability primarily results from the wavenumber of each frequency component within the soliton being different from the wavenumber of linear radiation at the same frequency [142]. Therefore, light can't easily escape from the soliton, as it has no available mode to leak into. In the presence of HOD, however, the soliton's dispersion relation may overlap with the linear dispersion relation at a frequency away from the pump. In this case, resonant radiation can occur [142], as the matching of wavenumbers will cause a continuous matching of phase over the soliton's length. (This phase matching can also allow a soliton to interact with an external signal of continuous-wave radiation [143].) It is possible for resonant radiation to be excited in a different waveguide mode to the soliton [144, 145], although this unlikely to occur in SOI, as the only other waveguide mode (as mentioned in section 2.1.2) has little projection onto the fundamental mode. Resonant radiation has been observed in both glass fibres [146, 147, 148, 149], and silicon wires [57].

When a charged particle travels faster than (the refractive phase velocity of) light, Čerenkov radiation is emitted. This is the optical equivalent of a sonic boom, and is most famously seen as the blue glow surrounding water-cooled nuclear reactors, where it is emitted by high-energy electrons. An optical soliton has a physical presence in the form of an index-shifted region of material, and this may also travel faster than (the refractive phase velocity of) light and thus emit Čerenkov radiation. It can be shown that this emission of Čerenkov radiation is in fact the same phenomenon as the above resonant radiation [142, 150]. They differ, however, in that soliton radiation requires phase matching, which is a consequence of the fact that whilst electrons are much smaller than the wavelength of the light they emit, solitons are much larger.

We can calculate the frequency of resonance by taking the ideal soliton solution (equation 3.1) and adding a small perturbation $\epsilon(\zeta,\tau)$ to it, such that

$$E(\zeta,\tau) = \left(\sqrt{2q}\,\mathrm{sech}\left(\sqrt{2q}\,\tau\right) + \epsilon(\zeta,\tau)\right) e^{iq\zeta} \tag{3.3}$$

Substituting this into the full equation of motion (equation 2.85) gives

$$iq\epsilon + \frac{\partial\epsilon}{\partial\zeta} = i\left[\hat{D} - \frac{1}{2}\frac{\partial^2}{\partial\tau^2}\right]\sqrt{2q}\,\mathrm{sech}\left(\sqrt{2q}\,\tau\right) + i\hat{D}\epsilon + 2iq\left(2\epsilon + \epsilon^*\right)\mathrm{sech}^2\left(\sqrt{2q}\,\tau\right) \tag{3.4}$$

where terms containing $\epsilon^2$ and $\epsilon^3$ have been discounted (as we are treating $\epsilon$ as a small perturbation, rather than a general correction). We have also removed damping. The left hand side of this equation admits sinusoidal solutions, and so the whole equation can be thought of as a linear oscillator in $\epsilon$ (oscillating not with time, but with space) driven by an oscillatory force of magnitude $\sqrt{2q}\,\mathrm{sech}\left(\sqrt{2q}\,\tau\right)$. We can search for resonances by determining the natural frequency of the oscillator system, and then matching this with the spatial wavenumber $q$. As $\epsilon$ is already modulated by $q$, these resonances will happen when $\epsilon$ shows no oscillation with respect to $\zeta$.

We therefore remove the driving terms (i.e. those not containing $\epsilon$). We also neglect the $2iq\left(2\epsilon+\epsilon^{*}\right)\operatorname{sech}^{2}\left(\sqrt{2q}\,\tau\right)$ term (which describes the refractive index change induced by the soliton field). Whilst this term is of importance when calculating the radiation amplitude [151], it can be neglected when we merely wish to determine the frequency of the resonance. This gives

$$iq\epsilon+\frac{\partial\epsilon}{\partial\zeta}=i\hat{D}\epsilon \tag{3.5}$$

We are looking for linear waves, and thus for solutions of the form $\epsilon=\epsilon' e^{ik\zeta-i\omega\tau}$. However, for resonance, we need zero $\zeta$ dependence, and so we set the wavenumber $k=0$, giving $\epsilon=\epsilon' e^{-i\omega\tau}$. This yields the resonant condition

$$q=D\left(\omega\right) \tag{3.6}$$

The left hand side of the equation gives the dispersion relation of the soliton (which is a constant due to the moving frame of reference), whilst the right hand side is the dispersion relation of linear waves. Solving this equation for $\omega$ gives the frequency of resonance (relative to the pump frequency, which is constructed so that $\omega=0$), as is demonstrated in figure 3.5. At the pump frequency the function $D\left(\omega\right)$ has a local maximum at $D\left(0\right)=0$ (which corresponds to the requirement of anomalous GVD). As $q$ is positive, it follows that $D\left(\omega\right)$ must have a point of inflection between the pump and Čerenkov frequencies. This point of inflection corresponds (by definition) to zero GVD, and so the Čerenkov radiation will be emitted at normally dispersive wavelengths.

A commonly used approximation of this result [152, 153, 154] is to assume that the Čerenkov radiation occurs *at* the ZDW, rather than on the other side of it. In the simplest possible case of $\beta_2$ and $\beta_3$ only, this gives a frequency (relative to the pump) of [155]

$$\omega=\frac{3|\beta_2|}{\beta_3} \tag{3.7}$$

In addition to starting with knowledge of the higher order dispersion and using it to calculate the Čerenkov frequency, the reverse can be also done. This is useful from an experimental standpoint, as determining the $\beta_3$ value of a waveguide requires many precise measurements of its group velocity over multiple wavelengths (as is described in section 3.3.1). Therefore, by measuring the position of the Čerenkov peak, a value of $\beta_3$ can be inferred [57, 155] using equation 3.7.

#### Numerical analysis and spectral recoil

In order to observe Čerenkov radiation, the above 220nm × 420 waveguide geometry is unsuitable, as the ZDWs are too far from the pump. Therefore, a 220nm × 380nm geometry was chosen, which shifts the red-end ZDW to 1.627$\mu$m. (The dispersion relation of this geometry is plotted in figure 2.3.) Modelling using this waveguide configuration is shown in figure 3.5. A 33.3fs pulse duration was used, as longer pulses (being spectrally narrower) were found to produce very little radiation. The solution to equation 3.6 (and thus the spectral position of

the Čerenkov radiation) is obtained graphically in figure 3.5.

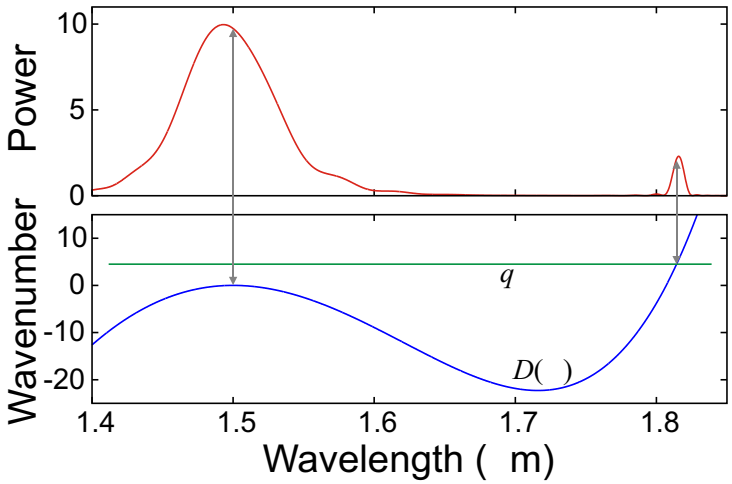


Figure 3.5: The output (after 0.6mm of propagation) of a 33.3fs pulse at 1.5$\mu$m fired into a 220nm $\times$ 380nm SOI guide is shown top. A soliton is formed (the left hand peak), producing Čerenkov radiation (the right hand peak). Equation 3.6 is solved graphically by matching the linear wavenumber $D(\omega)$ to the soliton wavenumber $q = 4.5$. Notably the soliton is slightly blueshifted, whilst the radiation is to the red of its predicted position. The model includes linear damping and 2PA.

Notably, the position of the Čerenkov peak (1.816$\mu$m) is slightly different from the predicted value (1.814$\mu$m). Similarly, the soliton itself is blueshifted slightly. To investigate this further, the spectral position of both were measured as a function of distance along the waveguide, as is shown in figure 3.6. This shows that the radiation peak is incrementally redshifted, whilst the soliton is incrementally blueshifted. This wavelength shifting is known as *spectral recoil*. This effect results from conservation of momentum, and causes the frequency of the soliton to be pushed away from the frequency of the emitted radiation [142]. (The effect will not be predicted by the above analysis, as it results from the driving terms removed between equations 3.4 and 3.5 [156].) This in turn causes the frequency of the radiation to be pushed further from the pump frequency [157].

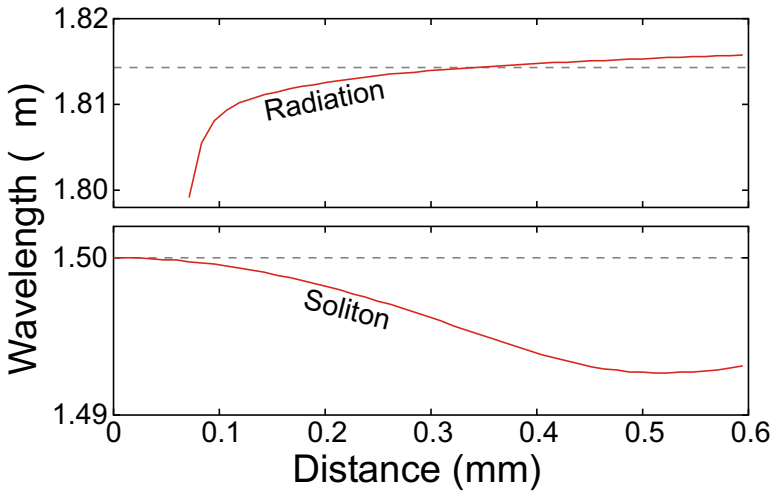


Figure 3.6: Spectral position of the soliton and the radiation peak (for the system described in figure 3.5) as a function of propagation distance. (The radiation peak is not shown before 0.07mm, as there was no local maximum to measure.) The soliton is incrementally blueshifted from its 1.5$\mu$m starting wavelength, whilst the radiation is incrementally redshifted. Notably the radiation peak starts off at shorter wavelengths to that predicted by equation 3.6, which is due to the initially weak peak being superposed with the soliton tail, thus moving its apparent maximum. As the amplitude grows, this effect rapidly vanishes.

Whilst Čerenkov radiation has been observed in SOI, direct comparison to these experiments is problematic, as the only papers reporting the phenomenon seem to be those using the above method of deriving the third order dispersion from the Čerenkov frequency [57, 62]. Therefore, agreement between theory and experiment would be by construction, rather than a meaningful physical result.

In section 5.3 we will return to the subject of Čerenkov radiation, and consider what happens in arrays of waveguides.

## 3.2 Pulse fission and spectral broadening

Nonlinear processes can cause the spectral width of a pulse to be hugely broadened [4, 5], in what is known as *supercontinuum generation*. This process involves the complex interplay between a wide range of physical effects. These can include pulse compression [147], soliton fission [158, 159], Raman scattering [160], four wave mixing [160, 161], Čerenkov radiation [148], modulational instability [162], and a novel effect whereby radiation is trapped within a gravity-like potential produced by accelerating solitons [163]. Supercontinuum generation has been observed in PCF [4, 164, 165] and tapered conventional fibres [166, 164, 165]. A similar effect has been observed in SOI waveguides [62], but with a far smaller spectral range.

### 3.2.1 Spectral broadening by soliton fission

At powers much higher than the soliton threshold, the self focussing caused by self phase modulation will overwhelm dispersive pulse broadening, causing pulse compression followed by fission, as is shown in figure 3.7. (As mentioned above, this can be thought of in terms of the input pulse being a superposition of many solitons, which separate under perturbation.) This fission is a starting point for spectral broadening, as is shown in figure 3.8, which gives the spectral output for a range of input powers. At the highest power of $640P_0$ (corresponding to a superposition of 25 solitons) the pulse broadens into a continuum with 800nm bandwidth. This was found to be roughly optimal, as further increases in power lead to no increase of the spectral width. This is notably greater than that previously observed in SOI waveguides [62]. It is, however, much less than the 4000nm bandwidth that can be achieved in PCF [167], and so it is more appropriate to call this process continuum generation, rather than supercontinuum generation.

Whilst the influence of free charge carriers was negligible for the analysis in section 3.1 it becomes significant at these much higher powers. The carrier cross section can be calculated as $\epsilon_{fc} = \epsilon_{2pa} T_0 P_0 \sigma_{fcc} / 2\hbar\omega S_{eff}$, but this is problematic as it requires knowledge of the soliton threshold $P_0$, which cannot be scaled away. Therefore, a physically reasonable order-of-magnitude estimate of $\epsilon_{fc} \simeq 10^{-3}\,(1 + 7.5i)$ was used.

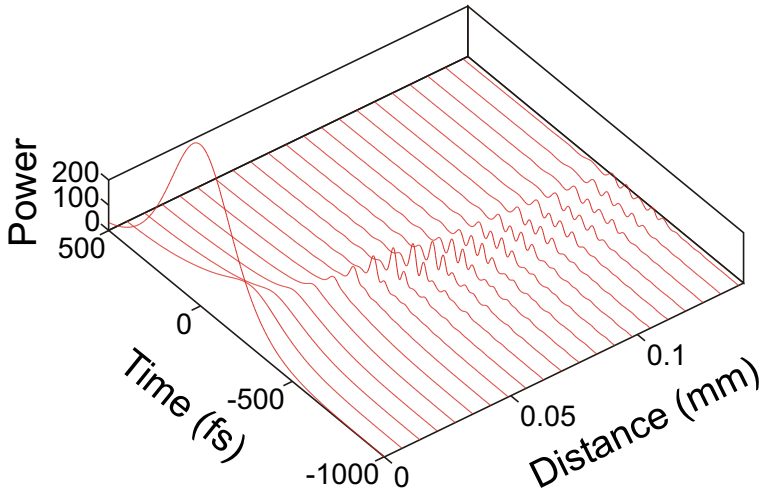


Figure 3.7: Evolution of a 100fs pulse with peak power $640P_0$ over the first 0.14mm of propagation through a 220nm × 380nm waveguide. The pulse is greatly compressed (and thus spectrally broadened) and shortly afterwards breaks up into a pulse chain.

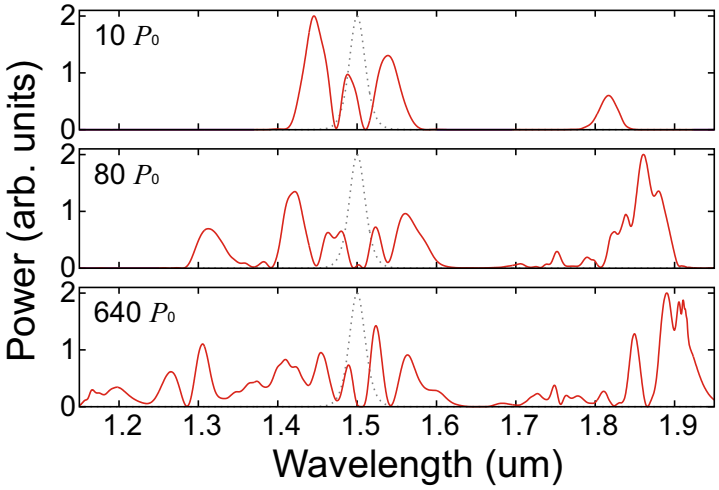


Figure 3.8: Spectral output after 1.2mm ($\zeta = 2$) of a 220nm × 380nm wire pumped with a 100fs 1.5$\mu$m pulse. Peaks powers of $10P_0$, $80P_0$ and $640P_0$ are used. Increasing the power increases the spectral range of the output.

Figure 3.9 shows the $640P_0$ output plotted as a FROG diagram. This technique (which is explained in more detail in appendix A.2) expands the signal into a two-dimensional image in which both the frequency and timing of optical features can be resolved. The features form an "S" shape across the diagram, which is due to the dependence of group velocity upon wavelength. The two ZDWs are (by definition) extremal points of the group velocity (with the 1.23$\mu$m wavelength being a local maximum and the 1.63$\mu$m wavelength being a local minimum), and so the curve changes direction at these points.

It should be noted that the chirp of a pulse (i.e. the difference in frequency between its leading and trailing edge) can be gauged by observing the angle at which its corresponding FROG feature lies on the diagram. A chirpless pulse will appear as an ellipse with axes parallel to those of time and frequency, but when chirp is present, these axes will be rotated. Dispersive pulses will steadily gain a chirp as they propagate along a waveguide, whilst solitons will not. There are several pulses in figure 3.9 which appear to have very little chirp (despite having travelled two dispersion lengths), and thus are probably solitons.

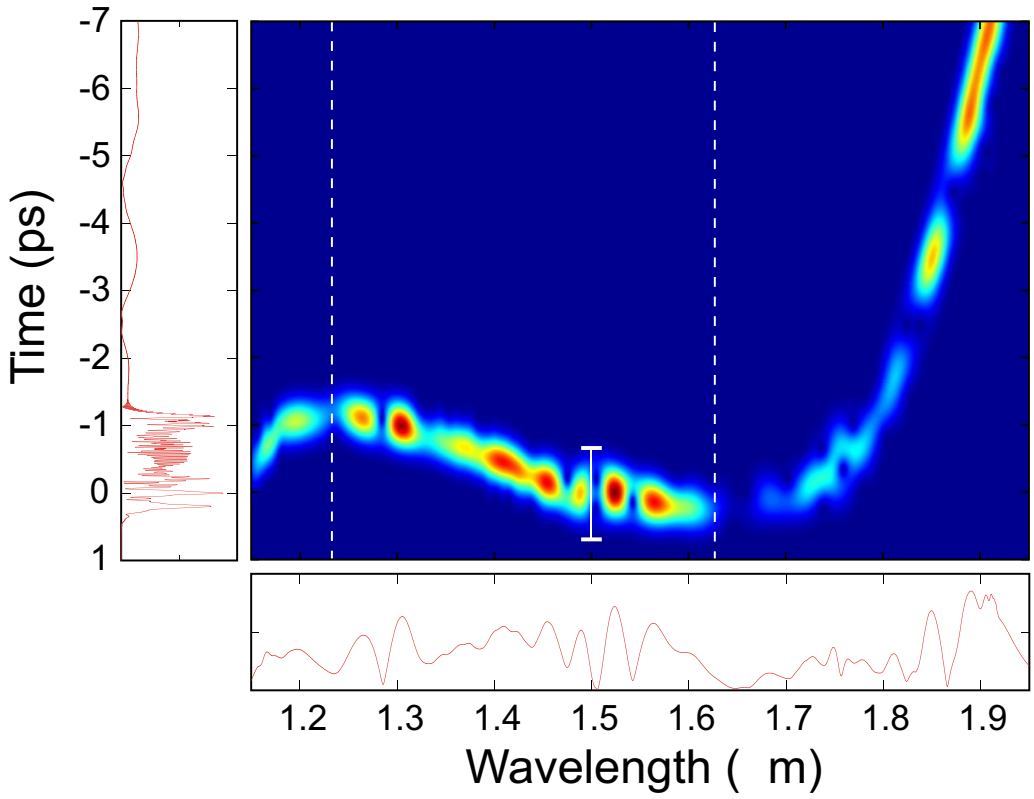


Figure 3.9: Output after 1.2mm ($\zeta = 2$) of a 220nm × 380nm wire pumped with a 100fs 1.5$\mu$m pulse with a peak power of $640P_0$. The region between the dashed vertical lines is anomalously dispersive, and within this there are several solitons.

### Role of Čerenkov radiation

If solitons are present, then Čerenkov radiation may also be present. To predict the resonances, equation 3.6 needs to be generalised for an arbitrary soliton frequency $\omega_{\mathrm{sol}}$. It can be shown that this general form is [151]

$$q + D\left(\omega_{\mathrm{sol}}\right) + \left(\omega - \omega_{\mathrm{sol}}\right) \left.\frac{dD}{d\omega}\right|_{\omega_{\mathrm{sol}}} = D\left(\omega\right) \tag{3.8}$$

As before, the left hand side is the dispersion relation of the soliton. Matching this to the linear dispersion relation $D\left(\omega\right)$ gives the resonant frequency. This analysis is performed for a variety of spectral peaks in figure 3.10. It is probable that the peak at 1.45$\mu$m is a soliton which is emitting the radiation at 1.85$\mu$m.

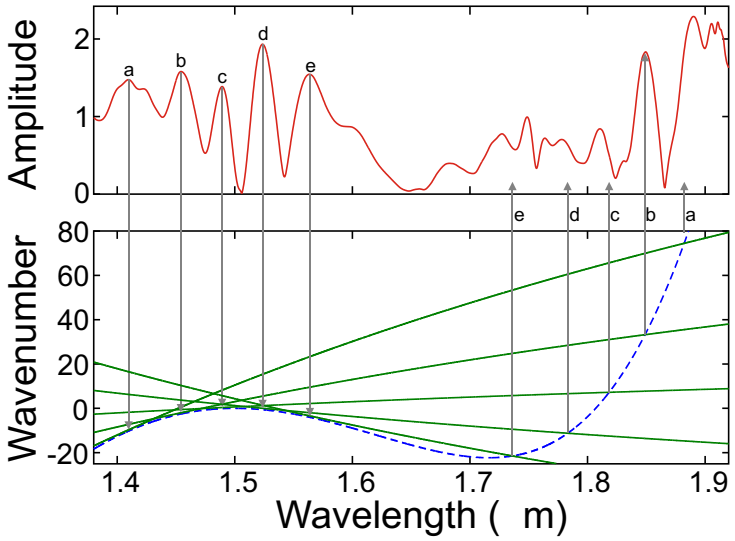


Figure 3.10: Čerenkov analysis for the signal displayed in figure 3.9. A variety of spectral peaks in the anomalous regime (labelled from a to e) are taken, and equation 3.8 solved graphically by matching the linear dispersion relation (dashed line) to the nonlinear relations (solid lines). An estimated soliton wavenumber of $q = 0.5$ was used. It can be seen that peak b (at 1.45$\mu$m) matches up well to a peak in the normal regime (at 1.85$\mu$m), suggesting that Čerenkov radiation is present. Whilst the other peaks don't match up, it is possible that more Čerenkov resonances are present, but that either the soliton or the radiation has been spectrally shifted.

### 3.2.2 Pumping at the zero dispersion wavelength

It is not necessary to start with a soliton in order to observe spectral broadening, as pumping at the zero dispersion wavelength will also give a continuum. (In fact, pumping at the ZDW is the classic way of realising continuum generation [4].) For this, a 220nm × 330nm waveguide was chosen, giving a relatively small (by SOI standards) normal GVD of $-1416\ \mathrm{ps\,nm^{-1}\,km^{-1}}$ at a 1.5$\mu$m pump wavelength. For 100fs pulses, this gives a dispersion length of 1.93mm. The dispersion relation of this geometry is given in figure 2.3. The initial condition was modulated by $e^{i\omega\tau}$, where the frequency difference $\omega = 0.6228$ was chosen to shift the pump wavelength to the ZDW at 1.487$\mu$m. The damping coefficient was rescaled to $\epsilon_1 = 0.05$ to account for the longer dispersion length.

The output spectra for multiple input powers are shown in figure 3.11. At the highest (and again, roughly optimal) power of $640P_0$, a continuum with bandwidth 550nm was generated. (The meaning of $P_0$ is slightly obscured here, as solitons are no longer possible. However the combination of variables is still mathematically valid.)

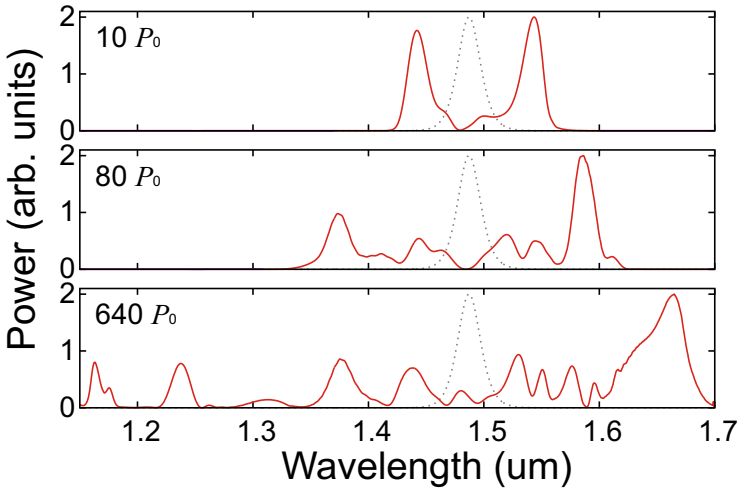


Figure 3.11: Spectral output after 3.86mm ($\zeta = 2$) of pulses with input powers of $10P_0$, $80P_0$ and $640P_0$ fired at the zero dispersion wavelength of a 220nm $\times$ 330nm wire. The pump wavelength was tuned to 1.487$\mu$m to match the ZDW.

A FROG diagram for the $640P_0$ case is shown in figure 3.12. There are several pulses in the anomalous regime, where solitons may potentially be formed. However all of the corresponding FROG features are strongly rotated. Furthermore, the angle of rotation is roughly tangential to the "S"-shaped curve, which suggests that the features are merely dispersive pulses.

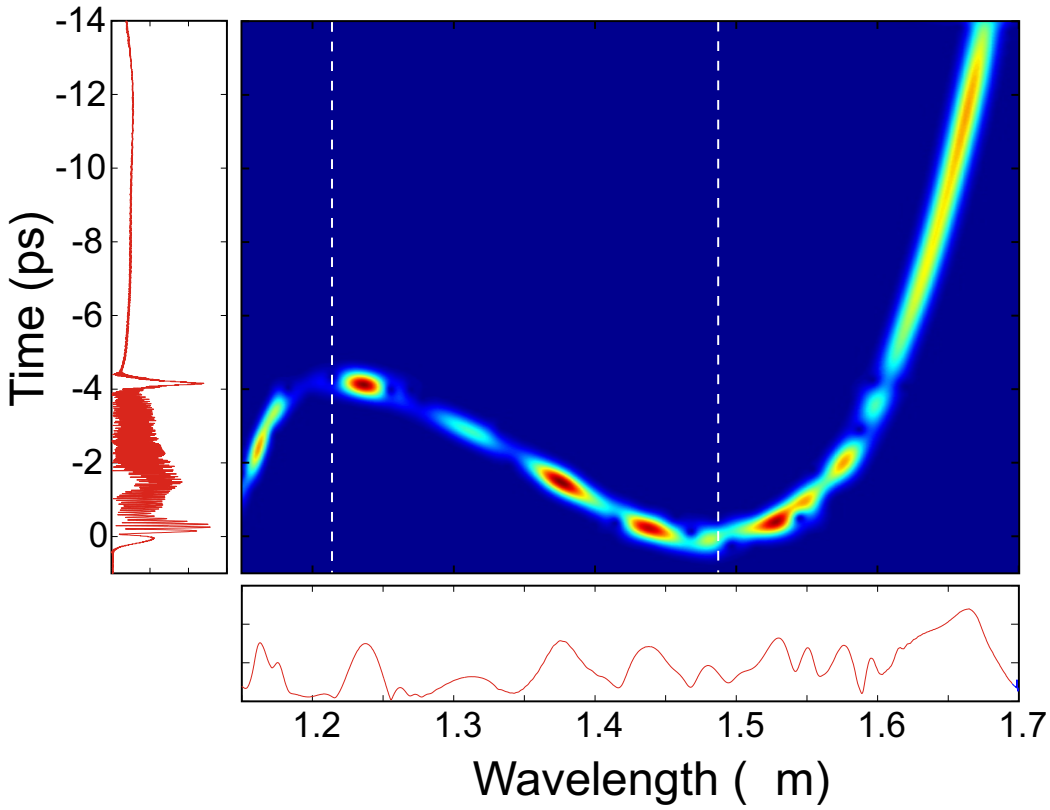


Figure 3.12: Result after 3.86mm ($\zeta = 2$) of a pulse with input power $640P_0$ fired at the zero dispersion wavelength of 220nm × 330nm wire. The pump wavelength was tuned to 1.487$\mu$m to match the ZDW.

### 3.2.3 Energy saturation

As the energy of the input pulse is increased, the output energy is increased by successively smaller amounts (see figure 3.13). This is caused by two-photon absorption, which being a two-photon effect has a far greater impact upon the high energy pulses, thus reducing the output energies to a similar value. Such an effect is well documented [57, 168, 169, 170]. At higher energies still, the effect of the free charge carriers excited by the 2PA becomes significant. Being a three-photon-effect (requiring two photons to excite a carrier, and a third to participate in a scattering or absorption event) it only becomes important at very high intensities. The energy out versus energy in was calculated, as is shown in figure 3.13.

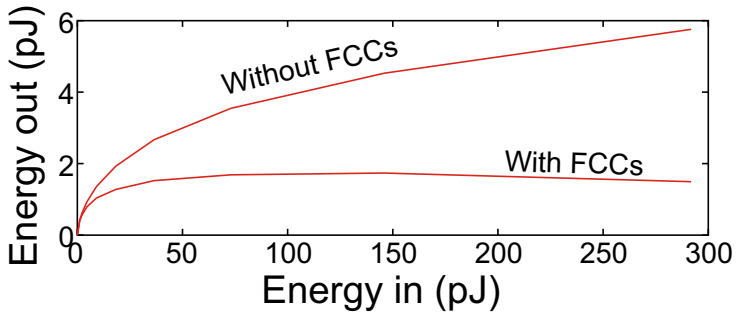


Figure 3.13: Energy saturation for 220nm × 330nm wire pumped at ZDW. (Scale assumes power unit is 1W.)

Notably, when free carriers are included, the output energy can actually *decrease* as the input energy is increased. This effect (which has been observed experimentally [57, 72, 169, 170]) can be explained through hysteresis, as the effect of the free charge carriers is not instantaneous. Consider two input pulses, one of low energy, and one of high energy: The two pulses will be reduced to a similar saturation energy by two photon absorption. However, the higher energy pulse will have induced many more charge carriers. As the charge carriers remain, they will continue to absorb light even after the saturation energy has been reached. When more carriers are present, this absorption will be greater, and may cause output energy to decrease with increasing input energy.

The effect of the free charge carriers can be compared to that of a resistor in which the resistance increases with temperature. Devices used as "resettable fuses" can work like this, and consist of carbon particles embedded in a polymer matrix. The temperature increase due to excessive current will cause the polymer to expand, increasing the distance between the particles and causing the resistance to greatly increase, thus allowing the fuse to "blow".

Consider the action of electrical pulses on the following electrical circuit:

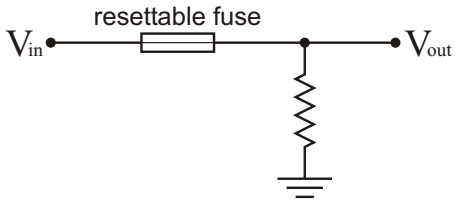


If the heating and cooling were instantaneous, the resettable fuse would simply act as a non-linear resistor. By analogy with the two photon absorption, a saturation effect would be observed, whereby increasing the peak voltage of the input pulses would give diminishing returns. However, the fuse could never blow, because once the voltage dropped, the resistance would instantaneously fall, and the remainder of the pulse could propagate as normal. It is only when hysteresis is present—by the fuse remaining hot—that the fuse can blow. This is analogous to

the remaining free charge carriers persisting, and continuing to absorb light.

## 3.3 Comparison to experiment

In this section numerical modelling is compared to experimental data gained in colloboration with others. A microchip was fabricated at the University of Glasgow by Marco Gnan, Marc Sorel and Richard De-La-Rue. Optical experiments were then performed upon the chip at the University of Bath by Wei Ding, William Wadsworth and Jonathan Knight. The results of this collaboration have been published in Optics Express [54].

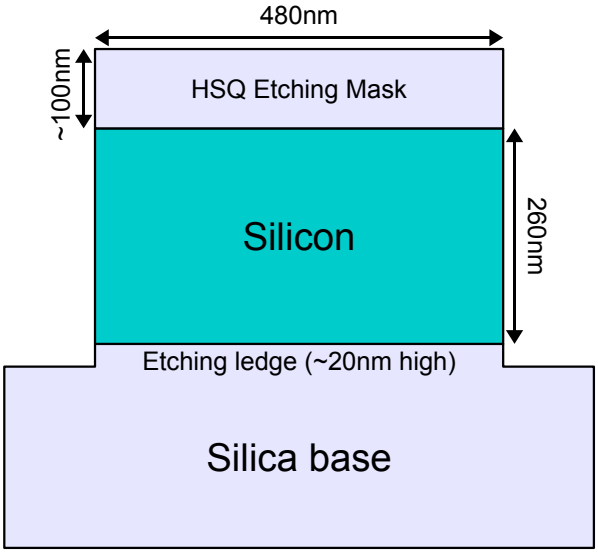


Figure 3.14: Schematic cross section of the 260nm × 480nm nanowire fabricated by Gnan, Sorel and De-La-Rue. The silica wire sits on top of a ledge of silica, due to overetching of the base and is covered with a layer of hydrogen silsesquioxane (HSQ) etching mask. Electron micrographs are shown in figure 1.2.

The chip consisted of SOI nanowires 260nm in height and 480nm wide on a base of silica. (An overview of the chip's fabrication is given in appendix B.1.) Electron micrographs of the wires are shown in figure 1.2, whilst a schematic cross section is given in figure 3.14. The wires were topped with a hydrogen silsesquioxane (HSQ) etching mask with a thickness of 100nm and a refractive index of about 1.35. They also sat upon a slight pedestal of silica (about 20nm in height), due to overetching of the base. The chip was 15mm in length, which is substantially longer than that used by other groups. (A more typical value is 5mm [57, 63].)

### 3.3.1 Measuring the linear dispersion

The initial work was concerned with the linear dispersion of the waveguides. The experiments yielded values of the group index at multiple wavelengths (see appendix B.1 for details). From this, the GVD could be calculated by fitting the values to a polynomial in $\omega$, and then differentiating the polynomial. Due to great expense of taking a high-accuracy group velocity measurement, only nine experimental datapoints were available. This small number can cause problems with polynomial fitting, due to the effect described in section 2.1.2. (This problem becomes greater still when calculating the third order dispersion, as the polynomial has to be differentiated twice, amplifying the fitting pathologies further. It is therefore not surprising that some groups have attempted to calculate the HOD indirectly, as was mentioned in section 3.1.3.)

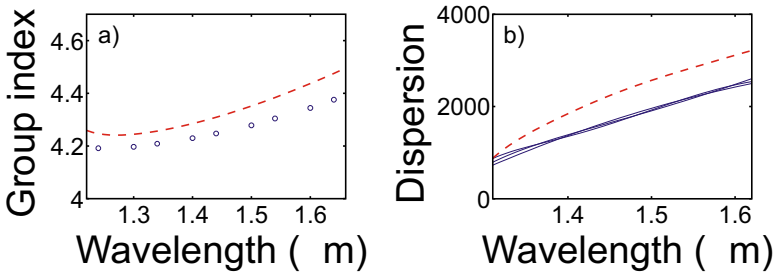


Figure 3.15: a) Group velocities measured at various wavelengths (gained experimentally by Ding, Wadsworth and Knight, as described in appendix B.2) shown by circles. The dashed line shows the theoretical values, derived using the techniques described in section 2.1.2. b) Dispersion parameter (given in units of $\mathrm{ps\,nm^{-1}\,km^{-1}}$) The solid lines show the empirical values (derived from the group velocities by curve fitting with third, fourth and fifth order polynomials). The dashed line gives the theoretical values.

The group velocities and the derived GVDs are plotted in figure 3.15. By taking all forms of error into account, Ding, Wadsworth and Knight were able to extract dipsersion coefficients (expanded about 1.5$\mu$m) of $\beta_2 = -2.31 \pm 0.04\,\mathrm{ps^2 m^{-1}}$ and $\beta_3 = 0.0119 \pm 0.0009\,\mathrm{ps^3 m^{-1}}$. The dispersion fitting was done with third, fourth and fifth order polynomials. These fits all yielded values of similar magnitude (with the differences contributing to the above error bars), and so the polynomial problem was not fatal.

This dispersion relation, however, differs substantially from that calculated using the techniques described in section 2.1.2. (This is also plotted in figure 3.15.) The coefficients obtained were $\beta_2 = -3.06\,\mathrm{ps^2 m^{-1}}$ and $\beta_3 = 0.0133\,\mathrm{ps^3 m^{-1}}$, which are well outside the error bars of the empirical values. A number of explanations for this discrepancy are possible:

- There may have been a discrepancy between the geometry of the waveguide and the geometry assumed in the modelling. The waveguide height and width are both subject to error, as is the overetching pedestal hight. Similarly, the waveguides had slight wall-slopage, which may also have affected the dispersion.

- The boundaries between the materials may have differed from the perfectly sharp and planar dielectric interfaces assumed in the model. For example, there may have been mixing at the silicon-silica interface, causing the refractive index profile to vary gradually rather than discontinuously. Roughness at the interfaces may have caused a similar effect.
- The material dispersion of the silica and silicon may have differed from the Sellmeier equations used to represent them. The silicon may have had its properties altered by doping, whilst both materials may have possessed atypical properties due to chemical or structural modifications suffered in the fabrication process. Similarly the dispersion relation of the etching mask may have differed from the assumption of a wavelength independent refractive index of 1.35.
- The effective refractive indices calculated in section 2.1.2 may have suffered from numerical error. However, tightening the mesh-size (which one would expect to reduce error) had a negligible effect on the results, indicating that an accurate solution to the equations had been obtained.

This discrepancy is slightly disconcerting when it comes to the experimental realisation of the other waveguide geometries assumed throughout this report. However it should be noted that the ultimate aim is not to make precise predictions for future experiments, but to gain qualitative predictions for systems with physically realistic parameters. Even if the parameters are not precise, it is safe to assume that they are reasonable.

This experimentally derived dispersion relation was used for further modelling. The scaled dispersion coefficients (for a dispersion length of 1.05mm) are $p_2 = -0.5$ and $p_3 = 0.0151$.

### 3.3.2 Nonlinear propagation and parameter fitting

The output spectra for waveguides pumped with 100fs FWHM 1.5$\mu$m pulses were measured at a range of input powers, as is shown in figure 3.16. (These experiments, performed with 800nm pulses from a Titanium Sapphire mode-locked laser which were down-converted to 1500nm by a $\beta$-barium-borate optical parametric amplifier, are described in appendix B.3.) The total power output was also measured, as is shown in figure 3.17. As the power is increased, the spectral width of the output broadens. There is also a saturation effect, whereby increased input power gives diminishing returns with respect to the output power.

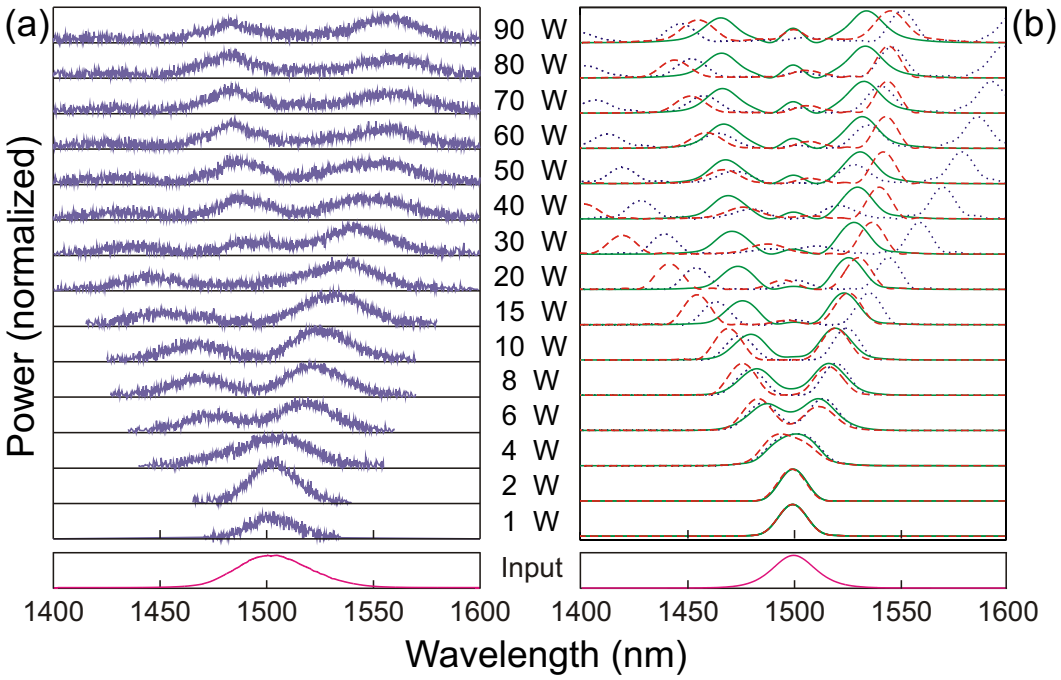


Figure 3.16: Experimental output spectra (obtained by Ding, Wadsworth and Knight) compared with best-fit numerical results. The dotted line gives modelling without the effect of 3PA or FCC interactions. The dashed line includes the effect of FCC interactions, whilst the solid line (which gives the best fit) includes the effect of 3PA.

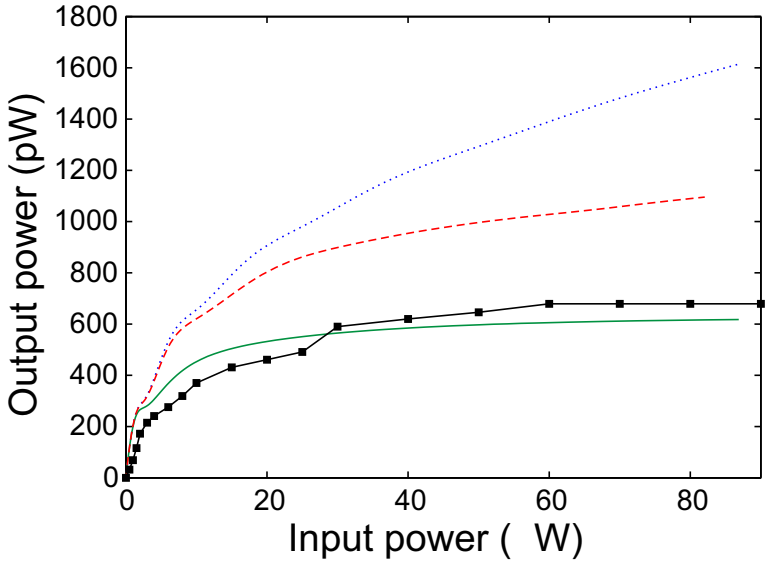


Figure 3.17: The experimental output powers (obtained by Ding, Wadsworth and Knight) for various input powers are given by the black squares. The dotted line gives modelling without the effect of 3PA or FCC interactions. The dashed line includes the effect of FCC interactions, whilst the solid line (which gives the best fit) includes the effect of 3PA.

The powers shown in figures 3.16 and 3.17 are not the peak powers of the pulses entering the waveguide, but the mean power of the pulse train fired at the waveguide. It can be shown (working in real units) that a sech-like pulse with peak power $P_{\max}$ and FWHM duration $T_{\mathrm{FWHM}}$ has a total energy $P_{\max}T_{\mathrm{FWHM}}/\ln\left(1+\sqrt{2}\right)$. It follows that the peak power in the waveguide is given in terms of the mean incident power $P_{\mathrm{inc}}$ by

$$P_{\max} = \frac{\nu \ln\left(1+\sqrt{2}\right)}{T_{\mathrm{FWHM}} f_{\mathrm{rep}}} P_{\mathrm{inc}} \tag{3.9}$$

where $f_{\mathrm{rep}}$ is the pulse repetition rate, and $\nu$ is the fraction of the incident light coupled into the waveguide. These had values of $f_{\mathrm{rep}} = 250\mathrm{KHz}$ and $\nu = 0.5\%$, yielding an all-inclusive conversion relation of $P_{\max} = 1.77 \times 10^5 \, P_{\mathrm{inc}}$.

Numerical modelling of the system was performed, as is shown in figures 3.16 and 3.17. The comparison of theory to experiment was made by treating the soliton threshold $P_0$ and the scaled 2PA coefficient $\epsilon_{2\mathrm{pa}}$ as being free parameters, and then using them as fitting parameters to gain the best match. The first of these parameters doesn't actually affect the numerical results, as it is scaled out of the model. Therefore, fitting is a simple matter of matching the experimental and theoretical spectra, and comparing their power values. The $\epsilon_{2\mathrm{pa}}$ parameter is more important, as it directly enters the model, and different values will give qualitatively different results. The model also included linear absorption, which was measured to be 3.4 dB $\mathrm{cm}^{-1}$.

In addition to free charge carriers, the effect of 3 photon absorption was also considered (and the coefficient $\epsilon_{3\mathrm{pa}}$ treated as a third fitting parameter). As mentioned in section 2.3.1, this effect is known when the photon energy is less than twice silicon's $\sim 1.1\mathrm{eV}$ indirect bandgap (precluding 2PA) [117], but here we consider it alongside 2PA.

The best fitting was found to occur roughly when the soliton threshold corresponded to an incident power of $P_{\mathrm{inc}} \simeq 2\mu\mathrm{W}$, giving an estimate for the soliton threshold of $P_0 = 0.36\mathrm{W}$, and thus (from equation 2.64) a nonlinear coefficient of $\gamma = 2000\,\mathrm{W}^{-1}\mathrm{m}^{-1}$. The best fit to the 2PA coefficient was found to be $\epsilon_{2\mathrm{pa}} = 0.1$.

For higher order absorption, the best match to experiment was actually found *without* the effect of FCC included, and a 3PA coefficient of $\epsilon_{3\mathrm{pa}} = 0.05$. However, it should be noted that 3PA and FCC absorption are very similar phenomena, as both involve three photons. (The difference between them is that FCC absorption exhibits hysteresis, whilst 3PA is instantaneous.) Therefore, the model may still be accounting for the carriers indirectly.

A notable problem when matching theory to experiment was the lack of information on the chirp of the laser system. Whilst the pulse's duration was known to be 100fs, its bandwidth was slightly wider than that of a transform limited pulse, suggesting that it was chirped. (This input spectrum is given in figure 3.16.) There was no data, however, to suggest whether the chirp was frequency increasing, frequency decreasing, or something more complicated. Therefore, for the purpose of modelling, the best approximation to this unknown pulse makeup was simply a transform limited pulse. The effect of this can be seen when comparing the numerical and

experimental output spectra, as whilst the positions of the spectral peaks agree, they appear broader in the experimental case.

### 3.3.3 Determining if solitons are present

It is probable that soliton propagation is present, and (from the above parameter fitting) the soliton threshold corresponds to the $2\mu$W mean input power. A useful test for determining if a pulse is or isn't a soliton involves the conservation of the parameter

$$S = T_{\mathrm{FWHM}} \sqrt{P_{\max}} \tag{3.10}$$

which is known as the *soliton area*. It can be shown that for an ideal sech-like soliton, the parameter is always given by $S_0 = 2\ln\left(1+\sqrt{2}\right)\sqrt{|\beta_2|/\gamma}$, where $\beta_2$ is the GVD, and $\gamma$ is the Kerr coefficient. This is independent of the soliton duration, thus making it a property of the waveguide only. The quantity is not fixed for pulses in general, and so provides a useful means of identifying solitons. Whilst the presence of higher order dispersion and damping will affect $S_0$ slightly (as the sech-like soliton will no longer be an exact solution of the equation of motion) we can still expect it to remain constant over the propagation distance. Therefore, if we see a pulse with a constant value of $S$ (similar to $S_0$) we have strong evidence that it is a soliton. (We will return to this technique for detecting solitons in multi-wire systems, in sections 4.3.3, 4.4.3 and 5.2.3.)

As the experiments provided no information as to the duration of the output pulses, this analysis must rely upon numerical data. However, now that the model has been fine-tuned with experimentally derived data, this can be done to a reasonable degree of accuracy. Figure 3.18 shows $S$ plotted for a range of input powers. For comparison, the temporal and spectral widths are also plotted. This plot shows a plateau with $S \simeq S_0$, over the input power range $1\mu$W to $3\mu$W. This region coincides with a strong supression of temporal pulse broadening, suggesting that soliton-like effects are at work. The soliton area remains roughly constant over propagation distance (figure 3.19), with an input power of $2\mu$W providing a good fit, and $1.7\mu$W providing the optimum match.

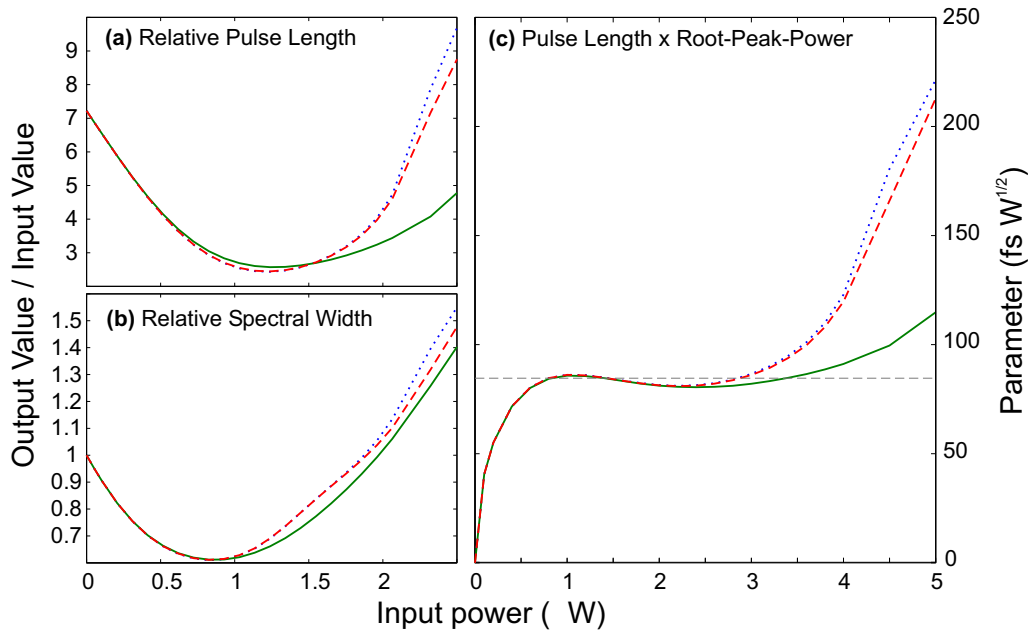


Figure 3.18: a) Temporal duration as a function of input power. b) Spectral width as a function of input power. c) Soliton area parameter $S$ as function of input power. The dashed line gives the ideal value $S_0$. (The line styles are as defined in figures 3.16 and 3.17.)

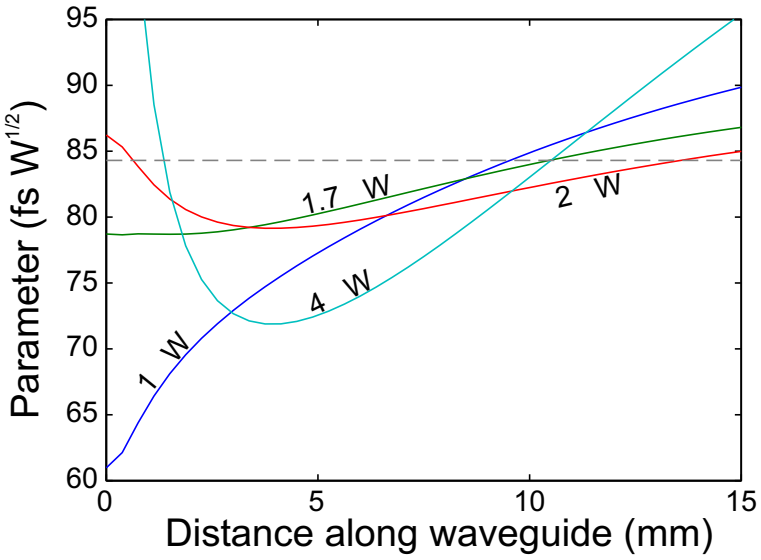


Figure 3.19: Soliton area parameter $S$ plotted over distance, for a variety of input powers. The dashed line gives the ideal value $S_0$. Powers of 1.7$\mu$W and 2$\mu$W show a roughly conserved value similar to $S_0$, suggesting that solitons are present.

The pulse at 2$\mu$W is a promising candidate for a soliton. Temporal evolution over distance (shown in figure 3.20) supports this hypothesis. Whilst temporal broadening does happen, this is over 14 dispersion lengths, and is much less than that seen without nonlinearity.

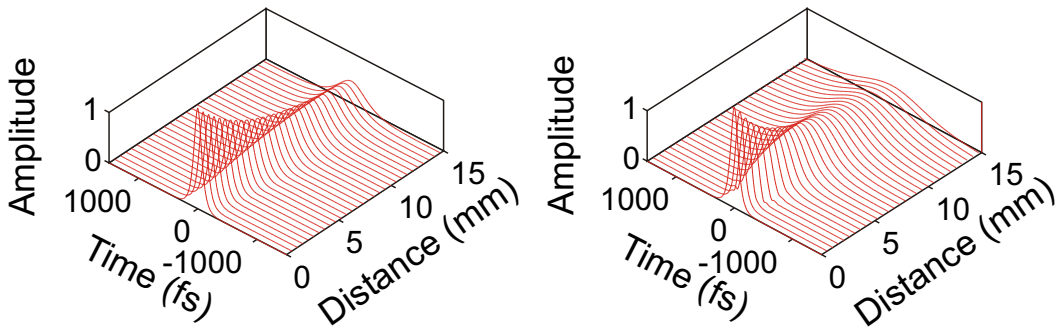


Figure 3.20: Temporal profile plotted over distance for a 100fs pulse in a 260nm × 480nm SOI waveguide. With nonlinearity (left) the pulse broadening is greatly suppressed in comparison to that without nonlinearity (right).

As a final test for the existence of solitons, the evolution of pulse pairs was considered, as is shown in figure 3.21. If two solitons are in close proximity, they will start to attract each other [8], which indeed is seen. In the ideal NLS model, we would expect the solitons to remain independent. Due to damping, however, we lose the property of two solitons being able to pass through one another with only a phase shift, and so the two solitons fuse into one. Integration of the equations of motion beyond the physical length of the waveguide was also performed, which revealed that the fused pulse remained in one piece.

Conversely, if a half-cycle phase-shift is introduced between the solitons, the attraction will be replaced by repulsion [8]. Again, this is seen in figure 3.21.

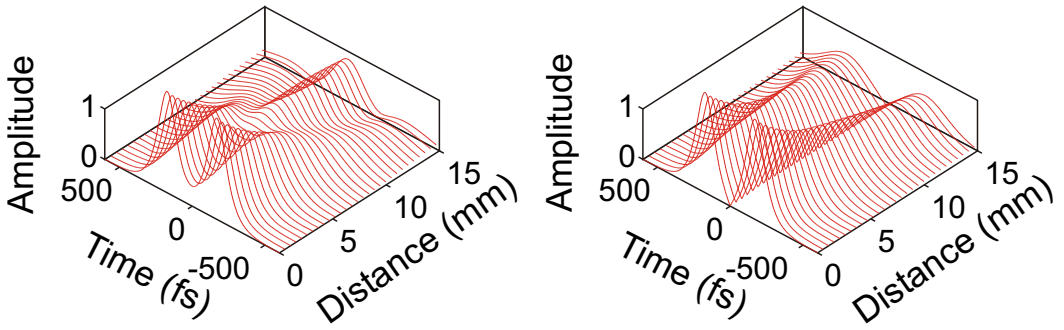


Figure 3.21: Evolution of pair of 100fs pulses with 340fs peak-to-peak separation in a 260nm × 480nm SOI waveguide. When the solitons are in phase (left), attraction occurs, and they seem to merge. When they are half a cycle out of phase (right) repulsion occurs.

In summary, the existence of solitons is supported by a range of tests. Firstly, pulse broadening is greatly suppressed, and this occurs a power corresponding to the soliton threshold. Secondly, the soliton area parameter $S$ is close to the predicted value, and is roughly conserved over the length of propagation. Thirdly, the pulses exhibit the attractive and repulsive behaviour seen by soliton pairs.

## 3.4 Continuous wave propagation and modulational instability

Modulational instability (MI) occurs when small deviations from the waveform are reinforced by nonlinearity, generating spectral sidebands and causing the eventual collapse of the waveform into a chain of pulses [8]. It has been both predicted [171] and observed [172] in SOI waveguides.

The distinctive spectral pattern formed by modulational instability can be predicted analytically. As a starting point, we take a continuous wave (CW) solution of equation 2.85

$$E = \sqrt{P} e^{iP\zeta} \tag{3.11}$$

where $P$ is a dimensionless power scaling coefficient, and we have ignored the effect of damping. (This solution is not a constant, as it would be for the envelope in a linear system, due to the intensity dependence of the refractive index. Therefore, the corresponding change in wavenumber causes the phase of the solution to be modulated in $\zeta$. It should be noted, however, that $P$ approaches zero faster than $\sqrt{P}$, and so at low powers, equation 3.11 tends towards being a constant.) We then perturb the CW solution as

$$E = \left(\sqrt{P} + \epsilon\right) e^{iP\zeta} \tag{3.12}$$

where the perturbation term $\epsilon(\zeta, t)$ shares the same phase modulation as $P$. Substituting this into the equation 2.85 (again without damping) gives

$$\frac{\partial \epsilon}{\partial \zeta} - i\hat{D}\epsilon = i\left(P\epsilon + P\epsilon^* + \sqrt{P}\epsilon^2 + 2\sqrt{P}\epsilon\epsilon^* + \epsilon^2\epsilon^*\right) \tag{3.13}$$

As we are only considering the early stages of the modulational instability, the perturbation will be small, and so we can reject all the higher order terms in $\epsilon$ to give

$$\frac{\partial \epsilon}{\partial \zeta} - i\hat{D}\epsilon = iP\left(\epsilon + \epsilon^*\right) \tag{3.14}$$

As we have terms in both $\epsilon$, and its conjugate, it is productive to use a trial function with a similar structure, namely the superposition of a wave, and its conjugated equivalent. Therefore we choose

$$\epsilon = \epsilon_1 e^{ik_\mathrm{m}\zeta - i\omega_\mathrm{m}\tau} + \epsilon_2 e^{-ik_\mathrm{m}\zeta + i\omega_\mathrm{m}\tau} \tag{3.15}$$

where the relative wavenumber $k_\mathrm{m}$ has yet to be determined. Substituting in (and rearranging) gives

$$\begin{aligned} &\left[\epsilon_1 D\left(\omega_\mathrm{m}\right) + \epsilon_1 P + \epsilon_2^* P - \epsilon_1 k\right] e^{ik_\mathrm{m}\zeta - i\omega_\mathrm{m}\tau} \\ &+ \left[\epsilon_2 D\left(-\omega_\mathrm{m}\right) + \epsilon_2 P + \epsilon_1^* P + \epsilon_2 k\right] e^{-ik_\mathrm{m}\zeta + i\omega_\mathrm{m}\tau} \quad = \quad 0 \end{aligned} \tag{3.16}$$

This is a valid solution, so long as the coefficients in front of the complex exponential terms are zero. This condition leads to a pair of coupled equations, which can be solved in $k_\mathrm{m}$ to provide a dispersion relation (giving the phase-matching condition required for MI to occur) of

the form

$$k_{\mathrm{m}} = D_{\mathrm{odd}}\left(\omega_{\mathrm{m}}\right) \pm \sqrt{D_{\mathrm{even}}^{2}\left(\omega_{\mathrm{m}}\right) + 2PD_{\mathrm{even}}\left(\omega_{\mathrm{m}}\right)} \tag{3.17}$$

where the dispersion operator has been split into even and odd components as $D = D_{\mathrm{even}} + D_{\mathrm{odd}}$. These are defined as

$$D_{\mathrm{even}}\left(\omega\right) \equiv \frac{1}{2}\left[D\left(\omega\right) + D\left(-\omega\right)\right] \tag{3.18}$$

$$D_{\mathrm{odd}}\left(\omega\right) \equiv \frac{1}{2}\left[D\left(\omega\right) - D\left(-\omega\right)\right] \tag{3.19}$$

so that $D_{\mathrm{even}}$ will contain only even powers of $\omega$, and $D_{\mathrm{odd}}$ will contain only odd powers. At frequencies where $k_{\mathrm{m}}$ has a non-zero imaginary component, exponential growth will occur. Defining a growth rate parameter $g \equiv 2\Im\left(k_{\mathrm{m}}\right)$ (where the factor of 2 converts the growth rate in amplitude to the growth rate in power) gives

$$g\left(\omega_{\mathrm{m}}\right) = \begin{cases} 2\sqrt{-D_{\mathrm{even}}^{2}\left(\omega_{\mathrm{m}}\right) - 2PD_{\mathrm{even}}\left(\omega_{\mathrm{m}}\right)} & ; \quad -D_{\mathrm{even}}^{2}\left(\omega_{\mathrm{m}}\right) - 2PD_{\mathrm{even}}\left(\omega_{\mathrm{m}}\right) \geq 0 \\ 0 & ; \quad -D_{\mathrm{even}}^{2}\left(\omega_{\mathrm{m}}\right) - 2PD_{\mathrm{even}}\left(\omega_{\mathrm{m}}\right) < 0 \end{cases} \tag{3.20}$$

It is apparent from the $-D_{\mathrm{even}}^{2}\left(\omega_{\mathrm{m}}\right) - 2PD_{\mathrm{even}}\left(\omega_{\mathrm{m}}\right) > 0$ condition that modulational instability will only occur when $D_{\mathrm{even}}$ is negative. This condition generally requires requires anomalous GVD, but it is sometimes possible for far-detuned spectral lines (as mentioned below) to be generated in a normally dispersive system. It is also apparent from the symmetry of equation 3.20 that the spectrum will be symmetric in frequency, so that each radiation peak will have a complement peak on the other side of the pump frequency.

With anomalous GVD, but without higher order dispersion, this reduces to

$$g\left(\omega_{\mathrm{m}}\right) = \begin{cases} \left|\omega_{\mathrm{m}}\right|\sqrt{4P - \omega_{\mathrm{m}}^{2}} & ; \quad 4P \geq \omega_{\mathrm{m}}^{2} \\ 0 & ; \quad 4P < \omega_{\mathrm{m}}^{2} \end{cases} \tag{3.21}$$

This describes two spectral side-lobes, with maxima at

$$\omega_{\mathrm{m}} = \pm\sqrt{2P} \tag{3.22}$$

With higher order dispersion, it is typical to see a extra pair of modulational instability peaks far away from the pump [173, 174, 175]. From equation 3.20, it can be seen that the maxima of these peaks coincide with the maxima of $x\left(\omega\right) \equiv -D_{\mathrm{even}}^{2}\left(\omega_{\mathrm{m}}\right) - 2PD_{\mathrm{even}}\left(\omega_{\mathrm{m}}\right)$. These maxima occur when $dx/d\omega = 0$, and so we can derive a necessary (but insufficient) condition for the positions of the MI peaks

$$D_{\mathrm{even}}\left(\omega_{\mathrm{m}}\right) + P = 0 \tag{3.23}$$

This equation can be solved numerically, after which the pathological values in which $dx/d\omega = 0$ doesn't correspond to a positively-valued maximum are removed.

### Modelling a real device

A 220nm × 380nm SOI geometry was chosen, due its relatively large HOD, and thus the possibility of seeing the extra pair of higher-order sidebands. The growth rate spectrum at multiple wavelengths is plotted in figure 3.22 and the positions of the growth rate maxima are plotted in figure 3.23. These show that for a pump wavelength of 1.5$\mu$m, four sidebands should be seen.

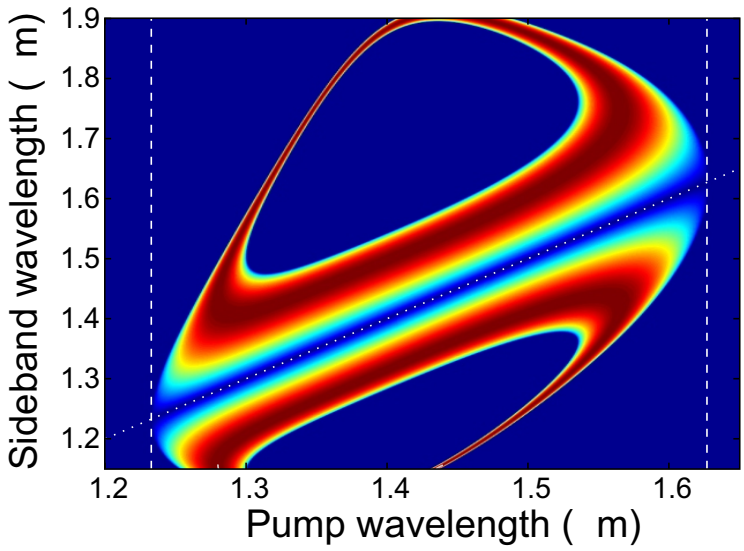


Figure 3.22: Modulational instability sideband growth rate $g$, plotted as a function of both the pump wavelength and the sideband wavelength for a 220nm × 380nm SOI waveguide. The solid background colour corresponds to a growth rate of zero. Anomalous GVD (on the pump axis) is in between the dashed vertical lines. The dotted line corresponds to $\omega_{\mathrm{m}} = 0$ (i.e. the pump and sideband wavelengths being the same).

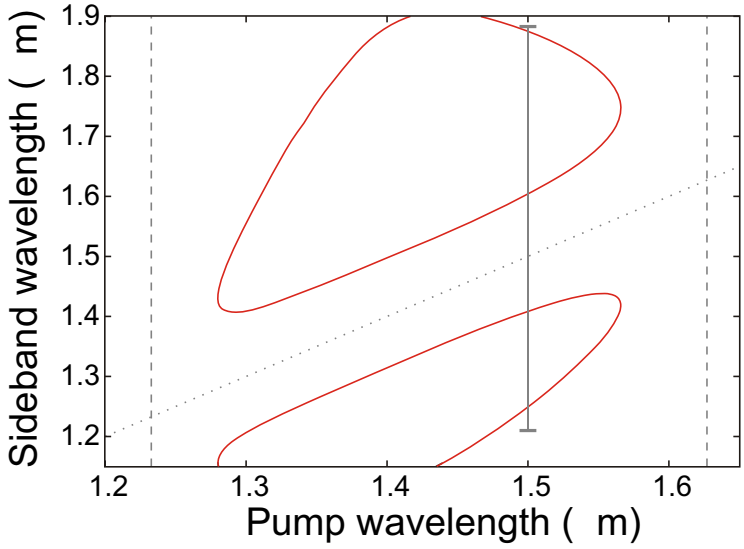


Figure 3.23: As for figure 3.22, but with the growth rate maxima plotted. A pump wavelength of 1.5$\mu$m (represented by the grey bar) should give four sideband frequencies.

Modelling was performed using 10ps rectangular pulses with power $10P_0$. Random noise (with a relative amplitude of 0.5%) was also added to help initiate the instability. The results of the simulation (together with an overlay of the predicted gain) is given in figure 3.24. The model included 2PA ($\epsilon_{2\text{pa}} = 0.1$) and linear absorption ($\epsilon_\text{l} = 0.01$). Free charge carriers were accounted for by assuming a carrier absorption cross section of $\epsilon_\text{fc} = 10^{-3}\,(1 + 7.5i)$. A FROG diagram for the resulting signal can be seen in figure 3.25.

This scheme is notably different to that considered in the literature. Previous work with silicon [85, 171, 172] assumes a scheme whereby the instability is seeded with light at one of the predicted gain wavelengths, which is then amplified. Here, the effect of a pulse on its own is considered. Whilst random noise is added in order to initiate the instability, this lacks any preferred frequency component.

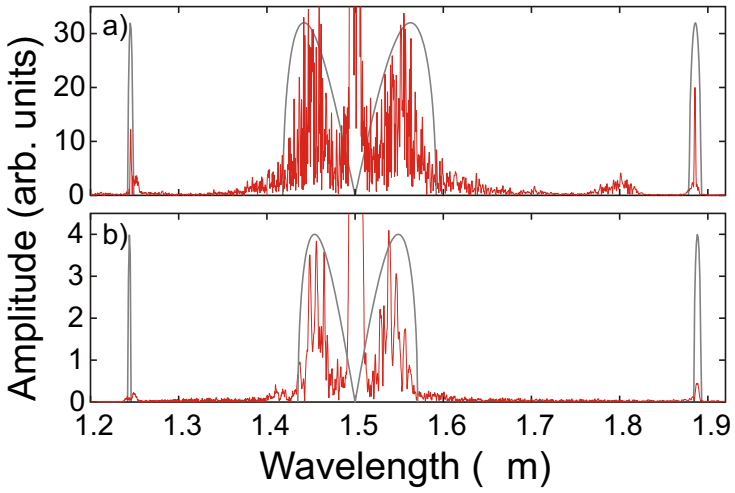


Figure 3.24: Spectral output of a 220nm × 380nm SOI wire pumped with a 10ps pulse with power $10P_0$. After 1.2mm, spectral sidebands due to modulational instability are present. a) Model includes linear absorption and 2PA, but not FCC effects. The predicted gain is overlaid, and was calculated for $P = 4P_0$ to account for the effect of damping. b) Model also includes FCC effects. The predicted gain is calculated for $P = 2.5P_0$ to account for further damping.

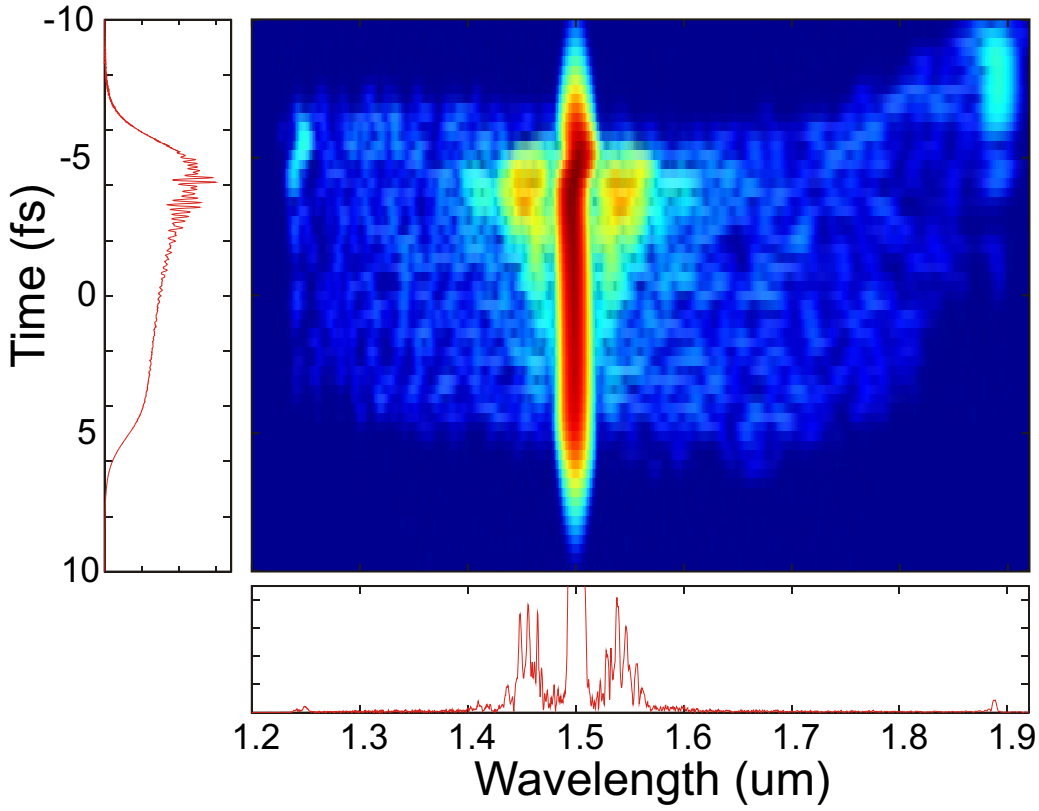


Figure 3.25: FROG diagram for the signal (inclusive of free carrier interactions) in figure 3.24. The colouration is logarithmic, over a 40dB range. The bright vertical feature is the pump, whilst the MI sidebands are visible as the four patches in the upper part of the image. It can be seen that these have a far shorter duration (of the order 1ps) than the pump. The peak at 1.89$\mu$m peak precedes its spectral counterpart at 1.24$\mu$m, due to group velocity difference causing them to separate.

# Chapter 4

# Nonlinear propagation in coupled waveguide arrays

If two waveguides are placed in close proximity, light will be transferred between them, due to the evanescent field surrounding one overlapping with the core of the other. Such a device is known as a directional coupler, and has been realised in both fibres [176] and in SOI [177]. This can be generalised to an array of waveguides, which again has been realised in both fibres [178] and SOI.

The use of silicon adds a novel feature to such devices, arising from the strong dependence of the coupling on frequency. The frequency dependence of couplers is well known [179], but in silicon it is so strong that the *second* derivative of the coupling with respect to frequency becomes substantial, giving it a group velocity dispersion (GVD).

The GVD of the coupling is almost always normal, but by choosing the relative phases within the wires, its effective sign can be changed. By exciting a coupler mode where the two wires are half a cycle out of phase, the effective coupling GVD can be made anomalous. This can be used to realise both solitons (section 4.3) and modulational instability (section 4.5) in coupled systems where the individual waveguides are normally dispersive.

In waveguide arrays, this effect generalises into an interplay between group velocity dispersion and diffraction. Anomalous GVD can be achieved by using *anomalous diffraction*, in which neighboring waveguides are out of phase. Again, this can be used to realise multi-wire solitons, as is shown in section 4.4.2.

Anomalous diffraction has been a widely studied topic in recent years [180]. A substantial fraction of this interest is due to its close association with negative index refraction [181, 182]. (Materials with negative refractive index have been hypothesised since the 1960s [183], but have only recently been realised [184], and even then in suboptimal highly-lossy form. They are of

prime importance to modern optics, as they promise exotic applications including "superlenses" which can resolve images at less than the wavelength of light [185], and even invisibility devices [186].) The similarity between refraction and dispersion results from the fact that both relate the wavenumber of propagation to another wavenumber. In the case of refraction, this wavenumber is in time (i.e. the frequency), whilst in diffraction it is the transverse spatial wavenumber. Therefore, reversing the sign of diffraction is analogous to reversing the sign of the refractive index. This chapter generalises that result, by showing that reversing the sign of diffraction is also akin to reversing the sign of dispersion.

The key results of this chapter have been published in Optics Express [187].

## 4.1 Modelling coupled SOI waveguides

The light guided by a silicon nanowire isn't totally confined to the silicon itself, and will in part travel in the surrounding medium. This can be seen in figure 4.1, which shows the waveguide modes to have evanescent tails which extend into the surrounding air and silica. If two waveguides are placed in close proximity, then the evanescent field of one will significantly overlap with the core of the other, allowing light to be transferred between them.

A coupled waveguide system can be thought of as being one big waveguide having two principal modes, known as *supermodes*. In the case of identical waveguides (which is the only case considered in this report), one of these modes will be perfectly symmetric (in that the field profiles in the two wires will be mirror images of one another), whilst the other will be perfectly antisymmetric (in that the mirror-imaging will be accompanied by a reversal of field direction). An example of such a mode pairing is given in figure 4.1. If a pulse of light is fired into just one wire, a superposition of the two supermodes will be excited. These will (in general) have different propagation constants and so beating between the two modes will occur. Each wire will alternately see constructive and destructive interference, and so the pulse will move back and forth between wires [179].

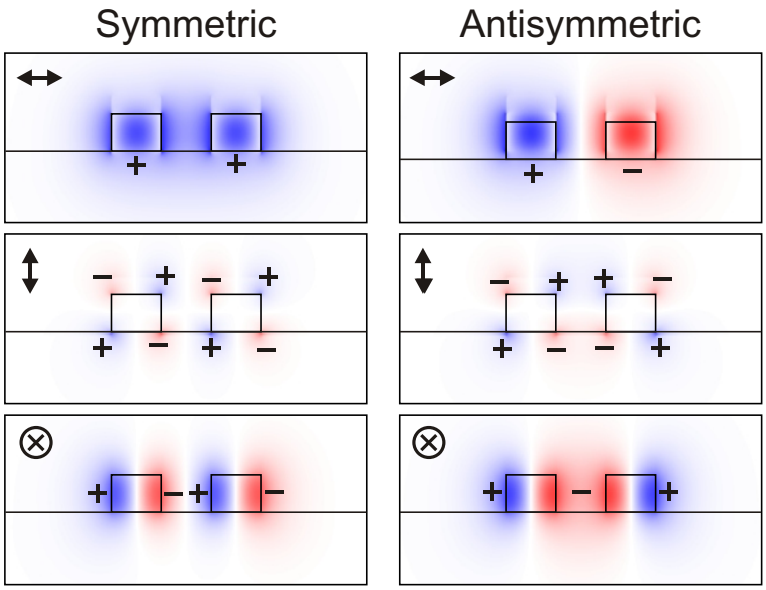


Figure 4.1: Symmetric (left) and antisymmetric (right) mode profiles, displayed over a $2\mu$m $\times$ $1\mu$m cross section for 220nm $\times$ 330nm waveguides placed 330nm apart. Silica is beneath the horizontal line, with the rectangles denoting the silicon. The electric field vector is split into Cartesian components, with transverse components parallel to the silica-air interface shown top, transverse perpendicular components shown middle, and longitudinal components shown bottom. Colour saturation gives absolute value. The + and − signs denote relative phase.

To extend the model derived in chapter 2 to a coupled-wire system, we start by making what is known as the tight-binding approximation [188]. This assumes that the supermodes are linear superpositions of the single-wire modes. (It is named after a similar approximation in solid state physics, in which the wavefunction of a crystal is assumed to be a linear superposition of the wavefunctions of the individual sites [189, 190].) This approach suffers from two main limitations: Firstly, it ignores the existence of higher order photonic bands in which the peaks of intensity no longer correspond to the waveguide cores [191]. Secondly, there is an upper limit to the coupling strength that can be considered, as when waveguides are in very close proximity, slot-guiding modes will form, in which light is trapped between the waveguides by total internal reflection [192].

To procede, we write the envelopes of the symmetric and antisymmetric supermodes (given by $A_\mathrm{s}$ and $A_\mathrm{a}$ respectively) as

$$A_\mathrm{s} = \frac{1}{2}\left(A_1 + A_2\right) \tag{4.1}$$

$$A_\mathrm{a} = \frac{1}{2}\left(A_1 - A_2\right) \tag{4.2}$$

where $A_1$ and $A_2$ are the slowly varying envelopes for the two wires. Subject to the tight-binding

approximation, the propagation coefficients can be written as

$$\beta_{\mathrm{s}}(\omega) = \beta(\omega) + \delta(\omega) \tag{4.3}$$

$$\beta_{\mathrm{a}}(\omega) = \beta(\omega) - \delta(\omega) \tag{4.4}$$

where $\delta$ is a parameter that corresponds to the strength of the coupling. It is almost always positive, meaning that the symmetric supermode has a higher effective index than the antisymmetric supermode. The sign can however be changed with certain exotic waveguide configurations. An example is of AlGaAs waveguides surrounded by a metamaterial consisting of AlGaAs rods in a sapphire matrix [193, 181].

For the study of solitons, the coupling coefficient is usually assumed to be a constant [179]. For silicon wires, however, it is necessary to consider the full dependence on frequency. This is represented using the Taylor expansion $\delta(\omega) = \sum_m (\delta_m/m!)(\omega-\omega_0)^m$. Rewriting equations 4.3 and 4.4 using these coefficients gives

$$\beta_{\mathrm{s}m} = \beta_m + \delta_m \tag{4.5}$$

$$\beta_{\mathrm{a}m} = \beta_m - \delta_m \tag{4.6}$$

The $\delta_m$ coupling coefficients were obtained by calculating $\beta_{\mathrm{s}m}$ and $\beta_{\mathrm{a}m}$ directly from Maxwell's equations, using the methods described in section 2.1.2. By altering the dimensions of the waveguides, it was possible (to a certain extent) to alter the magnitudes of the coupling coefficients. However, despite considering a large range of waveguides, the signs could not be changed. The reason for this can be seen by noting that the evanescent fields surrounding the waveguide scale roughly with the wavelength. If we then assume that the coupling into a wire is proportional to its overlap with the exponentially decaying tail of another wire, then the frequency dependence of coupling can be approximated as

$$\delta \approx \delta_0 e^{-x(\omega-\omega_0)} \tag{4.7}$$

where $x$ is a positive constant. Taylor expanding this in $\omega$ gives

$$\delta \approx \delta_0 + (-\delta_0 x)(\omega-\omega_0) + \frac{1}{2}\left(\delta_0 x^2\right)(\omega-\omega_0)^2 + \mathcal{O}(\omega-\omega_0)^3 \tag{4.8}$$

where we can identify the linear term $-\delta_0 x$ with $\delta_1$ and the quadratic term $\delta_0 x^2$ with $\delta_2$. It therefore follows (assuming that we are not using an exotic waveguide configuration with negative $c_0$) that $\delta_1$ is negative and $\delta_2$ is positive.

In the absence of all damping and nonlinearity, the two supermodes will propagate independently, with Schrödinger-like equations given by

$$\frac{\partial A_{\mathrm{s}}}{\partial z} + \sum_{m=0}^{M} i^{m-1}(\beta_m + \delta_m)\frac{\partial^m A_{\mathrm{s}}}{\partial t^m} = 0 \tag{4.9}$$

$$\frac{\partial A_{\mathrm{a}}}{\partial z} + \sum_{m=0}^{M} i^{m-1}(\beta_m - \delta_m)\frac{\partial^m A_{\mathrm{a}}}{\partial t^m} = 0 \tag{4.10}$$

where (unlike with a single wire) the zeroth and first order terms are still present, as they differ between the two modes and thus can't be scaled away. (This is highly significant, as it is these differences that cause the coupling.) If we substitute equations 4.1 and 4.2 into equations 4.9 and 4.10, we obtain

$$\frac{1}{2}\left(\frac{\partial A_1}{\partial z}+\frac{\partial A_2}{\partial z}\right)+\frac{1}{2}\sum_{m=0}^{M}\frac{i^{m-1}}{m!}\left(\beta_m+\delta_m\right)\left(\frac{\partial^m A_1}{\partial t^m}+\frac{\partial^m A_2}{\partial t^m}\right) = 0 \tag{4.11}$$

$$\frac{1}{2}\left(\frac{\partial A_1}{\partial z}-\frac{\partial A_2}{\partial z}\right)+\frac{1}{2}\sum_{m=0}^{M}\frac{i^{m-1}}{m!}\left(\beta_m-\delta_m\right)\left(\frac{\partial^m A_1}{\partial t^m}-\frac{\partial^m A_2}{\partial t^m}\right) = 0 \tag{4.12}$$

Adding or subtracting these gives

$$\frac{\partial A_1}{\partial z}+\sum_{m=0}^{M}\frac{i^{m-1}}{m!}\left(\beta_m\frac{\partial^m A_1}{\partial t^m}+\delta_m\frac{\partial^m A_2}{\partial t^m}\right) = 0 \tag{4.13}$$

$$\frac{\partial A_2}{\partial z}+\sum_{m=0}^{M}\frac{i^{m-1}}{m!}\left(\beta_m\frac{\partial^m A_1}{\partial t^m}+\delta_m\frac{\partial^m A_1}{\partial t^m}\right) = 0 \tag{4.14}$$

These are simply the wave equations for an isolated waveguide, with a coupling term of the form

$$\sum_{m=0}^{M} i^{m-1}\frac{\delta_m}{m!}\frac{\partial^m A'}{\partial t^m} \tag{4.15}$$

added on, where $A'$ is the envelope for the neighbouring waveguide.

### Coupling length

If we consider the simplest possible case of coupled waveguides, with all nonlinearity, frequency dependence and damping removed (i.e. the case of monochromatic light through a lossless waveguide at low power), we obtain

$$\frac{\partial A_1}{\partial z} = i\delta_0 A_2 \tag{4.16}$$

$$\frac{\partial A_2}{\partial z} = i\delta_0 A_1 \tag{4.17}$$

where $A_1$ and $A_2$ are the envelopes for the two guides. This has a solution of the form

$$A_1 = \cos\left(c_0 z\right) \tag{4.18}$$

$$A_2 = i\sin\left(c_0 z\right) \tag{4.19}$$

where we have imposed the boundary conditions that $A_1 = 1$ and $A_2 = 0$ at $z = 0$. (In other words, light has been fired into the first wire, but not into the second.) We can see that after a propagation distance of $\pi/2\delta_0$, all the light has been transferred in the second wire, and at $\pi/\delta_0$, all the light has returned to the first wire (with a phase shift). This will continue,

with light being transferred back-and-forth between the two wires. (This back-and-forth light transfer is precisely that alluded to above, and is caused by beating between the symmetric and antisymmetric supermodes.) Using this fact, we can define the *coupling length* as

$$L_{\mathrm{C}} \equiv \frac{\pi}{2\left|\delta_0\right|} \equiv \frac{\pi}{\left|\beta_{\mathrm{s}0} - \beta_{\mathrm{a}0}\right|} \tag{4.20}$$

This gives the distance taken for transfer of light from one wire into another. This (in the same manner as the dispersion length) provides a very useful metric with which to gauge the intrinsic length scales of coupling. It is also possible to calculate the coupling length in a more direct manner, by performing numerical integration of the full Maxwell equations in a coupled wire system [194].

### Conversion to dimensionless units

When converted into the familiar dimensionless units, the coupling term becomes

$$\sum_{m=0}^{M} i^{m-1} c_m \frac{\partial^m E_{\mathrm{c}}}{\partial \tau^m} \tag{4.21}$$

where the $m$th coupling coefficient is given by

$$c_m = \frac{L_{\mathrm{D}}}{m! T_0^m} \delta_m \tag{4.22}$$

It follows from the definition of the $\delta_m$ coefficients (in equations 4.5 and 4.6) that these coefficients are given by

$$c_m = \frac{L_{\mathrm{D}}}{2m! T_0^m} \left(\beta_{\mathrm{s}m} - \beta_{\mathrm{a}m}\right) \tag{4.23}$$

By analogy with the dispersion operator $\hat{D}$ given by equation 2.71, we can define a coupling operator $\hat{C}$ as

$$\hat{C} = \sum_{m=0}^{M} c_m \left(i \frac{\partial}{\partial \tau}\right)^m \tag{4.24}$$

This gives (for a single wire interacting with a second wire with envelope $E'$)

$$\frac{\partial E}{\partial \zeta} - i\hat{D}E = i|E|^2 E + i\hat{C}E' \tag{4.25}$$

which after reintroducing damping gives

$$\frac{\partial E}{\partial \zeta} - i\hat{D}E = i|E|^2 E + i\hat{C}E' - \epsilon_{\mathrm{l}} E_n - \epsilon_{2\mathrm{pa}}|E_n|^2 E - \epsilon_{3\mathrm{pa}}|E_n|^4 E - \epsilon_{\mathrm{fc}} E_n \nu \tag{4.26}$$

**Waveguide arrays**

The procedure for calculating waveguide coupling is linear, and so obeys the principle of superposition. Therefore, when multiple waveguides are present, the coupling between each pair of neighbours can be considered independently, and the resulting coupling terms simply added together. This can be extended to an arbitrarily large set of waveguides, so that the undamped equation for the $n$th waveguide is given by

$$\frac{\partial E_n}{\partial \zeta} - i\hat{D}E_n = i|E_n|^2 E_n + i\hat{C}\left(E_{n+1} + E_{n-1}\right) \tag{4.27}$$

where the out-of-bounds values of $E_n$ (i.e. those beyond the ends of the row of waveguides) are identically zero. Reintroducing damping gives

$$\frac{\partial E_n}{\partial \zeta} - i\hat{D}E_n = i|E_n|^2 E_n + i\hat{C}\left(E_{n+1} + E_{n-1}\right) - \epsilon_1 E_n - \epsilon_{2\mathrm{pa}}|E_n|^2 E - \epsilon_{3\mathrm{pa}}|E_n|^4 E - \epsilon_{\mathrm{fc}} E_n \nu_n \tag{4.28}$$

When $N$ wires are present, it follows that there must be $N$ separate equations to describe free carrier evolution. The equation for the $n$th waveguide is given by

$$\frac{d\nu_n}{d\tau} = |E_n|^4 - \frac{\nu_n}{\tau_{\mathrm{c}}} \tag{4.29}$$

where $\nu_n$ is the carrier density in that particular wire.

## 4.2 Device specifications

The aim of this chapter is to control dispersion with coupling. To demonstrate this point, a normally dispersive waveguide was chosen, which in isolation would not be capable of exhibiting soliton propagation or modulational instability. Therefore, transverse dimensions of 220nm $\times$ 330nm were chosen, giving a normal GVD of $-1416\ \mathrm{ps\,nm^{-1}\,km^{-1}}$ at a 1.5$\mu$m pump wavelength (Figure 4.2). For 100fs pulses, this gives a dispersion length of 1.93mm. Such waveguides were placed 330nm apart, providing very strong coupling (as is shown in figure 4.2), but remaining within the tight-binding approximation (as is shown in figure 4.3). The mode profiles were shown above (in figure 4.1). The leading coupling coefficients are $c_0 = 132.7$, $c_1 = -24.22$ and $c_2 = 2.254$, whilst the dispersion coefficient is $p_2 = 0.5$.

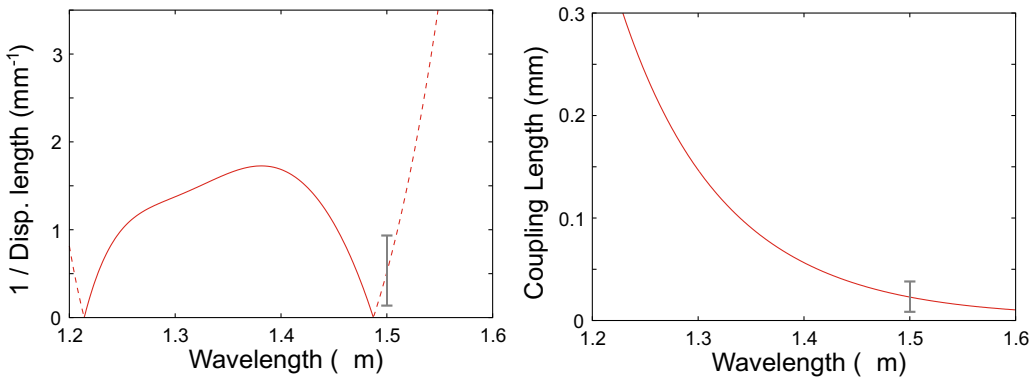


Figure 4.2: The left hand plot shows dispersion length (as a function of wavelength) of a 220nm × 330nm SOI waveguide for 100fs pulses. The solid line gives anomalous GVD, whilst the dashed line gives normal GVD. The vertical bar gives the position of the 1.5$\mu$m pump wavelength. The right hand plot shows the coupling length for the same waveguides placed 330nm apart.

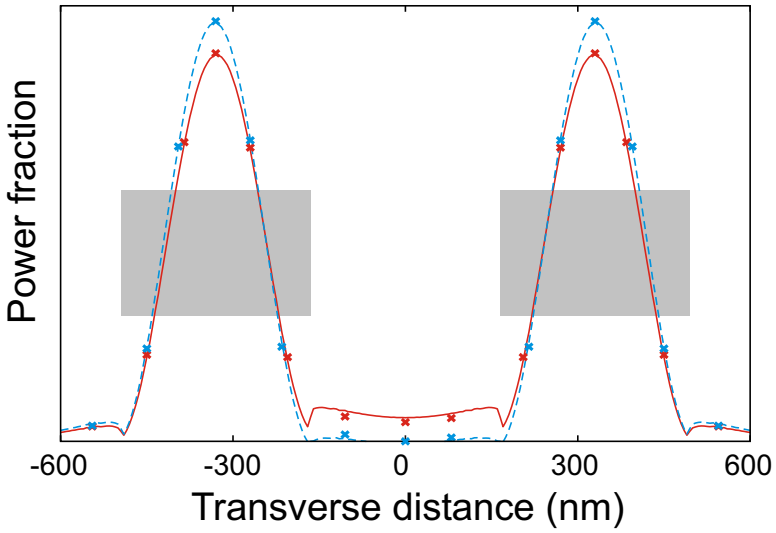


Figure 4.3: Demonstration of the validity of the tight binding approximation for 220nm × 330nm waveguides placed 330nm apart. The power transmission as a function of transverse distance is plotted, with the solid line giving the symmetric mode, and the dashed line giving the antisymmetric mode. The dots show the corresponding quantities calculated by linear superposition of the single-wire modes, showing a very good agreement. The grey blocks show the waveguide dimensions

## 4.3 Temporal solitons in a directional coupler

Directional couplers in silicon can support solitons, even if the constituent waveguides are normally dispersive at the pump frequency. The coupled system is described by the equations

$$\frac{\partial E_1}{\partial \zeta} - i\hat{D}E_1 = i|E_1|^2 E_1 + i\hat{C}E_2 \tag{4.30}$$

$$\frac{\partial E_2}{\partial \zeta} - i\hat{D}E_2 = i|E_2|^2 E_2 + i\hat{C}E_1 \tag{4.31}$$

where $E_1$ and $E_2$ are the field envelopes of the two wires. (For clarity the damping terms are not shown.) To find supermodal solitons, we switch to a supermodal basis of the form

$$X \equiv \frac{1}{2}(E_1 + E_2) \tag{4.32}$$

$$Y \equiv \frac{1}{2}(E_1 - E_2) \tag{4.33}$$

$$\tag{4.34}$$

where $X$ and $Y$ are the symmetric and antisymmetric modes respectively. Transforming equations 4.30 and 4.31 gives

$$\frac{\partial X}{\partial \zeta} - i\left(\hat{D} + \hat{C}\right)X = i|X|^2 X + 2i|Y|^2 X + iX^* Y^2 \tag{4.35}$$

$$\frac{\partial Y}{\partial \zeta} - i\left(\hat{D} - \hat{C}\right)Y = i|Y|^2 Y + 2i|X|^2 Y + iY^* X^2 \tag{4.36}$$

We now have equations for the two modes, which are connected only by nonlinear coupling terms. Truncating the operators to second order gives

$$\frac{\partial X}{\partial \zeta} + i(p_2 + c_2)\frac{\partial^2 X}{\partial \tau^2} - ic_0 X + c_1 \frac{\partial X}{\partial \tau} = i|X|^2 X + 2i|Y|^2 X + iX^* Y^2 \tag{4.37}$$

$$\frac{\partial Y}{\partial \zeta} + i(p_2 - c_2)\frac{\partial^2 Y}{\partial \tau^2} + ic_0 Y - c_1 \frac{\partial Y}{\partial \tau} = i|Y|^2 Y + 2i|X|^2 Y + iY^* X^2 \tag{4.38}$$

Soliton solutions can now be found by setting either $X$ or $Y$ to zero, whilst retaining the other term. Doing this, we obtain one of the following equations

$$\frac{\partial X}{\partial \zeta} + i(p_2 + c_2)\frac{\partial^2 X}{\partial \tau^2} - ic_0 X + c_1 \frac{\partial X}{\partial \tau} = i|X|^2 X \tag{4.39}$$

$$\frac{\partial Y}{\partial \zeta} + i(p_2 - c_2)\frac{\partial^2 Y}{\partial \tau^2} + ic_0 Y - c_1 \frac{\partial Y}{\partial \tau} = i|Y|^2 Y \tag{4.40}$$

These equations have the respective solutions

$$X = e^{iq\zeta}\sqrt{2(q - c_0)}\,\mathrm{sech}\left(\sqrt{\frac{q - c_0}{-(p_2 + c_2)}}(\tau - \zeta c_1)\right) \tag{4.41}$$

$$Y = e^{iq\zeta}\sqrt{2(q + c_0)}\,\mathrm{sech}\left(\sqrt{\frac{q + c_0}{-(p_2 - c_2)}}(\tau + \zeta c_1)\right) \tag{4.42}$$

These solutions have the same structure as the familiar $E = e^{iqz}\sqrt{2q}\,\mathrm{sech}\left(\sqrt{2q}\tau\right)$ solitons (and indeed become identical when we set the coupling terms to zero). Therefore, the waveguide pair is simply acting as a single quasi-waveguide, with modified propagation coefficients. The solutions are a generalisation of previously known solutions [179], to which they reduce in the case $c_1 = c_2 = 0$.

Three things about these solutions are notable:

- Firstly, the solitons no longer travel at the group velocity of the waveguide (which is zero in the moving frame in which the NLS equation is constructed). Instead it is increased in velocity by $1/c_1$ for the symmetric case, and reduced by $1/c_1$ for the antisymmetric case. This effect has been observed for pulses in two-core optical fibres [195].
- Secondly, the wavenumber condition for soliton existence is no longer $q > 0$, but $q > c_0$ for the symmetric mode and $q > -c_0$ for the antisymmetric mode. These cutoff points correspond to the wavenumbers of linear propagation ($c_0$ for the symmetric mode and $-c_0$ for the antisymmetric mode) at which point the pump frequency of the soliton would be phase matched to linear radiation modes.
- The third, and most important result is that the effective values of group velocity dispersion are $p_2 \pm c_2$, rather than just $p_2$. Therefore, the threshold condition for soliton formation is now $p_2 < -c_2$ for the symmetric mode, and $p_2 < c_2$ for the antisymmetric mode. This allows for the extension of the spectral window within which solitons are permitted into the normal regime. Due to the positive sign of $c_2$, this will occur in the antisymmetric mode. Conversely, a symmetric mode restricts the range of the soliton regime. The GVD of the coupling, and the effective dispersions of the supermodes are given in figure 4.4.

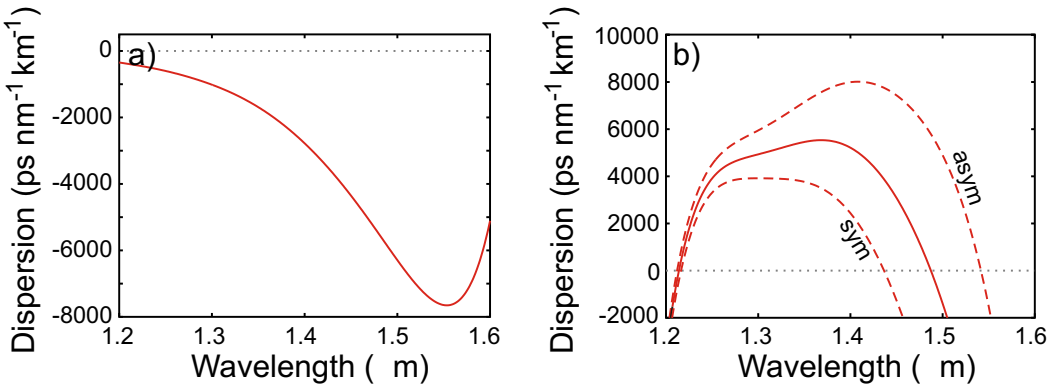


Figure 4.4: a) The dispersion parameter for the coupling between 220nm × 330nm wires placed 330nm apart, plotted over wavelength. This shows the coupling operator to be strongly normally dispersive. b) The dispersion parameters for the symmetric and antisymmetric supermodes (dashed lines) together with that of a single wire (solid line). It can be seen that the spectral range of anomalous GVD is restricted for the symmetric mode, and extended for the antisymmetric mode.

### 4.3.1 Stability analysis of the antisymmetric mode

Just because equations 4.41 and 4.42 are stationary solutions, doesn't mean that the corresponding solitons are stable. They could be mathematically analogous to a needle which is placed perfectly upright, balanced upon its point, such that the slightest perturbation will cause it to fall. Therefore, it is necessary to see how the solutions react to perturbation. Such analysis is widely established for models with frequency-independent coupling [196, 197], but here it is extended to systems where the coupling affects both the group velocity and GVD.

We will start by analysing the stability of solitons in the antisymmetric mode. We take a solution of the form $X = 0,\ Y = y(\zeta,\tau)\, e^{iq\zeta}$ (where $y(\zeta,\tau)\, e^{iq\zeta}$ is the solution given by equation 4.42 written in the form of a real amplitude $y$ multiplied by a complex phase $e^{iq\zeta}$). We then add perturbation terms to give

$$X = \epsilon_y(\zeta,\tau)\, e^{iq\zeta} \tag{4.43}$$

$$Y = y(\zeta,\tau)\, e^{iq\zeta} + e_y(\zeta,\tau)\, e^{iq\zeta} \tag{4.44}$$

where $\epsilon_y$ represents potential inter-modal instability, whilst $e_y$ represents instability within the mode. By only considering the initial stages of instability, we can linearise the problem by rejecting the higher powers of $\epsilon_y$ and $e_y$. Making the substitution into equations 4.37 and 4.38 gives

$$\frac{\partial\epsilon_y}{\partial\zeta} + i(p_2+c_2)\frac{\partial^2\epsilon_y}{\partial\tau^2} + i(q-c_0)\,\epsilon_y + c_1\frac{\partial\epsilon_y}{\partial\tau} = 2iy^2\epsilon_y + iy^2\epsilon_y^* \tag{4.45}$$

$$\frac{\partial e_y}{\partial\zeta} + i(p_2-c_2)\frac{\partial^2 e_y}{\partial\tau^2} + i(q+c_0)\,e_y - c_1\frac{\partial e_y}{\partial\tau} = 2iy^2 e_y + iy^2 e_y^* \tag{4.46}$$

It is inconvenient to have $y$ a function of both $\tau$ and $\zeta$. However, if we make the substitution $\tau \equiv \tau_y - \zeta c_1$, where $\tau_y$ is relative time in a shifted frame of reference, we obtain the univariate function

$$y(\tau_y) = \sqrt{2(q+c_0)}\ \mathrm{sech}\left(\sqrt{\frac{q+c_0}{-(p_2-c_2)}}\tau_y\right) \tag{4.47}$$

Transforming equations 4.45 and 4.46 likewise gives

$$\frac{\partial\epsilon_y}{\partial\zeta} + i(p_2+c_2)\frac{\partial^2\epsilon_y}{\partial\tau_y^2} + i(q-c_0)\,\epsilon_y + 2c_1\frac{\partial\epsilon_y}{\partial\tau_y} = 2iy^2\epsilon_y + iy^2\epsilon_y^* \tag{4.48}$$

$$\frac{\partial e_y}{\partial\zeta} + i(p_2-c_2)\frac{\partial^2 e_y}{\partial\tau_y^2} + i(q+c_0)\,e_y = 2iy^2 e_y + iy^2 e_y^* \tag{4.49}$$

We assume solutions of the form

$$\epsilon_y = \tilde{\epsilon}_y(\tau_y)\, e^{\lambda_y\zeta} \tag{4.50}$$

$$e_y = \tilde{e}_y(\tau_y)\, e^{l_y\zeta} \tag{4.51}$$

where $\lambda_y$ and $l_y$ are constants to be determined. This is an eigenvalue problem (as is shown in appendix C.1) with $\tilde{\epsilon}_y$ and $\tilde{e}_y$ as the eigenfunctions and $\lambda_y$ and $l_y$ as the eigenvalues.

Equations 4.50 and 4.51 exhibit a continuum of eigenvalues along the imaginary axis, which correspond to the set of all delocalised eigenfunctions. (This is derived in appendix C.2.) However when $c_1^2 + (p_2 + c_2)(q - c_0) < 0$, a bandgap exists in $\lambda_y$ over the range

$$-\left|q - c_0 + \frac{c_1^2}{p_2 + c_2}\right| \; < \Im[\lambda_y] < \; \left|q - c_0 + \frac{c_1^2}{p_2 + c_2}\right| \tag{4.52}$$

and when $(q + c_0)/(p_2 - c_2) < 0$, a bandgap in $l_y$ exists over the range

$$-|q + c_0| \; < \Im[l_y] < \; |q + c_0| \tag{4.53}$$

These delocalised modes are not particularly important in themselves, as having zero real part they will not contribute to exponential growth and instability. The band-gap *is* significant however, as within it discrete eigenvalues can exist, which correspond to localised eigenfunctions [23]. These *can* have non-zero real part, and if positive will lead to exponential growth and thus instability. A search for discrete eigenvalues was made numerically, as is shown in appendix C.3.

It is known that a bifurcation point should occur at $q = c_0$, corresponding to the existence of asymmetric nonlinear supermodes [196, 197]. (These modes are considered in more detail in section 4.5.2, in the context of modulation instability.) However no discrete eigenvalues corresponding to instabilities into these modes were found, despite scanning across both $q$ and the pump frequency. This is not entirely unexpected, as the exotic solitons that form in these asymmetric modes have a higher energy than those in the ordinary antisymmetric mode [196, 197], and thus the latter are already in the more stable state.

**Intramodal perturbation**

For the intramodal perturbation, the discrete eigenvalues (of which there are four) can be found analytically. (The resulting spectrum is shown in figure 4.5.) There is a 2-fold degenerate solution with eigenvalue $l_y = 0$ corresponding to the eigenfunction

$$e_y = i\,\mathrm{sech}\left(\sqrt{\frac{q + c_0}{-(p_2 - c_2)}}\tau_y\right) \tag{4.54}$$

and a second solution, again with 2-fold degeneracy and $l_y = 0$, with eigenfunction

$$e_y = 2\tanh\left(\sqrt{\frac{q + c_0}{-(p_2 - c_2)}}\,\tau_y\right)\mathrm{sech}\left(\sqrt{\frac{q + c_0}{-(p_2 - c_2)}}\,\tau_y\right) \tag{4.55}$$

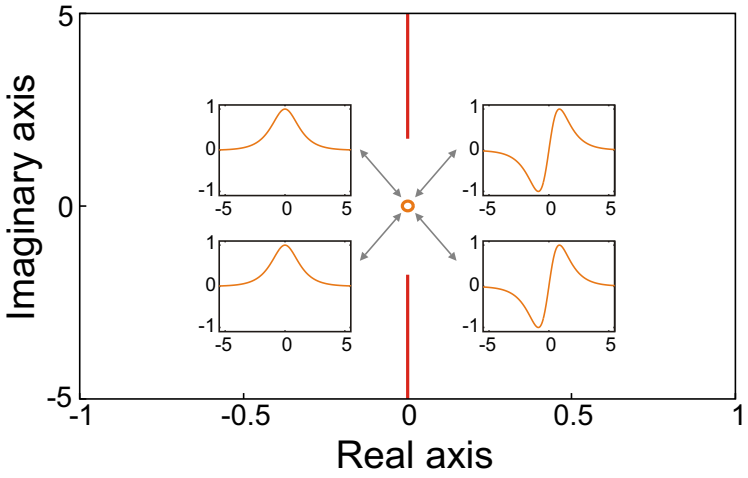


Figure 4.5: Spectrum of equation 4.49 shown for $q = -130.9$ (i.e. a pulse with unit duration) for the system described in section 4.2. A continuum of delocalised eigenvalues lies along the imaginary axis, with a bandgap in the range $-1.754 < e_y < 1.754$. Four discrete eigenvalues exist at the origin, which are plotted as functions of $\tau_y$.

None of these will contribute to instability, as they have no real part. A numerical search was made for additional discrete eigenvalues (again, using the method described in appendix C.3), but none were found. This suggests that the antisymmetric mode is also stable with respect to intramodal instability.

### 4.3.2 Bifurcation of the symmetric supermode

We can analyse the stability of the symmetric mode in the same way. (The solutions will not exist at a 1.5$\mu$m pump. Therefore a 1.4$\mu$m pump was used.) As before, we have a symmetric solution of the form $X = x(\zeta,\tau)\, e^{iq\zeta}$, $Y = 0$ (where $x(\zeta,\tau)\, e^{iq\zeta}$ is the solution given by equation 4.41 written in the form of a real amplitude $x$ multiplied by a complex phase $e^{iq\zeta}$), which we perturb to give

$$X = x(\zeta,\tau)\, e^{iq\zeta} + e_x(\zeta,\tau)\, e^{iq\zeta} \tag{4.56}$$

$$Y = \epsilon_x(\zeta,\tau)\, e^{iq\zeta} \tag{4.57}$$

where $\epsilon_x$ represents potential inter-modal instability, whilst $e_x$ represents instability within the mode. Substituting this into equations 4.37 and 4.38 and linearising gives

$$\frac{\partial e_x}{\partial \zeta} + i(p_2 + c_2)\frac{\partial^2 e_x}{\partial \tau^2} + i(q - c_0)\, e_x + c_1\frac{\partial e_x}{\partial \tau} = 2ix^2\epsilon_x + ix^2\epsilon_x^* \tag{4.58}$$

$$\frac{\partial \epsilon_x}{\partial \zeta} + i(p_2 - c_2)\frac{\partial^2 \epsilon_x}{\partial \tau^2} + i(q + c_0)\, \epsilon_x - c_1\frac{\partial \epsilon_x}{\partial \tau} = 2ix^2 e_x + ix^2 e_x^* \tag{4.59}$$

As before, we shift into a moving frame of reference in order to avoid $x$ being function of both $\tau$ and $\zeta$. We make the substitution $\tau \equiv \tau_x + \zeta c_1$, giving

$$x(\tau_x) = \sqrt{2(q-c_0)}\ \mathrm{sech}\left(\sqrt{\frac{q-c_0}{-(p_2+c_2)}}\tau_x\right) \tag{4.60}$$

Transforming equations 4.58 and 4.59 likewise gives

$$\frac{\partial e_x}{\partial \zeta} + i(p_2+c_2)\frac{\partial^2 e_x}{\partial \tau_x^2} + i(q-c_0)e_x = 2ix^2 e_x + ix^2 e_x^* \tag{4.61}$$

$$\frac{\partial \epsilon_x}{\partial \zeta} + i(p_2-c_2)\frac{\partial^2 \epsilon_x}{\partial \tau_x^2} + i(q+c_0)\epsilon_x - 2c_1\frac{\partial \epsilon_x}{\partial \tau_x} = 2ix^2\epsilon_x + ix^2\epsilon_x^* \tag{4.62}$$

Again, we assume solutions of the form

$$\epsilon_x = \tilde{\epsilon}_x(\tau_x)\, e^{\lambda_x \zeta} \tag{4.63}$$

$$e_x = \tilde{e}_x(\tau_x)\, e^{l_x \zeta} \tag{4.64}$$

where $\lambda_x$ and $l_x$ are constants to be determined. As before, this is an eigenvalue problem (as shown in appendix C.1) with $\tilde{\epsilon}_x$ and $\tilde{e}_x$ as the eigenfunctions and $\lambda_x$ and $l_x$ as the eigenvalues.

As with the antisymmetric case, 4.63 and 4.64 exhibit a continuum of eigenvalues along the imaginary axis, corresponding to the set of all delocalised eigenfunctions. (This is derived in appendix C.2.) When $c_1^2 + (p_2 - c_2)(q + c_0) < 0$ a bandgap exists in $\lambda_x$ over the range

$$-\left|q + c_0 + \frac{c_1^2}{p_2 - c_2}\right| < \Im[\lambda_x] < \left|q + c_0 + \frac{c_1^2}{p_2 - c_2}\right| \tag{4.65}$$

and when $(q - c_0)/(p_2 + c_2) < 0$, a bandgap in $l_x$ exists over the range

$$-|q - c_0| < \Im[l_x] < |q - c_0| \tag{4.66}$$

It is known that in the absence of coupling GVD, a bifurcation point occurs at $q = \frac{5}{3}c_0$, which (as for the instability mentioned in section 4.3.1) corresponds to the formation of an asymmetric mode [196, 197]. If we wish to find similar behaviour, we need to search for a discrete eigenvalue which gains a positive real part when $q$ exceeds a critical value. This search was made numerically (using the method described in appendix C.3), with the results shown in figure 4.6. This shows that as $q$ is increased, a pair of discrete eigenvalues in $\lambda_x$ (with values summing to zero) enter the band-gap and migrate along the imaginary axis towards the origin. When they reach it, they start heading in opposite directions along the real axis, and thus the soliton will become unstable.

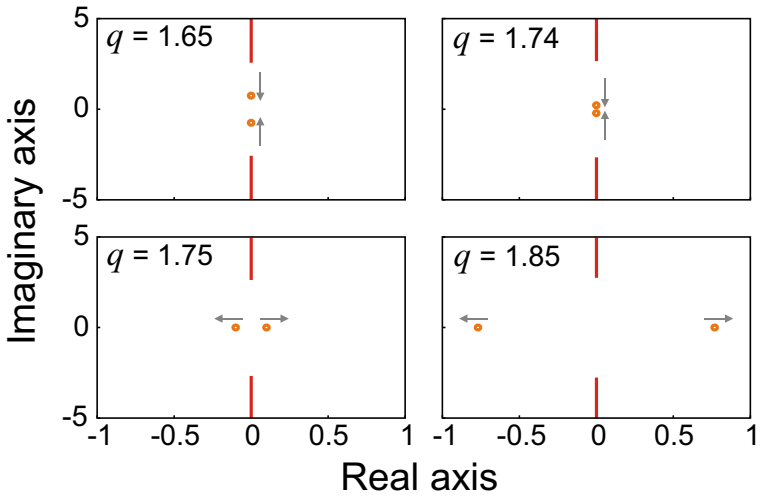


Figure 4.6: Movement of discrete eigenvalues as $q$ is increased. Starting at $q = 1.65$, the two eigenvalues lie on the imaginary axis. As $q$ is increased towards 1.74 the eigenvalues move towards the origin. Between $q = 1.74$ and $q$ 1.75, they reach the origin, and start moving along the real axis. At $q = 1.85$ they have a strong real part.

We therefore see a bifurcation when $\lambda_x = 0$. In the special case where $c_1 = 0$, we can find an analytical solution

$$\tilde{\epsilon}_x = \operatorname{sech}^2\left(\sqrt{\frac{q - c_0}{-(p_2 + c_2)}}\tau_x\right) \tag{4.67}$$

subject to the condition

$$q = \frac{2 - p_2 - c_2}{2 + p_2 + c_2}c_0 \tag{4.68}$$

Without coupling (when $c_2 = 0$, and $p_2$ must be $-\frac{1}{2}$), this reduces to $q = \frac{5}{3}c_0$, and thus the result is a generalisation of that seen in references [196] and [197]. We will return to the self-focussing effects that give rise to this instability in section 4.5.2.

**Intramodal perturbation**

For the intramodal perturbation, the discrete eigenvalues can (just as for the antisymmetric case) be found analytically. There is a 2-fold degenerate solution with eigenvalue $l_y = 0$ corresponding to the eigenfunction

$$e_y = i\operatorname{sech}\left(\sqrt{\frac{q - c_0}{-(p_2 + c_2)}}\tau_x\right) \tag{4.69}$$

and a second solution, again with 2-fold degeneracy and $l_y = 0$, with eigenfunction

$$e_y = 2\tanh\left(\sqrt{\frac{q - c_0}{-(p_2 + c_2)}}\,\tau_x\right)\operatorname{sech}\left(\sqrt{\frac{q - c_0}{-(p_2 + c_2)}}\,\tau_x\right) \tag{4.70}$$

Again, none of these will contribute to instability, as they have no real part. A numerical search was made for additional discrete eigenvalues, but none were found. This suggests that (as for

the antisymmetric case) there is no intramodal instability.

### 4.3.3 Soliton generation

Soliton evolution was modelled numerically. (See appendix A.1.) The supermodes can be generated directly by firing coherent light into the array such that both wires are excited. The antisymmetric mode can be generated by pumping at a non-zero angle of incidence, so that the differing path lengths cause an incremental phase shift between neighboring waveguides [198, 199]. It is more interesting, however, to fire light into just one wire, thus creating a superposition of the two modes, and then to rely upon the group-velocity difference noted above to split the modes. Pulse propagation for the linear regime is given in figure 4.7, and it can be seen that the pulse splits cleanly in two. Introducing nonlinearity (but not damping) in figure 4.8 shows that the antisymmetric pulse forms a soliton. The introduction of damping in figure 4.9 shows that the soliton survives.

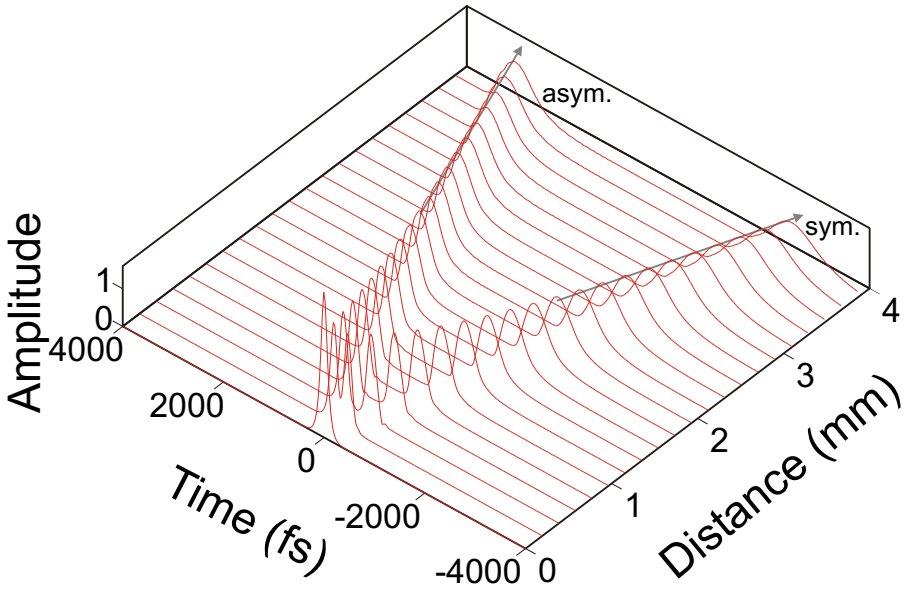


Figure 4.7: Evolution of a pulse with peak power $15P_0$ fired into the 1st wire of a 2 wire system. (Amplitude derived as $\sqrt{\sum_n |E_n|^2}$, which corresponds to incoherent mixing between the outputs of each wire.) Without damping or nonlinearity, the pulse splits into a pair of supermodal pulses due to the effect of coupling on group velocity.

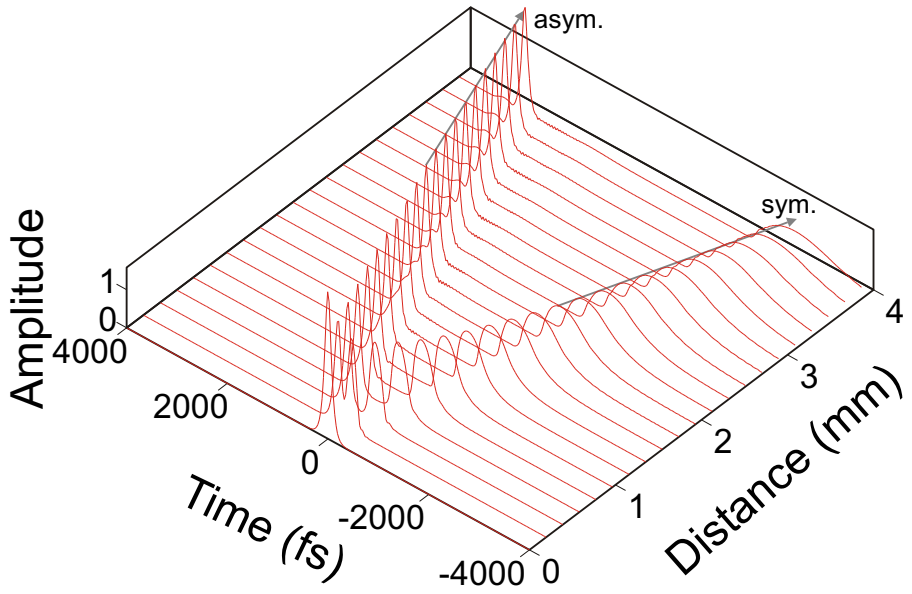


Figure 4.8: As with figure 4.7, but with nonlinearity turned on. The antisymmetric mode is anomalously dispersive, and so in the presence of nonlinearity, the pulse forms a soliton. Conversely, the symmetric supermode is normally dispersive, and so the nonlinearity accelerates pulse broadening.

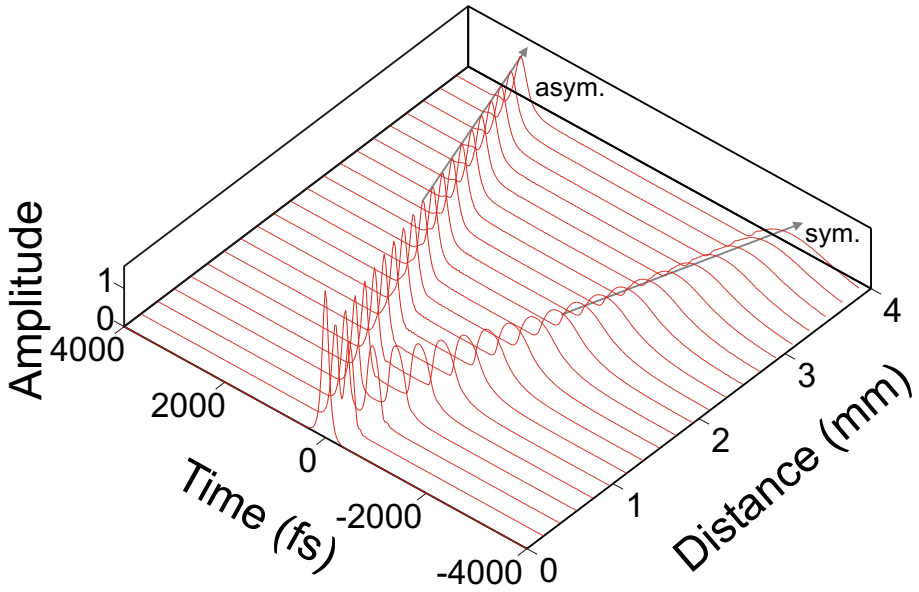


Figure 4.9: As with figure 4.8, but with realistic damping ($\epsilon_{2pa} = 0.1$, $\epsilon_l = 0.05$) turned on. Despite this, substantial nonlinear suppression of dispersive broadening of the antisymmetric pulse remains.

The soliton like pulse shown in figure 4.9 can be investigated further, by using the soliton area parameter defined in section 3.3.3. As before, we define a parameter $S = T_{\mathrm{FWHM}}\sqrt{P_{\mathrm{max}}}$. For the ideal soliton solution (equation 4.42) the peak power (summed over both of the channels)

is given (in terms of the intrinsic unit $P_0$) by

$$P_{\max} = 4\left(q + c_0\right) P_0 \tag{4.71}$$

Similarly, the FWHM duration is given (in terms of the intrinsic unit $T_0$) by

$$T_{\mathrm{FWHM}} = 2\ln\left(1+\sqrt{2}\right)\sqrt{\frac{c_2 - p_2}{q + c_0}}T_0 \tag{4.72}$$

This gives an ideal soliton area parameter of

$$S_0 = 4T_0\sqrt{P_0}\ln\left(1+\sqrt{2}\right)\sqrt{c_2 - p_2} \tag{4.73}$$

Figure 4.10 shows the soliton area parameter plotted as a function of distance. It remains roughly constant, having a value close to $S_0$, thus showing that the pulse is a soliton.

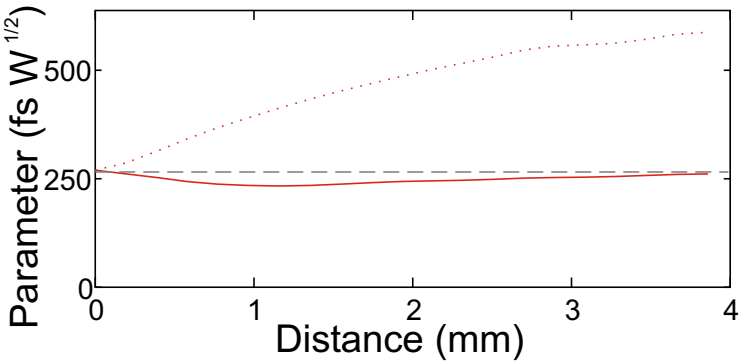


Figure 4.10: Soliton area parameter for the soliton in figure 4.9. The solid line gives the value of $S$ along the distance of propagation. This remains roughly constant and close to the ideal value $S_0$ (denoted by the dashed grey line). The dotted line gives the parameter with nonlinearity turned off, showing a stark contrast with the nonlinear regime. (The quantities are scaled such that the power unit $P_0 = 1\mathrm{W}$.)

## 4.4 Temporal solitons in multiwire waveguide arrays

### 4.4.1 Interplay between diffraction and dispersion

The above can be generalised to a system with an arbitrary number of waveguides, $N$. We start by rewriting the undamped equations of motion (equations 4.27) in a vector form, where $\vec{E}$ contains the values of $E_n$. This gives

$$\frac{\partial \vec{E}}{\partial \zeta} - i\hat{D}\vec{E} = if\left(\vec{E}\right) + i\hat{X}\hat{C}\vec{E} \tag{4.74}$$

where the function $f(\vec{x}) \equiv |\vec{x}|^2 \vec{x}$ acts independently on each element of the vector, and the matrix operator $\hat{X}$ is defined as

$$\hat{X}_{(\mu)(\nu)} \equiv \delta_{(\mu)(\nu-1)} + \delta_{(\mu)(\nu+1)} \tag{4.75}$$

where $\delta$ is the Kronecker symbol. (It should be noted that the matrix $\hat{X}$ will be encountered once again in section 5.3, when the radiation emitted by spatiotemporal solitons is considered.)

In order to proceed, we need to diagonalise this matrix equation. We write the eigenvalue equation for $\hat{X}$ as

$$\hat{X}\vec{x}_k = \chi_k \vec{x}_k \tag{4.76}$$

which yields eigenvalues of the form

$$\chi_k \equiv 2\cos\left(\frac{\pi k}{N+1}\right) \tag{4.77}$$

with corresponding (normalised) eigenvectors

$$(\vec{x}_k)_n = \sqrt{\frac{2}{N+1}} \sin\left(\frac{\pi n k}{N+1}\right) \tag{4.78}$$

It should be noted that the index $k$ is arbitrary, and thus may be replaced with other indices, as is done for $\chi_j$ and $\vec{x}_j$ below. The eigenvalue are distinct, as the argument of the cosine function is always within the range $0 < \theta < \pi$, over which the cosine function shows one-to-one correspondence. As $\hat{X}$ is both self-adjoint and distinct-eigenvalued, it follows that the normalised eigenvectors must form an orthonormal basis. This can be seen explicitly by defining a scalar product operation

$$\vec{a} \cdot \vec{b} \equiv \sum_{n=1}^{N} (a)_n^* (b)_n \tag{4.79}$$

Using the trigonometric identity

$$\frac{2}{N+1} \sum_{n=1}^{N} \sin\left(\frac{\pi n j}{N+1}\right) \sin\left(\frac{\pi n k}{N+1}\right) = \delta_{(j)(k)} \qquad \forall j,k \in \{1,2,\cdots,N\} \tag{4.80}$$

(where $\delta$ is the Kronecker symbol) gives $\vec{x}_k \cdot \vec{x}_j = \delta_{(j)(k)}$, as required. We can therefore diagonalise equation 4.74 by expanding $\vec{E}$ in this basis as

$$\vec{E} = \sqrt{\frac{2(N+1)}{3}} \sum_{k=1}^{N} \tilde{E}_k \vec{x}_k \tag{4.81}$$

where $\tilde{E}_k$ is the amplitude of each modal component. (The $\sqrt{2(N+1)/3}$ prefactor is a matter of convenience, chosen so that in a few steps further on, equation 4.92 will have unit nonlinearity.)

The basis conforms to the condition that $E_0 = E_{N+1} = 0$, meaning that the (non-existent) wires outside of the waveguide boundaries contain no light. It should also be noted that this

basis is a generalisation of that used for the $N = 2$ case in section 4.3, with $\tilde{E}_1 = X$ and $\tilde{E}_2 = Y$.

Substituting this into equation 4.27 and then taking the scalar product with any basis vector $\vec{x}_j$ (to project out the $j$th mode) gives

$$\frac{\partial \tilde{E}_j}{\partial \zeta} - i\hat{D}_j \tilde{E}_j = \frac{2}{3}(N+1)\,\vec{x}_j \cdot f\left(\sum_{k=1}^{N} \tilde{E}_k \vec{x}_k\right) \tag{4.82}$$

where the effective dispersion of each mode is given by

$$\hat{D}_j = \hat{D} + \chi_j \hat{C} \tag{4.83}$$

We have not fully diagonalised the equations, due to the nonlinear terms. However, there are no longer any *linear* terms linking the components of equation 4.82. Therefore, in the low power limit the system is diagonal and so each component of equation 4.82 will evolve independently.

**Normal and anomalous diffraction**

It is apparent from equation 4.83 that the dispersion and coupling are interlinked, with the eigenvalue $\chi_j$ controlling the extent of this interaction. The fact that these eigenvalues are distinct means that each mode has a unique dispersion relation. The values of $\chi_j$ occur in pairs having opposite sign (plus a zero-eigenvalue when $N$ is odd) due to the property that $\cos(\theta) \equiv -\cos(\pi - \theta)$. This is highly significant, as by choosing the appropriate mode, it is possible to effectively reverse the signs of the coupling coefficients.

It is instructive to rewrite equations 4.77 and 4.78 as

$$\chi_j = 2\cos(\kappa_x) \tag{4.84}$$

$$\vec{x}_j = \sqrt{\frac{2}{N+1}}\sin(\kappa_x n) \tag{4.85}$$

where the periodicity of the waveguide amplitudes is given by the *transverse wavenumber*

$$\kappa_x \equiv \frac{\pi j}{N+1} \tag{4.86}$$

In the limit of an infinitely large array, the transverse wavenumber becomes a continuous varying quantity. If we were to excite such an array with a coherent beam of light fired along the direction of the waveguides, then a mode with all the wires in phase (and thus $\kappa_x = 0$) would be excited. If the initial excitation was restricted to a finite region of the waveguide, then a spatial wavepacket centred about $\kappa_x = 0$ would be excited. Alternatively, by tilting the beam with respect to the direction of the waveguides, a phase shift would be introduced between each wire (due to the varying path length) thus exciting a mode with non-zero $\kappa_x$ [199]. In general, such a beam will spread into the surrounding waveguides, in what is essentially a discrete version of diffraction. It can be shown, for instance, that the width of a Gaussian beam

focused onto the array boundary will vary with propagation as [199]

$$W = W_0\sqrt{1+\left(\frac{2C\chi_j''}{W_0^2}\zeta\right)^2} \tag{4.87}$$

where $W_0$ is the initial width. The *diffraction coefficient* $\chi_j'' \equiv \partial^2\chi_j/\partial\kappa_x^2 = -\chi_j$ specifies the magnitude of the diffraction. It is the spatial equivalent of dispersion, and is almost always negative [198].

At $\kappa_x = 0$, the diffraction coefficient possesses its minimum value of $\chi_j'' = -2$. As $\kappa_x$ is increased from 0, the diffraction coefficient becomes less negative, until at $\kappa_x = \pi/2$ the diffraction vanishes, and the beam propagates with constant width. Increasing $\kappa_x$ beyond $\pi/2$ causes the diffraction coefficient to become positive, in what is known as anomalous diffraction [198]. At $\kappa_x = \pi$ the diffraction coefficient reaches its maximum value of $\chi_j'' = 2$. Notably, equation 4.87 is not dependent on the sign of $\chi_j''$, and so this state broadens in exactly the same manner as the $\kappa_x = 0$ state. More generally, the states with $0 \leq |\kappa_x| < \pi/2$ give normal diffraction, whilst the states with $\pi/2 < |\kappa_x| \leq \pi$ give anomalous diffraction. It can also be seen that normal diffraction corresponds to positive values of $\chi_j$, whilst anomalous diffraction corresponds to negative values.

The mode profiles for the $\kappa_x = 0$, $\pi/2$ and $\pi$ cases are plotted in figure 4.11. For $\kappa_x = 0$, the wires are all in phase, whilst for $\kappa_x = \pi$ every mode is maximally out of phase with its neighbours. The diffractionless mode at $\kappa_x = \pi/2$ corresponds to a mode in which every other wire has zero amplitude, as is shown in figure 4.11.

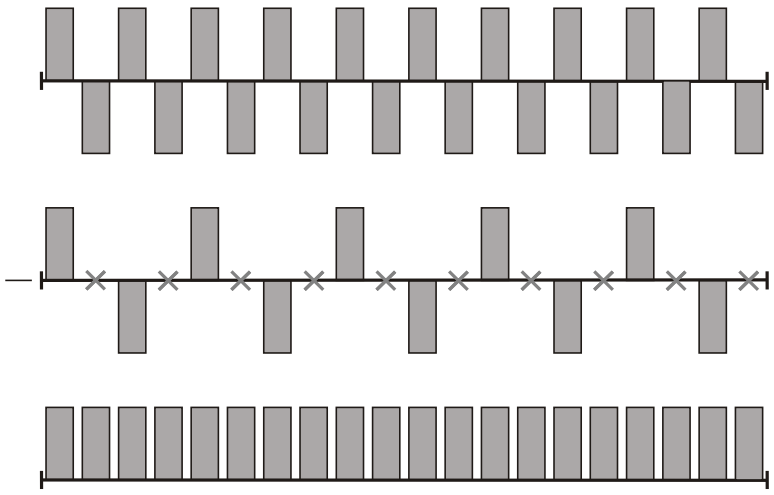

Figure 4.11: Examples of modes of an infinite waveguide array (shown over a 20-waveguide section). At a transverse wavenumber of $\kappa_x = 0$ (bottom), all the waveguides are in phase, giving normal diffraction. At a transverse wavenumber of $\kappa_x = \pi/2$ (middle) every other waveguide has zero amplitude (denoted with crosses), giving zero effective coupling and thus zero diffraction. At $\kappa_x = \pi$ every waveguide is out of phase with its neighbours, giving anomalous diffraction.

In the more general case, the relationship between the normally diffractive and anomalously

diffractive modes can be seen by defining a matrix $\hat{S}$ as

$$\hat{S}_{(\mu)(\nu)} \equiv -(-1)^{\mu}\delta_{(\mu)(\nu)} \tag{4.88}$$

where $\delta$ is the Kronecker symbol. This matrix anticommutes with $\hat{X}$ and thus multiplication of an eigenvector by $\hat{S}$ provides the eigenvector with oppositely signed eigenvalue. Therefore, multiplication by $\hat{S}$ (which is self-inverse) switches back-and-forth between states with normal and anomalous diffraction. The operation has the effect of shifting the phase of every other wire by half a cycle, which in turn has the effect of reversing the inter-wire phase relationship between each neighboring pair. Therefore, each normally diffractive mode is paired with an anomalously diffractive mode having the same amount of light in each waveguide, and the same beam widening properties, but opposing inter-wire phase relationships.

It should be noted that the scheme described above is not the only means of achieving anomalous diffraction. The most direct means is to invert the sign of coupling (as mentioned in section 4.1) by using systems consisting of (for example) AlGaAs waveguides separated by a metamaterial consisting of AlGaAs rods in a sapphire matrix [193, 181]. It can also be achieved by using higher order photonic bands [191, 200].

When a finite array of wires of wires is used, $\kappa_x$ becomes quantised to the values given by equation 4.86. Whilst the extremal $\kappa_x = 0$ and $\kappa_x = \pi$ modes can only exist in an infinite array, the $\kappa_x = \pi/2$ diffractionless modes *can* be seen, and exist for all arrays with odd $N$.

### Controlling dispersion with diffraction

From equation 4.83 it is apparent that for normally diffractive modes (with positive $\chi_j$), the coupling dispersion operator $\hat{C}$ will be added to the dispersion operator $\hat{D}$, whilst for anomalously diffractive modes (with negative $\chi_j$), $\hat{C}$ will be subtracted from $\hat{D}$. In otherwords, normal diffraction will cause the coupling dispersion to reinforce the waveguide dispersion, whilst anomalous diffraction will cause the coupling dispersion to counteract the waveguide dispersion.

As was described in section 4.1, the GVD of coupling is usually normal. However, by using anomalous diffraction, we can use it to create anomalous GVD. Figure 4.12 shows the parameter space (in wavelength and transverse wavenumber) giving anomalous GVD for a set of 220nm $\times$ 330nm waveguides placed 330nm apart. Examples of actual dispersion curves that can be created like this, are shown in figure 4.13.

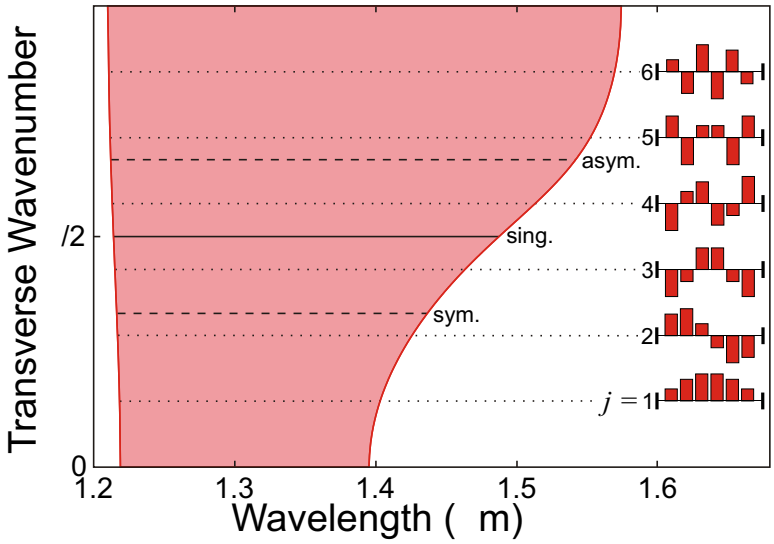


Figure 4.12: The relation between dispersion and diffraction in an array of 220nm × 330nm waveguides placed 330nm apart. The shaded region gives the parameter space (in wavelength and transverse wavenumber) giving anomalous supermode GVD. The transverse wavenumbers corresponding to 2 and 6 wire systems are highlighted with horizontal lines. The mode profiles for the 6 wire system are plotted, with the index $j$ corresponding to that in equation 4.83.

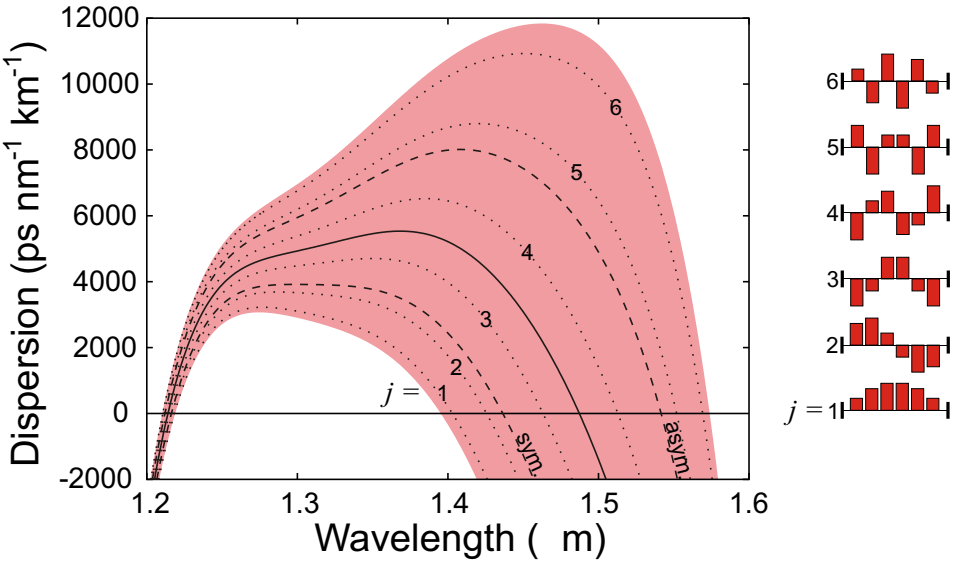


Figure 4.13: Supermodal dispersion plots in an array of 220nm × 330nm waveguides placed 330nm apart. The solid line gives the GVD of an isolated wire. The dashed lines gives the GVDs of the two-wire supermodes. The dotted lines give the GVDs of the six-wire supermodes, with the modes plotted to the right, and the index $j$ corresponding to that in equation 4.83. The shaded area gives the maximum possible extent of dispersion modification, with the boundaries corresponding to the $\kappa_x = 0$ and $\kappa_x = \pi$ cases of an infinite system.

As mentioned previously, there is a correspondence between anomalous diffraction and negative index refraction [181, 182]. Switching back into the unscaled units (defined in section 4.1), the

supermodal wavenumber is given by $\beta_{\text{mode}} = \beta + \chi_j \delta$, and so the supermodal effective index is given by

$$n_{\text{mode}} \equiv \frac{\lambda}{2\pi}\beta_{\text{mode}} = \frac{\lambda}{2\pi}\left(\beta + \chi_j \delta\right) \tag{4.89}$$

Whilst $\chi_j$ is not capable of changing the sign of the refractive index, it is capable of reversing the sign of one of the contributing terms.

### 4.4.2 Supermodal soliton solutions

When only one mode $\tilde{E}_j$ is present, equation 4.82 reduces to

$$\frac{\partial \tilde{E}_j}{\partial \zeta} - i\hat{D}_j \tilde{E}_j = i\frac{8}{3\left(N+1\right)}\sum_{k=1}^{N}\sin^4\left(\frac{k\pi j}{N+1}\right)|\tilde{E}_j|^2\tilde{E}_j \tag{4.90}$$

This can be simplified using the identity

$$\begin{aligned}\frac{8}{3\left(N+1\right)}\sum_{k=1}^{N}\sin^4\left(\frac{k\pi j}{N+1}\right) &= \begin{cases} 1 & ; \quad j \neq \frac{N+1}{2} \\ \\ \frac{4}{3} & ; \quad j = \frac{N+1}{2} \end{cases} \\ \forall j \in \{1, 2, \cdots, N\} & \end{aligned} \tag{4.91}$$

giving an uncoupled NLS equation of the form

$$\frac{\partial \tilde{E}_j}{\partial \zeta} - i\hat{D}_j \tilde{E}_j = i\Gamma_{Nj}|\tilde{E}_j|^2\tilde{E}_j \tag{4.92}$$

where the coefficient $\Gamma_{Nj}$ is given by

$$\Gamma_{Nj} \equiv \begin{cases} 1 & ; \quad j \neq \frac{N+1}{2} \\ \\ \frac{4}{3} & ; \quad j = \frac{N+1}{2} \end{cases} \tag{4.93}$$

The exceptional cases at $j = (N+1)/2$ correspond to the $\kappa_x = \pi/2$ non-diffractive modes, in which the wires are effectively uncoupled. (They also correspond to the trivial $N = 1$ case, where only a single wire is present.) Given the lack of any interaction between dispersion and diffraction, these modes are not particularly interesting, and will not be considered further.

Taking this single-mode equation, and truncating the operators to second order gives

$$\frac{\partial \tilde{E}_j}{\partial \zeta} + i(p_2 + \chi_j c_2)\frac{\partial^2 \tilde{E}_j}{\partial \tau^2} - i\chi_j c_0 \tilde{E}_j + \chi_j c_1 \frac{\partial \tilde{E}_j}{\partial \tau} = i\Gamma_{Nj}|\tilde{E}_j|^2\tilde{E}_j \tag{4.94}$$

This has solutions of the form

$$\tilde{E}_j = e^{iq\zeta}\sqrt{\frac{2\left(q - \chi_j c_0\right)}{\Gamma_{Nj}}}\ \text{sech}\left(\sqrt{\frac{q - \chi_j c_0}{-\left(p_2 + \chi_j c_2\right)}}\left(\tau - \zeta\chi_j c_1\right)\right) \tag{4.95}$$

From equations 4.78 and 4.81, it follows that the transformation out of the modal basis is made as

$$E_n = \sqrt{\frac{4}{3}} \sum_{k=1}^{N} \sin\left(\frac{\pi n k}{N+1}\right) \tilde{E}_k \tag{4.96}$$

Doing so, gives multi-wire soliton solutions of the form

$$E_n = e^{iq\zeta} \sqrt{\frac{8}{3\Gamma_{Nj}} (q - \chi_j c_0)} \sin\left(\frac{\pi n j}{N+1}\right) \operatorname{sech}\left(\sqrt{\frac{q - \chi_j c_0}{-(p_2 + \chi_j c_2)}} (\tau - \zeta \chi_j c_1)\right) \tag{4.97}$$

It can be seen that in the single wire $N = 1$ case (where $p_2 = -\frac{1}{2}$, $\Gamma_{Nj} = \frac{4}{3}$ and $\chi_j = 0$) this reduces to the conventional solution of $E = \sqrt{2q} \operatorname{sech}\left(\sqrt{2q}\,\tau\right) e^{iq\zeta}$. The solutions are a further generalisation of previously known solutions [179], to which they reduce in the case $N = 2$ and $c_1 = c_2 = 0$.

### 4.4.3 Soliton formation

Soliton evolution was modelled numerically. As with the two wire case, the anomalously diffractive supermodes can be excited directly by pumping at a non-zero angle of incidence [198]. However, as before, the method of pumping a single wire and then letting the resulting superposition of modes separate was used. Pulse propagation for the linear regime is given in figure 4.14, and it can be seen that the input pulse splits into a train of six pulses. Introducing nonlinearity (but not damping) in figure 4.15 shows that the final pulse in the train forms a soliton. The introduction of damping in figure 4.16 shows that the soliton survives.

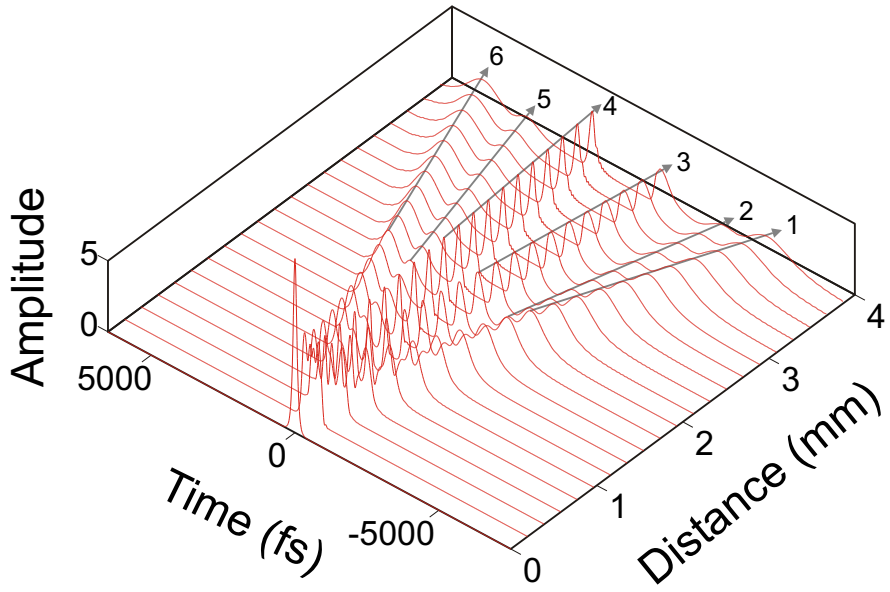


Figure 4.14: Evolution of a pulse with peak power $150P_0$ fired into the 3rd wire of a 6 wire system. (Amplitude derived as $\sqrt{\sum_n |E_n|^2}$, which corresponds to incoherent mixing between the outputs of each wire.) Without damping or nonlinearity, the pulse splits into a train of 6 supermodal pulses (with numbering corresponding to $j$ in equation 4.83).

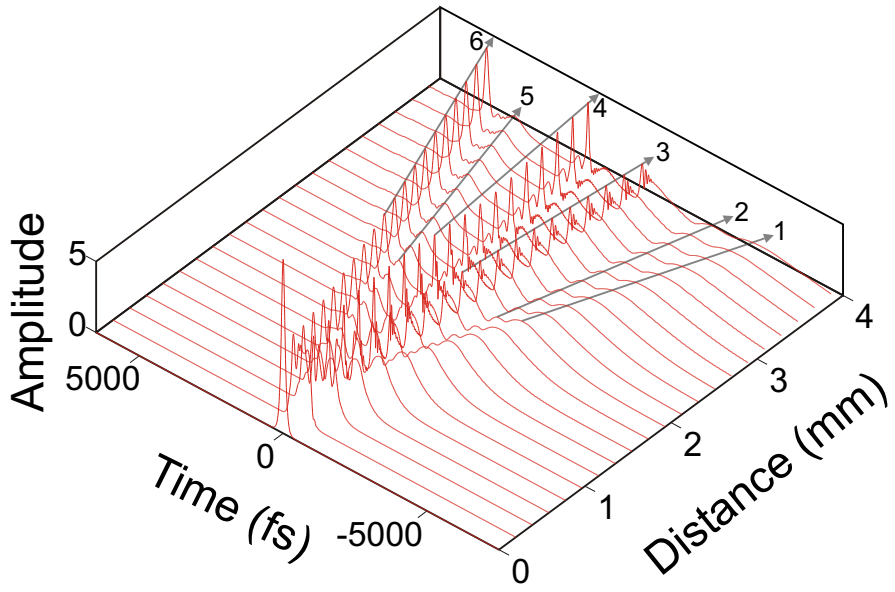


Figure 4.15: As with figure 4.14, but with nonlinearity turned on. The 6th pulse forms a soliton.

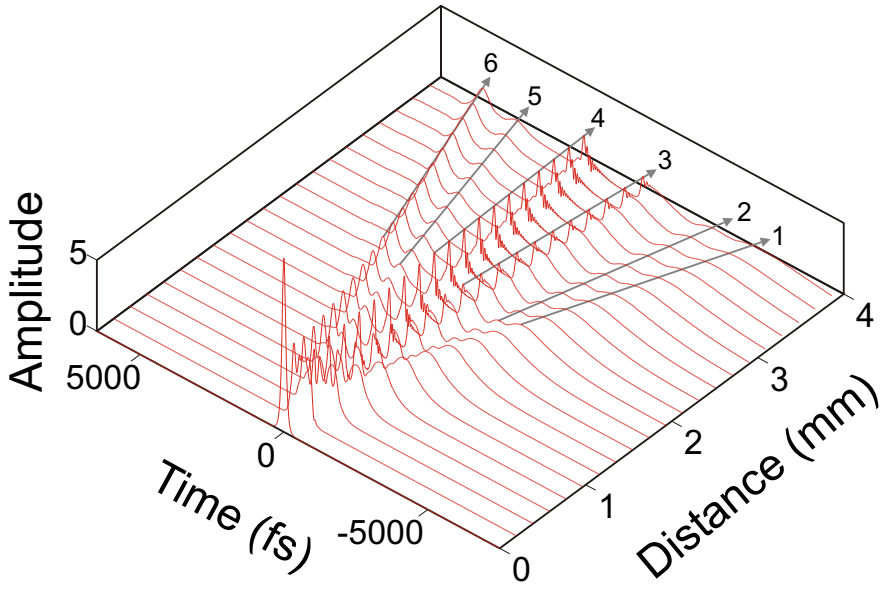


Figure 4.16: As with figure 4.15, but with realistic damping ($\epsilon_{2pa} = 0.1$, $\epsilon_l = 0.05$) turned on. Despite this, substantial nonlinear supression of pulse broadening of the 6th pulse remains.

The soliton-like $j = 6$ pulse shown in figure 4.16 can be investigated (as in section 4.3.3) by using the soliton area parameter. For the ideal soliton solution (equation 4.97) the peak power summed over all of the channels is given by

$$P_{\max} = \frac{4\left(q - \chi_j c_0\right)(N+1)}{3\Gamma_{Nj}} P_0 \tag{4.98}$$

and the FWHM duration is given by

$$T_{\mathrm{FWHM}} = 2\ln\left(1+\sqrt{2}\right)\sqrt{\frac{-\left(p_2+\chi_j c_2\right)}{q-\chi_j c_0}}T_0 \tag{4.99}$$

This gives an ideal soliton area parameter of

$$S_0 = \frac{4}{\sqrt{3}}T_0\sqrt{P_0}\ln\left(1+\sqrt{2}\right)\sqrt{\frac{-\left(p_2+\chi_j c_2\right)(N+1)}{\Gamma_{Nj}}} \tag{4.100}$$

Figure 4.17 shows the soliton area parameter plotted as a function of distance. It remains roughly constant, having a value close to $S_0$, thus showing that the pulse is a soliton.

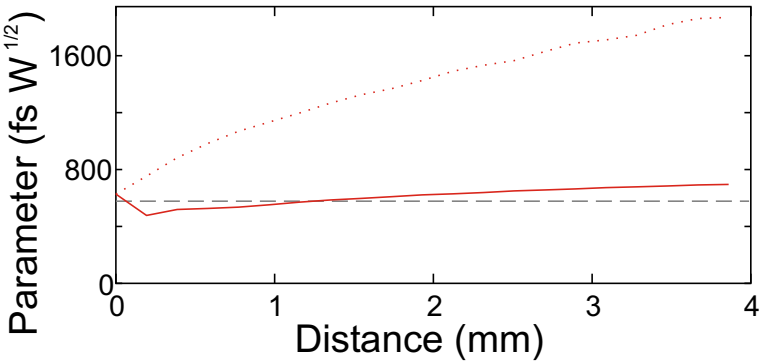


Figure 4.17: Soliton area parameter for the $j = 6$ soliton shown in figure 4.16. The solid line gives the value of $S$ along the distance of propagation. This remains roughly constant and close to the ideal value $S_0$ (denoted by the dashed grey line). The dotted line gives the parameter with nonlinearity turned off, showing a stark contrast with the nonlinear regime. (The quantities are scaled such that the power unit $P_0 = 1$W.)

## 4.5 Modulation instability in couplers

Modulation instability (which was considered for a single wire in section 3.4) can also happen in coupled waveguide systems [201, 202]. As for soliton propagation, the conventional models assume a frequency independent coupling term. Likewise, when coupling GVD is introduced, it can be seen that the dynamics are greatly changed, and that modulation instability can occur in normally dispersive waveguides.

Equations 4.35 and 4.36 possess continuous wave solutions of the form

$$X = \sqrt{P}e^{i(P+c_0)\zeta} \tag{4.101}$$

for the symmetric mode, and

$$Y = \sqrt{P}e^{i(P-c_0)\zeta} \tag{4.102}$$

for the antisymmetric mode. As in section 3.4, $P$ is related to the optical power. It follows

from the transformation in equations 4.32 and 4.33 that $P$ is the power *per wire*, and so the total power in the system in given by $2P$.

As with the single wire case, perturbations from these solutions can be reinforced by the non-linearity, creating spectral sidebands. However, two very different phenomena can result, depending on whether these sidebands are emitted into the same mode as the pump signal, or into the other mode. Both cases are considered below.

### 4.5.1 Intra-modal modulation instability

Taking the antisymmetric solution, we can perturb it as

$$Y = \left(\sqrt{P} + \epsilon\right) e^{i(P-c_0)\zeta} \tag{4.103}$$

where $\epsilon(\zeta, \tau)$ is a small perturbation into the same mode. Substituting this into equation 4.36 gives

$$\frac{\partial \epsilon}{\partial \zeta} - \left(\hat{D} - \hat{C} + c_0\right)\epsilon = iP\left(\epsilon + \epsilon^*\right) \tag{4.104}$$

where terms in $\epsilon^2$ and $\epsilon^3$ have been removed, as we are only considering the first stage of perturbation. This is the same as equation 3.14, except we have replaced the dispersion operator $\hat{D}$ with a modified operator $\hat{D} - \hat{C} + c_0$. We can therefore use the same procedure to derive an expression for the modulation instability side-lobes. The gain spectrum is given by

$$g(\omega_{\mathrm{m}}) = 2\Im\sqrt{\left(\hat{D}_{\mathrm{even}} - \hat{C}_{\mathrm{even}} + c_0\right)^2 + 2P\left(\hat{D}_{\mathrm{even}} - \hat{C}_{\mathrm{even}} + c_0\right)} \tag{4.105}$$

where (as before) the even operators are defined as

$$D_{\mathrm{even}}(\omega) \equiv \frac{1}{2}\left[D(\omega) + D(-\omega)\right] \tag{4.106}$$

$$C_{\mathrm{even}}(\omega) \equiv \frac{1}{2}\left[C(\omega) + C(-\omega)\right] \tag{4.107}$$

so that they only hold components with even powers of $\omega$. Notably, equation 4.105 does not depend on $c_0$, as the explicit $c_0$ term cancels with the implicit term in the $\hat{C}$ operator. Therefore, the modulation instability depends only on the GVD of the coupling, and not its overall value. The gain maxima occur when

$$\hat{D}_{\mathrm{even}}(\omega_{\mathrm{m}}) - \hat{C}_{\mathrm{even}}(\omega_{\mathrm{m}}) + c_0 + P = 0 \tag{4.108}$$

where as described in section 3.4, this is a necessary but insufficient condition, requiring the explicit removal of pathological solutions. The predicted modulation instability peak positions are given in figure 4.18, whilst the numerical spectra are given in figure 4.19. As with a single wire case, four modulation instability peaks can be seen. However, these become obscured in the presence of free carrier interactions. (As in section 3.2.1, a physically reasonable estimate for the carrier cross section of $\epsilon_{fc} \simeq 10^{-3}(1 + 7.5i)$ was used.) It should be noted, however, that techniques exist to sweep away free charge carriers [59], and so a more favourable experimental

result may be possible.

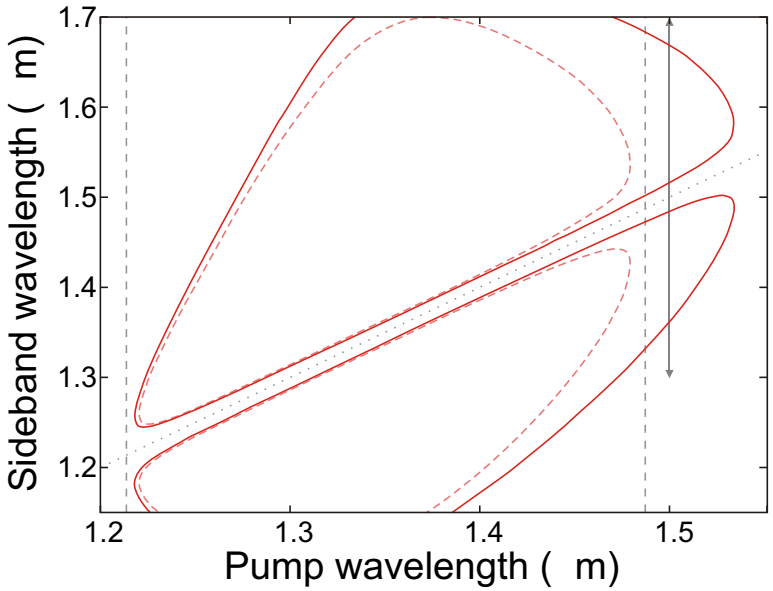


Figure 4.18: Predicted modulation instability sideband wavelengths for a 220nm × 330nm SOI waveguide. For an isolated waveguide (denoted by the dashed lines) the modulation instability only occurs for pump wavelengths where the waveguide is anomalously dispersive (between the dashed vertical lines). When coupling GVD is present, by using the antisymmetric supermode of two such waveguides placed 330nm apart (denoted by the solid line) the modulation instability is extended into the anomalous regime.

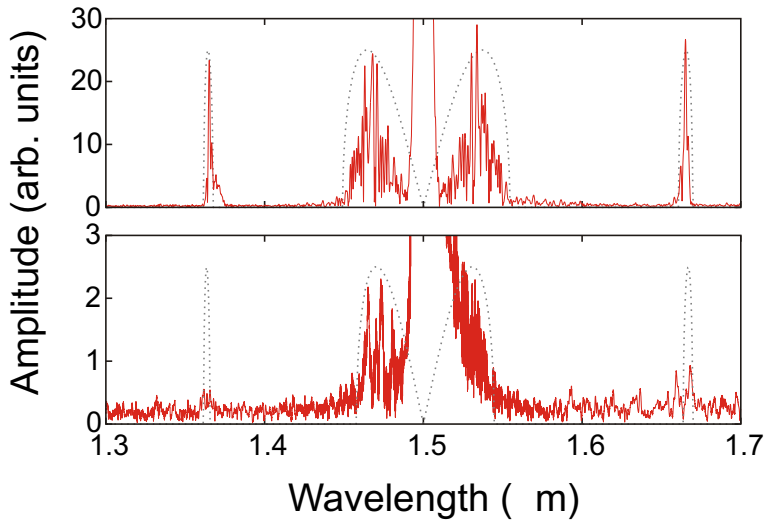


Figure 4.19: Spectral output of a pair of 220nm × 330nm SOI wires placed 330nm apart pumped with a 10ps rectangular pulse with power $10P_0$ in the antisymmetric mode after 3.9mm. The top plot includes 2PA and linear damping ($\epsilon_{2pa} = 0.1$, $\epsilon_l = 0.05$) but not free carrier effects, whilst the bottom plot does include them. The dashed lines give the predicted gain spectra. The powers used to calculate these have been reduced to $5P_0$ and $3.5P_0$ respectively, to allow for the effect of damping.

### 4.5.2 Cross-modal modulation instability

In the symmetric supermode, the effect of coupling GVD is to restrict the wavelength range in which conventional modulational instability is possible. A different picture emerges, however, when the effect of cross-modal instability is considered. This can be seen by taking the symmetric supermodal solution, and modifying it as

$$X = \sqrt{P}e^{i(P+c_0)\zeta} \tag{4.109}$$

$$Y = \epsilon e^{i(P+c_0)\zeta} \tag{4.110}$$

where $\epsilon$ is the cross-modal perturbation. Strictly speaking, the equation for $X$ should also be perturbed, to account for the energy loss into the other mode. When analysing $\epsilon$, however, this is a second-order effect, and can be neglected for the first stages of propagation. Following the same procedure as above gives the gain spectrum as

$$g\left(\omega_{\mathrm{m}}\right) = 2\Im\sqrt{\left(\hat{D}_{\mathrm{even}} - \hat{C}_{\mathrm{even}} - c_0\right)^2 + 2P\left(\hat{D}_{\mathrm{even}} - \hat{C}_{\mathrm{even}} - c_0\right)} \tag{4.111}$$

Unlike equation 4.105, this *does* depend on the value of $c_0$, as the explicit and implicit values reinforce one another. This is a result of the wavenumber mismatch between the mode of the signal and the mode of the emitted radiation. The gain maxima occur at the solutions to

$$\hat{D}_{\mathrm{even}}\left(\omega_{\mathrm{m}}\right) - \hat{C}_{\mathrm{even}}\left(\omega_{\mathrm{m}}\right) - c_0 + P = 0 \tag{4.112}$$

This gain spectrum is notably different from the inter-modal case, in that we can have non-zero gain at the pump frequency. We can see this by setting $\omega_{\mathrm{m}} = 0$, which reduces equation 4.111 to

$$g\left(0\right) = 4\Im\sqrt{c_0^2 - Pc_0} \tag{4.113}$$

We therefore have a critical power at $P_{\mathrm{c}} = c_0$, above which the pump itself is unstable.

#### Modal instability and asymmetric nonlinear supermodes

This phenomenon of the pump itself becoming unstable is well documented, and results from the fact that the modes themselves are altered by the nonlinearity [179]. These modes can be investigated by rewriting equations 4.30 and 4.31 in a different basis as [203]

$$\frac{dS_1}{d\zeta} = 2c_0S_3 \tag{4.114}$$

$$\frac{dS_2}{d\zeta} = -S_1S_3 \tag{4.115}$$

$$\frac{dS_3}{d\zeta} = S_1S_2 - 2c_0S_1 \tag{4.116}$$

where the parameters $S_1$, $S_2$ and $S_3$ are defined has

$$S_1 = |E_1|^2 - |E_2|^2 \tag{4.117}$$

$$S_2 = 2\Re\left[E_1 E_2^*\right] \tag{4.118}$$

$$S_3 = 2\Im\left[E_1 E_2^*\right] \tag{4.119}$$

(We have assumed evolution in the continuous wave regime, and so the time dependent terms are zero.) Conservation of energy subjects these variables to the condition

$$|S_1|^2 + |S_2|^2 + |S_3|^2 = (2P)^2 \tag{4.120}$$

where (in keeping with the above notation) $P = \frac{1}{2}\left(|E_1|^2 + |E_2|^2\right)$ gives the mean power per wire. If $S_1$, $S_2$ and $S_3$, are regarded as the Cartesian coordinates of a three-dimensional vector $\vec{S}$, then equation 4.120 defines a sphere of radius $2P$, on which $\vec{S}$ must lie. (This is extremely similar to the Stokes formation of optical polarisation, with $\vec{S}$ being a modified Stokes vector [204], which is not surprising, as instead of having light split between two principal polarisation states, we have light split between two wires.)

We can proceed by noting that

$$\Gamma \equiv S_2 + S_1^2/\left(4c_0\right) \tag{4.121}$$

is a conserved quantity. This allows us to combine equations 4.114, 4.115 and 4.116 into a single second order equation of the form [203]

$$\frac{d^2 S_1}{d\zeta^2} + \left(4c_0^2 - 2c_0\Gamma + \frac{1}{2}S_1^2\right) S_1 = 0 \tag{4.122}$$

This is an anharmonic oscillator (which oscillates in $\zeta$). We can analyse its dynamics by defining a Lagrangian

$$\mathcal{L}\left(S_1, \frac{dS_1}{d\zeta}, \zeta\right) = \frac{1}{2}\left(\frac{dS_1}{d\zeta}\right)^2 - \left[\left(2c_0^2 - c_0\Gamma\right) S_1^2 + \frac{1}{8}S_1^4\right] \tag{4.123}$$

which upon substitution into the Euler Lagrange equation

$$\frac{d}{d\zeta}\left(\frac{\partial\mathcal{L}}{\partial\left(\frac{dS_1}{d\zeta}\right)}\right) - \frac{\partial\mathcal{L}}{\partial S_1} = 0 \tag{4.124}$$

gives equation 4.122 as required. We can separate the Lagrangian, into a quasi-kinetic energy ($dS_1/d\zeta$ dependent) term $\mathcal{T}$ and a quasi potential energy ($S_1$ dependent) term $\mathcal{V}$, using the standard energy construction of the Lagrangian ($\mathcal{L} = \mathcal{T} - \mathcal{V}$). This gives

$$\mathcal{T} = \frac{1}{2}\left(\frac{dS_1}{d\zeta}\right)^2 \tag{4.125}$$

$$\mathcal{V} = \left(2c_0^2 - c_0\Gamma\right) S_1^2 + \frac{1}{8}S_1^4 \tag{4.126}$$

The stability is dependent on the shape of the quasi potential energy function $\mathcal{V}$. (See figure 4.20.) When $2c_0^2 > c_0\Gamma$ it is monostable, with a single potential well centred about $S_1 = 0$. If the two waveguides have equal amplitude (such that $S_1$ is also zero) this mode will sit at

the bottom of the potential well, making it stable. However, when $c_0\Gamma > 2c_0^2$, the potential becomes bistable, with the mode sitting at the critical point between two potential wells (with minima at $S_1 = \pm 2\sqrt{c_0\Gamma - 2c_0^2}$), making it unstable. It follows that $\Gamma = 2c_0$ is the seperatrix between the regimes of stability and instability.

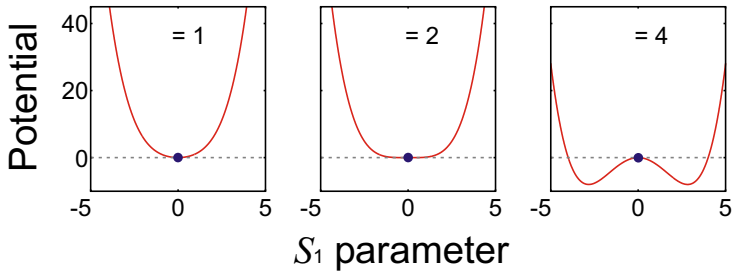


Figure 4.20: Quasi potential energy function $\mathcal{V}$ (given by equation 4.126), versus Stokes parameter $S_1$. Plotted for $c_0 = 1$ and for varying values of $\Gamma$. When $\Gamma = 1$ (such that $c_0\Gamma < 2c_0^2$), the potential is monostable. When $\Gamma = 2$ (such that $c_0\Gamma = 2c_0^2$), the potential is on the seperatrix. When $\Gamma = 4$ (such that $c_0\Gamma > 2c_0^2$), the potential becomes bistable. It follows that the symmetric mode solution (denoted by the dot) is stable for the first two cases, but unstable for the third case.

It should be noted that $S_1$ measures the asymmetry between the intensities in each wire, such that a value different from $S_1 = 0$ corresponds to a mode in which one wire contains more light than the other. Therefore, the potential wells that form when $c_0\Gamma > 2c_0^2$ correspond to the influence of asymmetric modes. These asymmetric modes are the result of self focussing, whereby the intensity dependence of the refractive index causes a waveguide with more light to become more confining, thus reinforcing any asymmetry. (Self focussing in coupled systems is a well known phenomenon for both continuous wave [205] and for solitons [206], which will be considered in more detail in chapter 5.) This self focussing can only happen when there is an existing asymmetry, and so (when $c_0\Gamma > 2c_0^2$) the symmetric supermode is metastable.

This behaviour can be understood by returning to the analogy of a needle placed perfectly upright, balanced upon its point (as mentioned in section 4.3.1). If the needle is completely isolated from all external forces, then it will remain in position. However, any perturbation will be reinforced by gravity, and the needle will topple over. Notably, the initial state has rotational symmetry (about the axis defined by the shaft of the needle), as do the equations of motion describing the system. When the needle topples (and the system falls into a "vacuum state"), *spontaneous symmetry breaking* occurs, in which a new parameter (namely the azimuthal angle of the needle's position) emerges. In the coupler we also have a symmetry, namely an invariance under swapping the wires. This is present both in the initial conditions, and in the equations of motion (which can be seen by swapping $E_1$ and $E_2$ in equations 4.30 and 4.31. Under perturbation, a new parameter (namely the sign of $S_1$) emerges, and thus we have symmetry breaking into one of two states.

It is also possible to "seed" the instability by introducing a small asymmetric signal, which causes the system to collapse into a particular state. This effect has been suggested as the basis

of optical switches, whereby a weak signal can control the direction of a much stronger signal [207].

The symmetric supermodal solution has $E_1 = E_2 = \sqrt{P}e^{i(P+c_0)}$, giving a value for $\Gamma$ (from equation 4.121) of $\Gamma = 2P$. This sets the seperatrix between the stable and unstable regimes at $P = c_0$, which agrees with the result derived from equation 4.113. We therefore see that the cross-modal modulation instability is a frequency-dependent generalisation of ordinary coupler instability. Notably, this means that self focussing can occur *below* the critical power, but that it happens indirectly, via the generation of frequencies away from the pump.

### Numerical modelling

For a system with 220nm × 330nm wires placed 330nm apart pumped at 1.5$\mu$m, equation 4.112 can be solved to give two gain peaks at 1.33$\mu$m and 1.74$\mu$m. This system was modelled numerically, as is shown in figure 4.21. This shows that sub-critical-power self-focussing does occur via the generation of spectral sidebands. The effect seems to vanish in the presence of free charge carriers. However, as noted previously, it is possible to sweep away free charge carriers [59], and so it may be possible to observe the phenomenon in a real device.

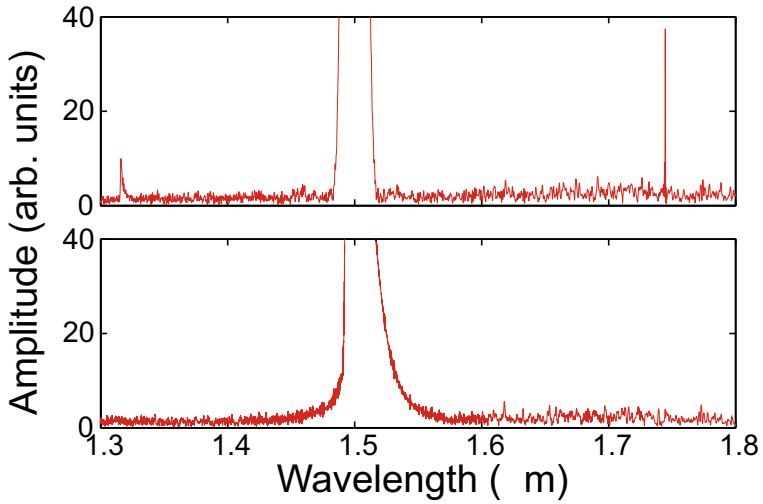


Figure 4.21: Spectral output of a pair of 220nm × 330nm SOI wires placed 330nm apart pumped with a 10ps rectangular pulse with power $10P_0$ in the symmetric mode after 3.9mm. The top plot includes 2PA and linear damping ($\epsilon_{2pa} = 0.1$, $\epsilon_l = 0.05$) but not free carrier effects, whilst the bottom plot does include them. Spectral lines are generated at 1.33$\mu$m and 1.74$\mu$m as predicted, but these are obscured when free charge carriers are present.

# Chapter 5

# Spatiotemporal solitons in waveguide arrays

In the previous chapter, solitons were considered that occupied the entire width of a waveguide array. In this chapter, spatial self-confinement is introduced, leading to spatiotemporal solitons, or "light bullets". Whilst a bullet is usually self-localised into a small region of a larger continuous medium [18, 29], these bullets are slightly different, in that they are self-localised into a few waveguides of a larger array. Therefore, they may be better described as *discrete* bullets.

In the case of continuous wave radiation, *discrete spatial solitons* were first proposed by Demetrios Christodoulides and Richard Joseph in 1988 [26] and experimentally realised 10 years later [27]. Spatiotemporal solitons have proved more elusive, as they are subject to difficulties including the need for sufficiently strong nonlinearity [35] and the need to balance the intrinsic length scales of dispersion and diffraction [34]. If the former condition is not met, then the bullet will require impractically high input powers, whilst if the latter condition is violated, the powers required for temporal and spatial localisation will greatly differ. Despite these problems, bullets have been tentatively observed in silica waveguides [32]. They have also been proposed in multi-core fibres, [208, 209], which may soon become a reality due to recent advances in the fabrication of such fibres [178].

There are two principal types of bullet: A *central bullet* is self-localised in the middle of an array, whilst an *edge bullet* is self-trapped against the array boundary [17, 28]. A related concept is the X-wave [210], but this consists of a wave-shape which is naturally diffractionless, rather than one in which diffraction is present but suppressed by nonlinearity.

In this chapter, silicon on insulator is proposed as a medium for realising bullets. A distinctive pattern of radiation emitted by such bullets is also predicted. The key results were published in Physical Review A [211].

## 5.1 Finding bullet solutions

Bullet solutions were found by removing the higher order dispersion terms from equation 4.27 to give

$$\frac{\partial E_n}{\partial \zeta} - \frac{i}{2}\frac{\partial^2 E_n}{\partial \tau^2} = i|E_n|^2 E_n + ic_0\left(E_{n-1} + E_{n+1}\right) \tag{5.1}$$

The spatial wavenumber $q$ was fixed by assuming bullet solutions of the form $E_n(\zeta,\tau) = F_n(\tau)\, e^{iq\zeta}$. Substituting this in yields

$$\frac{d^2 F_n}{d\tau^2} = 2qF_n - 2|F_n|^2 F_n - 2c_0\left(F_{n-1} + F_{n+1}\right) \tag{5.2}$$

Therefore, we have reduced the system to a coupled set of real ordinary differential equations. (Technically speaking, the system will accept complex solutions, but since the equations are symmetric under the transformation $\{F_n\} \rightarrow \{F_n e^{i\phi}\}$, these are likely to be trivial. Treating the equations as being complex will simply introduce another degree of freedom, and greatly complicate matters.) It can be shown analytically that soliton solutions (stable or unstable) exist when $q > 2c_0\cos(\pi/(N+1))$. The reason for this fundamental cutoff is explained in section 5.3.

The equations were solved numerically (using a method described in appendix A.3), yielding bullet solutions. An example of a central bullet solution for $q = 4$, $c_0 = 1$ and $N = 21$ is given in figure 5.1. Central bullets like this, with a single principal wire in the middle are in fact a special case. It is also possible to have a central bullet with two principal wires of equal amplitude, as described in appendix D.

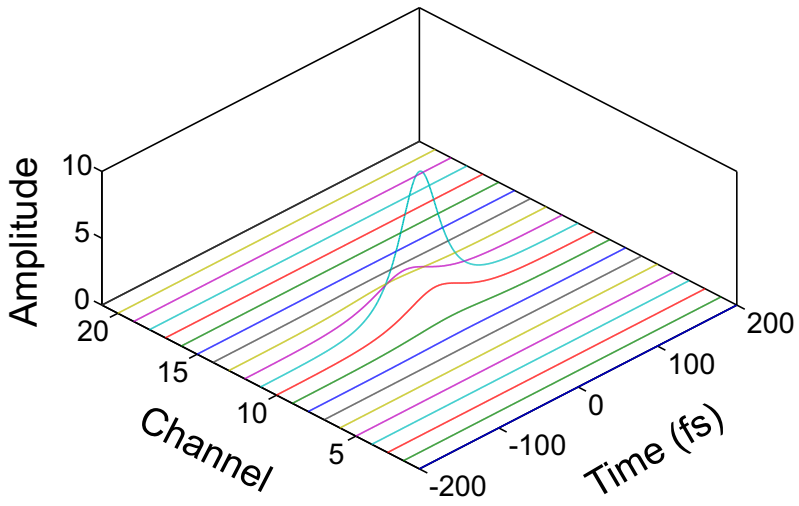


Figure 5.1: A bullet solution in a 21 wire array, calculated with $q = 4$ and $c_0 = 1$.

As was shown in section 4.4.1, the frequency dependence of coupling leads to a change in the

effective dispersion relation of the waveguides. Bullets, like temporal solitons, require anomalous GVD, and so it may seem that we can extend the spectral range in which they exist by using anomalous diffraction. This will not work, however, as the switch from normal to anomalous diffraction will also switch the self-focussing to a self-defocussing [200, 212, 213]. Therefore, the effect of coupling GVD will always be to shrink the spectral range within which bullets are permitted. This was not a great problem, however, as waveguides with relatively weak coupling GVD were used.

### 5.1.1 Stability criteria

The stability of a bullet can be analysed by considering the total amount of energy within it. It may seem that this energy is independently a function of both $q$ and $c_0$, but if we transform equation 5.2 using $F'_n(\tau) \equiv \sqrt{2q}F_n\left(\sqrt{2q}\tau\right)$ we obtain

$$\frac{d^2F'_n}{d\tau^2} = F'_n - 2|F'_n|^2F'_n - \frac{1}{V}\left(F'_{n-1} + F'_{n+1}\right) \tag{5.3}$$

where the parameter $V$ is given by $V \equiv q/c_0$. This is extremely useful, as the numerical solution of equation 5.2 needs only one free parameter (namely $V$), and thus from a 1-dimensional set of solutions, we can obtain all of the solutions from simple scaling. The energy in the bullet can be obtained by integrating the intensity $|E|^2$ over all time, and summing over all the wires. This gives

$$U_{\text{bull}} \equiv \sum_{n=1}^{N}\int_{-\infty}^{\infty}|F_n|^2d\tau = \sqrt{2q}\sum_{n=1}^{N}\int_{-\infty}^{\infty}|F'_n|^2d\tau \tag{5.4}$$

This can be written more concisely as

$$U_{\text{bull}} = \sqrt{c_0}\,f_N(V) \tag{5.5}$$

where the scaled energy function $f_N(V)$ is derived from the solution to 5.3 as

$$f_N(V) = \sqrt{2V}\sum_{n=1}^{N}\int_{-\infty}^{\infty}|F'_n|^2d\tau \tag{5.6}$$

The function $f_N$ differs between central and edge bullets, with the values being smaller for the latter. Decreasing the value of $N$ reduces the energy slightly, as light cannot diffract beyond the edge of the array, and so a lesser nonlinearity is required to surpress it. Figure 5.2 shows the energy curves for both central and odd bullets. Notably, the curves have a minimum, corresponding to the lowest possible bullet energies.

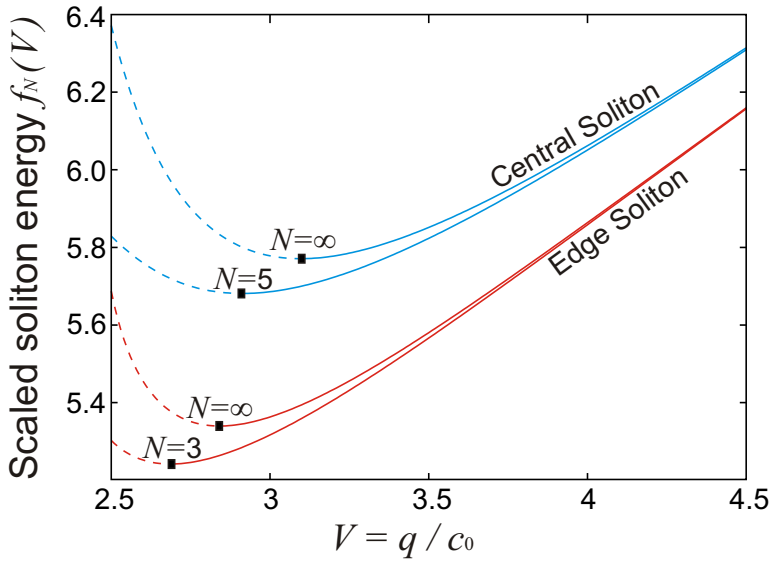


Figure 5.2: Normalised energy of edge and central bullets $f_N = U/\sqrt{c_0}$, as a function of $V = q/c_0$ shown with $N = \infty$ for both types of solitons, and with $N = 3$ and $N = 5$ for edge and central solitons respectively. The unstable ($\partial U/\partial q < 0$) solitons are denoted by dashed lines. The energy unit $P_0T_0$ is typically in the vicinity of 100 to 1000 femtojoules.

It can be shown that the quantity $\partial U/\partial q$ must be positive for soliton stability [214], a condition known as the Vakhitov-Kolokolov criterion [215]. The physical reason for this can be seen by considering what happens when particles (in this case, photons) are added to a soliton. This addition will normally cause the soliton to decrease in duration, as a result of the nonlinear self focussing. If, however, the soliton increases in duration, the nonlinearity is not acting to confine the extra particles, and the soliton will be unstable. The energy $U$ increases with the number of particles, whilst the wavenumber $q$ increases with a reduction of duration. Therefore positive values of $\partial U/\partial q$ correspond to the stable case of extra particles giving shorter durations. This stability criterion can be rewritten as $V \geq V_{\mathrm{vk}}$, where $V_{\mathrm{vk}}$ is defined to be the position of the energy minimum.

As the number of wires will inevitably be finite, a potential problem arises in that the confinement may result from boundary conditions, rather than being intrinsic to the equations of motion. Furthermore, when Čerenkov radiation is considered in section 5.3, systems with a small number of wires are found to be of particular interest, making this problem more pressing.

Figure 5.3 shows how edge effects affect the values of $V_{\mathrm{vk}}$ and the corresponding minimum energy. In order to meaningfully compare central and edge solitons, we define $\Delta N$ as the number of wires separating the maximum intensity wire from the edge. This is given by $N-1$ for an edge soliton, and $(N-1)/2$ for a central soliton (in a system with odd $N$). The edge effects rapidly diminish as $\Delta N$ is increased, with the quasi-infinite regime being effectively reached at $\Delta N = 5$ or 6. In this regime $V_{\mathrm{vk}}$ has values of 3.097 and 2.841 for central and edge bullets respectively. The corresponding scaled energies $f_\infty(V_{\mathrm{vk}})$ are given by 5.771 and 5.340

respectively.

Even before this limit is reached, it can be seen that the corrections are relatively minor, indicating that the structures are still essentially bullets. Numerical modelling in section 5.2.4 supports this view: Bullets are simulated for an $N = 5$ system, but no pathalogical behaviour is seen.

In the case of $\Delta N = 1$ however (corresponding to $N = 2$ for the edge soliton and $N = 3$ for the central soliton) it is difficult to determine the locations of the $V = V_{\mathrm{vk}}$ points. This is because the computations have to be performed near to the fundamental cutoff points at $V = 2\cos(\pi/(N+1))$ (see equation 5.25 in section 5.3) leading to numerical instability. Therefore the $\Delta N = 1$ cases in figure 5.3 are shown with crosses.

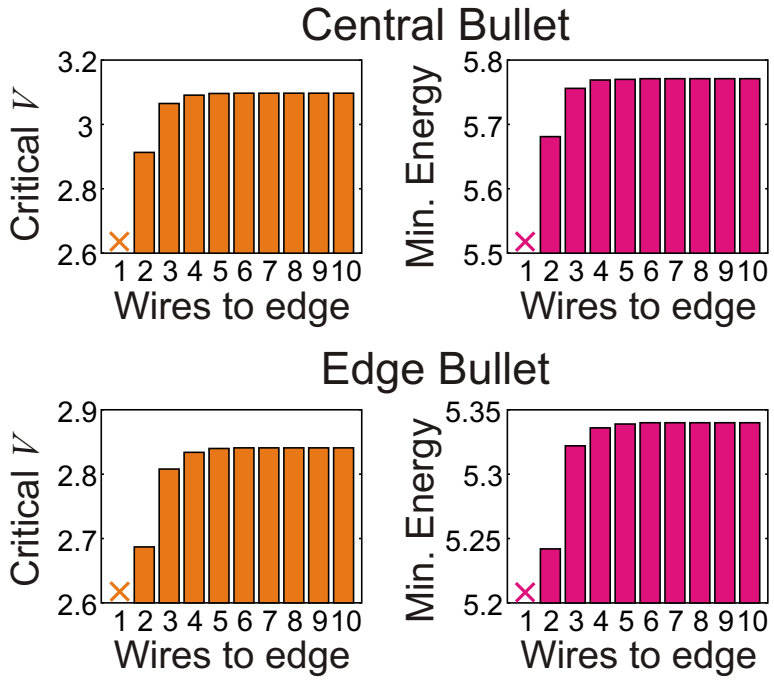


Figure 5.3: Effect of the array edges on the (scaled) minimum soliton energy $f_N(V_{\mathrm{vk}})$ and the (scaled) critical wavenumber $V_{\mathrm{vk}}$ at which it occurs. The horizontal axes show $\Delta N$, the number of wires separating the maximum intensity wires from the boundary. The quasi-infinite regime is effectively reached at $\Delta N = 5$ or 6. The energy unit $P_0T_0$ is typically in the vicinity of 100 to 1000 femtojoules.

### 5.1.2 Maximum duration

The lower bound to $q/c_0$ also imposes an upper bound to the bullet duration. (We define the duration of the bullet to be the FHWM of its central peak. Although this construction is fairly arbitrary, it gives a reasonable metric with which to gauge the overall time scales of the bullet.) By taking the solutions to 5.3 and measuring their duration, we gain the quantity $\tau'_{\mathrm{bull}}(V)$,

which (like $F'$) has been scaled by a factor of $\sqrt{2q}$. Transforming back gives

$$\tau_{\text{bull}} = a\,(V)\,\frac{1}{\sqrt{c_0}} \tag{5.7}$$

where $a\,(V) \equiv \tau'_{\text{bull}}\,(V)\,/\sqrt{2V}$.

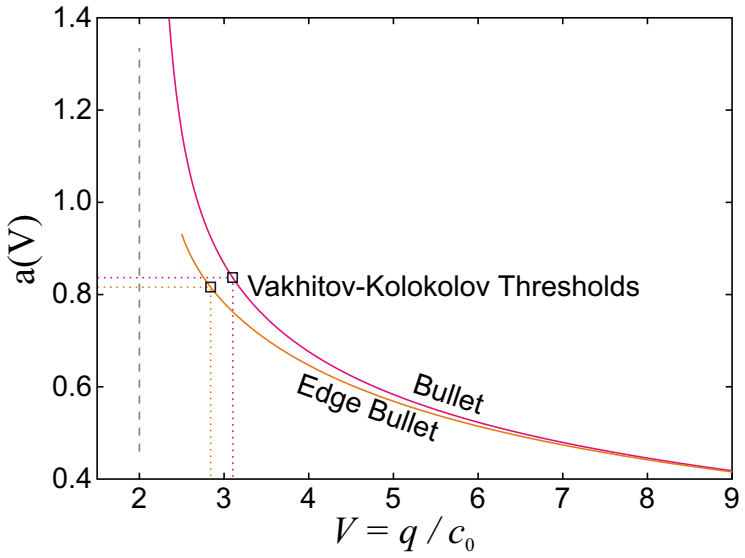


Figure 5.4: The scaled duration of a bullet (or edge bullet) $a$, shown as a function of the ratio between the spatial wavenumber $q$ and the coupling constant $c_0$. The duration at the threshold of Vakhitov Kolokolov instability is marked, yielding (in the quasi-infinite case) a value of $a \approx 0.839$ for a central bullet, and $a \approx 0.816$ for an edge bullet.

The parameter $a$ (in the quasi-infinite case) was calculated as a function of $V$, as is shown in figure 5.4. If we require a stable bullet (with respect to Vakhitov Kolokolov instability), we can read off an upper bound for the bullet width (which occurs when $V = V_{\text{vk}}$), yielding a value of $a_{\text{max}} \approx 0.839$ for a central bullet and $a \approx 0.816$ for an edge bullet. Therefore, we can see that the duration of a stable bullet is limited by the expression

$$\tau_{\text{bull}} \leq \frac{a_{\text{max}}}{\sqrt{c_0}} \tag{5.8}$$

In this expression, equality corresponds to the case of minimum bullet energy (for the given value of $c_0$).

As this criterion impinges on the physical limits of the system (in particular, the need to generate ultrashort pulses of light), it is important to consider it in terms of real units. Abandoning our scaled units gives

$$t_{\text{bull}} \leq \alpha_{\text{max}} \sqrt{2|\beta_2| L_{\text{C}}} \tag{5.9}$$

where $\beta_2$ is the unscaled GVD, and $L_{\text{C}}$ is the coupling length. The numerically derived constant $a_{\text{max}}$ has been rescaled as $\alpha_{\text{max}} \equiv a_{\text{max}}/\sqrt{\pi}$. In the quasi-infinite case, this has values of

$\alpha_{\max} \approx 0.473$ for central bullets and $\alpha_{\max} \approx 0.460$ for edge bullets. Having a finite number of wires imposes slight upwards corrections to $\alpha_{\max}$, as is shown in figure 5.5.

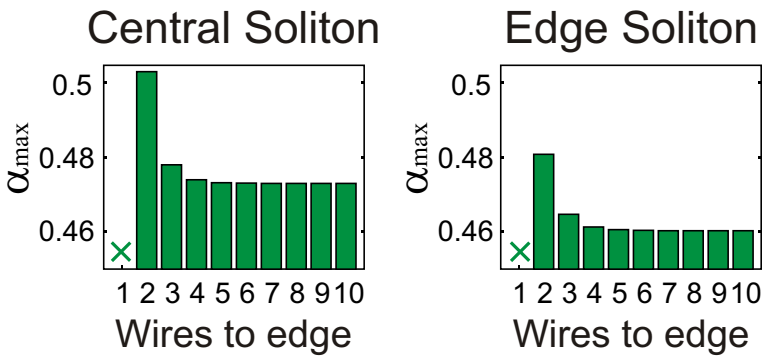


Figure 5.5: Parameter $\alpha_{\max}$ (defining maximum soliton duration) as a function of the number of wires between the maximum intensity wire and the array boundary.

### 5.1.3 Bullet energy versus soliton energy

It is instructive to consider the energy of a bullet in relation to that of a soliton travelling through an equivalent waveguide. The energy of the familiar $E = e^{iqz}\sqrt{2q}\,\mathrm{sech}\left(\sqrt{2q}\tau\right)$ soliton solution is given by

$$U_{\mathrm{sol}} \equiv \int |E|^2 dt = \sqrt{8q} \tag{5.10}$$

Considering this in terms of the FWHM duration $\tau_{\mathrm{sol}}$ gives.

$$U_{\mathrm{sol}} = \frac{4\ln\left(1+\sqrt{2}\right)}{\tau_{\mathrm{sol}}} \approx \frac{3.525}{\tau_{\mathrm{sol}}} \tag{5.11}$$

If we combine the relations 5.5 and 5.8 for the case of minimum bullet energy, we can eliminate $c_0$ to give

$$U_{\mathrm{bull}} = \frac{u_\tau}{\tau_{\mathrm{bull}}} \tag{5.12}$$

where the constant $u_\tau \equiv a_{\max} f_N\left(V_{\mathrm{vk}}\right)$ has (in the quasi-infinite case) a value of approximately 4.84 for a central bullet and 4.36 for an edge bullet. This relationship is identical to that for the soliton (equation 5.11), except that the energy within a bullet or edge bullet is larger than a soliton with the same duration. In the following section, this result will become important, as if a bullet is created from a pulse being injected into a single channel, that pulse will have a power above the soliton threshold, and so will be compressed.

## 5.2 Modelling of bullets in a realisable SOI device

### 5.2.1 Device specifications

Waveguides of the type used in chapter 3 were chosen. The first of these was the 220nm × 420nm waveguide, with ZDWs placed well away from the 1.5$\mu$m pump. As for the single wires, this was chosen to give straightforward soliton evolution, without the complication of other physical effects. The second type was the 220nm × 380nm waveguide, having a ZDW relatively close to the pump at 1.627$\mu$m, thus allowing for observation of Čerenkov radiation.

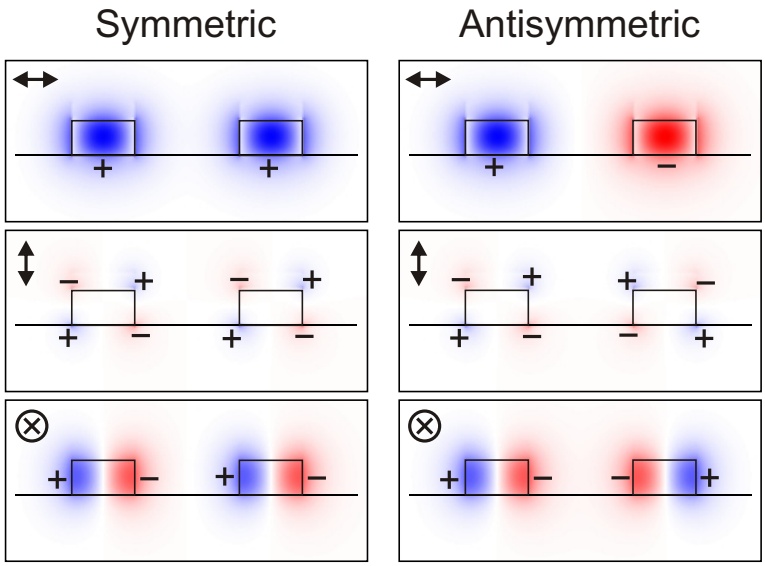


Figure 5.6: Symmetric (left) and antisymmetric (right) mode profiles, displayed over a 2.4$\mu$m × 1$\mu$m cross section. Silica is beneath the horizontal line, with the rectangles denoting the silicon. The electric field vector is split into Cartesian components, with transverse components parallel to the silica-air interface shown top, transverse perpendicular components shown middle, and longitudinal components shown bottom. Colour saturation gives absolute value. The + and − signs denote relative phase. (For clarity, the saturation of the middle figure has been doubled.)

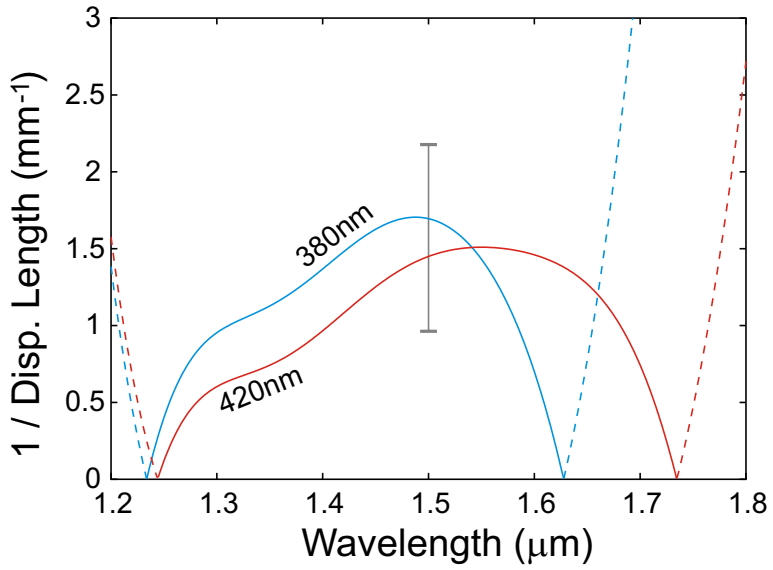


Figure 5.7: $1/L_{\mathrm{D}}(\lambda)$ for the two waveguide widths. Anomalous (normal) GVD is represented by solid (dashed) line-style. The vertical bar highlights the 1.5$\mu$m pump wavelength. The leading (scaled) dispersion coefficients are $d_2 = -0.5$, $d_3 = -0.00326$, $d_4 = 0.00148$, $d_5 = -6.16 \times 10^{-5}$ for the 380nm wide wire and $d_2 = -0.5$, $d_3 = 0.00615$, $d_4 = 7.00 \times 10^{-4}$, $d_5 = -4.06 \times 10^{-6}$ for the 420nm wide wire.

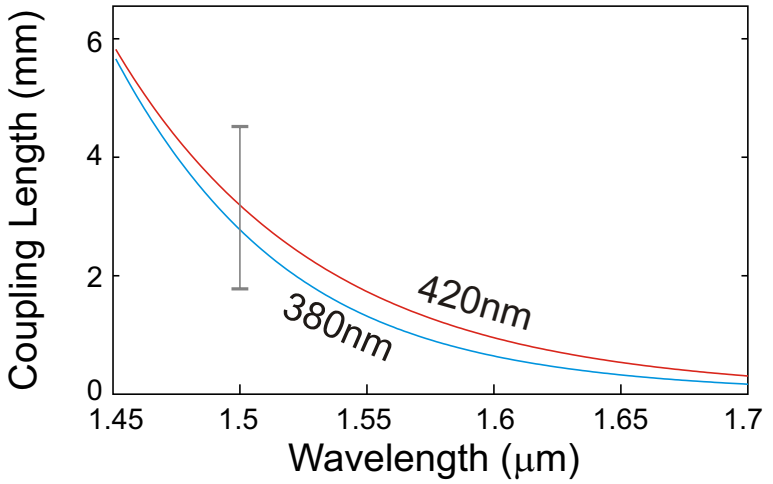


Figure 5.8: $L_{\mathrm{C}}(\lambda)$ for the two waveguide widths. The vertical bar highlights the 1.5$\mu$m pump wavelength. The leading (scaled) coupling coefficients are $c_0 = 0.336$, $c_1 = -0.106$, $c_2 = 0.0187$, $c_3 = -0.00213$ for the 380nm wide wire and $c_0 = 0.337$, $c_1 = -0.0868$, $c_2 = 0.0124$, $c_3 = -0.00129$ for the 420nm wide wire.

The upper limit to pulse duration (equation 5.9) greatly complicates the process of seeing bullets experimentally. This is for two reasons: Firstly a short pulse corresponds to a required high peak intensity, which makes the bullet vulnerable to nonlinear absorption. Secondly, the generation of ultrashort pulses is extremely difficult, and so there is a practical lower limit to the duration that can be used. A 100fs second system (like that used in section 3.3) was

considered.

From equation 5.9 it is apparent that both the GVD and coupling length both need to be as high as possible. The selected 380nm and 420nm wires are close to the point of maximum dispersion, and have GVDs of 5400 $\mathrm{fs}^2\,\mathrm{mm}^{-1}$ and 4700 $\mathrm{fs}^2\,\mathrm{mm}^{-1}$ respectively.

The coupling length is far more problematic, as we must find a compromise between the need to increase the pulse duration, and the need to have a respectable degree of coupling along the chip. (Nonlinear wire confinement cannot be observed if the wires are too far apart for any significant coupling to happen in the first place.) As a compromise, wire separations of 700nm were chosen, providing coupling lengths of 5.6mm and 6.4mm for the 380nm and 420nm wires respectively.

The chosen parameters impose an upper limit to the bullet duration of about 80fs. This appears to be problematic, as it is shorter than the 100fs duration of the input pulse. However, from equations 5.11 and 5.12 it can be seen that a pulse with sufficient energy to form a bullet will be substantially above the soliton threshold for a single wire. Such a pulse will be compressed, as was documented for a wire with the same geometry in section 3.1.2. (The coupling is irrelevant here, as the evolution happens of a distance scale which is much less than the coupling length.) It was seen that a 100fs pulse (with power $3.5P_0$) is compressed to 34fs after only 0.7mm propagation, which is well below the upper duration limit.

### 5.2.2 Bullet propagation in an ideal system

Before performing realistic modelling, it is instructive to consider the undamped system being pumped with a precalculated bullet solution. The bullet solutions gained in section 5.1 were inexact, as they ignored the effect of coupling dispersion, and higher order dispersion. Despite this, they propagated robustly through the simulation for both the central bullet (figure 5.9) and edge bullet (figure 5.10) cases, indicating that the approximation was valid. Conversely, when the nonlinearity was removed, the solutions dispersed in both time and space.

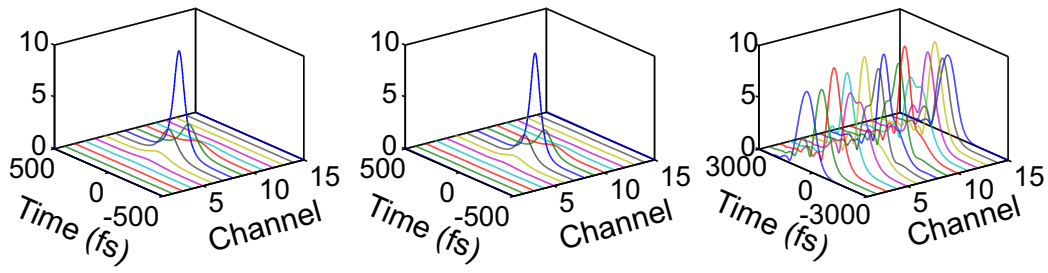


Figure 5.9: Propagation of an ideal bullet solution in a system of fifteen 220nm × 420nm wires. The left hand plot shows the input (a solution of equation 5.1), whilst the middle plot shows the bullet after 6.7mm of propagation (at $\zeta = 10$). It can be seen that the bullet has survived with negligible change, indicating that it is stable with respect to the perturbations introduced by higher order dispersion. To demonstrate the fundamental role played by the nonlinearity, the right hand plot shows the same scenario, but with the nonlinear term removed.

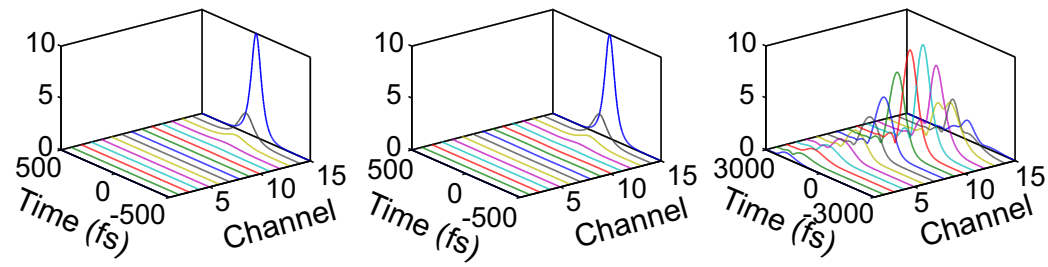


Figure 5.10: Propagation of an ideal edge bullet solution in a system of fifteen 220nm × 420nm wires. The left hand plot shows the input (a solution of equation 5.1), whilst the middle plot shows the bullet after 6.7mm of propagation (at $\zeta = 10$). It can be seen that the edge bullet has survived with negligible change, indicating that it is stable with respect to the perturbations introduced by higher order dispersion. To demonstrate the fundamental role played by the nonlinearity, the right hand plot shows the same scenario, but with the nonlinear term removed.

### 5.2.3 Bullet formation in a realistic system

We will now consider bullet evolution in a more realistic manner, and so we will include both linear absorption and 2PA. We will also excite the system with a sech-like pulse into a single wire, rather than a pre-existing bullet solution, thus emulating a more realistic experimental set-up.

By scanning across multiple values, the optimal input power for bullet formation was found to be 3.5 times the soliton threshold for a single wire. Below this power, the wire confinement is insufficient. Above this power, the pulses split temporally, due to them being a higher order solitons which separate under perturbation. By using 100fs pulses of this power, both bullets, and edge bullets could be created.

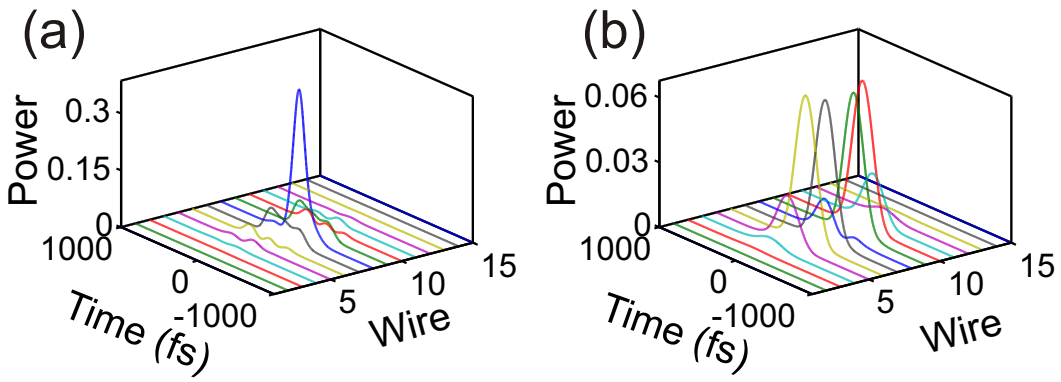


Figure 5.11: Result of a 100fs pulse being fired into the central wire (wire 8) of a 15 wire array (of 220nm × 420nm waveguides placed 700nm apart). Shown after 2.7mm propagation ($\zeta = 4$). The right hand plot shows the very low power (and hence linear) regime, in which diffraction has transferred nearly all the light to the neighbouring wires. The left hand plot shows the result for an input pulse having a power 3.5 times the soliton threshold for a single wire. The light is confined spatially, and the pulse broadening is notably less than for the linear case; this suggests a bullet is present.

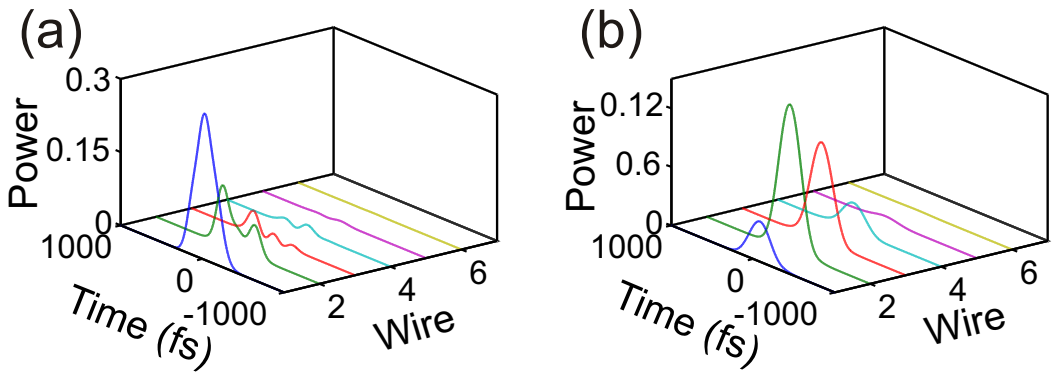


Figure 5.12: Result of a 100fs pulse being fired into the edge wire (wire 1) of a 15 wire array (of 220nm × 420nm waveguides placed 700nm apart). Shown after 2.7mm propagation ($\zeta = 4$), with the final 8 (almost completely dark) wires removed for the sake of clarity. The right hand plot shows the very low power (and hence linear) regime, in which diffraction has transferred nearly all the light to the second and third wires. The left hand plot shows the result for an input pulse having a power 3.5 times the soliton threshold for a single wire. The light is trapped against the edge of the array, and the pulse broadening is notably less than for the linear case; this suggests an edge bullet is present.

The data displayed in figures 5.11 and 5.12 is highly encouraging. Other tests were applied to analyse the data in more detail. One useful metric is the fraction of energy that remains in the central wire (or the edge wire, in the case of an edge bullet). This is displayed (as a function of distance) in figure 5.13. In both cases, there is an initial decline, as the pulse settles into a bullet. Next, there is a roughly flat region, coresponding to stable bullet propagation. The start of this flat region is marked by a sudden departure from the linear profile, indicating that nonlinear processes have, at that point, assumed a major role in the pulse evolution. Eventually, the parameter starts to decline, indicating that the bullet is breaking apart.

It follows from the scaling of equation 5.3 that the quantity $S \equiv t_{\text{bull}}\sqrt{P}$ (where $P$ is the peak power) will be conserved for an ideal bullet. (This parameter is similar to the soliton area defined in section 3.3.3 and used to detect the presence of temporal solitons.) The parameter can be used to analyse soliton formation, as is shown in figure 5.13. It should be noted that an increase of $S$ corresponds to pulse broadening, whilst a decrease corresponds to compression or attenuation. Both figures show an initial regime of pulse compression (when conversely, evolution in the linear regime shows broadening). This coincides with the region where the pulse is diffracting. $\partial S/\partial\zeta$ then reaches zero (as is expected from a bullet) at the same distance as the wire confinement starts to level off and becomes quasi-constant. This is notable, as two important indicators of bullet formation have happened simultaneously. Finally, $S$ starts to increase, which corresponds to pulse broadening, and eventual decay.

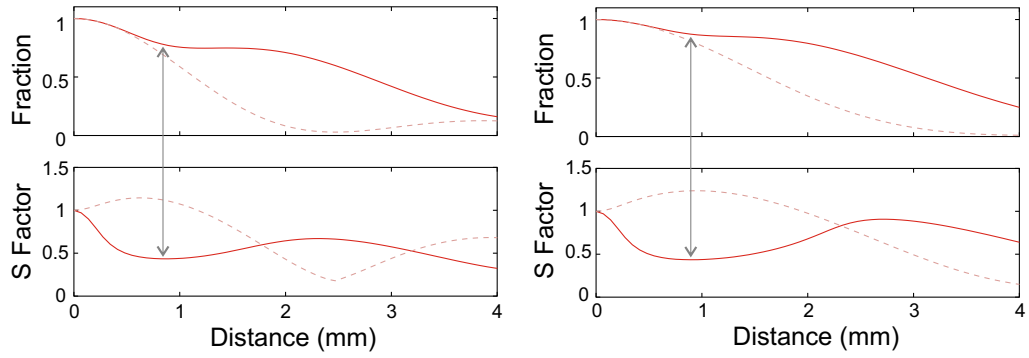


Figure 5.13: Analysis of bullet propagation over distance. The left hand plots are for the central bullet shown in figure 5.11, whilst the right hand plots are for the edge bullet shown in figure 5.12. The upper plots show the fraction of total energy remaining in the pump wires, whilst the lower plot shows the parameter $S$, which has been scaled by the input value. The dashed lines show the low power (and hence linear) results. The pump wire fractions start to become constant at the points where $\partial S/\partial\zeta$ reach zero (denoted by grey arrows), suggesting bullet formation.

### 5.2.4 Bullet formation in a small system

In order to study the edge effects, numerical simulations were performed for a system with a restricted number of wires, as is shown in figure 5.14 for a central bullet, and figure 5.15 for an edge bullet. Despite the close proximity to the waveguide boundaries, these bullets still show strong localisation, which is in sharp contrast to the results seen in the linear regime.

An analysis of propagation over distance was performed, as is shown in figure 5.16. Both the evolution of the $S$ parameter, and the fraction of light in the pump wire show very similar profiles to those for the larger system, again demonstrating that the structures can be considered bullets. This result is important from the point of view of the Čerenkov radiation considered in section 5.3.3, as the instance of a small number of wires is of particular interest.

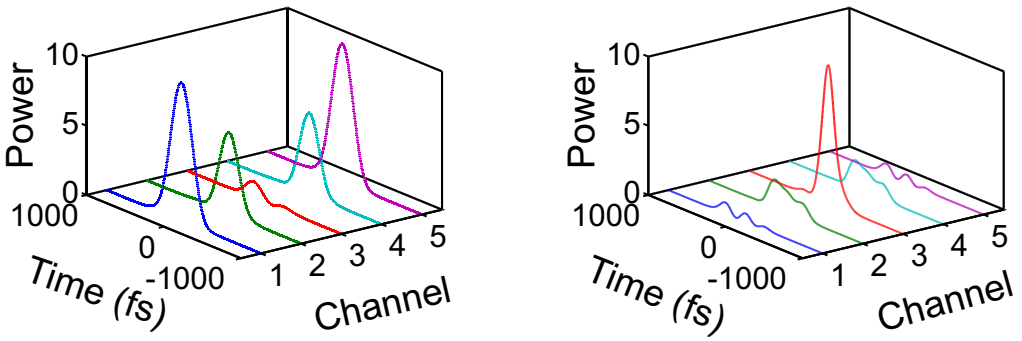


Figure 5.14: Result of a 100fs pulse being fired into the central wire (wire 3) of a five-wire array (of 220nm × 420nm waveguides placed 700nm apart). Shown after 2.7mm propagation ($\zeta = 4$). The left hand plot shows the very low power (and hence linear) regime, in which diffraction has transferred nearly all the light to the edge wires. The right hand plot shows the result for an input pulse having a power 3.5 times the soliton threshold for a single wire. The light is confined spatially, and the pulse broadening is notably less than for the linear case; this suggests a bullet is present.

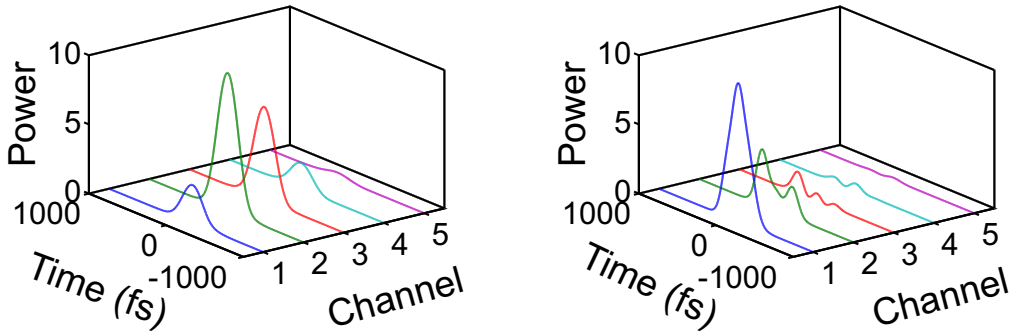


Figure 5.15: Result of a 100fs pulse being fired into the edge wire (wire 1) of a five-wire array (of 220nm × 420nm waveguides placed 700nm apart). Shown after 2.7mm propagation ($\zeta = 4$). The left hand plot shows the very low power (and hence linear) regime, in which diffraction has transferred nearly all the light to the second and third wires. The right hand plot shows the result for an input pulse having a power 3.5 times the soliton threshold for a single wire. The light is trapped against the edge of the array, and the pulse broadening is notably less than for the linear case; this suggests an edge bullet is present.

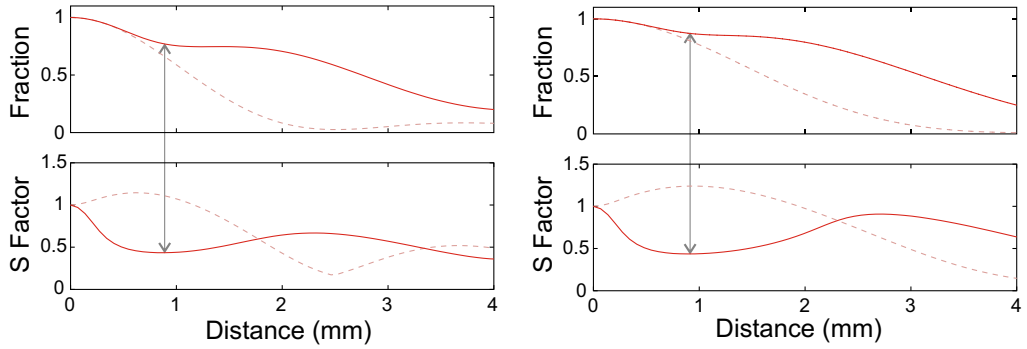


Figure 5.16: Analysis of bullet propagation over distance. The left hand plots are for the central bullet shown in figure 5.14, whilst the right hand plots are for the edge bullet shown in figure 5.15. The upper plots show the fraction of total energy remaining in the pump wires, whilst the lower plot shows the $S$ parameter, which has been scaled by the input value. The dashed lines show the low power (and hence linear) results. The pump wire fractions start to become constant at the points where $\partial S/\partial\zeta$ reach zero (denoted by grey arrows), suggesting bullet formation.

## 5.3 Bullet radiation

The emission of Čerenkov radiation from temporal solitons has been widely studied, as was discussed in section 3.1.3. In this section, we extend the topic to include discrete spatiotemporal solitons. The most notable result is that for an $N$ wire system, $N$ separate resonant frequencies are emitted. Some of these, however, may be "forbidden" for symmetry reasons.

We start by taking the $E_n(\zeta,\tau) = F_n(\tau)\, e^{iq\zeta}$ solution (which is exact in the absence of higher order dispersion and coupling dispersion) and perturbing it as

$$E_n(\zeta,\tau) = \left[F_n(\tau) + \epsilon_n(\zeta,\tau)\right] e^{iq\zeta} \tag{5.13}$$

where $\epsilon_n(\zeta,\tau)$ is the perturbation for the $n$th wire. Substituting this into equation 4.27 (thus reintroducing the higher order dispersion and coupling dispersion), gives

$$\begin{aligned} iq\epsilon_n + \frac{\partial\epsilon_n}{\partial\zeta} &= (2\epsilon_n + \epsilon_n^*)\, F_n^2 + i\hat{D}\epsilon_n + i\hat{C}\left(\epsilon_{n+1} + \epsilon_{n-1}\right) \\ &+ i\left[\hat{D} - \frac{1}{2}\frac{\partial^2}{\partial\tau^2}\right] F_n + i\left[\hat{C} - c_0\right]\left(F_{n+1} + F_{n-1}\right) \end{aligned} \tag{5.14}$$

where terms containing $\epsilon_n^2$ and $\epsilon_n^3$ have been discounted (as we are treating $\epsilon_n$ as a small perturbation, rather than a general correction). We have also removed damping.

This equation is a generalisation of equation 3.4 in section 3.1.3. As before, the left hand side admits sinusoidal solutions, and so can be though of as an oscillator, but we now have a set of $N$ oscillators rather than just one. The oscillators (which, as before, oscillate in space rather than time) have amplitude $\epsilon_n$, and are driven by forces specified by $F_n$. As before, we need

to find resonances with the spatial wavenumber $q$, and so (due to the fact that $\epsilon$ is already modulated by $q$) we look for solutions where $\epsilon$ shows no oscillation with respect to $\zeta$. As for the single wire system, we remove the driving terms (i.e. those containing $F_n$ but not $\epsilon_n$), and the refractive index changing $(2\epsilon_n + \epsilon_n^*) F_n^2$ term. This gives

$$iq\epsilon_n + \frac{\partial \epsilon_n}{\partial \zeta} = i\hat{D}\epsilon_n + i\hat{C}\left(\epsilon_{n+1} + \epsilon_{n-1}\right) \tag{5.15}$$

Again, we look for linear wave solutions with no $\zeta$ dependence, and so we take

$$\epsilon_n = \epsilon'_n e^{-i\omega\tau} \tag{5.16}$$

Substituting this in gives

$$q\epsilon'_n = D\left(\omega\right)\epsilon'_n + C\left(\omega\right)\left(\epsilon'_{n+1} + \epsilon'_{n-1}\right) \tag{5.17}$$

This can be reframed as an eigenvalue problem

$$\hat{X}\vec{\epsilon'} = \lambda\vec{\epsilon'} \tag{5.18}$$

where the column vector $\vec{\epsilon'}$ holds the values of $\epsilon'_n$, the matrix $\hat{X}$ is defined as

$$\hat{X}_{(\mu)(\nu)} \equiv \delta_{(\mu)(\nu-1)} + \delta_{(\mu)(\nu+1)} \tag{5.19}$$

(where $\delta$ is the Kronecker symbol) and the eigenvalues have been written as

$$\lambda_j \equiv \frac{q - D\left(\omega_j\right)}{C\left(\omega_j\right)} \tag{5.20}$$

where $\lambda_j$ is the $j$th eigenvalue of $\hat{X}$, and $\omega_j$ is the corresponding resonant frequency. The matrix $\hat{X}$ is the same as that defined by equation 4.75 in section 4.4.2. This is not surprising, as we are once again considering the linear supermodes of a multiwire system. As before, the eigenvalues are

$$\lambda_j = 2\cos\left(\frac{j\pi}{N+1}\right) \tag{5.21}$$

with corresponding normalised eigenvectors of the form

$$\left[\epsilon'_n\right]_j = \sqrt{\frac{2}{N+1}}\sin\left(\frac{nj\pi}{N+1}\right) \tag{5.22}$$

The eigenvectors for a selection of values of $N$ are shown in figure 5.17.

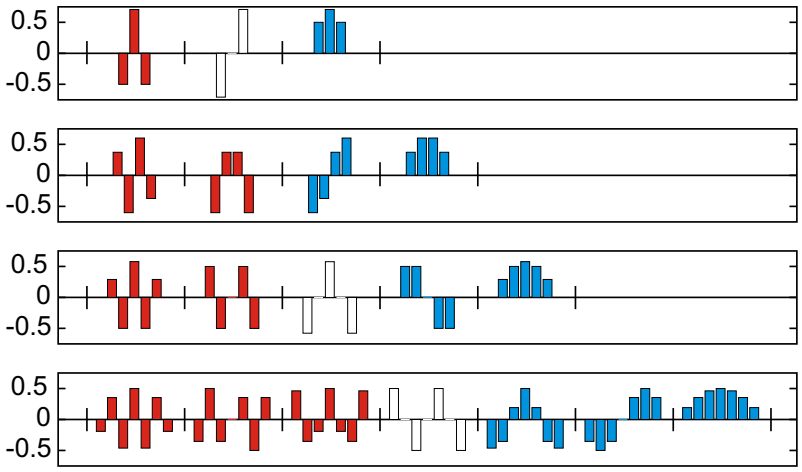


Figure 5.17: Normalised eigenvectors for equation 5.18 shown for (top to bottom) $N = 3$, 4, 5 and 7. The eigenvectors are arranged by order of their corresponding eigenvalue, which increases from left to right. Negative eigenvalues are shown in red, whilst positive eigenvalues are shown in blue. Notably, many of the solutions do not resemble sinusoids. This is because they involve discrete sampling at intervals with a similar magnitude to the sine function's periodicity.

As was shown in section 4.4.1, each linear mode will see a different dispersion relation. Each of these dispersion relations will (in general) yield a different frequency of resonant radiation. Therefore, for an $N$ wire array, we expect there to be $N$ resonant frequencies. (However, a particular resonance will only be excited if the bullet has a non-zero projection on it, and as will shortly be shown, this is not always the case.)

Combining equations 5.20 and 5.21 gives

$$q = D(\omega) + 2C(\omega)\cos\left(\frac{j\pi}{N+1}\right) \tag{5.23}$$

Therefore Čerenkov radiation should be observed at the values of $\omega$ which satisfy equation 5.23 for $j = 1, 2 \ldots N$.

### Bullet cutoff

This resonance analysis also explains the fundamental cutoff mentioned in section 5.1.1. At the pump frequency, the right hand side of equation 5.23 reduces to

$$q = 2c_0 \cos\left(\frac{j\pi}{N+1}\right) \tag{5.24}$$

Therefore, resonant solutions can only exist within a limited range, due to the finite range of the cosine function. However, if a bullet is to exist, the equation must *not* have a solution, because if it did, it would describe resonant interactions (between the bullet and the linear modes of the system) at the pump frequency, which would destroy the bullet immediately. Therefore, for bullet existence we require that

$$V > 2\cos\left(\frac{\pi}{N+1}\right) \tag{5.25}$$

where (as before) $V \equiv q/c_0$. The lower bound on $V$ increases with $N$, and tends towards 2 as $N$ goes to infinity.

### 5.3.1 Symmetry considerations and "Forbidden" resonances

The waveguide array is symmetric, in that reversing the order of its wires has no effect on its dynamics. We can investigate this symmetry using the exchange matrix $\hat{J}$, which is defined as

$$\hat{J} = \begin{bmatrix} 0 & 0 & \cdots & 0 & 0 & 1 \\ 0 & 0 & \cdots & 0 & 1 & 0 \\ 0 & 0 & \cdots & 1 & 0 & 0 \\ \vdots & \vdots & \iddots & \vdots & \vdots & \vdots \\ 0 & 1 & \cdots & 0 & 0 & 0 \\ 1 & 0 & \cdots & 0 & 0 & 0 \end{bmatrix} \tag{5.26}$$

This has the effect of has the effect of reversing the order of the elements in a vector it is multiplied by, and so when applied to $\vec{\epsilon'}$ corresponds to reversal of the wire ordering. The matrix $\hat{J}$ has two distinct families of eigenvalues: The set of all symmetric vectors is an eigenspace of $\hat{J}$, which corresponds to an eigenvalue of 1. For an $N \times N$ matrix, this is $\lceil N/2 \rceil$-fold degenerate (where the $\lceil x \rceil$ brackets denote the rounding up of $x$ to the nearest integer). Similarly, the set of all antisymmetric vectors is an eigenspace corresponding to an eigenvalue of $-1$. This is $\lfloor N/2 \rfloor$-fold degenerate (where the $\lfloor x \rfloor$ brackets denote the rounding down of $x$ to the nearest integer).

The matrix $\hat{X}$ commutes with $\hat{J}$, and thus its eigenvectors must also be eigenvectors of $\hat{J}$. (On the other hand, it doesn't follow what the eigenvectors of $\hat{J}$ are eigenvectors of $\hat{X}$ due to the degeneracy of the former's eigenvalues.) Therefore, for an $N$ wire system, $\lceil N/2 \rceil$ of the modes will be symmetric, and the remaining $\lfloor N/2 \rfloor$ will be antisymmetric.

This is highly significant, as a symmetric bullet will not radiate into the antisymmetric modes. We can see this by taking equation 5.14 and replacing the wire index $n$ with a reverse-ordered wire index $\tilde{n} \equiv N + 1 - n$. For a symmetric bullet we have $F_n = F_{\tilde{n}}$ and for an antisymmetric

mode we have $\epsilon_n = -\epsilon_{\tilde{n}}$. This gives

$$\begin{aligned} iq\epsilon_{\tilde{n}} + \frac{\partial \epsilon_{\tilde{n}}}{\partial \zeta} &= \left(2\epsilon_{\tilde{n}} + \epsilon_{\tilde{n}}^*\right) F_{\tilde{n}}^2 + i\hat{D}\epsilon_{\tilde{n}} + i\hat{C}\left(\epsilon_{\tilde{n}+1} + \epsilon_{\tilde{n}-1}\right) \\ &\quad -i\left[\hat{D} - \frac{1}{2}\frac{\partial^2}{\partial \tau^2}\right] F_{\tilde{n}} - i\left[\hat{C} - c_0\right]\left(F_{\tilde{n}+1} + F_{\tilde{n}-1}\right) \end{aligned} \tag{5.27}$$

Transforming equation 5.27 out of the $\tilde{n}$ notation and adding it to equation (5.14) gives

$$iq\epsilon_n + \frac{\partial \epsilon_n}{\partial \zeta} = \left(2\epsilon_n + \epsilon_n^*\right) F_n^2 + i\hat{D}\epsilon_n + i\hat{C}\left(\epsilon_{n-1} + \epsilon_{n+1}\right) \tag{5.28}$$

This lacks any form of driving term, and so for an initial condition of $\epsilon_n = 0$, the solution will remain at $\epsilon_n = 0$. Therefore, a symmetrical soliton will not radiate into the antisymmetric modes. As $\lfloor N/2 \rfloor$ antisymmetric modes are present, we can therefore predict that $\lfloor N/2 \rfloor$ spectral peaks will be "forbidden". For an edge soliton, however, the above argument will no longer hold (due to the $F_n = F_{\tilde{n}}$ predicate being no longer true). Therefore, all of the modes are permitted for edge bullets.

### 5.3.2 Idealised Čerenkov generation

Before considering Čerenkov generation in the most realistic case, it is instructive to consider the simplified case of ideal bullet solutions propagating in an undamped medium. Equation 5.23 is solved graphically in figure 5.18 for a variety of cases, thus showing that $N$ resonant frequencies are indeed present for an $N$-wire system. In figures 5.19 and 5.20, the results of numerical simulations for an $N = 5$ system are shown for central and edge bullets respectively. Instead of being plotted in a wire-by-wire basis, these figures are plotted in a supermodal basis. (In other words, they are expanded in the eigenvectors of $\hat{X}$.) This shows the absence of the antisymmetric modal components for the central bullets, thus explaining why some of the resonances are forbidden. As expected, figure 5.19 shows 3 Čerenkov peaks, whilst figure 5.20 shows 5.

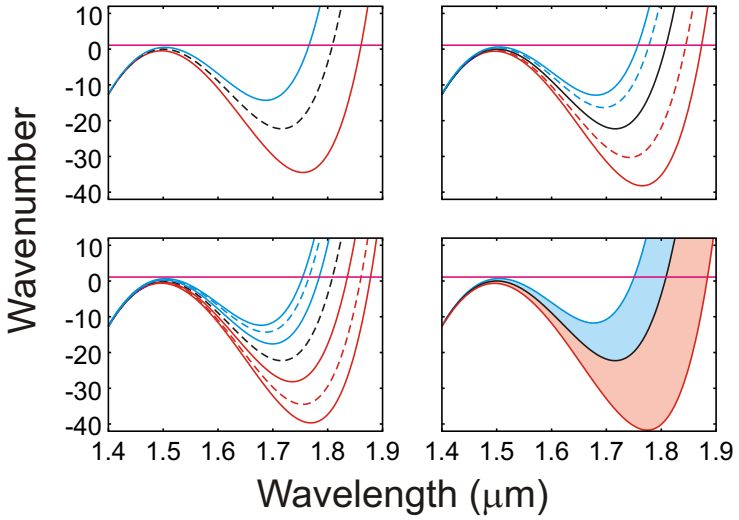


Figure 5.18: Resonance conditions for 220nm × 380nm wires placed 700nm apart, for systems with (top-left) 3, (top-right) 5, (bottom-left) 7 and (bottom-right) $\infty$ wires. The soliton wavenumber $q = 1.1$ is given by horizontal dotted line. Antisymmetric modes (which are "forbidden" for central bullets are shown by dashed lines, whilst symmetric modes are shown in full lines. Modes with negative eigenvalues are shown in red, and those with positive eigenvalues are shown in blue.

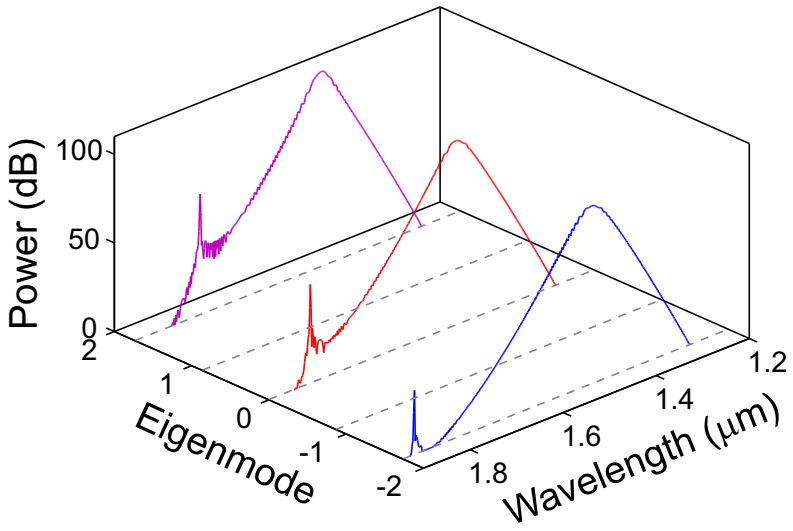


Figure 5.19: Čerenkov generation in a system of five 220nm × 380nm wires, after 5.8mm of propagation (at $\zeta = 10$) for an ordinary bullet. Expanded in terms of the eigenvectors of $\vec{X}$, which are labelled by eigenvalue. Two of the modes are precisely zero, due to them being antisymmetric and thus not part of the symmetric bullet solution. Therefore, only three Čerenkov peaks are generated.

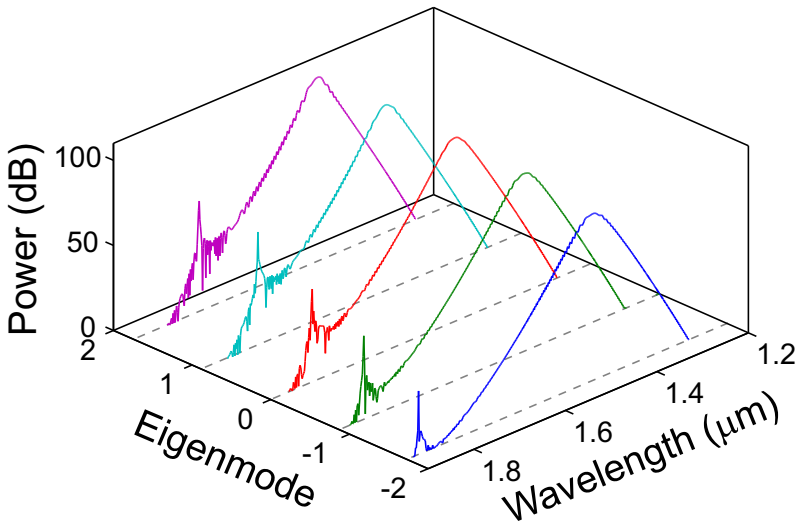


Figure 5.20: Čerenkov generation in a system of five 220nm × 380nm wires, after 5.8mm of propagation (at $\zeta = 10$) for an edge bullet. Displayed in terms of the eigenvectors of $\vec{X}$, arranged by eigenvalue. The edge bullet contains both symmetric and antisymmetric modes, and thus all five Čerenkov peaks are generated.

### 5.3.3 Čerenkov spectra in a realistic system

We will now consider Čerenkov radiation in the realistic case. Of particular interest is the scenario in which the number of peaks is small, allowing a set number of distinct Čerenkov peaks (as opposed to an indistinct continuum of many overlapping peaks) to be seen. This is particularly important from the point of seeing if certain resonances are forbidden.

Both central bullets and edge bullets were modelled, as is shown in figures 5.21, 5.22 and 5.23. As predicted the edge bullets show $N$ Čerenkov peaks, whereas the central bullets show $\lceil N/2 \rceil$ Čerenkov peaks.

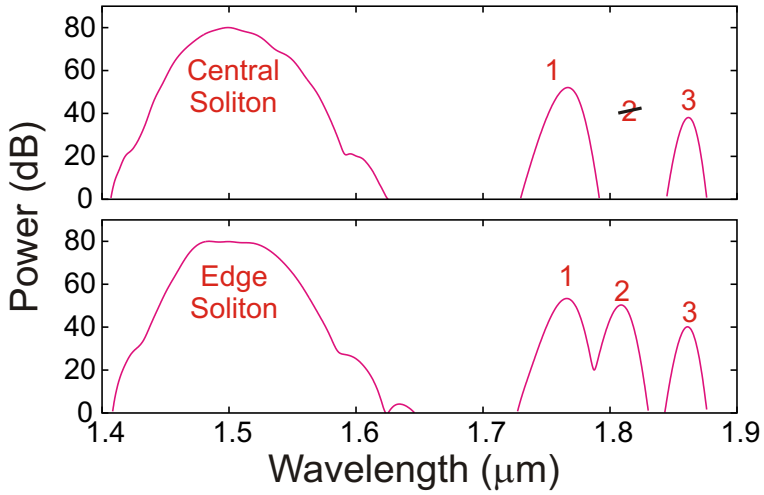


Figure 5.21: Power spectrum summed over all wires (after 2.4mm propagation, $\zeta = 4$) for $N = 3$ array of 220nm×380nm wires with 700nm separation. Shown for centre-wire input (top) and edge-wire input (bottom). As predicted, all 3 Čerenkov peaks are present for the edge soliton, but 1 of these is suppressed for the central soliton. The input pulse is taken as $\sqrt{3.5P_0}\,\mathrm{sech}\,(\tau)$.

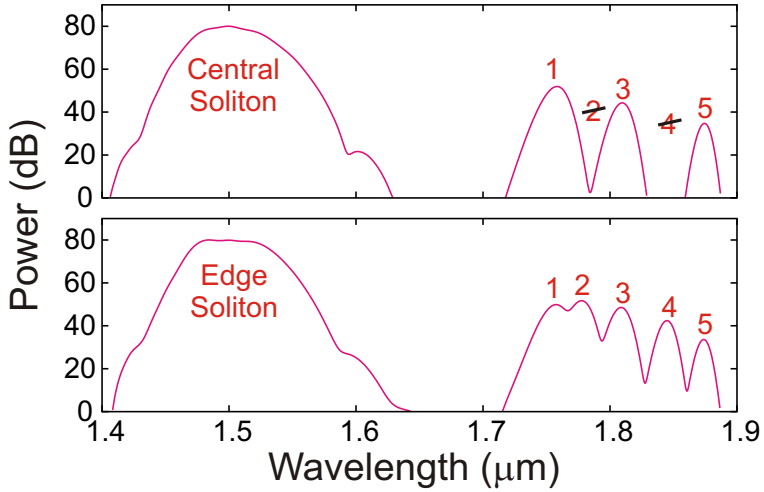


Figure 5.22: The same as Fig. 5.21, but for $N = 5$. All 5 Čerenkov peaks are present for the edge soliton, but 2 of them are suppressed for the central soliton.

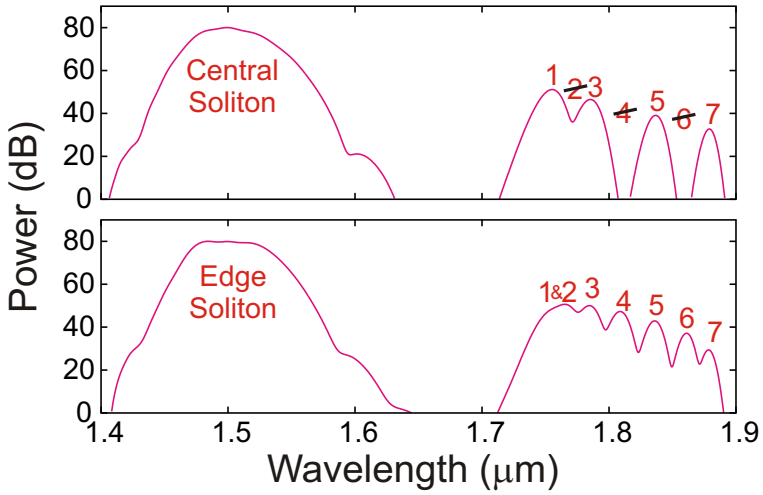


Figure 5.23: The same as Figs. 5.21 and 5.22, but for $N = 7$. All 7 Čerenkov peaks are present for the edge soliton, but 3 of them are suppressed for the central soliton. Peaks 1 and 2 cannot be resolved here, but by observing the modal profiles it can be shown that two resonances are indeed present.

# Chapter 6

# Solitons in Raman media

In this section, solitons supported by the Raman effect, rather than Kerr nonlinearity are considered. Raman scattering is the inelastic scattering of light, in which a photon is exchanged for a photon of slightly different energy. This energy exchange corresponds to a quantum transition within the medium, which is usually rotational or vibrational in nature. The Raman effect occurs when this transition is forbidden, but may happen indirectly via higher energy "virtual" levels. In the first stage of the process, a molecule accepts an incoming photon, and is excited to one of the virtual levels. In the second stage, the molecule decays from the virtual level to the second level, with the emission of the outgoing photon. This process can be subdivided into three separate phenomena (as shown in figure 6.1):

- *Stokes Scattering* occurs when the final state has a higher energy than the initial state. Therefore, the photons are effectively redshifted, and the medium absorbs energy.
- *Anti-Stokes Scattering* occurs when the final state has a lower energy than the initial state. Therefore, the photons are blueshifted, and the medium releases energy. Due to conservation of energy, anti-Stokes scattering must occur in tandem with another process that excites the medium. (Stokes scattering is one such process.) As the molecules can revert to the ground state by other means, anti-Stokes scattering will usually occur to a lesser extent than Stokes scattering, and so the ultimate effect of Raman scattering is usually a net redshifting.
- *Rayleigh Scattering* occurs when the final state has the same energy as the initial state. Therefore, no energy is transferred, and hence Raman scattering has not occurred. This in fact is the most common outcome, but it results in no change to the photon energy, and so will not be considered further.

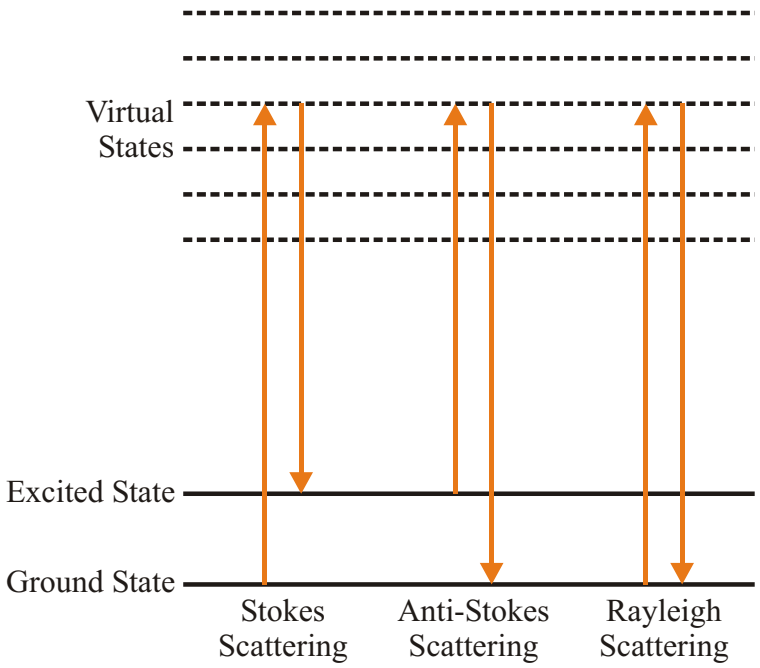


Figure 6.1: Schematic of the Scattering Types in a Two-Level Raman Medium.

The Raman effect requires the quantum coherence between the two energy levels to have an appropriate value. (This quantity will be defined in section 6.1, when the equations of motion are derived.) In this chapter, *Stimulated Raman Scattering* (SRS) is considered, whereby the coherence is provided by light already at the Stokes or anti-Stokes frequency. The Raman effect will then cause this frequency to be amplified, at the expense of the pump frequency. (Not surprisingly, optical amplifiers based on this principle are widespread [8].) In addition to SRS, the Raman effect can be initiated by vacuum noise, in what is known as *Spontaneous Raman Scattering*. A Stokes line or anti-Stokes line can itself undergo Raman scattering, to create a further line. These lines can create more lines, and so on, generating a comb of frequencies in what is known as *cascading Raman scattering*.

Like Kerr nonlinearity, SRS can support a variety of soliton solutions. These include hybrid bright-dark temporal solitons in which a bright-soliton of Stokes-shifted light co-moves with a dark-soliton in the optical pump [38], and more conventional bright solitons [39, 216, 217]. It is also possible to see solitons where the Raman effect and the Kerr effect are combined [218], but here we consider pure Raman solitons.

A Raman soliton consisting of three or more discrete frequency components requires that these components be phase matched. When phase mismatch is present, instability will occur, and the soliton will break up [219]. In this chapter, however, a new class of solutions are found, which *can* exist in the presence of strong phase mismatch.

The solutions derived aren't applicable to silicon waveguides. This is due to the fact that they require the absence of Kerr nonlinearity, which is not the case for silicon. Furthermore, the

Raman effect in silicon is difficult to observe; it has a very narrow bandwidth, and only becomes important in devices designed to exploit it [76, 77, 78, 79], where a signal frequency precisely tuned to the Raman-shifted pump frequency is amplified. In fact, from the point of view of solitons, the Raman effect in silicon is largely irrelevant [116], which is why it was not included in the model derived in chapter 2. When it is considered (e.g. [60]), it is usually represented using a modified Kerr nonlinearity term with hysteresis [60], rather that the coupled envelope model derived below. Finally, the solitons require an exotic state consisting of two levels with equal populations in each, which would not be possible in silicon.

A more suitable medium is hydrogen or deuterium [220, 221]. In addition to being placed in a gas cell, these gases can be placed in a hollow-core photonic crystal fibre [222]. These fibres have a hole running along their entire length, surrounded by a structured region of glass and air spaces, designed so that the majority of the light travels through the hole. Using such an arrangement, the gas can provide the Raman activity, whilst the fibre provides a tightly controlled dispersion relation.

## 6.1 Equations of stimulated Raman scattering

We now need to derive a set of equations describing how light evolves in a Raman active medium. (This derivation is shown in [97], but only in the much simpler case where only two field components are present.) We will assume that there are two real energy levels in the medium, plus $N-1$ Raman levels which mediate scattering between $N$ frequency components in the fields. This is shown in figure 6.2.

For clarity, we will use upper-case omega ($\Omega$) to represent the frequencies corresponding to quantum energy levels, and lower case omega ($\omega$) to represent the frequencies of components in the electric field. We number these frequencies starting from the highest (i.e. $\Omega_1$, $\omega_1$) and decreasing to the lowest (i.e. $\Omega_{N-1}$, $\omega_N$). At no point do we make a distinction between the numbering of Stokes, anti-Stokes, or pump frequencies. Therefore we can arbitrarily choose one of frequency components to be the pump frequency, in which case all of the components with lower ordinal numbers become anti-Stokes lines, and those with higher ordinal numbers become Stokes lines.

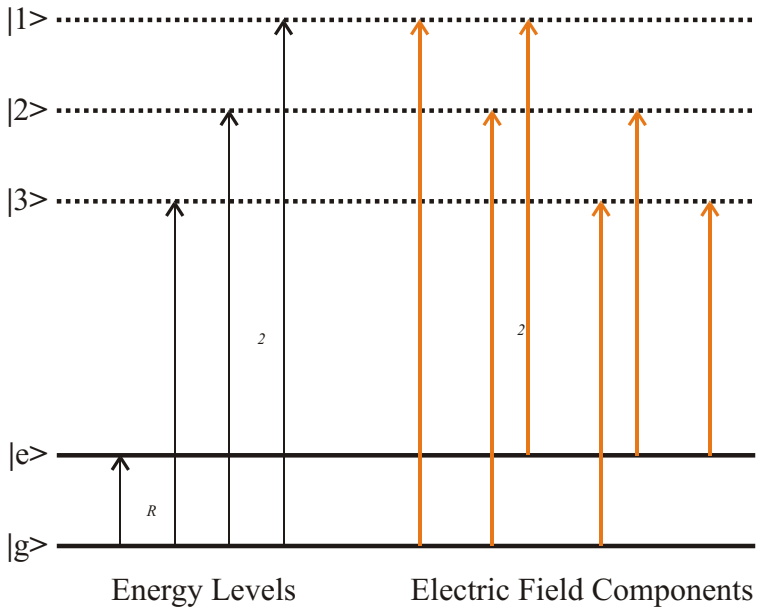


Figure 6.2: Outline of energy levels in the optical medium and their relation to the frequency components of the electric field (shown in simplified case, where $N = 4$). $|g\rangle$ and $|e\rangle$ are the ground and excited states, separated by energy $\hbar\Omega_R$. The states $|1\rangle$, $|2\rangle$ and $|3\rangle$ are the Raman levels.

As we know the allowed states of the system, it is convenient to use a matrix formulation of quantum mechanics. We start by assuming that the states of the system, plus the virtual states form a complete orthonormal basis set. Therefore we can write an arbitrary wavefunction $|\psi\rangle$ in this basis as

$$|\psi\rangle = c_g|g\rangle + c_e|e\rangle + \sum_{n=1}^{N-1} c_n|n\rangle \tag{6.1}$$

where $|g\rangle$ is the ground state, $|e\rangle$ is the excited state, and $|n\rangle$ (where $n = 1, 2, \cdots, N-1$) is the $n$th Raman level. The coefficients $c_g$, $c_e$ and $c_n$ correspond to the relative amplitude of each state. This mixed state can be represented by a column vector

$$|\psi\rangle = \begin{bmatrix} c_g \\ c_e \\ c_1 \\ c_2 \\ \vdots \\ c_{N-1} \end{bmatrix} \tag{6.2}$$

As we are using the eigenvectors of the unperturbed Hamiltonian as our basis, the matrix form of the unperturbed Hamiltonian will be a diagonal matrix consisting of the corresponding

eigenvalues (i.e. the energies of those states). Therefore, we obtain

$$\hat{H}_0 = \hbar \begin{bmatrix} 0 & 0 & 0 & 0 & \cdots & 0 \\ 0 & \Omega_R & 0 & 0 & \cdots & 0 \\ 0 & 0 & \Omega_1 & 0 & \cdots & 0 \\ 0 & 0 & 0 & \Omega_2 & & 0 \\ \vdots & \vdots & \vdots & & \ddots & 0 \\ 0 & 0 & 0 & 0 & 0 & \Omega_{N-1} \end{bmatrix} \tag{6.3}$$

where we have defined the ground state to have zero energy, $\hbar\Omega_R$ is the energy of the excited state, and $\hbar\Omega_n$ is the energy of the $n$th Raman level. The frequency $\Omega_R$ is the frequency change caused by the Raman scattering.

The interaction Hamiltonian for a dipole transition from state $x$ to state $y$ is $-\langle y|\vec{E}\cdot\vec{\mu}|x\rangle$ where $\vec{\mu}$ is the dipole moment associated with that transition. Therefore, if we assume that each allowed transition is a dipole transition with a dipole moment of $\mu$ (whilst all the forbidden transitions have a dipole moment of zero), then the interaction Hamiltonian is

$$\hat{H}_{\text{int}} = -\vec{E}\cdot\hat{\mu} \tag{6.4}$$

where $E$ is the electric field, and $\hat{\mu}$ is the polarisation operator, which is given by

$$\hat{\mu} = \vec{\mu} \begin{bmatrix} 0 & 0 & 1 & 1 & \cdots & 1 \\ 0 & 0 & 1 & 1 & \cdots & 1 \\ 1 & 1 & 0 & 0 & \cdots & 0 \\ 1 & 1 & 0 & 0 & & 0 \\ \vdots & \vdots & \vdots & & \ddots & 0 \\ 1 & 1 & 0 & 0 & 0 & 0 \end{bmatrix} \tag{6.5}$$

Assuming that the number of Raman-active sites per unit volume ($N_0$) is very large, then the nonlinear part of the polarisation density (as defined in section 2.2.3) can be given statistically as

$$\vec{P}_{\text{NL}} = N_0\langle\hat{\mu}\rangle \tag{6.6}$$

where $\langle\hat{\mu}\rangle$ is the expectation value of the polarisation operator. This can be calculated in terms of the density matrix $\hat{\rho}$, giving

$$\vec{P}_{\text{NL}} = N_0\text{Trace}\left[\hat{\mu}\hat{\rho}\right] \tag{6.7}$$

Substituting the individual elements of $\hat{\mu}$ and $\hat{\rho}$ into this gives

$$\vec{P}_{\text{NL}} = N_0\vec{\mu}\sum_{n=1}^{N-1}\left[\rho_{gn} + \rho_{ng} + \rho_{en} + \rho_{ne}\right] \tag{6.8}$$

where subscript $g$ and $e$ correspond to the ground and excited states respectively, and subscript $n$ corresponds to the $n$th Raman level. The evolution of a density matrix is given by

$$i\hbar\frac{\partial\hat{\rho}}{\partial t} = -[\hat{\rho}, \hat{H}] \tag{6.9}$$

where $\hat{H}$ is the full Hamiltonian (given by $\hat{H}_0+\hat{H}_{\text{int}}$). We now need to reduce this into equations describing how the electric field evolves.

**Evolution of the electric field**

We proceed by taking two of the (generalised) components of equation 6.9, specifically

$$i\hbar\frac{\partial\rho_{ng}}{\partial t} = \vec{E}\cdot\vec{\mu}\left(\rho_{gg}+\rho_{eg}-\sum_{n'=1}^{N-1}\left[\rho_{nn'}\right]\right)+\hbar\Omega_n\rho_{ng} \tag{6.10}$$

$$i\hbar\frac{\partial\rho_{ne}}{\partial t} = \vec{E}\cdot\vec{\mu}\left(\rho_{ge}+\rho_{ee}-\sum_{n'=1}^{N-1}\left[\rho_{nn'}\right]\right)-\hbar\left(\Omega_R-\Omega_n\right)\rho_{ne} \tag{6.11}$$

We then write the electric field in slowly varying envelope form. However, instead of using a single envelope (as we did when deriving the NLS in section 2.2.2), we use a separate envelope for each spectral line. The electric field is therefore given by

$$\vec{E}=\Re\sum_{n=1}^{N}\vec{F}'A_n\left(z,t\right)e^{i\beta_{0n}z-i\omega_{0n}t} \tag{6.12}$$

where $A_n\left(z,t\right)$ is the slowly varying envelope for the $n$th line, with frequency $\omega_{0n}$ and wavenumber $\beta_{0n}$. Instead of directly substituting this into equations 6.10 and 6.11, we will first prepare for what is known as the *Rotating Wave Approximation*. We start by representing the density matrix elements in the form

$$\rho_{xy}\equiv\rho'_{xy}e^{i(K_x-K_y)z-i(\Omega_x-\Omega_y)t} \tag{6.13}$$

where $\rho'_{xy}$ is the density matrix in a Rotating Wave Basis, $\Omega_x$ and $\Omega_y$ are the De Broglie frequencies of the given levels, and $K_x$ and $K_y$ are the De Broglie wavenumbers. (In the above notation, $\Omega_g=0$ and $\Omega_e=\Omega_R$). The reason for this is as follows: If there is no interaction between two levels, then their coherence will be precisely $e^{i(K_x-K_y)z-i(\Omega_x-\Omega_y)t}$, which is the beat oscillation between the two wavefunctions. If the levels do interact, then this oscillation will remain, but it will be modulated by $\rho'_{xy}$, which in general is slowly varying. Therefore, we can split the coherence into a rapidly oscillating part ($e^{i(K_x-K_y)z-i(\Omega_x-\Omega_y)t}$) which accounts for the innate quantum oscillation between the wavefunctions, and a slowly varying part $\rho'_{xy}$ which accounts for non-trivial interactions between the levels.

Transforming into this basis, and collecting all the oscillating terms onto one side yields

$$\frac{\partial \rho'_{ng}}{\partial t} = \frac{\vec{E}\cdot\vec{\mu}}{i\hbar}\left(\rho_{gg}e^{-iK_nz+i\Omega_nt} + \rho'_{eg}e^{i(K_R-K_n)z-i(\Omega_R-\Omega_n)t} - \sum_{n'=1}^{N-1}\left[\rho'_{nn'}e^{-iK_{n'}z+i\Omega_{n'}t}\right]\right) \tag{6.14}$$

$$\frac{\partial \rho'_{ne}}{\partial t} = \frac{\vec{E}\cdot\vec{\mu}}{i\hbar}\left(\rho'_{ge}e^{-iK_nz+i\Omega_nt} + \rho_{ee}e^{i(K_R-K_n)zt-i(\Omega_R-\Omega_n)t} - \sum_{n'=1}^{N-1}\left[\rho'_{nn'}e^{i(K_R-K_{n'})z-i(\Omega_R-\Omega_{n'})t}\right]\right) \tag{6.15}$$

We now substitute equation 6.12 into these transformed equations to give

$$\frac{\partial \rho'_{ng}}{\partial t} = \frac{\vec{F'}\cdot\vec{\mu}}{2i\hbar}\sum_{n''=1}^{N}\left(e^{i\beta_{0n''}z-i\omega_{0n''}t}A_{n''} + e^{-i\beta_{0n''}z+i\omega_{0n''}t}A^*_{n''}\right)\times \left(\rho_{gg}e^{-iK_nz+i\Omega_nt} + \rho'_{eg}e^{i(K_R-K_n)z-i(\Omega_R-\Omega_n)t} - \sum_{n'=1}^{N-1}\left[\rho'_{nn'}e^{-iK_{n'}z+i\Omega_{n'}t}\right]\right) \tag{6.16}$$

$$\frac{\partial \rho'_{ne}}{\partial t} = \frac{\vec{F'}\cdot\vec{\mu}}{2i\hbar}\sum_{n''=1}^{N}\left(e^{i\beta_{0n''}z-i\omega_{0n''}t}A_{n''} + e^{-i\beta_{0n''}z+i\omega_{0n''}t}A^*_{n''}\right)\times \left(\rho'_{ge}e^{-iK_nz+i\Omega_nt} + \rho_{ee}e^{i(K_R-K_n)zt-i(\Omega_R-\Omega_n)t} - \sum_{n'=1}^{N-1}\left[\rho'_{nn'}e^{i(K_R-K_{n'})z-i(\Omega_R-\Omega_{n'})t}\right]\right) \tag{6.17}$$

We make the rotating wave approximation by selecting the resonant terms. These occur when $\omega_{0n} = \Omega_n$ (corresponding to a transition from the ground state to the $n$th Raman level) and when $\omega_{0,n+1} = \Omega_n - \Omega_R$ (corresponding to a transition from the excited state to the $n$th Raman level). This yields

$$\frac{\partial \rho'_{ng}}{\partial t} = \frac{\vec{F'}\cdot\vec{\mu}}{2i\hbar}\left(\rho_{gg}A_n + \rho'_{eg}A_{n+1}\right)e^{-i\delta t} \tag{6.18}$$

$$\frac{\partial \rho'_{ne}}{\partial t} = \frac{\vec{F'}\cdot\vec{\mu}}{2i\hbar}\left(\rho_{ee}A_{n+1} + \rho'_{ge}A_n\right)e^{-i\delta t} \tag{6.19}$$

where $\delta$ is detuning from exact resonance. If we assume that this detuning is sufficiently large, we can integrate equations 6.18 and 6.19 by assuming that the $e^{-i\delta t}$ term oscillates so rapidly that the other variables can be treated as constants [97]. This gives

$$\rho'_{ng} = \frac{\vec{F'}\cdot\vec{\mu}}{2\hbar\delta}\left(\rho_{gg}A_n + \rho'_{eg}A_{n+1}\right)e^{-i\delta t} \tag{6.20}$$

$$\rho'_{ne} = \frac{\vec{F'}\cdot\vec{\mu}}{2\hbar\delta}\left(\rho_{ee}A_{n+1} + \rho'_{ge}A_n\right)e^{-i\delta t} \tag{6.21}$$

Finally, switching out of the rotating frame gives

$$\rho_{ng} = \frac{\vec{F'} \cdot \vec{\mu}}{\hbar\delta}\left(\frac{1}{2}\rho_{gg}A_n + \frac{1}{4}QA_{n+1}\right)e^{iK_nz - i\Omega_nt} \tag{6.22}$$

$$\rho_{ne} = \frac{\vec{F'} \cdot \vec{\mu}}{\hbar\delta}\left(\frac{1}{2}\rho_{ee}A_{n+1} + \frac{1}{4}Q^*A_n\right)e^{i(K_n - K_R)z - i(\Omega_n - \Omega_R)t} \tag{6.23}$$

where we have dropped the $e^{i\delta t}$ detuning factors (which are negligible in relation to the equivalent oscillations in $\Omega_n$). The quantity

$$Q \equiv 2\rho_{eg}e^{-iK_Rz + i\Omega_Rt} \tag{6.24}$$

gives the coherence between the energy levels, as was mentioned above. The $\rho_{ee}$ and $\rho_{gg}$ terms in equations 6.22 and 6.23 correspond to an oscillating Stark shifting of the levels [97]. (The Stark effect is the phenomenon whereby the energy levels of a quantum system are shifted by an applied electric field.) This term can be removed, as it oscillates with the electric field, and thus will integrate to zero over a short time span [97]. We can then substitute the remaining terms of the matrix elements into equation 6.8 to give

$$\vec{P}_{\mathrm{NL}} = \frac{N_0\vec{\mu}\left(\vec{F'} \cdot \vec{\mu}\right)}{4\hbar\delta}\sum_{n=1}^{N-1}\left(QA_{n+1}e^{iK_nz - i\Omega_nt} + Q^*A_ne^{i(K_n - K_R)z - i(\Omega_n - \Omega_R)t} + \mathrm{c.c.}\right) \tag{6.25}$$

Assuming that the dipoles point in the same direction as the electric field (specified by $\vec{F'}$), this can be rewritten as

$$\vec{P}_{\mathrm{NL}} = \vec{F'}\frac{N_0\mu^2}{4\hbar\delta}\sum_{n=1}^{N-1}\left(QA_{n+1}e^{iK_nz - i\Omega_nt} + Q^*A_ne^{i(K_n - K_R)z - i(\Omega_n - \Omega_R)t} + \mathrm{c.c.}\right) \tag{6.26}$$

where $\mu$ is the dipole magnitude. This is very similar in structure to the polarisation in slowly varying envelope form, which (from equation 2.60 in section 2.2.3) is

$$\vec{P}_{\mathrm{NL}} = \frac{1}{2}\vec{F'}\sum_{n=1}^{N}\left(\Lambda_{\mathrm{NLn}}e^{i\beta_{0n}z - i\omega_{0n}t} + \Lambda^*_{\mathrm{NLn}}e^{-i\beta_{0n}z + i\omega_{0n}t}\right) \tag{6.27}$$

Therefore, by matching together the parts which oscillate at the same frequency, we can identify the polarisation envelopes as

$$\Lambda_{\mathrm{NLn}} = \frac{N_0\mu^2}{2\hbar\delta}\left(QA_{n+1} + Q^*A_{n-1}\right) \tag{6.28}$$

Substituting these envelopes into equation 2.58 gives

$$\frac{\partial A_n}{\partial z} - i\sum_{m=0}^{M} i^m\frac{\beta_{mn}}{m!}\frac{\partial^m A_n}{\partial t^m} = i\frac{\omega_0N_0\mu^2}{4\epsilon_0n_0c\hbar\delta}\left(QA_{n+1} + Q^*A_{n-1}\right) \tag{6.29}$$

where $\beta_{mn}$ is the $m$th dispersion coefficient for the $n$th field envelope. It should be noted that the summation index now starts from 0 rather than 2, as the $\beta_{0n}$ and $\beta_{1n}$ coefficients will in general be different.

We have also replaced the $\omega_{0n}$ coefficients with a single value of $\omega_0$, to remove the explicit frequency dependence of the nonlinearity. This is valid so long as the spectral range of the frequency comb is relatively narrow. (In principal we could have a formulation where the nonlinearity terms were different for each line. However, to do this properly, it would also be necessary to replace the dipole magnitude $\mu$ and the detuning $\delta$ with a separate value for each possible transition. This would require a substantial amount of physical data, and would also greatly complicate mathematical analysis. It is sufficient for our purposes to replace the nonlinearity coefficient with a single value that can be scaled away.)

As the individual spectral peaks span a frequency range that is narrower than the whole comb, the effect of group velocity dispersion (GVD) will predominantly occur between the spectral peaks, rather than within them. We can therefore make a common [218], but not universal [217], approximation of removing the terms in $\beta_{2n}$ to give

$$\frac{\partial A}{\partial z} - i\beta_{0n}A_n + \beta_{1n}\frac{\partial A_n}{\partial t} = i\frac{\omega_0 N_0 \mu^2}{4\epsilon_0 n_0 c\hbar\delta}\left(QA_{n+1} + Q^* A_{n-1}\right) \tag{6.30}$$

This does not amount to ignoring the GVD, as it still manifests itself in the differences between the values of $\beta_{1n}$.

**Evolution of the Raman coherence**

It is now necessary to determine how the Raman Coherence evolves. This can be done by considering the $\rho_{eg}$ component of equation 6.9, which is

$$i\hbar\frac{\partial \rho_{eg}}{\partial t} = \hbar\Omega_R\rho_{eg} + E\mu\sum_{n=1}^{N-1}\left(\rho_{ng} - \rho_{ne}^*\right) \tag{6.31}$$

Replacing $\rho_{eg}$ with $Q$ (using equation 6.24) gives

$$\frac{i\hbar}{2}\frac{\partial Q}{\partial t} = E\mu\sum_{n=1}^{N-1}\left(\rho_{ng} - \rho_{ne}^*\right)e^{-iK_R z + i\Omega_R t} \tag{6.32}$$

Substituting in the values for $\rho_{ng}$ and $\rho_{ne}$ (using equations 6.22 and 6.23), and resolving $E$ into a set of envelope functions (using equation 6.12) gives

$$\begin{aligned}\frac{i\hbar}{2}\frac{\partial Q}{\partial t} \quad = \quad & \frac{\mu^2}{2\hbar\delta}\sum_{n'=1}^{N}\left(e^{i\beta_{0n'}z - i\omega_{0n'}t}A_{n'} + e^{-i\beta_{0n'}z + i\omega_{0n'}t}A_{n'}^*\right)\times\sum_{n=1}^{N-1}\Bigg[ \\ & \left(\frac{1}{2}\rho_{gg}A_n + QA_{n+1}\right)e^{-i\delta t}e^{i(K_n - K_R)z - i(\Omega_n - \Omega_R)t} \\ & - \left(\frac{1}{2}\rho_{ee}A_{n+1}^* + QA_n^*\right)e^{i\delta t}e^{-iK_n z + i\Omega_n t}\Bigg]\end{aligned} \tag{6.33}$$

We can simplify this by selecting the resonant terms. (As the equations link together the envelope functions and $Q$, all of which are slowly varying, the resonant terms are those in

which the coefficients of the complex exponential terms are small). This gives

$$i\frac{\partial Q}{\partial t} = \frac{\mu^2}{\hbar^2\delta}\sum_{n=1}^{N-1}\left(\frac{1}{2}A_nA_{n+1}^*\rho_{gg} - \frac{1}{2}A_nA_{n+1}^*\rho_{ee} + Q|A_{n+1}|^2 - Q|A_n|^2\right) \tag{6.34}$$

The $Q|A_{n+1}|^2 - Q|A_n|^2$ terms sum to zero, and hence we are left with

$$i\frac{\partial Q}{\partial t} = -\frac{\mu^2}{2\hbar^2\delta}\sigma\sum_{n=1}^{N-1}A_nA_{n+1}^* \tag{6.35}$$

where $\sigma$ (defined as $\sigma \equiv \rho_{ee} - \rho_{gg}$) is the *Population Inversion Parameter*.

### Evolution of the population inversion parameter

It is now necessary to determine how the population inversion parameter evolves. This can be done by considering the $\rho_{ee}$ and $\rho_{gg}$ components of equation 6.9, which subtracted from one another give

$$\frac{\partial\sigma}{\partial t} \equiv \frac{\partial\rho_{ee}}{\partial t} - \frac{\partial\rho_{gg}}{\partial t} = \frac{E\mu}{i\hbar}\sum_{n=1}^{N-1}\left(\left(\rho_{ng} - \rho_{ng}^*\right) - \left(\rho_{ne} - \rho_{ne}^*\right)\right) \tag{6.36}$$

By an essentially identical process to that used in deriving the equation for $Q$ (i.e substituting in the equations for the electric field and matrix elements, and then selecting the resonant terms), we obtain

$$\frac{\partial\sigma}{\partial t} = \frac{\mu^2}{2\hbar^2\delta}\sum_{n=1}^{N-1}\Im\left(A_nA_{n+1}^*Q^*\right) \tag{6.37}$$

This assumes that deexcitation can only happen via anti-Stokes scattering. In general, however, other processes can deexcite the medium, and so a term of the form $r\,(\sigma - 1)$ should be added to the right hand side of equation 6.37, where $r$ is the decay rate.

### Conservation of population

It should be noted that the quantity $\sigma^2 + |Q|^2$ is an integral of motion. If we decompose it into the constituent wavefunctions, we obtain

$$\sigma^2 + |Q|^2 = 4\rho_{eg}\rho_{eg}^* + \left(\rho_{ee} - \rho_{gg}\right)^2 = \left(|e\rangle^2 + |g\rangle^2\right)^2 \tag{6.38}$$

where $|g\rangle$ and $|e\rangle$ are the wavefunctions of the ground and excited states of the system. Therefore, the integral of motion corresponds to the conservation of the population of states. The wavefunctions are normalised, and so we require that

$$\sigma^2 + |Q|^2 = 1 \tag{6.39}$$

**Equations in intrinsic units**

The equations for N-field Raman scattering (equations 6.30, 6.35 and 6.37) can be made dimensionless by choosing intrinsic units such that

$$A_n = \sqrt{\frac{1}{2T_0R}}B_n \tag{6.40}$$

$$t = T_0\tau \tag{6.41}$$

$$z = Z_0\zeta \tag{6.42}$$

The time scaling coefficient $T_0$ can be chosen arbitrarily. Given that the total energy in a particular field component is proportional to $\int_{-\infty}^{\infty}|A_n|^2(t)\,dt$, it follows that any solution will in fact correspond to a continuous set of solutions having different durations but the same total energy. The Raman coupling coefficient $R$ and the intrinsic distance unit $Z_0$ are defined as

$$R \equiv \frac{\mu^2}{4\hbar^2\delta} \tag{6.43}$$

$$Z_0 \equiv \frac{4\epsilon_0 cn_0\hbar\delta}{N_0\mu^2\omega_n} \tag{6.44}$$

Making these substitutions gives

$$i\frac{\partial}{\partial\zeta}\begin{bmatrix}B_1\\B_2\\\cdots\\B_N\end{bmatrix}+i\frac{\partial}{\partial\tau}\begin{bmatrix}v_1B_1\\v_2B_2\\\cdots\\v_NB_N\end{bmatrix} = -\begin{bmatrix}\eta_1 & Q & & \\ Q^* & \eta_2 & \cdots & \\ & \cdots & \cdots & Q\\ & & Q^* & \eta_N\end{bmatrix}\begin{bmatrix}B_1\\B_2\\\cdots\\B_N\end{bmatrix} \tag{6.45}$$

$$i\frac{\partial Q}{\partial\tau} = -\sigma\sum_{n=1}^{N-1}B_nB_{n+1}^* \tag{6.46}$$

$$\frac{\partial\sigma}{\partial\tau} = \sum_{n=1}^{N-1}\Im\left(B_nB_{n+1}^*Q^*\right) \tag{6.47}$$

where for convenience we have written the set of field equations in matrix form. To simplify the notation, the $\beta_{0n}$ parameters have been rewritten as $\eta_n \equiv \beta_{0n}$. These are known as the phase mismatch parameters, as for non-zero values, they introduce a distance varying phase shift between the frequency components of the electric field. Likewise, the $\beta_{1n}$ terms have been rewritten as $v_n \equiv \beta_{1n}$. These give the reciprocal group velocity at that particular frequency.

An example of a pure Raman medium (i.e. one that conforms to the above model, without complications due to Kerr nonlinearity and other physical effects) is deuterium gas. At a pump frequency of $\omega_n = 3.71\times10^{14}$, this has a Raman coupling coefficient of $R = 4.5\times10^{-7}$ $\mathrm{C^2m^2J^{-2}s^{-1}}$ [220]. At atmospheric pressure (where the volumetric density $N_0 = 2.45\times10^{25}$ $\mathrm{m^{-3}}$ $\mathrm{m^{-3}}$), this gives a distance unit of $Z_0 = 1\mathrm{mm}$.

## 6.2 Raman solitons with phase mismatch

When a Raman soliton consists of only two spectral lines, the phase mismatch is irrelevant, as it can be scaled away by switching to a moving frame of reference. With three or more lines, however, it is impossible to remove phase mismatch in the general case. Existing multi-line solutions simply ignore the phase mismatch parameters [223, 224], and so are only valid in the limit of short pulses. (The reason for this limit can be seen by noting that the phase mismatch parameter is in fact a measure of phase mismatch per unit length. Therefore, the total phase shift in a pulse is given by $\theta_n = \eta_n \Delta\zeta$, where $\Delta\zeta$ is its approximate spatial length. For the phase shift to be irrelevant, it must be much less than a wavecycle, giving the condition $\theta_n \ll 2\pi$, and thus $\Delta\zeta \ll 2\pi/\eta_n$.)

In this section, these solutions are extended to include dispersion relations with phase mismatch.

### 6.2.1 Band-gaps and tail analysis

Before attempting to find soliton solutions, we will explore the preconditions for soliton existence. Firstly, we need to know the linear dispersion relation (and the position of the band-gap that exists within it), so that we can avoid the instability resulting from an intersection between a soliton's dispersion relation and a linear mode.

The dispersion relation of linear waves can be obtained by substituting $B_n = b_n e^{ik\zeta - i\omega\tau}$ into equations 6.45. The complex constants $b_n$ give the amplitudes and phases of each field component. This gives

$$M_N \begin{bmatrix} b_1 \\ b_2 \\ \cdots \\ b_N \end{bmatrix} = 0 \tag{6.48}$$

where the matrix $M_N$ is defined as

$$M_N \equiv \begin{bmatrix} \eta_1 - k + v_1\omega & Q & & \\ Q^* & \eta_2 - k + v_2\omega & \cdots & \\ & \cdots & \cdots & Q \\ & & Q^* & \eta_N - k + v_N\omega \end{bmatrix} \tag{6.49}$$

Therefore, the dispersion relation is given by $|M_N| = 0$, which can be written recursively as

$$|M_N| \equiv (\eta_N - k + v_N\omega)\,|M_{N-1}| - |Q|^2 |M_{N-2}| = 0 \tag{6.50}$$

where $|M_1| = \eta_1 - k + v_1\omega$ and $|M_0| = 1$. This equation will trace out $N$ curved paths in $(k, \omega)$ space, which correspond to the possible linear wave dispersion relations. For very large values

of $\omega$ or $k$ (in both the negative and positive directions), the equation approaches the limit

$$\prod_{n=1}^{N} (v_n \omega - k) = 0 \tag{6.51}$$

and so the set of velocities $(\omega/k)$ for linear waves in this limit is

$$V = \{1/v_1, 1/v_2, 1/v_3, \cdots 1/v_N\} \tag{6.52}$$

Therefore, at each extreme of $k$ or $\omega$, the linear wave dispersion curve velocities must approach a set of values that matches up to the set $V$. We can sort the linear wave dispersion curves given by equation 6.50 into three distinct categories, by using this knowledge of how the curves behave at their extremal values. Each individual curve can:

1. Change from a positive velocity at $\omega = -\infty$ to a negative velocity at $\omega = \infty$, reaching a maximum value of $k$ somewhere in between. (A negative velocity simply means a retardation with respect to the moving frame of reference, rather than backwards propagation.)
2. Change from a negative velocity at $\omega = -\infty$ to a positive velocity at $\omega = \infty$, reaching a minimum value of $k$ somewhere in between.
3. Have the same sign of velocity at both extremes of $\omega$ and so cover the entire range of $k$.

(This excludes the unimportant degenerate cases where $v_n = v$ for one of the field components.)

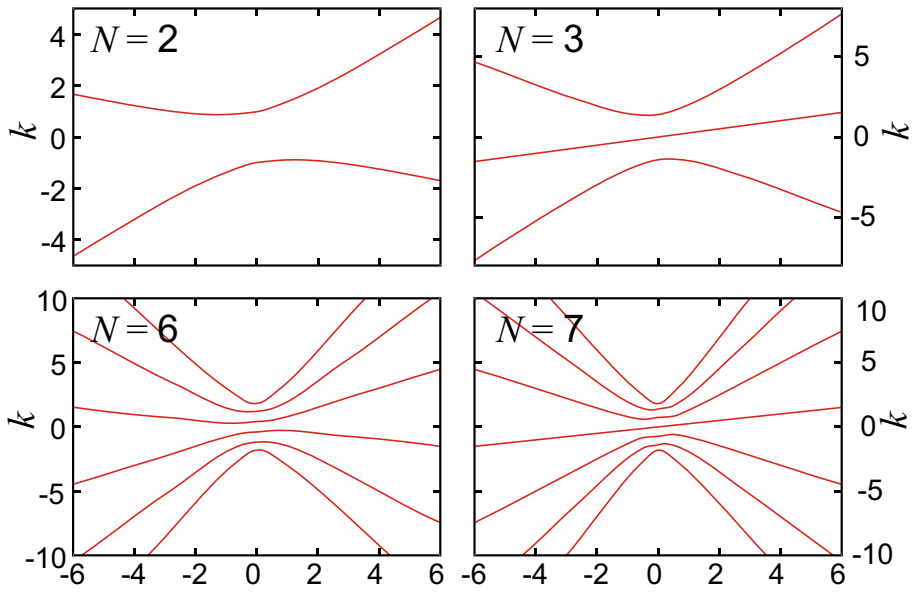


Figure 6.3: Linear dispersion curves for a variety of $N$. For even $N$, a bandgap exists, whilst for odd $N$, the bandgap is obstructed. Shown for $\eta_n = 0$ and $v_n = n - \frac{N}{2} - \frac{1}{4}$.

When all of the curves fall into the first and second categories, there will exist a band-gap

between the maxima and minima. This allows a soliton to exist without its dispersion relation overlapping with that of a linear wave mode. When a bandgap does exist, it allows for a range of soliton velocities between the least negative and the least positive values of $v_n$.

It should be noted that for this band gap to exist, exactly half of the $v_n$ coefficients must be positive, and the other half negative, so that each of the dispersion curves can have a negative gradient at one end, and a positive gradient at the other. (As we are working in a moving frame of reference, a negative group velocity doesn't necessarily correspond to a negative group velocity in the lab frame.) This precludes the existence of a band gap when the number of field components is odd, as at least one dispersion curve must fit into the third category. In figure 6.3, linear wave dispersion relations for a selection of $N$ field systems are shown, where $\eta_n = 0$ and $v_n = n - N/2 - 1/4$. For even $N$ a bandgap exists, whilst for odd $N$ it is obstructed.

**Tail analysis**

If we assume that soliton solutions have exponentially decaying tails, we can investigate these tails by substituting

$$B_n = b_n e^{\lambda \tau'} \tag{6.53}$$

into the equations of motion, where $\tau' \equiv \tau - v_s \zeta$ is the retarded time for a soliton moving at (reciprocal) speed $v_s$, and $\lambda$ is the exponential constant, which should have a positive real part for the leading edge of the pulse, and a negative real part for the trailing edge. It should be noted that this procedure is very similar to the above bandgap analysis, because mathematically speaking, an exponential decay is equivalent to a sinusoidal oscillation with imaginary frequency. Therefore, we can derive the same equation by the making the transformation

$$\omega \rightarrow i\lambda \tag{6.54}$$

$$k \rightarrow \kappa \tag{6.55}$$

$$v_n \rightarrow v_n - v_s \tag{6.56}$$

where in addition to selecting an imaginary frequency, we have switched to the prospective soliton's frame of reference and have replaced the general wavenumber $k$, with the soliton wavenumber $\kappa$. This gives

$$L_N \begin{bmatrix} b_1 \\ b_2 \\ \cdots \\ b_N \end{bmatrix} = 0 \tag{6.57}$$

where the matrix $L_N$ is defined as

$$L_N \equiv \begin{bmatrix} \eta_1 - \kappa - i\,(v_s - v_1)\,\lambda & Q & & \\ Q^* & \eta_2 - \kappa - i\,(v_s - v_2)\,\lambda & \cdots & \\ & \cdots & \cdots & Q \\ & & Q^* & \eta_N - \kappa - i\,(v_s - v_N)\,\lambda \end{bmatrix} \tag{6.58}$$

The solutions for $\lambda$ are given by $|L_N| = 0$, which can be written recursively as

$$|L_N| \equiv (\eta_N - \kappa - i\,(v_s - v_N)\,\lambda)\,|L_{N-1}| - |Q|^2|L_{N-2}| = 0 \tag{6.59}$$

where $|L_1| = \eta_1 - \kappa - i\,(v_s - v_1)\,\lambda$ and $|L_0| = 1$. This is an $N$th degree polynomial in $\lambda$, and so $\lambda$ has $N$ solutions. The polynomial is unchanged by the transformation $\lambda \to -\lambda^*$. Therefore, solutions must exist in pairs of the form $\{\lambda, -\lambda^*\}$. When $N$ is even, each value of $\lambda$ is generally complex. However, when $N$ is odd, there must be a lone solution of $\lambda$ that pairs up with itself. To satisfy the relationship between pairs, this root must lie on the imaginary-axis. A purely imaginary decay constant corresponds to a simple harmonic wave (or in the degenerate case of $\lambda = 0$, a constant amplitude). As with the band-gap analysis, this suggests instability for odd $N$.

### 6.2.2 Analytical soliton solutions

We can obtain analytical solutions by making the following ansatzes:

- $Q$ can be written in the form $Q = \alpha + iq$, where $q$ is a real function, and $\alpha$ is a real constant.
- The fields can be written in the form

  $$B_n = b_n f\,(x)\,e^{i\kappa\zeta} \tag{6.60}$$

  where $f$ is a function common to all the fields, $x \equiv c\,(\tau - v_s\zeta)$ is the retarded time scaled by a width parameter $c$, and $\kappa$ is the wavenumber. The amplitudes and phases of each soliton are given by the complex constants $b_1, b_2, \cdots b_N$.

Substituting these into equations 6.45, 6.46 and 6.47 gives

$$ic\frac{df}{dx}\begin{bmatrix} (v_s - v_1)\,b_1 \\ (v_s - v_2)\,b_2 \\ \cdots \\ (v_s - v_N)\,b_N \end{bmatrix} = f\begin{bmatrix} \eta_1 - \kappa & \alpha + iq & & \\ \alpha - iq & \eta_2 - \kappa & \cdots & \\ & \cdots & \cdots & \alpha + iq \\ & & \alpha - iq & \eta_N - \kappa \end{bmatrix}\begin{bmatrix} b_1 \\ b_2 \\ \cdots \\ b_N \end{bmatrix} \tag{6.61}$$

$$\frac{dq}{dx} = \sigma|f|^2\gamma \tag{6.62}$$

$$\frac{d\sigma}{dx} = |f|^2\,(\alpha\Im\,(\gamma) - q\Re\,(\gamma)) \tag{6.63}$$

where the constant $\gamma$ is given by

$$\gamma \equiv \frac{1}{c}\sum_{n=1}^{N-1} b_n b_{n+1}^* \tag{6.64}$$

By making the further ansatz that

$$\frac{df}{dx} = qf \tag{6.65}$$

we can manipulate equation 6.61 into the form

$$ic\frac{df}{dx}S_N\begin{bmatrix} b_1 \\ b_2 \\ \cdots \\ b_N \end{bmatrix} = fT_N\begin{bmatrix} b_1 \\ b_2 \\ \cdots \\ b_N \end{bmatrix} \tag{6.66}$$

where the matrices $S_N$ and $T_N$ are given by

$$S_N \equiv \begin{bmatrix} v_s - v_1 & -\frac{1}{c} & & \\ \frac{1}{c} & v_s - v_2 & \cdots & \\ & \cdots & \cdots & -\frac{1}{c} \\ & & \frac{1}{c} & v_s - v_N \end{bmatrix} \tag{6.67}$$

$$T_N \equiv \begin{bmatrix} \eta_1 - \kappa & \alpha & & \\ \alpha & \eta_2 - \kappa & \cdots & \\ & \cdots & \cdots & \alpha \\ & & \alpha & \eta_N - \kappa \end{bmatrix} \tag{6.68}$$

As $f$ and $df/dx$ are not constant, equation 6.66 can only be satisfied if

$$S_N\begin{bmatrix} b_1 \\ b_2 \\ \cdots \\ b_N \end{bmatrix} = 0 \tag{6.69}$$

$$T_N\begin{bmatrix} b_1 \\ b_2 \\ \cdots \\ b_N \end{bmatrix} = 0 \tag{6.70}$$

As $S_N$ and $T_N$ are both real, all the values of $b_n$ will have the same complex phase, and so $\gamma$ will be real. Therefore, from equations 6.62, 6.63 and 6.65 we obtain the simplified equations

$$\frac{df}{dx} = qf \tag{6.71}$$

$$\frac{dq}{dx} = \sigma|f|^2\gamma \tag{6.72}$$

$$\frac{d\sigma}{dx} = -q|f|^2\gamma \tag{6.73}$$

These equations possess an integral of motion

$$J \equiv \gamma|f|^2 - 2\sigma \tag{6.74}$$

In this form, the population of the system is given by

$$|Q|^2 + \sigma^2 = q^2 + \alpha^2 + \sigma^2 \tag{6.75}$$

and hence the population normalisation condition is given by

$$q = \pm\sqrt{1-\alpha^2-\sigma^2} \tag{6.76}$$

Substituting equations 6.74 and 6.76 into equation 6.73 yields an uncoupled equation for $\sigma$

$$\frac{d\sigma}{dx} = \pm\left(J+2\sigma\right)\sqrt{1-\alpha^2-\sigma^2} \tag{6.77}$$

This can be separated to give

$$\pm\int \frac{d\sigma}{\left(J+2\sigma\right)\sqrt{1-\alpha^2-\sigma^2}} = \int dx \tag{6.78}$$

Evaluating these integrals yields

$$\mp\frac{\log\left(\frac{\frac{8-8\alpha^2+4J\sigma}{\sqrt{4-4\alpha^2-J^2}}+4\sqrt{1-\alpha^2-\sigma^2}}{J+2\sigma}\right)}{\sqrt{4-4\alpha^2-J^2}} = x + C \tag{6.79}$$

where $C$ is the integration constant. Rearranging this to give an equation in $\sigma$ is not possible in closed form. However, if we assume that $J = 0$, the equation reduces to

$$\mp\frac{\log\left(\frac{2\sqrt{1-\alpha^2}+2\sqrt{1-\alpha^2-\sigma^2}}{\sigma}\right)}{2\sqrt{1-\alpha^2}} = x + C \tag{6.80}$$

Physically speaking, the assumption of $J = 0$ means a pulse of light is being fired into a medium with an equal population between the two states, and perfect coherence between those states. It is possible to prepare such a medium [224], and so this is a realistic scenario. The equation can now be solved to give

$$\sigma(x) = \mp\frac{2}{\frac{1}{(1-\alpha^2)}e^{2\sqrt{1-\alpha^2}x} + e^{-2\sqrt{1-\alpha^2}x}} \tag{6.81}$$

where we have set $C = 0$, as this merely shifts the solution in time. The solution can be written as

$$\sigma(x) = -\frac{2}{\frac{1}{(\alpha')^2}e^{2\alpha' x} + e^{-2\alpha' x}} \tag{6.82}$$

where

$$\alpha' \equiv \sqrt{1-\alpha^2} \tag{6.83}$$

This in turn can be written as

$$\sigma(x) = -\mathrm{F}_{\alpha'}(2x) \tag{6.84}$$

where the $\mathrm{F}_n$ function is defined as

$$\mathrm{F}_n(x) \equiv \frac{2}{\frac{1}{n^2}e^{nx} + e^{-nx}} \tag{6.85}$$

This function is a generalisation of the familiar sech function, to which it is identical when $n = 1$. Substituting equation 6.84 into equation 6.72 gives an uncoupled equation for $q$

$$\frac{dq}{dx} = 2\,\mathrm{F}_{\alpha'}^{2}\,(2x) \tag{6.86}$$

This has a solution

$$q = \frac{2\,(\alpha')^{3}}{e^{4\alpha' x} + (\alpha')^{2}} - \alpha' \tag{6.87}$$

and so the coherence can be written as

$$Q = \alpha - \left(\alpha' - \frac{2\,(\alpha')^{3}}{e^{4\alpha' x} + (\alpha')^{2}}\right) i \tag{6.88}$$

Substituting equation 6.84 into equation 6.74 gives a solution for $|f|^2$. The equations of motion are satisfied by taking the real positive route of this function, to give

$$f(x) = \sqrt{\frac{2}{|\gamma|}\,\mathrm{F}_{\alpha'}\,(2x)} \tag{6.89}$$

Before solving equations 6.69 and 6.70 (in order to calculate the actual field envelopes) we should note that it is homogenous, and so the values $b_n$ will have an arbitrary multiplicative constant, $m$. From its definition, $\gamma$ is proportional to $m^2$, and so $f$ is proportional to $m^{-1}$. Therefore, when we multiply $f$ by $b_n$ to obtain the field envelopes, $m$ will cancel out. We can remove $m$ from our calculations entirely by specifying that the values of $b_n$ must satisfy the condition

$$\sum_{n=1}^{N-1} b_n b_{n+1}^{*} = c \tag{6.90}$$

We can then write the field envelopes as

$$B_n = b_n \sqrt{2\,\mathrm{F}_{\alpha'}\,(2c\,(\tau - v_s\zeta))} \tag{6.91}$$

where the coefficients $b_n$ have yet to be found.

This type of solution is notable for carrying a topological charge [223]. The sech-like Kerr soliton considered in section 3.1 is non-topological, as it can be continuously deformed into a non-solitonic (uniformly zero) solution, by letting the wavenumber tend towards zero. The Raman soliton, however, cannot be deformed like this, as the coherence $Q$ is different between the extremes of time, and no form of scaling will remove it.

### 6.2.3 Calculation of field amplitudes

Equations 6.69 and 6.70 impose contradictory requirements on the values of $b_n$. However, a limited set of solutions can be obtained by solving equation 6.69 (as is shown below), and then matching $T_N$ to this solution by explicitly requiring that the phase-mismatch coefficients

conform to

$$\eta_n = \kappa - \alpha \frac{b_{n+1} + b_{n-1}}{b_n} \tag{6.92}$$

The constants $\alpha$ and $\kappa$ can be chosen arbitrarily (subject to the above condition that $-1 < \alpha < 1$), and hence can be used to gain a certain amount of control over the phase mismatch parameters. It should be noted that in the case $\alpha = \kappa = 0$, the phase mismatch coefficients all become zero. This special case is already known in the literature [224], but the phase mismatched generalisation is novel.

The reciprocal group velocity parameters were chosen as

$$v_n = \xi \left( n - \frac{N}{2} + \phi \right) \tag{6.93}$$

where the parameter $\xi$ is the group velocity dispersion, with positive values giving normal dispersion, and negative values giving anomalous dispersion. The values of $v_n$ are shifted in order to guide the soliton's spectrum through the bandgap derived in section 6.2.1. (In the case of odd $N$, when the band gap is always occluded, only one linear band will intersect with the soliton spectrum.) The constant $\phi$ can lie within the range $-\frac{1}{2} < \phi < \frac{1}{2}$.

If 6.69 is to have non-zero solutions in $b_n$, then the soliton width $c$, must be chosen such that.

$$|S_N(c)| = 0 \tag{6.94}$$

It is helpful to consider the soliton velocity in relation to the group velocity dispersion, and so we define the proportional soliton velocity $v_p$, by the identity $v_s \equiv \xi v_p$. This enables us to write $S_N$ as

$$S_N = \xi \begin{bmatrix} v_p - \left(1 - \frac{N}{2} + \phi\right) & -\frac{1}{\xi c} & & \\ \frac{1}{\xi c} & v_p - \left(2 - \frac{N}{2} + \phi\right) & \cdots & \\ & \cdots & \cdots & -\frac{1}{\xi c} \\ & & \frac{1}{\xi c} & v_p - \left(N - \frac{N}{2} + \phi\right) \end{bmatrix} \tag{6.95}$$

Therefore, we can determine the soliton width for all values of $\xi$ by solving

$$|S_N(\xi c)| = 0 \tag{6.96}$$

for $\xi c$. It is apparent that the width, $1/c$, of a soliton is proportional to the group velocity dispersion parameter. Furthermore, the values of $b_n$ are independent of $\xi$. Solutions for $\xi c$ were found numerically. For certain parameter sets, the solutions are all non-real, and so the soliton solutions are not applicable. The regions where real solutions for $c$ exist are shown in figure 6.4.

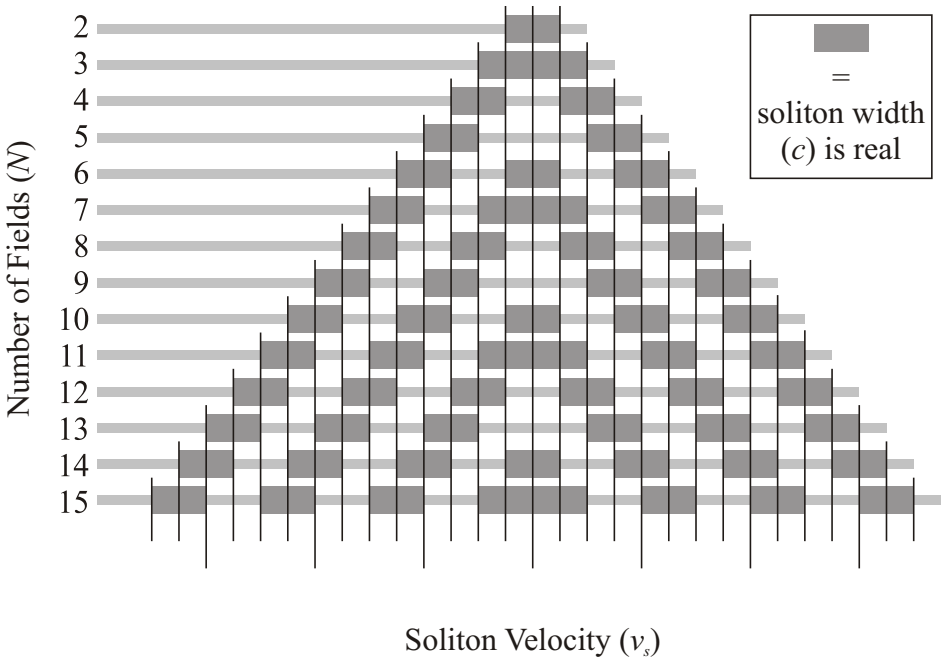


Figure 6.4: Parameters for which real solutions in $c$ exist. The horizontal axis is scaled in terms of $\xi$ and $\phi$. The chart then shows the soliton velocities (measured against this scale), which give real solutions for $c$.

For cases where real values of $c$ exist, the values of $b_n$ (subject to condition 6.90) were calculated numerically. Solutions at $v_s = 0.05$, for the six first applicable cases are shown

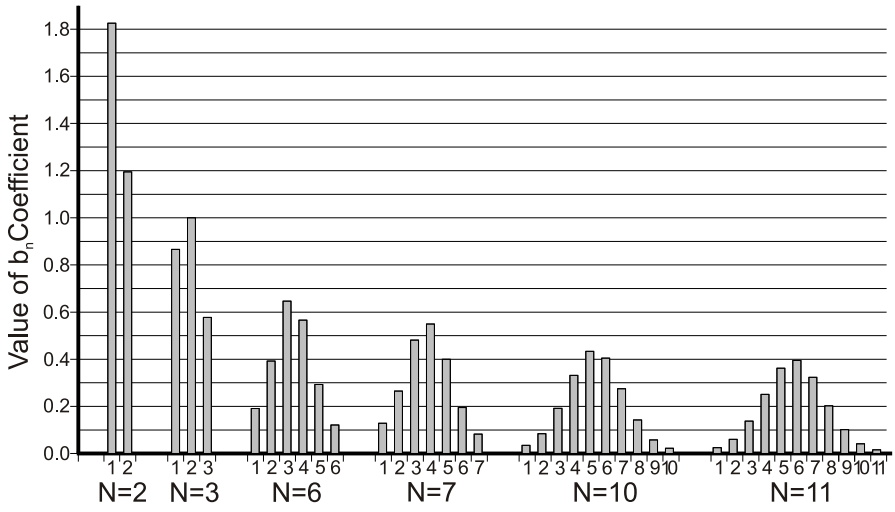


Figure 6.5: Field amplitude coefficients for the first six cases where $c$ has real solutions. (Where multiple real values of $c$ exists, the lowest positive value is used). Parameters $\phi = -0.25$ and $v = 0.05$ have been chosen.

Substituting these values of $b_n$ and $c$ into 6.91, gives a soliton solution. This solution is a

generalisation of the solutions given in [224].

### Gaussian profile of the field amplitude coefficients

As $N$ increases, the shape of the $b_n$ distribution tends towards a Gaussian profile. This can be shown by considering an arbitrary row of equation 6.69, such that

$$\frac{1}{c}b_{n-1} + (v_s - v_n)\, b_n - \frac{1}{c}b_{n+1} = 0 \tag{6.97}$$

This can be rearranged to give

$$\frac{b_{n+1} - b_{n-1}}{2} = \frac{c}{2}\,(v_s - v_n)\, b_n \tag{6.98}$$

For a large number of fields, $b_n$ can be approximated by a continuous function $b(n)$, where the values of $b$ are approximately equal for adjacent values of $n$. Similarly, $v_n$ can be represented by a continuous function $v(n)$. Therefore, we can approximate the left hand side of equation 6.98 with a derivative, giving

$$\frac{db}{dn} \approx \frac{c}{2}\,(v_s - v)\, b \tag{6.99}$$

This can be solved to give

$$b_n \approx \exp\left(-\frac{1}{2}c\int v(n)dn\right) \tag{6.100}$$

(where the $\frac{cv_s}{2}$ term has been absorbed into the arbitrary constant of the remaining integral). For the values of $v$ given by equation 6.93, we obtain

$$b_n \approx m\exp\left(\xi c\left(\frac{1}{4}N - \frac{1}{2}\phi\right)n - \frac{1}{4}\xi c n^2\right) \tag{6.101}$$

where $m$ is the integration constant. This is a Gaussian function centred about the zero group velocity point (at $n = \frac{1}{2}N - \phi$) of the dispersion relation. Notably, to see this Gaussian distribution (and hence to have spectral localisation), the GVD parameter $\xi$ must be positive. Therefore, unlike Kerr solitions, this class of soliton requires normal GVD.

### Phase mismatch parameters

Once the values of $b_n$ have been calculated, the permitted values of $\eta_n$ can be trivially calculated from equation 6.92. It follows from the Gaussian profile of $b_n$ that the phase mismatch parameters will have a profile of the form

$$\eta_n = \kappa - \alpha\left(e^{\xi c\left(\frac{1}{4}N - \frac{1}{2}\phi\right) - \frac{1}{2}\xi c n} + e^{-\xi c\left(\frac{1}{4}N - \frac{1}{2}\phi\right) + \frac{1}{2}\xi c n}\right) \tag{6.102}$$

where the approximation $N \gg 1$ has been made. This is a hyperbolic cosine function centred about the zero-velocity point (at $n = N/2 - \phi$) of the dispersion relation.

### 6.2.4 Simulation of soliton propagation

The full equations were solved numerically, using the soliton solutions as an initial condition at $\zeta = 0$, and then integrating equations 6.45, 6.46 and 6.47 using the methods described in appendix A.4. Random noise with a relative amplitude of 1% was added to the initial fields, in order to demonstrate soliton stability under perturbation. The simulation results are displayed in terms of the magnitude of the electric field, assuming that the Raman frequency is $\Omega_R = 10$. In each simulation, the parameters $\phi = -0.25$ and $v = 0.05$ were chosen. As a proof of concept, the propagation of these solutions was tested with (essentially arbitrary) non-zero values of $\alpha$ and $\kappa$, and hence of $\eta_n$. A ten field soliton was chosen, thus avoiding the potential instabilities that can occur for an odd number.

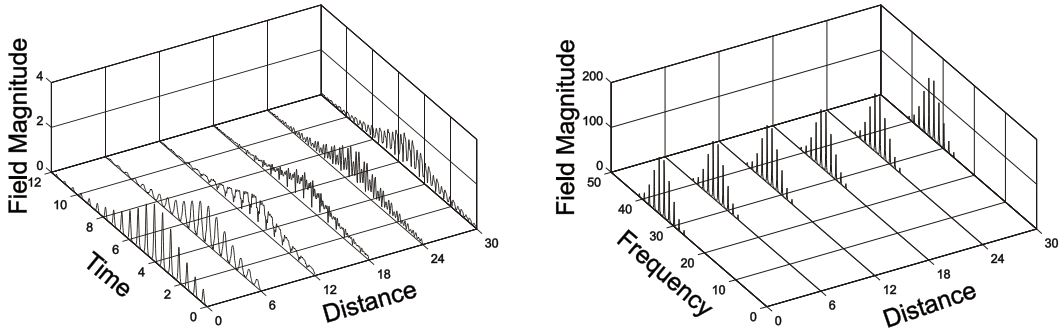


Figure 6.6: Propagation of 10-component Raman soliton over 30 distance units for $\alpha = 0.5$ and $\kappa = 0.8$. Shown in time domain (left) and frequency domain (right).

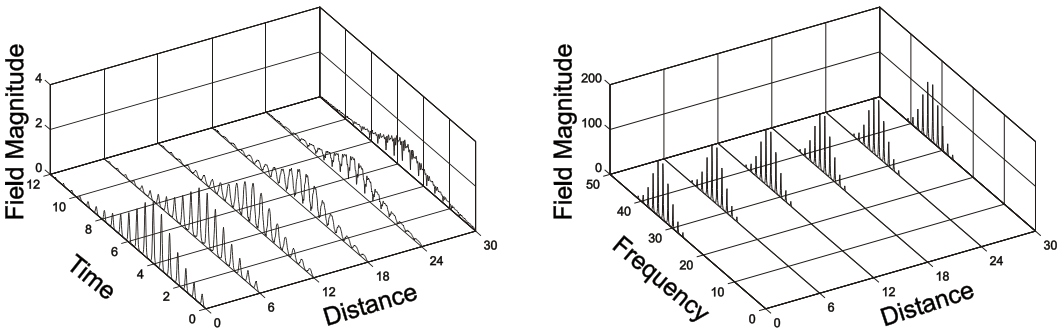


Figure 6.7: Propagation of 10-component Raman soliton over 30 distance units for $\alpha = 0.25$ and $\kappa = 0.4$. Shown in time domain (left) and frequency domain (right).

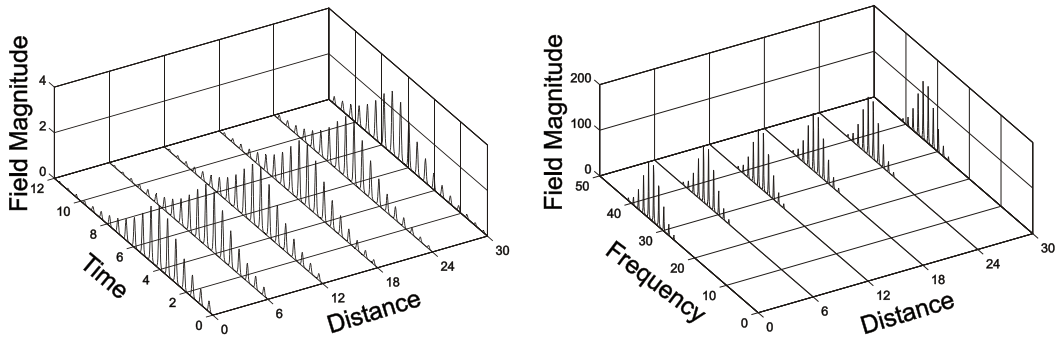


Figure 6.8: Propagation of 10-component Raman soliton over 30 distance units for $\alpha = 0$ and $\kappa = 0$. Shown in time domain (left) and frequency domain (right).

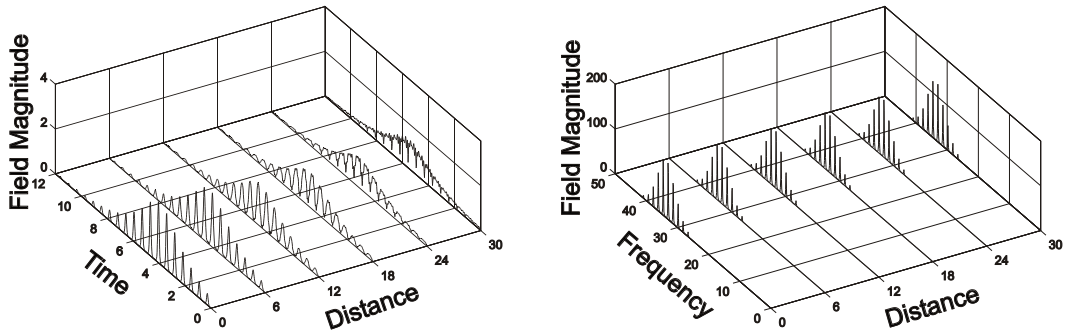


Figure 6.9: Propagation of 10-component Raman soliton over 30 distance units for $\alpha = -0.25$ and $\kappa = -0.4$. Shown in time domain (left) and frequency domain (right).

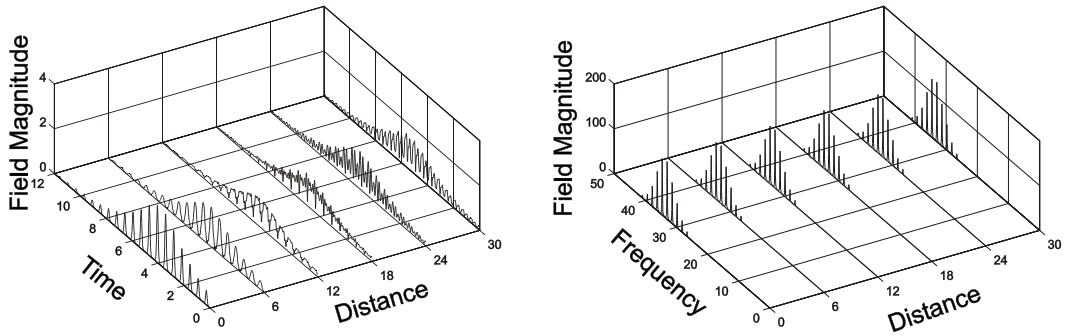


Figure 6.10: Propagation of 10-component Raman soliton over 30 distance units for $\alpha = -0.5$ and $\kappa = -0.8$. Shown in time domain (left) and frequency domain (right).

With zero-phase mismatch ($\alpha = 0$, $\kappa = 0$ in figure 6.8), the soliton propagates stably, despite the addition of noise. When phase match is introduced, slight perturbations appear in the time domain. Despite this (and despite the very long propagation distance) the pulse remains localised. Furthermore, in the frequency domain the amplitude of each field component is

constant, indicating that no net Stokes or anti-Stokes shifting is occurring. Therefore, the waveforms are almost certainly solitons.

# Chapter 7

# Summary of original findings and published works

The following original results were obtained:

- It was shown that experimental results by Wei Ding, William Wadsworth and Jonathan Knight were consistent with soliton evolution, thus strengthening the base of evidence for the existence of solitons in silicon wires. (Optics Express, 16:3310, 2008.)
- It was shown that the dispersion of linear coupling can be used to control the group velocity dispersion of supermodes in silicon waveguide arrays. The possibility of soliton generation and modulation instability in normally dispersive waveguides was demonstrated. (Optics Express 17:5879, 2009.)
- It was shown that silicon waveguide arrays are capable of supporting spatiotemporal solitons. A theory of resonant radiation generation in waveguide arrays was developed. A novel phenomenon was predicted, whereby a bullet will emit radiation at multiple frequencies, but that some of these will be "forbidden" for symmetry reasons. (Physical Review A, 78:033818, 2008.)
- The presence of Raman solitons in the presence of phase-mismatch was shown to be possible. (Presented at the 2006 annual meeting of the European Optical Society.)

# Appendix A

# Numerical methods

## A.1 Split-step Fourier method for integrating NLS equation

Equation 2.85 (as derived in chapter 2) describes the evolution of light through an SOI waveguide:

$$\frac{\partial E}{\partial \zeta} - i\hat{D}E = i|E|^2E - \epsilon_1 E - \epsilon_{2\mathrm{pa}}|E|^2E - \epsilon_{3\mathrm{pa}}|E|^4E - \epsilon_{\mathrm{fc}}En \tag{A.1}$$

Given a function $E(\tau)$ at $\zeta = 0$, it must be integrated to give $E(\tau)$ at an arbitrary value of $\zeta$.

Without the nonlinear terms, the equation can be solved in the frequency domain, as the dispersion operator $\hat{D}$ becomes a simple multiplication factor. The nonlinear terms, however, are more easily evaluated in the time domain. The solution to this is the split-step Fourier technique, in which a Fourier transform and an inverse Fourier transform are performed at each step in $\zeta$, thus allowing calculations in both the frequency and time domains to be made. The precise scheme (implemented in C++) is as follows:

- In the first step, the free-charge-carrier density at $\zeta$ was calculated over all time, using equation 2.84

$$\nu = e^{-\tau/\tau_c}\int_{\tau'=0}^{\tau}|E|^4e^{\tau'/\tau_c}d\tau' + \nu_{\tau=0}e^{-\tau/\tau_c} \tag{A.2}$$

  where $\nu_{\tau=0}$ is the starting value of the carrier density. It should be noted that as $\tau$ increases, the expression involves a potentially very small value ($e^{-\tau/\tau_c}$) being multiplied by a potentially very large value ($\int|E|^4e^{\tau'/\tau_c}d\tau'$), which could result in numerical error. To avoid this, the integral factor was represented as $\int|E|^4e^{\tau'/\tau_c}d\tau' = xe^{\gamma}$, where each time $x$ grew too large, it was divided by $e$, and the integer exponent $\gamma$ increased by one. The full term could then be evaluated as $e^{\gamma-\tau/\tau_c}x$, which is numerically safer.

- In the second step, the nonlinear parts of the equation were advanced in distance by removing the time dependent terms and then solving the equation

$$\frac{\partial E}{\partial \zeta} = i|E|^2E - \epsilon_{2\mathrm{pa}}|E|^2E - \epsilon_{3\mathrm{pa}}|E|^4E - \epsilon_{\mathrm{fc}}En \tag{A.3}$$

  using the previous value as a boundary condition. In the absence of damping, this can be solved analytically to give

$$E^{\mathrm{new}} = E^{\mathrm{old}}e^{i|E^{\mathrm{old}}|^2\Delta\zeta} \tag{A.4}$$

  where $\Delta\zeta$ is the distance increment. In the general case, the increment was made using a single step of the fourth-order Runge-Kutta integration scheme.

- In the third step, the linear parts of the equation were advanced in distance, thus accounting for the time dependent terms which were ignored in the previous step. The Fourier transform was taken, changing the time derivatives into frequency factors. A Fast Fourier Transform (FFT) routine from the GNU Scientific Library [225] was used. The linear advance could then be made analytically as

$$E^{\mathrm{new}} = E^{\mathrm{old}}e^{(D(\omega)-\epsilon_1)\Delta\zeta} \tag{A.5}$$

  The inverse FFT was then computed, thus completing the distance increment.

This process was repeated for an arbitrary number of steps, until the desired distance of propagation was reached. A time window with a range of $500T_0$ consisting of $2^{15} = 32768$ points was typically used. For each distance iteration, a step of $\Delta\zeta = 10^{-5}$ was typically used.

**Coupled equations**

The coupled equations were integrated using a modified version of the above scheme. As was shown in section 4.4.1, the equations in a supermodal basis are uncoupled with respect to the linear terms. Therefore the linear step can be made by transforming into a frequency and modal basis, and then advancing the solutions in distance using the supermodal version of equation A.5, which for the $j$th mode is given by

$$\tilde{E}_j^{\mathrm{new}} = \tilde{E}_j^{\mathrm{old}}e^{(D_j(\omega)-\epsilon_1)\Delta\zeta} \tag{A.6}$$

where $D_j$ is the supermodal dispersion operator defined in section 4.4.1. Transforming back into a temporal, non-modal basis completes the linear step.

In the non-modal basis, the nonlinear terms are uncoupled. Therefore, the nonlinear step can be made by independently advancing each equation in distance. The same is true for the free carrier evolution equations.

## A.2 FROG diagrams

Determining the structure of complicated signals is often problematic, particularly when they have multiple peaks in both the time and frequency domains. Given a particular spectral peak, for example, it may be difficult to identify the temporal feature to which it corresponds.

A useful tool for analysing such signals is the Frequency Resolved Optical Gating (FROG) technique, which turns a 1D signal into a 2D plot, with time shown on one axis and frequency on the other. It is generated by multiplying the signal with a pulse-like gating function, which selects a small time region. This is then Fourier transformed to provide a slice of the FROG diagram. The gating function is then shifted in time, and the process repeated, providing the next slice of the diagram, and so on.

A function $f(t)$ can be converted into a FROG (in time $t$ and frequency $\omega$) as

$$I_{\mathrm{FROG}}(t,\omega) = \left| \int_{t'=-\infty}^{\infty} g(t'-t)\, f(t')\, e^{-i\omega t'}\, dt' \right|^2 \tag{A.7}$$

where $g(t)$ is the gating function. It may seem that the pulse width of this gating function should be as narrow as possible, in order to maximise the temporal resolution. However, narrowing the pulse in the time domain amounts to widening it in the frequency domain, and so the frequency resolution would be correspondingly reduced. This problem is in fact a fundamental feature of wave mechanics, and if the frequency is associated with photon energy, becomes a manifestation of Heisenberg's uncertainty principal. A Gaussian shape was chosen, as this corresponds to the minimum of Heisenberg uncertainty [226], and thus to the best possible tradeoff between time resolution and frequency resolution. The pulse width was selected on a case by case basis, optimised so that as much detail as possible could be seen.

The above procedure is in fact the mathematical equivalent of an experimental technique in which a signal is passed through a nonlinear crystal along with a gating pulse. In the time interval where the signal and the gating pulse overlap, a variety of physical processes can be used to extract that region of the signal. (These include second harmonic generation, and the creation of new polarisation states.) The spectrum of the gated signal is then recorded, and by varying the delay of the input pulse, it is possible to extract temporal information. [227].

## A.3 Finite-difference Newton-Raphson method for bullet finding

Equation 5.2 in section 5.1 describes the evolution of a pulse with fixed shape in a coupled-waveguide system without damping, higher order dispersion or coupling dispersion:

$$\frac{d^2 F_n}{d\tau^2} = 2qF_n - 2|F_n|^2 F_n - 2c_0 (F_{n-1} + F_{n+1}) \tag{A.8}$$

Solutions which are self localised in both $\tau$ and $n$ must be found. The equation was discretised in time to yield

$$\begin{aligned}\frac{F_n(m-1)-2F_n(m)+F_n(m+1)}{(\Delta\tau)^2} &= 2qF_n(m)-2|F_n(m)|^2F_n(m) \\ &\quad -2c_0\left(F_{n-1}(m)+F_{n+1}(m)\right)\end{aligned} \tag{A.9}$$

where $F_n(m)$ is the field at the $m$th time point, and $\Delta\tau$ is the time difference between adjacent points. The left hand term is a finite step approximation to the second derivative, which becomes exact in the limit $\Delta\tau \to 0$.

Two-point boundary conditions were used: At one end, the implicit $n = 0$ points were set to zero. This can be problematic, as it can lead to solutions where the localisation is forced by the boundary conditions, rather than intrinsic to the equations of motion. Therefore, care was taken to ensure a sufficiently large time window, so that the solution could naturally decay to zero before reaching the boundary. (The time window was typically 100 times larger than the bullet FWHM.) At the other end, the implicit $n = N + 1$ values were forced to mirror the corresponding values at $n = N - 1$, thus causing the solution to represent one half of a wider time-symmetric solution centred about $n = N$.

For $M$ time points and $N$ wires, equation A.9 is in fact a set of $L = M \times N$ algebraic equations. The variables were represented using a single index $l = 1, 2, \cdots L$ as

$$x_l \equiv F_{1+(l-1 \bmod N)}\left(\lceil l/N \rceil\right) \tag{A.10}$$

and the components of equation A.9 were written as

$$f_k(x_1, x_2, \cdots x_L) = 0 \tag{A.11}$$

This can be solved numerically, by noting that if the solutions of equation A.11 are perturbed by $\Delta x_l$, then the values of $f_k$ can be approximated to first order as

$$f_k(x_1, x_2, \cdots x_L) = \sum_l \frac{\partial f_k}{\partial x_l}\Delta x_l \tag{A.12}$$

The Newton-Raphson method works by applying this perturbation formula in reverse, so that the values of $f_k$ and the Jacobian matrix $\partial f_k/\partial x_l$ at a trial value for $x_l$ can be used to estimate how far that value is from the true solution. Therefore, from a trial solution $x_l^{\text{old}}$, a better solution can be obtained as $x_l^{\text{new}} = x_l^{\text{old}} - \Delta x_l$. Applying multiple corrections allows the solution to be found to arbitrary accuracy.

Equation A.12 itself is an inhomogeneous matrix equation, and was solved using the banded matrix solver routines from Numerical Recipes in C [228]. (This exploits the fact that the Jacobian matrix is uniformly zero except for a $2N+1$ wide band along the main diagonal, thus allowing values outside the band to be ignored.)

The Newton-Raphson scheme was initialised with a trial value solution consisting of a sech like

pulse (with its maximum at $n = N$) in the central wire (or at the edge of the array when an edge bullet was required) and zero elsewhere. A half-window with a time range of $50T_0$ and $2^{14} = 16384$ time points was typically used. Correction were made until the root-mean-square value of $\Delta x_l$ was less than $10^{-9}$ the root-mean-square value of $x_l$, which usually took fewer than 10 iterations.

## A.4 Alternating directions method for integrating Raman equations

Equations 6.45 to 6.47 in section 6.1 describe the evolution of light through a Raman medium:

$$i\frac{\partial}{\partial\zeta}\begin{bmatrix} B_1 \\ B_2 \\ \cdots \\ B_N \end{bmatrix} + i\frac{\partial}{\partial\tau}\begin{bmatrix} v_1 B_1 \\ v_2 B_2 \\ \cdots \\ v_N B_N \end{bmatrix} = -\begin{bmatrix} \eta_1 & Q & & \\ Q^* & \eta_2 & \cdots & \\ & \cdots & \cdots & Q \\ & & Q^* & \eta_N \end{bmatrix}\begin{bmatrix} B_1 \\ B_2 \\ \cdots \\ B_N \end{bmatrix} \tag{A.13}$$

$$i\frac{\partial Q}{\partial\tau} = -\sigma\sum_{n=1}^{N-1} B_n B_{n+1}^* \tag{A.14}$$

$$\frac{\partial\sigma}{\partial\tau} = \sum_{n=1}^{N-1}\Im\left(B_n B_{n+1}^* Q^*\right) \tag{A.15}$$

Given a set of functions $B_n(\tau)$ at $\zeta = 0$, they must be integrated to give $B_n(\tau)$ at an arbitrary value of $\zeta$. This was done using The Method of Alternating Directions (implemented in C++), as shown in figure A.1. In step A, the values of $B_n$ were integrated in $\zeta$, whilst holding $\sigma$ and $Q$ constant. In step $B$, the values of $\sigma$ and $Q$ were integrated in time, using the newly advanced values of $B$.

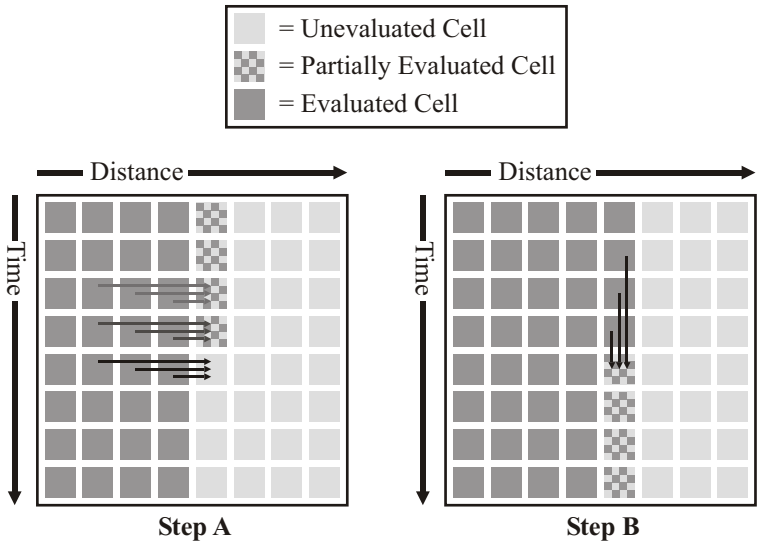


Figure A.1: Schematic of the numerical scheme used in the simulation.

In both directions, the integration was performed using a 3rd order Adams-Bashforth scheme. This is a refinement of the Euler method, in which the value at each time point is evaluated using the values from the previous three points. When integrating $dy/dx = f(x, y)$ the scheme gives the next value as

$$y_{k+1} = y_k + \left( \frac{23}{12} f(x_k, y_k) - \frac{4}{3} f(x_{k-1}, y_{k-1}) + \frac{5}{12} f(x_{k-2}, y_{k-2}) \right) \Delta x \tag{A.16}$$

where $k$ labels each point, and $\Delta x$ is the step size. For the first and second steps (when back-values weren't available), the Euler method and 2nd order Adams-Bashforth schemes were used.

### Monitoring of Numerical Accuracy

Unlike the split-step Fourier routine considered in section A.1, the integration scheme used here is inherently unstable. Numerical errors can be amplified, causing the solutions to wildly diverge. In order to verify that the simulation was running accurately, the conserved quantity $\sigma^2 + |Q|^2$ was regularly evaluated. The requirement that this quantity must always equal 1 was not explicitly coded into the integration scheme, and so numerical instabilities would generally cause it to drift away. The greatest deviation from unity was stored for each simulation, and was typically found to be between $10^{-5}$ and $10^{-4}$.

# Appendix B

# Overview of third-party experiments

## B.1 SOI fabrication

A chip containing SOI waveguides was fabricated at the University of Glasgow by Marco Gnan, Marc Sorel and Richard De la Rue. The chip started with a silicon wafer, on top of which lay a 1$\mu$m thick layer of silica (which was to become the base of the waveguide), and on top of that a 260nm thick layer of silicon (which was to become the waveguide itself).

An etching mask was applied, marking out the pattern of the waveguide. The chip was coated with a 100nm thick layer of hydrogen silsesquioxane (HSQ). An electron beam was scanned along the desired path of the waveguide, modifying the chemical structure of the HSQ beneath it. The chip was then treated with a developer, which dissolved away the unmodified HSQ, thus leaving a mask in the shape of the pattern drawn by the electron beam.

The chip was then etched using inductively coupled plasma reactive ion etching. A mixture of octafluorocyclobutane ($C_4F_8$) and sulphur hexafluoride ($SF_6$) was exposed to a high intensity radio-frequency electric field, superheating and ionising it. This highly reactive plasma was directed towards the chip, where it completely etched away the silicon, except for that beneath the HSQ mask. The silica revealed by the etching was slightly etched itself, causing the waveguide to sit upon a ledge a few tens of nanometres in height.

## B.2 Linear dispersion measurement

A schematic of the apparatus used by Wei Ding, William Wadsworth and Jonathan Knight to measure the linear dispersion of the SOI waveguide is given in figure B.1. The group refractive indices over a range of wavelengths were measured, thus providing the data used in section 3.3.1.

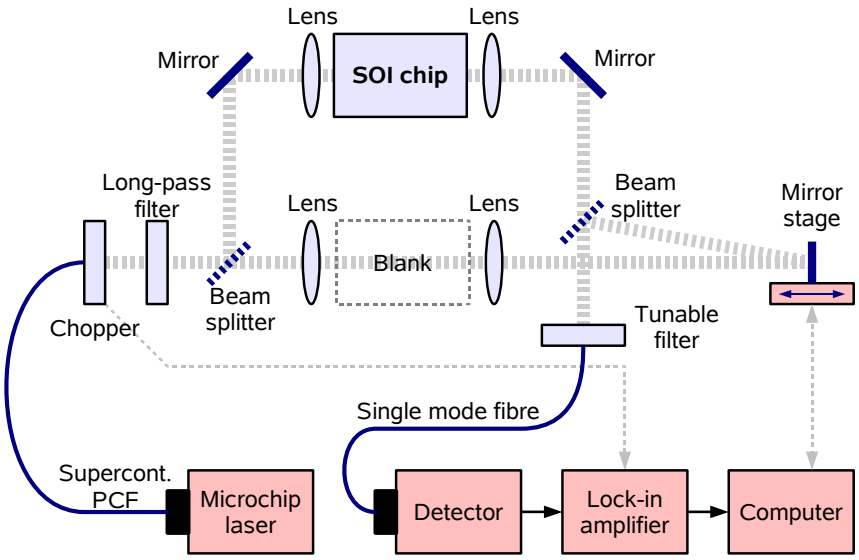


Figure B.1: Experimental setup used by Ding, Wadsworth and Knight to measure the linear dispersion of the waveguide.

The light was generated by a microchip laser, and passed through a piece of photonic crystal fibre to generate an optical supercontinuum. A long-pass filter was used to remove short-wavelength light beyond the range of interest. The light was then passed through a beam chopper, adding a known periodicity to the signal in order to aid later detection.

The light was directed towards a beam-splitter, to create two separate beams. The first beam was focused into the sample chip with a lens, and then coupled out with a further lens. The second beam passed through a dummy sample consisting of focussing lenses but no chip. It was then delayed by a variable path length, using a computer controlled movable mirror. The two beams were recombined using another beam splitter, thus creating a Mach-Zehnder interferometer. A tunable filter was used to select a particular wavelength, providing an interferogram from which dispersion information could be extracted.

A spatial sample of the interferogram was taken by coupling it into a single mode fibre that lead to a light detector. The detected signal was then passed through a lock-in amplifier, which used the timing of the beam chopper as its reference frequency, allowing the interferogram signal to be separated from any background noise. By scanning the position of the motorised mirror, the relative delay due to the group velocity in the waveguide could be determined by detecting the

presence of a packet of interference fringes at a particular point. Subtracting the value taken with the sample absent, gave the absolute group delay. From this, the group index could be calculated.

## B.3 Nonlinear propagation

A schematic of the apparatus used by Wei Ding, William Wadsworth and Jonathan Knight to measure the nonlinear propagation through the waveguide is given in figure B.2. The output spectra and total output powers for a variety of input powers were recorded, thus providing the data used in section 3.3.2. The coupling efficiency into the waveguide was also recorded.

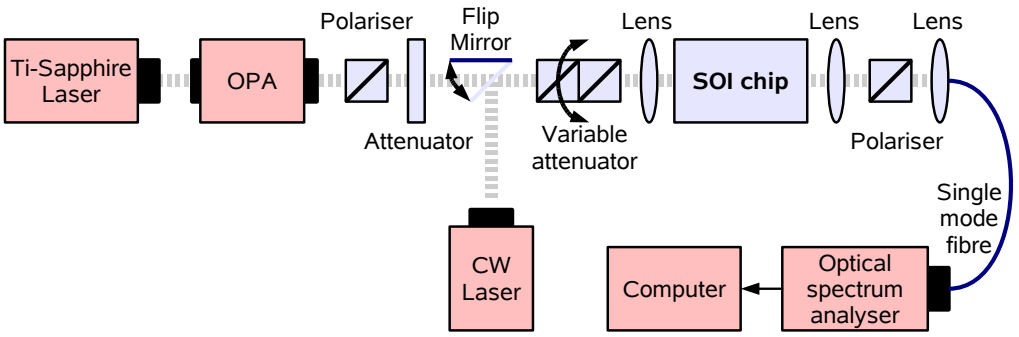


Figure B.2: Experimental setup used by Ding, Wadsworth and Knight to measure nonlinear waveguide propagation.

100fs pulses at a wavelength of 800nm were generated by a Titanium Sapphire mode-locked laser system. These were downconverted to a wavelength of 1500nm using a $\beta$-barium-borate optical parametric amplifier (OPA). The pulses were attenuated by varying amounts and focused into the SOI chip with a lens. The outgoing light was focused into a single-mode fibre with another lens, and then directed into an optical spectrum analyser.

To measure the coupling efficiency into the chip, the main laser source could be replaced (via a flip mirror system) with a second low-power continuous wave (CW) laser. This provided a linear propagation regime, and so by comparing the laser's power to the output power, the total attenuation due to coupling inefficiency and loss within the waveguide could be measured.

# Appendix C

# Analysis of coupled supermode perturbation equations

In sections 4.3 and 4.3.2, we have a pair of equations describing the perturbation from a coupled-pair soliton in the antisymmetric mode

$$\frac{\partial \epsilon_y}{\partial \zeta} + i(p_2 + c_2)\frac{\partial^2 \epsilon_y}{\partial \tau_y^2} + i\,(q - c_0)\,\epsilon_y + 2c_1\frac{\partial \epsilon_y}{\partial \tau_y} = 2iy^2\epsilon_y + iy^2\epsilon_y^* \tag{C.1}$$

$$\frac{\partial e_y}{\partial \zeta} + i(p_2 - c_2)\frac{\partial^2 e_y}{\partial \tau_y^2} + i\,(q + c_0)\,e_y = 2iy^2 e_y + iy^2 e_y^* \tag{C.2}$$

and a further pair describing perturbation from a soliton in the symmetric mode

$$\frac{\partial \epsilon_x}{\partial \zeta} + i(p_2 - c_2)\frac{\partial^2 \epsilon_x}{\partial \tau_x^2} + i\,(q + c_0)\,\epsilon_x - 2c_1\frac{\partial \epsilon_x}{\partial \tau_x} = 2ix^2\epsilon_x + ix^2\epsilon_x^* \tag{C.3}$$

$$\frac{\partial e_x}{\partial \zeta} + i(p_2 + c_2)\frac{\partial^2 e_x}{\partial \tau_x^2} + i\,(q - c_0)\,e_x = 2ix^2 e_x + ix^2 e_x^* \tag{C.4}$$

To these, we wish to find analytical solutions of the form $\epsilon_y = \tilde{\epsilon}_y(\tau_y)\,e^{\lambda_y \zeta}$, $e_y = \tilde{e}_y(\tau_y)\,e^{l_y \zeta}$, $\epsilon_x = \tilde{\epsilon}_x(\tau_x)\,e^{\lambda_x \zeta}$ and $e_x = \tilde{e}_x(\tau_x)\,e^{l_x \zeta}$. These can be formulated as eigenvalue problems, where the eigenfunctions $\tilde{\epsilon}_y(\tau_y)$, $\tilde{e}_y(\tau_y)$, $\tilde{\epsilon}_x(\tau_x)$ and $\tilde{e}_x(\tau_x)$ describe the perturbations, whilst their corresponding eigenvalues $\lambda_y$, $l_y$, $\lambda_x$ and $l_x$ determine whether the perturbations will grow and thus lead to instability.

## C.1 Reduction to eigenvalue problem form

**Antisymmetric mode**

We split $\epsilon_y$ and $e_y$ into their real and imaginary components as $\epsilon_y = \epsilon'_y + \epsilon''_y i$ and $e_y = e'_y + e''_y i$. Equations C.1 and C.2 can then be written as matrix equations of the form

$$\hat{\Lambda}_y \begin{bmatrix} \epsilon'_y \\ \epsilon''_y \end{bmatrix} = \frac{\partial}{\partial \zeta} \begin{bmatrix} \epsilon'_y \\ \epsilon''_y \end{bmatrix} \tag{C.5}$$

$$\hat{L}_y \begin{bmatrix} e'_y \\ e''_y \end{bmatrix} = \frac{\partial}{\partial \zeta} \begin{bmatrix} e'_y \\ e''_y \end{bmatrix} \tag{C.6}$$

where the matrix operators $\hat{\Lambda}_y$ and $\hat{L}_y$ are defined by

$$\hat{\Lambda}_y = \begin{bmatrix} -2c_1 \frac{\partial}{\partial \tau_y} & (p_2 + c_2) \frac{\partial^2}{\partial \tau_y^2} + q - c_0 - y^2 \\ -(p_2 + c_2) \frac{\partial^2}{\partial \tau_y^2} - q + c_0 + 3y^2 & -2c_1 \frac{\partial}{\partial \tau_y} \end{bmatrix} \tag{C.7}$$

$$\hat{L}_y = \begin{bmatrix} 0 & (p_2 - c_2) \frac{\partial^2}{\partial \tau_y^2} + q + c_0 - y^2 \\ -(p_2 - c_2) \frac{\partial^2}{\partial \tau_y^2} - q - c_0 + 3y^2 & 0 \end{bmatrix} \tag{C.8}$$

Our trial functions are of the form

$$\epsilon_y = \tilde{\epsilon}_y(\tau_y) e^{\lambda_y \zeta} \tag{C.9}$$

$$e_y = \tilde{e}_y(\tau_y) e^{l_y \zeta} \tag{C.10}$$

and we split the time dependent parts $\tilde{\epsilon}_y$ and $\tilde{e}_y$ up as

$$\tilde{\epsilon}_y(\tau_y) = \Re[\alpha_y(\tau_y)] + \Re[\beta_y(\tau_y)] i \tag{C.11}$$

$$\tilde{e}_y(\tau_y) = \Re[a_y(\tau_y)] + \Re[b_y(\tau_y)] i \tag{C.12}$$

Therefore, the vectors representing $e_y$ and $\epsilon_y$ can be rewritten as

$$\begin{bmatrix} \epsilon'_y(\zeta, \tau_y) \\ \epsilon''_y(\zeta, \tau_y) \end{bmatrix} = \frac{1}{2} \left( \begin{bmatrix} \alpha_y(\tau_y) \\ \beta_y(\tau_y) \end{bmatrix} e^{\lambda_y \zeta} + \begin{bmatrix} \alpha^*_y(\tau_y) \\ \beta^*_y(\tau_y) \end{bmatrix} e^{\lambda^*_y \zeta} \right) \tag{C.13}$$

$$\begin{bmatrix} e'_y(\zeta, \tau_y) \\ e''_y(\zeta, \tau_y) \end{bmatrix} = \frac{1}{2} \left( \begin{bmatrix} a_y(\tau_y) \\ b_y(\tau_y) \end{bmatrix} e^{l_y \zeta} + \begin{bmatrix} a^*_y(\tau_y) \\ b^*_y(\tau_y) \end{bmatrix} e^{l^*_y \zeta} \right) \tag{C.14}$$

Substituting these into equations C.19 and C.20 yields

$$\hat{\Lambda}_y \begin{bmatrix} \alpha_y \\ \beta_y \end{bmatrix} + \hat{\Lambda}_y \begin{bmatrix} \alpha^*_y \\ \beta^*_y \end{bmatrix} = \lambda_y \begin{bmatrix} \alpha_y \\ \beta_y \end{bmatrix} + \lambda^*_y \begin{bmatrix} \alpha^*_y \\ \beta^*_y \end{bmatrix} \tag{C.15}$$

$$\hat{L}_y \begin{bmatrix} a_y \\ b_y \end{bmatrix} + \hat{L}_y \begin{bmatrix} a^*_y \\ b^*_y \end{bmatrix} = l_y \begin{bmatrix} a_y \\ b_y \end{bmatrix} + l^*_y \begin{bmatrix} a^*_y \\ b^*_y \end{bmatrix} \tag{C.16}$$

which can be reduced to eigenvalue problems of the form

$$\hat{\Lambda}_y \begin{bmatrix} \alpha_y \\ \beta_y \end{bmatrix} = \lambda_y \begin{bmatrix} \alpha_y \\ \beta_y \end{bmatrix} \tag{C.17}$$

$$\hat{L}_y \begin{bmatrix} a_y \\ b_y \end{bmatrix} = l_y \begin{bmatrix} a_y \\ b_y \end{bmatrix} \tag{C.18}$$

as any solutions to equations C.17 and C.18 will automatically satisfy equations C.15 and C.16.

**Symmetric mode**

We split $\epsilon_x$ and $e_x$ into their real and imaginary components as $\epsilon_x = \epsilon'_x + \epsilon''_x i$ and $e_x = e'_x + e''_x i$. Equations C.1 and C.2 can then be written as matrix equations of the form

$$\hat{\Lambda}_x \begin{bmatrix} \epsilon'_x \\ \epsilon''_x \end{bmatrix} = \frac{\partial}{\partial \zeta} \begin{bmatrix} \epsilon'_x \\ \epsilon''_x \end{bmatrix} \tag{C.19}$$

$$\hat{L}_x \begin{bmatrix} e'_x \\ e''_x \end{bmatrix} = \frac{\partial}{\partial \zeta} \begin{bmatrix} e'_x \\ e''_x \end{bmatrix} \tag{C.20}$$

where the matrix operators $\hat{\Lambda}_x$ and $\hat{L}_x$ are defined by

$$\hat{\Lambda}_x = \begin{bmatrix} 2c_1 \frac{\partial}{\partial \tau_x} & (p_2 - c_2) \frac{\partial^2}{\partial \tau_x^2} + q + c_0 - x^2 \\ -(p_2 - c_2) \frac{\partial^2}{\partial \tau_x^2} - q - c_0 + 3x^2 & 2c_1 \frac{\partial}{\partial \tau_x} \end{bmatrix} \tag{C.21}$$

$$\hat{L}_x = \begin{bmatrix} 0 & (p_2 + c_2) \frac{\partial^2}{\partial \tau_x^2} + q - c_0 - x^2 \\ -(p_2 + c_2) \frac{\partial^2}{\partial \tau_x^2} - q + c_0 + 3x^2 & 0 \end{bmatrix} \tag{C.22}$$

Our trial functions are of the form

$$\epsilon_x = \tilde{\epsilon}_x(\tau_x) e^{\lambda_x \zeta} \tag{C.23}$$

$$e_x = \tilde{e}_x(\tau_x) e^{l_x \zeta} \tag{C.24}$$

and we split the time dependent parts $\tilde{\epsilon}_x$ and $\tilde{e}_x$ up as

$$\tilde{\epsilon}_x(\tau_x) = \Re[\alpha_x(\tau_x)] + \Re[\beta_x(\tau_x)] i \tag{C.25}$$

$$\tilde{e}_x(\tau_x) = \Re[a_x(\tau_x)] + \Re[b_x(\tau_x)] i \tag{C.26}$$

Therefore, the vectors representing $\epsilon_x$ and $e_x$ can be rewritten as

$$\begin{bmatrix} \epsilon'_x(\zeta, \tau_x) \\ \epsilon''_x(\zeta, \tau_x) \end{bmatrix} = \frac{1}{2} \left( \begin{bmatrix} \alpha_x(\tau_x) \\ \beta_x(\tau_x) \end{bmatrix} e^{\lambda_x \zeta} + \begin{bmatrix} \alpha_x^*(\tau_x) \\ \beta_x^*(\tau_x) \end{bmatrix} e^{\lambda_x^* \zeta} \right) \tag{C.27}$$

$$\begin{bmatrix} e'_x(\zeta, \tau_x) \\ e''_x(\zeta, \tau_x) \end{bmatrix} = \frac{1}{2} \left( \begin{bmatrix} a_x(\tau_x) \\ b_x(\tau_x) \end{bmatrix} e^{l_x \zeta} + \begin{bmatrix} a_x^*(\tau_x) \\ b_x^*(\tau_x) \end{bmatrix} e^{l_x^* \zeta} \right) \tag{C.28}$$

Substituting these into equations C.19 and C.20 yields

$$\hat{\Lambda}_x \begin{bmatrix} \alpha_x \\ \beta_x \end{bmatrix} + \hat{\Lambda}_x \begin{bmatrix} \alpha_x^* \\ \beta_x^* \end{bmatrix} = \lambda_x \begin{bmatrix} \alpha_x \\ \beta_x \end{bmatrix} + \lambda_x^* \begin{bmatrix} \alpha_x^* \\ \beta_x^* \end{bmatrix} \tag{C.29}$$

$$\hat{L}_x \begin{bmatrix} a_x \\ b_x \end{bmatrix} + \hat{L}_x \begin{bmatrix} a_x^* \\ b_x^* \end{bmatrix} = l_x \begin{bmatrix} a_x \\ b_x \end{bmatrix} + l_x^* \begin{bmatrix} a_x^* \\ b_x^* \end{bmatrix} \tag{C.30}$$

which can be reduced to eigenvalue problems of the form

$$\hat{\Lambda}_x \begin{bmatrix} \alpha_x \\ \beta_x \end{bmatrix} = \lambda_x \begin{bmatrix} \alpha_x \\ \beta_x \end{bmatrix} \tag{C.31}$$

$$\hat{L}_x \begin{bmatrix} a_x \\ b_x \end{bmatrix} = l_x \begin{bmatrix} a_x \\ b_x \end{bmatrix} \tag{C.32}$$

as any solutions to equations C.31 and C.32 will automatically satisfy equations C.29 and C.30.

## C.2 Continuum spectrum of delocalised modes and its band-gap

If an eigenfunction is delocalised, it will (by definition) not tend towards zero at the extremities of time. By working at these extremities (at which the magnitude of the soliton tends towards zero) we can solve the equations of motion exactly, revealing an infinite set of sinusoidal eigenfunctions corresponding to a continuum of eigenvalues. In the locality of the soliton, the eigenfunctions will be pertubed, but the eigenvalues (which are time independent) will remain the same.

This continuum spectrum of delocalised-mode eigenvalues lies along the imaginary axis. This can be broken by a band-gap in which no delocalised-mode eigenvalues exist. The extent of this band-gap, and the conditions for its existence are derived below.

#### Antisymmetric mode

In the tails of the soliton, where $y(\tau_y) \to 0$, we choose trial functions of the form

$$\begin{bmatrix} \alpha_y \\ \beta_y \end{bmatrix} = \begin{bmatrix} \tilde{\alpha}_y e^{i\gamma_y \tau_y} \\ \tilde{\beta}_y e^{i\gamma_y \tau_y} \end{bmatrix} \tag{C.33}$$

$$\begin{bmatrix} a_y \\ b_y \end{bmatrix} = \begin{bmatrix} \tilde{a}_y e^{ig_y \tau_y} \\ \tilde{b}_y e^{ig_y \tau_y} \end{bmatrix} \tag{C.34}$$

where the constants $\tilde{a}_y$, $\tilde{b}_y$, $\tilde{\alpha}_y$, $\tilde{\beta}_y$ define the complex arguments of $\epsilon_y$ and $e_y$. The wavenumbers $\gamma_y$ and $g_y$ must be real for a continuous wave solution. Substituting equations C.33 and C.34

into equations C.17 and C.18 shows the solutions to be valid, given the respective conditions

$$i\lambda_y = 2c_1\gamma_y \pm \left(\left(p_2+c_2\right)\gamma_y^2 + c_0 - q\right) \tag{C.35}$$

$$il_y = \pm\left(\left(p_2-c_2\right)g_y^2 - c_0 - q\right) \tag{C.36}$$

If the condition that $\gamma_y$ or $g_y$ must be real is violated, a band-gap will occur. We can search for band-gaps by solving equations C.35 and C.36 for $\gamma_y$ and $g_y$ respectively to give

$$\gamma_y = \frac{\mp 2c_1 \pm' \sqrt{c_1^2 + \left(p_2+c_2\right)\left(q - c_0 \pm i\lambda_y\right)}}{p_2+c_2} \tag{C.37}$$

$$g_y = \pm' \sqrt{\frac{q + c_0 \pm il_y}{p_2 - c_2}} \tag{C.38}$$

where the operators $\pm$ and $\pm'$ denote that the signs may be chosen independently. Non-real solutions (and hence a band-gap) will exist when the arguments in the square-root functions of equations C.37 and C.38 become negative. Therefore, about the point $\lambda_y = 0$, a band-gap will exist when $c_1^2 + \left(p_2+c_2\right)\left(q-c_0\right) < 0$. Similarly, about the point $l_y = 0$, a band-gap will exist when $\left(q+c_0\right)/\left(p_2-c_2\right) < 0$.

The edges of the bandgap occur when the arguments of the square-root functions become zero. Solving the resulting equations gives the extent of the band gaps as

$$-\left|q - c_0 + \frac{c_1^2}{p_2+c_2}\right| < \Im\left[\lambda_y\right] < \left|q - c_0 + \frac{c_1^2}{p_2+c_2}\right| \tag{C.39}$$

$$-\left|q+c_0\right| < \Im\left[l_y\right] < \left|q+c_0\right| \tag{C.40}$$

**Symmetric mode**

In the tails of the soliton, where $x\left(\tau_x\right) \to 0$, we choose trial functions of the form

$$\begin{bmatrix} \alpha_x \\ \beta_x \end{bmatrix} = \begin{bmatrix} \tilde{\alpha}_x e^{i\gamma_x\tau_x} \\ \tilde{\beta}_x e^{i\gamma_x\tau_x} \end{bmatrix} \tag{C.41}$$

$$\begin{bmatrix} a_x \\ b_x \end{bmatrix} = \begin{bmatrix} \tilde{a}_x e^{ig_x\tau_x} \\ \tilde{b}_x e^{ig_x\tau_x} \end{bmatrix} \tag{C.42}$$

where the constants $\tilde{\alpha}_x$, $\tilde{\beta}_x$, $\tilde{a}_x$ and $\tilde{b}_x$ define the complex arguments of $\epsilon_x$ and $e_x$. The wavenumbers $g_y$ and $\gamma_y$ must be real for a continuous wave solution. Substituting equations C.41 and C.42 into equations C.31 and C.32 shows the solutions to be valid, given the respective conditions

$$i\lambda_x = -2c_1\gamma_x \pm \left(\left(p_2-c_2\right)\gamma_x^2 - c_0 - q\right) \tag{C.43}$$

$$il_x = \pm\left(\left(p_2+c_2\right)g_x^2 + c_0 - q\right) \tag{C.44}$$

If the condition that $\gamma_x$ or $g_x$ must be real is violated, a band-gap will occur. We can search for band-gaps by solving equations C.43 and C.44 for $\gamma_x$ and $g_x$ respectively to give

$$\gamma_x = \frac{\pm 2c_1 \pm' \sqrt{c_1^2 + (p_2 - c_2)(q + c_0 \pm i\lambda_x)}}{p_2 - c_2} \tag{C.45}$$

$$g_x = \pm' \sqrt{\frac{q - c_0 \pm i l_y}{p_2 + c_2}} \tag{C.46}$$

where the operators $\pm$ and $\pm'$ denote that the signs may be chosen independently. Non-real solutions (and hence a band-gap) will exist when the arguments in the square-root functions of equations C.45 and C.46 become negative. Therefore, about the point $\lambda_x = 0$, a band-gap will exist when $c_1^2 + (p_2 - c_2)(q + c_0) < 0$. Similarly, about the point $l_x = 0$, a band-gap will exist when $(q - c_0)/(p_2 + c_2) < 0$.

The edges of the bandgap occur when the arguments of the square-root functions become zero. Solving the resulting equations gives the extent of the band gaps as

$$-\left|q + c_0 + \frac{c_1^2}{p_2 - c_2}\right| < \Im[\lambda_x] < \left|q + c_0 + \frac{c_1^2}{p_2 - c_2}\right| \tag{C.47}$$

$$-|q - c_0| < \Im[l_x] < |q - c_0| \tag{C.48}$$

## C.3 General numerical solutions

We can find approximate general solutions to equations C.17, C.18, C.31 and C.32 by discretising $\epsilon_y(\tau_y)$, $e_y(\tau_y)$, $\epsilon_x(\tau_x)$ and $e_x(\tau_x)$ into $N$-membered column vectors $\hat{\epsilon}_y$, $\hat{e}_y$, $\hat{\epsilon}_x$ and $\hat{e}_x$.

In such a basis, differential operators become $N \times N$ matrices of the form

$$\frac{\partial}{\partial\tau} \longrightarrow \hat{I}' \equiv \frac{1}{2\Delta\tau}\begin{bmatrix} 0 & 1 & & & & \\ -1 & 0 & 1 & & & \\ & -1 & 0 & \ddots & & \\ & & \ddots & \ddots & 1 & \\ & & & -1 & 0 & \end{bmatrix} \tag{C.49}$$

$$\frac{\partial^2}{\partial\tau^2} \longrightarrow \hat{I}'' \equiv \frac{1}{(\Delta\tau)^2}\begin{bmatrix} -2 & 1 & & & & \\ 1 & -2 & 1 & & & \\ & 1 & -2 & \ddots & & \\ & & \ddots & \ddots & 1 & \\ & & & 1 & -2 & \end{bmatrix} \tag{C.50}$$

where $\Delta\tau$ is the time step. Making the transformation gives ordinary (i.e. not containing

differential operators) matrices of the form

$$\hat{\Lambda}_y \longrightarrow \begin{bmatrix} -2c_1\hat{I}' & (p_2+c_2)\,\hat{I}'' + q\hat{I} - c_0\hat{I} - y^2\hat{I} \\ -(p_2+c_2)\,\hat{I}'' - q\hat{I} + c_0\hat{I} + 3y^2\hat{I} & -2c_1\hat{I}' \end{bmatrix} \quad \text{(C.51)}$$

$$\hat{L}_y \longrightarrow \begin{bmatrix} 0 & (p_2-c_2)\,\hat{I}'' + q\hat{I} + c_0\hat{I} - y^2\hat{I} \\ -(p_2-c_2)\,\hat{I}'' - q\hat{I} - c_0\hat{I} + 3y^2\hat{I} & 0 \end{bmatrix} \quad \text{(C.52)}$$

$$\hat{\Lambda}_x \longrightarrow \begin{bmatrix} 2c_1\hat{I}' & (p_2-c_2)\,\hat{I}'' + q\hat{I} + c_0\hat{I} - x^2\hat{I} \\ -(p_2-c_2)\,\hat{I}'' - q\hat{I} - c_0\hat{I} + 3x^2\hat{I} & 2c_1\hat{I}' \end{bmatrix} \quad \text{(C.53)}$$

$$\hat{L}_x \longrightarrow \begin{bmatrix} 0 & (p_2+c_2)\,\hat{I}'' + q\hat{I} - c_0\hat{I} - x^2\hat{I} \\ -(p_2+c_2)\,\hat{I}'' - q\hat{I} + c_0\hat{I} + 3x^2\hat{I} & 0 \end{bmatrix} \quad \text{(C.54)}$$

where $\hat{I}$ is the $N \times N$ identity matrix. Finding the eigenvalues ($\lambda_y$, $l_y$, $\lambda_x$ and $l_x$ respectively) is a straightforward numerical task, for which the "eigs" function of MATLAB was used. Any eigenvalues lying outside the analytically predicted band structures were recorded, thus providing the results given in sections 4.3.1 and 4.3.2.

# Appendix D

# Bullets with two principal channels

In the analysis of central bullets in section 5.1, we have in fact been considering a special case, in which there is a single principal channel which is brighter than all the others. A plane of symmetry exists along this channel, with the channels on one side having the same field profile as the corresponding channel on the other side. However, it is also possible to have this plane of symmetry in the gap between channels. Therefore, there will be two principal channels, having equal brightness.

The type with a single principal channel is known as an *odd* bullet, and the type with two principal channels is known as an *even* bullet. By analogy with a similar phenomenon in condensed matter physics, the two types can also be refered to as *site centred* and *bond centred* [17, 28].

Even bullet solutions are readily found by using the same Newton-Raphson method described in appendix A.3, but by initialising the calculation with pulses in two neighboring channels. A typical example is given in figure D.1. The energy profiles of even and odd bullets are given in figure D.2. In both cases, 14 channels are used, providing a quasi-infinite regime.

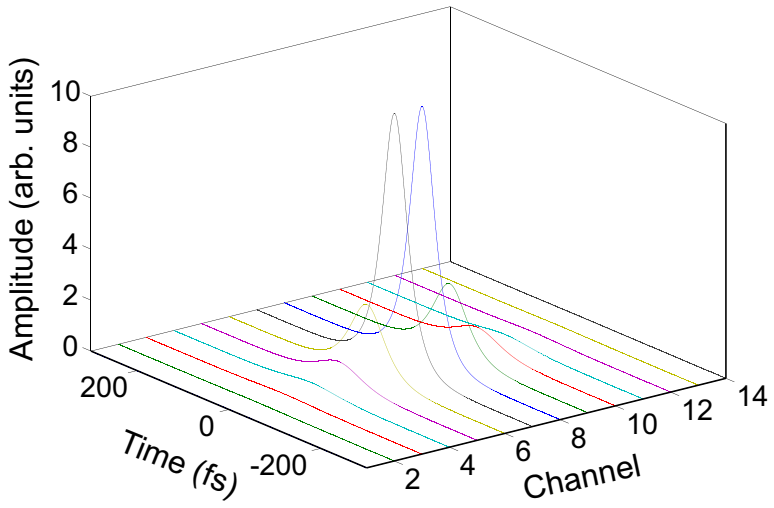


Figure D.1: A bullet solution in a 14 channel array, calculated with $q = 5$ and $c_0 = 1.546$. The bullet is of the "even" (or "bond centred") type, with two central channels in the middle.

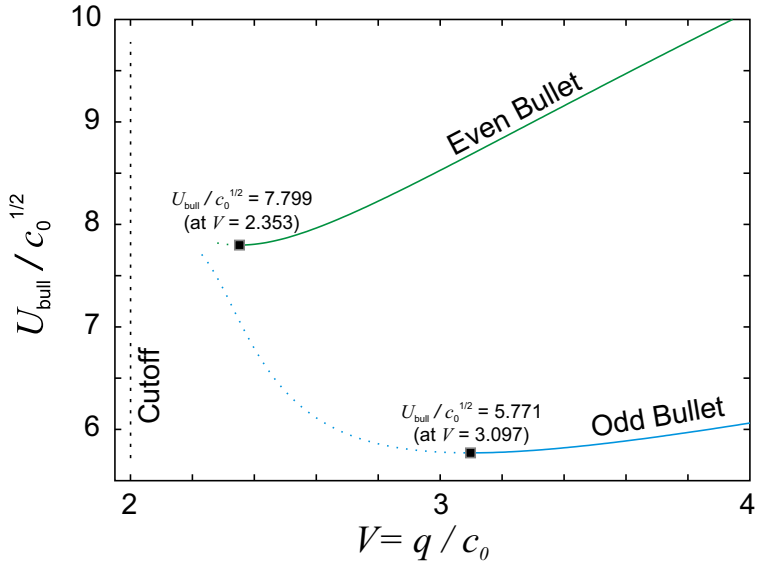


Figure D.2: Total energy content of odd and even bullets (for a quasi-infinite number of channels), as a function of spatial wavenumber $q$ divided by coupling coefficient $c_0$. Plots are given for both odd and even bullet configurations. The unstable regions are denoted by dotted lines, whilst the total cutoff is denoted by the vertical dashed line.

The higher energy of even bullets makes them unstable (as a lower energy state exists). This makes them a much poorer candidate for the experimental observation of optical bullets. Therefore, having noted their existance, we will not consider this type of bullet any further.

# References


[1] P. A. Franken, A. E. Hill, C. W. Peters, and G. Weinreich. Generation of optical harmonics. *Physical Review Letters*, 7:118–119, 1961.

[2] K. Inoue. Four-wave mixing in an optical fiber in the zero-dispersion wavelength region. *Journal of Lightwave Technology*, 10:1553–1561, 1992.

[3] R. E. Slusher, L. W. Hollberg, B. Yurke, J. C. Mertz, and J. F. Valley. Observation of squeezed states generated by four-wave mixing in an optical cavity. *Physical Review Letters*, 55:2409–2412, 1985.

[4] Jinendra K. Ranka, Robert S. Windeler, and Andrew J. Stentz. Visible continuum generation in air-silica microstructure optical fibers with anomalous dispersion at 800 nm. *Optics Letters*, 25:25–27, 2000.

[5] John M. Dudley, Goery Genty, and Stephane Coen. Supercontinuum generation in photonic crystal fiber. *Review of Modern Physics*, 78:1135–1184, 2006.

[6] M. Fleischhauer, A. Imamoglu, and J. P. Marangos. Electromagnetically induced transparency: Optics in coherent media. *Reviews of Modern Physics*, 77:633–673, 2005.

[7] Gisela Eckhardt, R. W. Hellwarth, F. J. McClung, S. E. Schwarz, D. Weiner, and E. J. Woodbury. Stimulated raman scattering from organic liquids. *Physical Review Letters*, 9:455–457, 1962.

[8] Govind P. Agrawal. *Nonlinear Fiber Optics*. Academic Press, 2001.

[9] R. W. Boyd and D. J. Gauthier. Slow and fast light. *Progress in Optics*, 43:497–530, 2002.

[10] J. S. Russell. Report on waves, 1844. Report of the fourteenth meeting of the British Association for the Advancement of Science.

[11] P. De Gasperis, R. Marcelli, and G. Miccoli. Magnetostatic soliton propagation at microwave frequency in magnetic garnet films. *Physics Review Letters*, 59:481–484, 1987.

[12] H. Y. Hao and H. J. Maris. Experiments with acoustic solitons in crystalline solids. *Physical Review B*, 64:064302, 2001.

[13] L. F. Mollenauer and R. H. Stolen. Experimental observation of picosecond pulse narrowing and solitons in optical fibers. *Physical Review Letters*, 45:1095–1098, 1980.

[14] E. Pelinovsky, T. Talipova, A. Kurkin, and C. Kharif. Nonlinear mechanism of tsunami wave generation by atmospheric disturbances. *Natural Hazards and Earth System Sciences*, 1:243–250, 2001.

[15] Thomas Heimburg and Andrew D. Jackson. On soliton propagation in biomembranes and nerves. In *Proceedings of the National Academy of Sciences*, 2005.

[16] Qi Wang and Ikuo Awai. Frequency characteristics of the magnetic spatial solitons on the surface of an antiferromagnet. *Journal of Applied Physics*, 83:382, 1998.

[17] Dumitru Mihalache, Dumitru Mazilu, Falk Lederer, and Yuri S. Kivshar. Stable discrete surface light bullets. *Optics Express*, 15:589–595, 2007.

[18] A. B. Blagoeva, S. G. Dinev, A. A. Dreischuh, and A. Naidenov. Light bullets formation in a bulk media. *IEEE Journal of Quantum Electronics*, 27:2060–2065, 1991.

[19] Isaac Chuang, Ruth Durrer, Neil Turok, and Bernard Yurke. Cosmology in the laboratory: Defect dynamics in liquid crystals. *Science*, 251:1336–1342, 1991.

[20] R. M. Kiehn. Falaco solitons - cosmic strings in a swimming pool. arXiv:gr-qc/0101098v1, 2004.

[21] C. Buerle, Yu. M. Bunkov, S. N. Fisher, H. Godfrin, and G. R. Pickett. Laboratory simulation of cosmic string formation in the early universe using superfluid 3he. *Nature*, 382:332–334, 1996.

[22] T. W. B. Kibble. Topology of cosmic domains and strings. *Journal of Physics A*, 9:1387–1398, 1976.

[23] Y. S. Kivshar and G. P. Agrawal. *Optical Solitons: From Fibers to Photonic Crystals*. Academic Press, 2003.

[24] Nicholas S Manton. Solitons as elementary particles: a paradigm scrutinized. *Nonlinearity*, 21:T221–T232, 2008.

[25] R. Y. Chiao, E. Garmire, and C. H. Townes. Self-trapping of optical beams. *Phyical Review Letters*, 13:479–482, 1964.

[26] D. N. Christodoulides and R. I. Joseph. Discrete self-focusing in nonlinear arrays of coupled waveguides. *Optics Letters*, 12:794–796, 1988.

[27] H. S. Eisenberg, Y. Silberberg, R. Morandotti, A. R. Boyd, and J. S. Aitchison. Discrete spatial optical solitons in waveguide arrays. *Physical Review Letters*, 81:3383–3386, 1998.

[28] Dumitru Mihalache, Dumitru Mazilu, Falk Lederer, and Yuri S. Kivshar. Spatiotemporal surface solitons in two-dimensional photonic lattices. *Optics Letters*, 32:3173–3175, 2007.

[29] Boris A. Malomed, Dumitru Mihalache, Frank Wise, and Lluis Torner. Spatiotemporal optical solitons. *Journal of Optics B*, 7 7:R53–R72, 2005.

[30] D. Mihalache, D. Mazilu, F. Lederer, and Y. S. Kivshar. Interface discrete light bullets in waveguide arrays. *Optics Letters*, 32(15):2091–2093, August 2007.

[31] P. Di Trapani, G. Valiulis, A. Piskarskas, O. Jedrkiewicz, J. Trull, C. Conti, and S. Trillo. Spontaneously generated x-shaped light bullets. *Physical Review Letters*, 91(9):093904, August 2003.

[32] D. Cheskis, S. Bar-Ad, R. Morandotti, J. S. Aitchison, H. S. Eisenberg, Y. Silberberg, and D. Ross. Strong spatiotemporal localization in a silica nonlinear waveguide array. *Physical Review Letters*, 91(22):223901, November 2003.

[33] I. Babushkin, A. Husakou, J. Herrmann, and Y. S. Kivshar. Frequency-selective self-trapping and supercontinuum generation in arrays of coupled nonlinear waveguides. *Optics Express*, 15(19):11978–11983, September 2007.

[34] X. Liu, K. Beckwitt, and F. Wise. Transverse instability of optical spatiotemporal solitons in quadratic media. *Physical Review Letters*, 85(9):1871–1874, August 2000.

[35] Per Dalgaard Rasmussen, Andrey A. Sukhorukov, Dragomir N. Neshev, Wieslaw Krolikowski, Ole Bang, Jesper Lgsgaard, and Yuri S. Kivshar. Spatiotemporal control of light by bloch-mode dispersion in multi-core bers. *Optics Express*, 16:5878–5891, 2008.

[36] Alexander V. Buryak and Yuri S. Kivshar. Spatial optical solitons governed by quadratic nonlinearity. *Optics Letters*, 19:1612–1614, 1994.

[37] P. Di Trapani, D. Caironi, G. Valiulis, A. Dubietis, R. Danielius, and A. Piskarskas. Observation of temporal solitons in second-harmonic generation with tilted pulses. *Physical Review Letters*, 81(3):570–573, July 1998.

[38] K. Druhl, R. G. Wenzel, and J. L. Carlsten. Observation of solitons in stimulated Raman scattering. *Physical Review Letters*, 51:1171–1174, 1983.

[39] Frdric Druon, Nicolas Sanner, Galle Lucas-Leclin, Patrick Georges, Kim P. Hansen, and Anders Petersson. Self-compression and Raman soliton generation in a photonic crystal fiber of 100-fs pulses produced by a diode-pumped Yb-doped oscillator. *Applied Optics*, 42:6768–6770, 2003.

[40] Y. R. Shen and N. Bloembergen. Theory of stimulated Brillouin and Raman scattering. *Physical Review*, 137:A1787–A1805, 1965.

[41] Eric Picholle, Carlos Montes, Claude Leycuras, Olivier Legrand, and Jean Botineau. Observation of dissipative superluminous solitons in a brillouin fiber ring laser. *Physical Review Letters*, 66:1454–1457, 1991.

[42] Albert Ferrando, Humberto Michinel, Marcos Seco, and Daniele Tommasini. Nonlinear phase shift from photon-photon scattering in vacuum. *Physical Review Letters*, 99:150404, 2007.

[43] Marin Soljai and Mordechai Segev. Self-trapping of electromagnetic beams in vacuum supported by QED nonlinear effects. *Physical Review A*, 64:043817, 2000.

[44] P. G. Drazin and R. S. Johnson. *Solitons: An Introduction*. Cambridge University Press, 1989.

[45] G. I. Stegeman and M. Segev. Optical spatial solitons and their interactions: Universality and diversity. *Science*, 286:1518–1523, 1999.

[46] David F. Edwards. *Handbook of Optical Constants of Solids*, chapter Silicon (Si), page 547. Academic Press, 1985.

[47] Amy C. Turner, Christina Manolatou, Bradley S. Schmidt, Michal Lipson, Mark A. Foster, Jay E. Sharping, and Alexander L. Gaeta. Tailored anomalous group-velocity dispersion in silicon channel waveguides. *Optics Express*, 14:4357–4362, 2006.

[48] M. A. Foster, A. C. Turner, M. Lipson, and A. L. Gaeta. Nonlinear optics in photonic nanowires. *Optics Express*, 16(2):1300–1320, January 2008.

[49] Eric Dulkeith, Fengnian Xia, Laurent Schares, William M. J. Green, and Yurii A. Vlasov. Group index and group velocity dispersion in silicon-on-insulator photonic wires. *Optics Express*, 14:3853–3863, 2006.

[50] Paul Mllner and Rainer Hainberger. Structural optimization of silicon-on-insulator slot waveguides. *IEEE Photonics Technology Letters*, 24:2557–2559, 2006.

[51] Pablo Sanchis, Javier Blasco, Alejandro Martnez, and Javier Mart. Design of silicon-based slot waveguide congurations for optimum nonlinear performance. *Journal of Lightwave Technology*, 25:1298–1305, 2007.

[52] Rong Sun, Po Dong, Ning ning Feng, Ching yin Hong, Jurgen Michel, Michal Lipson, and Lionel Kimerling. Horizontal single and multiple slot waveguides: optical transmission at $\lambda = 1550$ nm. *Optics Express*, 15:17967–17972, 2007.

[53] F. Riboli, P. Bettotti, and L. Pavesi. Band gap characterization and slow light effects in one dimensional photonic crystals based on silicon slot-waveguides. *Optics Express*, 15:11769–11775, 2007.

[54] W. Ding, C. Benton, A. V. Gorbach, W. J. Wadsworth, J. C. Knight, D. V. Skryabin, M. Gnan, M. Sorrel, and R. M. De-La-Rue. Solitons and spectral broadening in long silicon-on- insulator photonic wires. *Optics Express*, 16:3310–3319, 2008.

[55] Q. Lin, J. Zhang, G. Piredda, R. W. Boyd, P. M. Fauchet, and G. P. Agrawal. Dispersion of silicon nonlinearities in the near infrared region. *Applied Physics Letters*, 91:021111, 2007.

[56] Alan D. Bristow, Nir Rotenberg, and Henry M. van Driel. Two-photon absorption and kerr coefcients of silicon for 850 2200 nm. *Applied Physics Letters*, 90:191104, 2007.

[57] I-Wei Hsieh, Xiaogang Chen, Jerry I. Dadap, Nicolae C. Panoiu, and Richard M. Osgood. Ultrafast-pulse self-phase modulation and third-order dispersion in Si photonic wire-waveguides. *Optics Express*, 14:12380–12387, 2006.

[58] C. Koos, L. Jacome, C. Poulton, J. Leuthold, and W. Freude. Nonlinear silicon-on-insulator waveguides for all-optical signal processing. *Optics Express*, 15:5976–5990, 1997.

[59] Pieter Dumon, Gino Priem, Luis Romeu Nunes, Wim Bogaerts, Dries Van-Thourhout, Peter Bienstman, Tak Keung Liang, Masahiro Tsuchiya, Patrick Jaenen, Stephan Beckx, Johan Wouters, and Roel Baets. Linear and nonlinear nanophotonic devices based on silicon-on-insulator wire waveguides. *Japanese Journal of Applied Physics*, 45:6589–6602, 2006.

[60] Q. Lin, Oskar J. Painter, and Govind P. Agrawal. Nonlinear optical phenomena in silicon waveguides: modeling and applications. *Optics Express*, 15:16604–16644, 2007.

[61] R Dekker, N Usechak, M Frst, and A Driessen. Ultrafast nonlinear all-optical processes in silicon-on-insulator waveguides. *Journal of Physics D*, 40:R249–R271, 2008.

[62] I-Wei Hsieh, Xiaogang Chen, Xiaoping Liu, Jerry I. Dadap, Nicolae C. Panoiu, Cheng-Yun Chou, Fengnian Xia, William M. Green, Yurii A. Vlasov, and Richard M. Osgood. Supercontinuum generation in silicon photonic wires. *Optics Express*, 15:15242–15249, 2007.

[63] Jidong Zhang, Qiang Lin, Giovanni Piredda, Robert W. Boyd, Govind P. Agrawal, and Philippe M. Fauchet. Optical solitons in a silicon waveguide. *Optics Express*, 15:7682–7688, 2007.

[64] Lianghong Yin, Qiang Lin, and Govind P. Agrawal. Soliton fission and supercontinuum generation in silicon waveguides. *Optics Letters*, 32:391–393, 2007.

[65] Vilson R. Almeida, Carlos A. Barrios, Roberto R. Panepucci, and Michal Lipson. All-optical control of light on a silicon chip. *Nature*, 431:1081–1084, 2004.

[66] Michal Lipson. Guiding, modulating, and emitting light on silicon – challenges and opportunities. *Journal of Lightwave Technology*, 23:4222–4238, 2005.

[67] Richard De-La-Rue, Harold Chong, Marco Gnan, Nigel Johnson, Iraklis Ntakis, Pierre Pottier, Marc Sorel, Ahmad Md Zain, Hua Zhang, Edilson Camargo, Chongjun Jin, Mario Armenise, and Caterina Ciminelli. Photonic crystal and photonic wire nano-photonics based on silicon-on-insulator. *New Journal of Physics*, 8:256, 2006.

[68] Q. F. Xu, V. R. Almeida, R. R. Panepucci, and M.Lipson. Experimental demonstration of guiding and confining light in nanometer-size low-refractive index material. *Optics Letters*, 29:1626–1628, 2004.

[69] Qianfan Xu, Vilson R. Almeida, and Michal Lipson. Micrometer-scale all-optical wavelength converter on silicon. *Optics Letters*, 30:2733–2735, 2005.

[70] Fengnian Xia, Lidija Sekaric, and Yurii A. Vlasov. Mode conversion losses in silicon-on-insulator photonic wire based racetrack resonators. *Optics Express*, 14:3872–3886, 2006.

[71] F. N. Xia, L. Sekaric, and Y. Vlasov. Ultracompact optical buffers on a silicon chip. *Nature Photonics*, 1(1):65–71, January 2007.

[72] Ozdal Boyraz, Tejaswi Indukuri, and Bahram Jalali. Self-phase-modulation induced spectral broadening in silicon waveguides. *Optics Express*, 12:829–834, 2004.

[73] R. Claps, V. Raghunathan, D. Dimitropoulos, and B. Jalali. Influence of nonlinear absorption on raman amplification in silicon waveguides. *Optics Express*, 12:2774–2780, 2004.

[74] T. K. Liang and H. K. Tsang. Role of free carriers from two-photon absorption in raman amplification in silicon-on-insulator waveguides. *Applied Physics Letters*, 84:2745, 2004.

[75] X. G. Chen, N. C. Panoiu, and R. M. Osgood. Theory of Raman-mediated pulsed amplification in silicon-wire waveguides. *IEEE Journal of Quantum Electronics*, 42(1-2):160–170, 2006.

[76] R. Claps, D. Dimitropoulos, V. Raghunathan, Y. Han, and B. Jalali. Observation of stimulated Raman amplification in silicon waveguides. *Optics Express*, 11:1731, 2003.

[77] Richard Espinola, Jerry Dadap, Richard Osgood, Sharee McNab, and Yurii Vlasov. Raman amplification in ultrasmall silicon-on-insulator wire waveguides. *Optics Express*, 12:3713–3718, 2004.

[78] Haisheng Rong, Ansheng Liu, Remus Nicolaescu, and Mario Paniccia. Raman gain and nonlinear optical absorption measurements in a low-loss silicon waveguide. *Applied Physics Letters*, 85:2196–2198, 2004.

[79] Richard Jones, Haisheng Rong, Ansheng Liu, Alexander W. Fang, and Mario J. Paniccia. Net continuous wave optical gain in a low loss silicon-on-insulator waveguide by stimulated raman scattering. *Optics Express*, 13:519–525, 2005.

[80] Haisheng Rong, Ansheng Liu, Richard Jones, Oded Cohen, Dani Hak, Remus Nicolaescu, Alexander Fang, and Mario Paniccia. An all-silicon raman laser. *Nature*, 433:292–294, 2005.

[81] Haisheng Rong, Richard Jones, Ansheng Liu, Oded Cohen, Dani Hak, Alexander Fang, and Mario Paniccia. A continuous-wave raman silicon laser. *Nature*, 433:725–728, 2005.

[82] Varun Raghunathan, Ricardo Claps, Dimitrios Dimitropoulos, and Bahram Jalali. Parametric raman wavelength conversion in scaled silicon waveguides. *Journal of lightwave technology*, 23:2094–2102, 2005.

[83] D. Dimitropoulos, V. Raghunathan, R. Claps, and B. Jalali. Phase-matching and nonlinear optical processes in silicon waveguides. *Optics Express*, 12:149–160, 2004.

[84] Qiang Lin, Jidong Zhang, Philippe M. Fauchet, and Govind P. Agrawal. Ultrabroadband parametric generation and wavelength conversion in silicon waveguides. *Optics Express*, 14:4786–4799, 2006.

[85] Mark A. Foster, Amy C. Turner, Jay E. Sharping, Bradley S. Schmidt, Michael Lipson, and Alexander L. Gaeta. Broad-band optical parametric gain on a silicon photonic chip. *Nature*, 441:04932, 2006.

[86] Mark A. Foster, Amy C. Turner, Reza Salem, Michal Lipson, and Alexander L. Gaeta. Broad-band continuous-wave parametric wavelength conversion in silicon nanowaveguides. *Optics Express*, 15:12949–12958, 2007.

[87] Qianfan Xu, Bradley Schmidt, Sameer Pradhan, and Michal Lipson. Micrometre-scale silicon electro-optic modulator. *Nature*, 435:325–327, 2005.

[88] Qianfan Xu, Sasikanth Manipatruni, Brad Schmidt, Jagat Shakya, and Michal Lipson. 12.5 gbit/s carrier-injection-based silicon micro-ring silicon modulators. *Optics Express*, 15:430–436, 2007.

[89] William M. Green, Michael J. Rooks, Lidija Sekaric, and Yurii A. Vlasov. Ultra-compact, low rf power, 10 gb/s silicon mach-zehnder modulator. *Optics Express*, 15:17106–17113, 2007.

[90] Michael Hochberg, Tom Baehr-Jones, Guangxi Wang, and Michael Shearn. Terahertz all-optical modulation in a siliconpolymer hybrid system. *Nature Materials*, 5:703–709, 2006.

[91] zdal Boyraz, Prakash Koonath, Varun Raghunathan, and Bahram Jalali. All optical switching and continuum generation in silicon waveguides. *Optics Express*, 12:4094–4102, 2004.

[92] Laurent Vivien, Mathieu Rouvire, Jean-Marc Fdli, Delphine Marris-Morini, Jean Franois Damlencourt, Juliette Mangeney, Paul Crozat, Loubna El Melhaoui, Eric Cassan, Xavier Le Roux, Daniel Pascal, and Suzanne Laval. High speed and high responsivity germanium photodetector integrated in a silicon-on-insulator microwaveguide. *Optics Express*, 15:9843–9848, 2007.

[93] Y. Vlasov, W. M. J. Green, and F. Xia. High-throughput silicon nanophotonic wavelength-insensitive switch for on-chip optical networks. *Nature Photonics*, 2(4):242–246, April 2008.

[94] T. Barwicz, H. Byun, F. Gan, C. W. Holzwarth, M. A. Popovic, P. T. Rakich, M. R. Watts, E. P. Ippen, F. X. Krtner, H. I. Smith, J. S. Orcutt, R. J. Ram, V. Stojanovic, O. O. Olubuyide, J. L. Hoyt, S. Spector, M. Geis, M. Grein, T. Lyszczarz, and J. U. Yoon. Silicon photonics for compact, energy-efficient interconnects. *Journal of Optical Networking*, 6:63–73, 2006.

[95] B. Analui, D. Guckenberger, D. Kucharski, and A. Narasimha. A fully integrated 20-gb/s optoelectronic transceiver implemented in a standard 0.13- m CMOS SOI technology. *IEEE Journal of Solid-State Circuits*, 41:2945–2955, 2006.

[96] Allen Taflove and Susan Hagness. *Computational Electrodynamics*. Artech House, 2005.

[97] J. V. Moloney and A. C. Newell. *Nonlinear Optics*. Westview Press, 2004.

[98] R.W. Boyd. *Nonlinear Optics (Second Edition)*. Academic Press, 2003.

[99] M. Dinu, F. Quochi, and H. Garcia. Third-order nonlinearities in silicon at telecom wavelengths. *Applied Physics Letters*, 82:2954–2956, 2003.

[100] Xiaogang Chen, Nicolae C. Panoiu, Iwei Hsieh, Jerry I. Dadap, and Richard M. Osgood Jr. Third-order dispersion and ultrafast-pulse propagation in silicon wire waveguides. *IEEE Photonics Technology Letters*, 24:2617–2619, 2006.

[101] J. I. Dadap, N. C. Panoiu, Xiaogang Chen, I-Wei Hsieh, Xiaoping Liu, Cheng-Yun Chou, E. Dulkeith, S. J. McNab, Fengnian Xia, W. M. J. Green, L. Sekaric, Y. A. Vlasov, and Jr. R. M. Osgood. Nonlinear-optical phase modification in dispersion-engineered Si photonic wires. *Optics Express*, 16:1280–1299, 2008.

[102] John S. Toll. Causality and the dispersion relation: Logical foundations. *Physical Review*, 104:1760 – 1770, 1956.

[103] D. Kovalev, G. Polisski, J. Diener H. Heckler, N. Knzner, V. Yu. Timoshenko, and F. Koch. Strong in-plane birefringence of spatially nanostructured silicon. *Applied Physics Letters*, 78:916, 2001.

[104] Berge Tatian. Fitting refractive-index data with the sellmeier dispersion formula. *Applied Optics*, 23:4477–4485, 1984.

[105] Bradley J. Frey, Douglas B. Leviton, and Timothy J. Madison. Temperature-dependent refractive index of silicon and germanium. *Optomechanical Technologies for Astronomy*, 6273:62732J, 2006.

[106] Sadao Adachi. Model dielectric constants of Si and Ge. *Physical Review B*, 38:12966–12976, 1988.

[107] I. H. Malitson. Interspecimen comparison of the refractive index of fused silica. *Journal of the Optical Society of America*, 55:1205–1209, 1965.

[108] John D. Joannopoulos, Robert D. Meade, and Joshua N. Winn. *Photonic Crystals*. Princeton University Press, 1995.

[109] RSoft Design Group Inc. (http://www.rsoftdesign.com).

[110] John F. Monahan. *Numerical Methods of Statistics*. Cambridge University Press, 2001.

[111] T. Kato, Y. Suetsugu, and M. Nishimura. Estimation of nonlinear refractive index in various silica-based glasses for optical fibers. *Optics Letters*, 20:2279–2281, 1995.

[112] Hermann A. Haus. Theory of mode locking with a slow saturable absorber. *IEEE Journal of Quantum Electronics*, 11:736–746, 1975.

[113] H. A. Haus, U. Keller, and W. H. Knox. Theory of coupled-cavity mode locking with a resonant nonlinearity. *Journal of the Optical Society of America B.*, 8:1252–1258, 1991.

[114] Frederic Grillot, Laurent Vivien, Suzanne Laval, and Eric Cassan. Propagation loss in single-mode ultrasmall square silicon-on-insulator optical waveguides. *Journal of Lightwave Technology*, 24:891–896, 2006.

[115] T. Baehr-Jones, M. Hochberg, C. Walker, and A. Scherer. High-q optical resonators in silicon-on-insulator-based slot waveguides. *Applied Physics Letters*, 86:081101, 2005.

[116] L. H. Yin, Q. Lin, and G. P. Agrawal. Dispersion tailoring and soliton propagation in silicon waveguides. *Optics Letters*, 31:1295–1297, 2006.

[117] Amir H. Nejadmalayeri, Peter R. Herman, Jonas Burghoff, Matthias Will, Stefan Nolte, and Andreas Tnnermann. Inscription of optical waveguides in crystalline silicon by mid-infrared femtosecond laser pulses. *Optics Letters*, 30:964–966, 2005.

[118] M. Gnan, S. Thoms, D.S. Macintyre, R.M. De-La-Rue, and M. Sorel. Fabrication of low-loss photonic wires in silicon-on-insulator using hydrogen silsesquioxane electron-beam resist. *Electronics Letters*, 44:115, 2008.

[119] H. K. Tsang, C. S. Wong, T. K. Liang, I. E. Day, S. W. Roberts, A. Harpin, J. Drake, and M. Asghari. Optical dispersion, two-photon absorption and self-phase modulation in silicon waveguides at 1.5 m wavelength. *Applied Physics Letters*, 80:416, 2001.

[120] D L Griscom. Electronic structure of SiO2 - a review of recent spectroscopic and theoretical advances. *Journal of Non-Crystalline Solids*, 24:155–234, 1977.

[121] M. Sheik-Bahae, D.C. Hutchings, D.J. Hagan, and E.W. Van Stryland. Dispersion of bound electronic nonlinear refraction in solids. *IEEE Journal of Quantum Electronics*, 27:1296–1309, 1991.

[122] D. C. Hutchings, M. Sheik-Bahae, D. J. Hagan, and E. W. Van Stryland. Kramers-krnig relations in nonlinear optics. *Optical and Quantum Electronics*, 24:1–30, 1992.

[123] Y. Silberberg. Solitons and 2-photon absorption. *Optics Letters*, 15(18):1005–1007, September 1990.

[124] Lianghong Yin and Govind Agrawal. Impact of two-photon absorption on self-phase modulation in silicon waveguides: Free-carrier effects. *Optics Letters*, 32:2031–2033, 2007.

[125] Qianfan Xu and Michal Lipson. Carrier-induced optical bistability in silicon ring resonators. *Optics Letters*, 31:341–343, 2006.

[126] R. A. Soref and B. R. Bennett. Electrooptical effects in silicon. *IEEE Journal of Quantum Electronics*, 23:123–129, 1987.

[127] C. Angulo Barrios, V. R. Almeida, R. Panepucci, and M. Lipson. Electrooptic modulation of silicon-on-insulator submicrometer-size waveguide devices. *Journal of Lightwave Technology*, 21:2332–2339, 2003.

[128] M. A. Mendicino. *Properties of Crystalline Silicon*, chapter Comparison of properties of available SOI materials, page 992. IET, 1999.

[129] D. Dimitropoulos, R. Jhaveri, R. Claps, J. C. S. Woo, and B. Jalali. Lifetime of photogenerated carriers in silicon-on-insulator rib waveguides. *Applied Physics Letters*, 86:071115, 2005.

[130] Akira Hasegawa and Frederick Tappert. Transmission of stationary nonlinear optical pulses in dispersive dielectric fibers. i. anomalous dispersion. *Applied Physics Letters*, 23:142, 1973.

[131] J. D. Kafka, T. Baer, and D. W. Hall. Mode-locked erbium-doped fiber laser with soliton pulse shaping. *Optics Letters*, 14:1269–1271, 1989.

[132] M. N. Islam. Ultrafast all-optical logic gates based on soliton trapping in fibers. *Optics Letters*, 14:1257–1259, 1989.

[133] Hermann A. Haus and William S. Wong. Solitons in optical communications. *Review of Modern Physics*, 68:423–444, 1996.

[134] A.R. Pratt, P. Harper, S.B. Alleston, P. Bontemps, B. Charbonnier, W. Forysiak, L. Gleeson, D.S. Govan, G.L. Jones, D. Nesset, J.H.B. Nijhof, I.D. Phillips, M.F.C. Stephens, A.P. Walsh, T. Widdowson, and N.J. Doran. 5,745 km DWDM transcontinental field trial using 10 Gbit/s dispersion managed solitons and dynamic gain equalization. In *Optical Fiber Communications Conference*, 2003.

[135] W.J. Wadsworth, J.C. Knight, A. Ortigosa-Blanch, J. Arriaga, E. Silvestre, and P.St.J. Russell. Soliton effects in photonic crystal fibres at 850 nm. *Electronics Letters*, 36:53–55, 2000.

[136] P. Emplit, J. P. Hamaide, F. Reynaud, C. Froehly, and A. Barthelemy. Picosecond steps and dark pulses through nonlinear single mode fibers. *Optics Communications*, 62:374–379, 1987.

[137] P. Dumais and A. Villeneuve. Bright temporal solitonlike pulses in self-defocusing AlGaAs waveguides near 800 nm. *Optics Letters*, 21:260–262, 1996.

[138] Takashi Yamada and Kazuhiro Nozaki. Effects of dissipative perturbation on bound-state solitons of nonlinear schrdinger equation. *Journal of the Physical Society of Japan*, 58:1944–1947, 1989.

[139] V. E. Zakharov and A. B. Shabat. Exact theory of two-dimensional self- focusing and one-dimensional self-modulation of waves in nonlinear media. *Soviet Physics JETP*, 34:62–69, 1972.

[140] Mark Foster, Alexander Gaeta, Qiang Cao, and Rick Trebino. Soliton-effect compression of supercontinuum to few-cycle durations in photonic nanowires. *Optics Express*, 13:6848–6855, 2005.

[141] S. V. Chernikov, E. M. Dianov, D. J. Richardson, and D. N. Payne. Soliton pulse compression in dispersion-decreasing fiber. *Optics Letters*, 18:476–478, 1993.

[142] Nail Akhmediev and Magnus Karlsson. Cherenkov radiation emitted by solitons in optical fibers. *Physical Review A*, 51:2602–2607, 1995.

[143] A. Efimov, A. V. Yulin, D. V. Skryabin, J. C. Knight, N. Joly, F. G. Omenetto, A. J. Taylor, and P. Russell. Interaction of an optical soliton with a dispersive wave. *Physical Review Letters*, 95:213902, 2005.

[144] S. O. Konorov, D. A. Akimov, E. E. Serebryannikov, A. A. Ivanov, M. V. Alfimov, K. V. Dukel'skii, A. V. Khokhlov, V. S. Shevandin, Yu. N. Kondrat'ev, and A. M. Zheltikov. High-order modes of photonic wires excited by the cherenkov emission of solitons. *Laser Physics Letters*, 2:258–261, 2005.

[145] Jennifer H. Lee, James van Howe, Chris Xu, Siddharth Ramachandran, Samir Ghalmi, and Man F. Yan. Generation of femtosecond pulses at 1350 nm by erenkov radiation in higher-order-mode fiber. *Optics Letters*, 32:1053–1055, 2007.

[146] D. V. Skryabin, F. Luan, J. C. Knight, and P. S. Russell. Soliton self-frequency shift cancellation in photonic crystal fibers. *Science*, 301(5640):1705–1708, September 2003.

[147] W. H. Reeves, D. V. Skryabin, F. Biancalana, J. C. Knight, P. St. J. Russell, F. G. Omenetto, A. Emov, and A. J. Taylor. Transformation and control of ultra-short pulses in dispersion-engineeredphotonic crystal bres. *Nature*, 424:511–515, 2003.

[148] Ilaria Cristiani, Riccardo Tediosi, Luca Tartara, and Vittorio Degiorgio. Dispersive wave generation by solitons in microstructured optical fibers. *Optics Express*, 12:124, 2004.

[149] Anatoly Efimov, A. Taylor, F. Omenetto, A. Yulin, N. Joly, F. Biancalana, D. Skryabin, J. Knight, and P. Russell. Time-spectrally-resolved ultrafast nonlinear dynamics in small-core photonic crystal bers: Experiment and modelling. *Optics Express*, 12:6498, 2004.

[150] P. K. Tien, R. Ulrich, and R. J. Martin. Optical second harmonic generation in form of coherent cerenkov radiation from a thin-film waveguide. *Applied Physics Letters*, 17:447, 1970.

[151] F. Biancalana, D. V. Skryabin, and A. V. Yulin. Theory of the soliton self-frequency shift compensation by the resonant radiation in photonic crystal fibers. *Physical Review E*, 70:016615, 2004.

[152] P. K. A. Wai, C. R. Menyuk, Y. C. Lee, and H. H. Chen. Nonlinear pulse propagation in the neighborhood of the zero-dispersion wavelength of monomode optical fibers. *Optics Letters*, 11:464–466, 1986.

[153] P. K. A. Wai, H. H. Chen, and Y. C. Lee. Radiations by "solitons" at the zero group-dispersion wavelength of single-mode optical fibers. *Physical Review A*, 41:426–439, 1990.

[154] N.C. Panoiu, D. Mihalache, D. Mazilu, I.V. Mel'nikov, J.S. Aitchison, F. Lederer, and R.M. Osgood. Dynamics of dual-frequency solitons under the influence of frequency-sliding filters, third-order dispersion, and intrapulse raman scattering. *IEEE Journal of Selected Topics in Quantum Electronics*, 10:885–892, 2004.

[155] I-Wei Hsieh, Xiaogang Chen, J.I. Dadap, N.C. Panoiu, and R.M. Osgood. Determination of third-order dispersion coefficient and observation of soliton radiation in si-wire waveguides. In *Conference on Lasers and Electro-Optics*, 2007.

[156] D. V. Skryabin and A. V. Yulin. Theory of generation of new frequencies by mixing of solitons and dispersive waves in optical fibers. *Physical Review E*, 72:016619, 2005.

[157] Dane R. Austin, C. Martijn de Sterke, Benjamin J. Eggleton, and Thomas G. Brown. Dispersive wave blue-shift in supercontinuum generation. *Optics Express*, 14:11997–12007, 2006.

[158] A. V. Husakou and Herrmann J. Supercontinuum generation of higher-order solitons by fission in photonic crystal fibers. *Physical Review Letters*, 87:203901, 2001.

[159] J. Herrmann, U. Griebner, N. Zhavoronkov, A. Husakou, D. Nickel, J. C. Knight, W. J. Wadsworth, P. St. J. Russell, and G. Korn. Experimental evidence for supercontinuum generation by fission of higher-order solitons in photonic fibers. *Physical Review Letters*, 88:173901, 2002.

[160] Stphane Coen, Alvin Hing Lun Chau, Rainer Leonhardt, John D. Harvey, Jonathan C. Knight, William J. Wadsworth, and Philip St. J. Russell. White-light supercontinuum generation with 60-ps pump pulses in a photonic crystal fiber. *Optics Letters*, 26:13561358, 2001.

[161] A. V. Gorbach, D. V. Skryabin, J. M. Stone, and J. C. Knight. Four-wave mixing of solitons with radiation and quasi-nondispersive wave packets at the short-wavelength edge of a supercontinuum. *Optics Express*, 14:9854–9863, 2006.

[162] J. Nathan Kutz, C Lyng, and B. Eggleton. Enhanced supercontinuum generation through dispersion-management. *Optics Express*, 13:3989, 2005.

[163] A. V. Gorbach and D. V. Skryabin. Light trapping in gravity-like potentials and expansion of supercontinuum spectra in photonic-crystal fibres. *Nature Photonics*, 1:653 – 657, 2007.

[164] William J. Wadsworth, Arturo Ortigosa-Blanch, Jonathan C. Knight, Tim A. Birks, T.P. Martin Man, and Phillip St. J. Russell. Supercontinuum generation in photonic crystal fibers and optical fiber tapers: a novel light source. *Journal of the Optical Society of America B*, 19:2148–2155, 2002.

[165] S. Leon-Saval, T. Birks, W. Wadsworth, P. St. J. Russell, and M. Mason. Supercontinuum generation in submicron fibre waveguides. *Optics Express*, 12:2864, 2004.

[166] T. A. Birks, W. J. Wadsworth, and P. S. J. Russell. Supercontinuum generation in tapered fibers. *Optics Letters*, 25:1415–1417, 2000.

[167] P. Domachuk, N. A. Wolchover, M. Cronin-Golomb, A. Wang, A. K. George, C. M. B. Cordeiro, J. C. Knight, and F. G. Omenetto. Over 4000 nm bandwidth of mid-ir supercontinuum generation in sub-centimeter segments of highly nonlinear tellurite PCFs. *Optics Express*, 16:7161–7168, 2008.

[168] Georg W. Rieger, Kuljit S. Virk, and Jeff F. Young. Nonlinear propagation of ultrafast 1.5$\mu$m pulses in high-index-contrast silicon-on-insulator waveguides. *Applied Physics Letters*, 84:900–902, 2004.

[169] Eric Dulkeith, Yurii A. Vlasov, Xiaogang Chen, Nicolae C. Panoiu, and Richard M. Osgood. Self-phase-modulation in submicron silicon-on-insulator photonic wires. *Optics Express*, 14:5524–5534, 2006.

[170] Allan R. Cowan, Georg W. Rieger, and Jeff F. Young. Nonlinear transmission of 1.5 m pulses through single-mode silicon-on-insulator waveguide structures. *Optics Express*, 12:1611–1621, 2004.

[171] Nicolae C. Panoiu, Xiaogang Chen, and Jr. Richard M. Osgood. Modulation instability in silicon photonic nanowires. *Optics Letters*, 31:3609, 2006.

[172] Stephane Clemmen, Kien Phan Huy, Roel Baets, Dirk Taillaert, Wim Bogaerts, Philippe Emplit, and Serge Massar. Modulation instability in silicon nanophotonic waveguides.

[173] F. Biancalana, D. V. Skryabin, and P. S. Russell. Four-wave mixing instabilities in photonic-crystal and tapered fibers. *Physical Review E*, 68:046603, 2003.

[174] Fabio Biancalana and Dmitry V. Skryabin. Vector modulational instabilities in ultra-small core optical fibres. *Journal of the Optics B*, 6:301–306, 2004.

[175] M. Yu, C. J. Mckinstrie, and G. P. Agrawal. Modulational instabilities in dispersion-flattened fibers. *Physical Review E*, 52:1072–1080, 1995.

[176] R.A. Bergh, G. Kotler, and H.J. Shaw. Single-mode fibre optic directional coupler. *Electronics Letters*, 16:260–261, 1980.

[177] P.D. Trinh, S. Yegnanarayanan, and B. Jalali. Integrated optical directional couplers in silicon-on-insulator. *Electronics Letters*, 31:2097–2098, 1995.

[178] U. Ropke, H. Bartelt, S. Unger, K. Schuster, and J. Kobelke. Two-dimensional high-precision fiber waveguide arrays for coherent light propagation. *Optics Express*, 15(11):6894–6899, May 2007.

[179] Govind P. Agrawal. *Applications of Nonlinear Fiber Optics*. Academic Press, 2001.

[180] Falk Lederer, George I. Stegeman, Demetri N. Christodoulides, Gaetano Assanto, Moti Segev, and Yaron Silberberge. Discrete solitons in optics. *Physics Reports*, 463:1–126, 2008.

[181] Andrea Locatelli, Matteo Conforti, Daniele Modotto, and Costantino De Angelis. Discrete negative refraction in photonic crystal waveguide arrays. *Optics Letters*, 31:1343, 2006.

[182] Christian R. Rosberg, Dragomir N. Neshev, Andrey A. Sukhorukov, and Yuri S. Kivshar. Tunable positive and negative refraction in optically induced photonic lattices. *Optics Letters*, 30:2293, 2005.

[183] Viktor G Veselago. The electrodynamics of substances with simultaneously negative values of epsilon and mu. *Soviet Physics Uspekhi*, 10:509–514, 1968.

[184] R. A. Shelby, D. R. Smith, and S. Schultz. Experimental verification of a negative index of refraction. *Science*, 292:5514, 2001.

[185] J. B. Pendry. Negative refraction makes a perfect lens. *Physical Review Letters*, 85:3966–3969, 2000.

[186] Ulf Leonhardt. Optical conformal mapping. *Science*, 312:5781, 2006.

[187] Christopher J. Benton and Dmitry V. Skryabin. Coupling induced anomalous group velocity dispersion in nonlinear arrays of silicon photonic wires. *Optics Express*, 17:5879, 2009.

[188] Amnon Yariv, Yong Xu, Reginald K. Lee, and Axel Scherer. Coupled-resonator optical waveguide: a proposal and analysis. *Optics Letters*, 24:711–713, 1999.

[189] Neil W. Ashcroft and N. David Mermin. *Solid State Physics*. Holt, Rinehart and Winston, 1976.

[190] C. Kittel and P. McEuen. *Introduction to solid state physics*. John Wiley & Sons, Inc, 1986.

[191] D. Mandelik, H. S. Eisenberg, Y. Silberberg, R. Morandotti, and J. S. Aitchison. Band-gap structure of waveguide arrays and excitation of floquet-bloch solitons. *Physical Review Letters*, 90:053902, 2003.

[192] V. R. Almeida, Q. F. Xu, C. A. Barrios, and M.Lipson. Guiding and confining light in void nanostructure. *Optics Letters*, 29:1209–1211, 2004.

[193] Andrea Locatelli, Matteo Conforti, Daniele Modotto, and Costantino De Angelis. Diffraction engineering in arrays of photonic crystal waveguides. *Optics Letters*, 30:2894–2896, 2005.

[194] Keji Huang, Shuangyang Yang, and Limin Tong. Modeling of evanescent coupling between two parallel optical nanowires. *Applied Optics*, 9:1429–1434, 2007.

[195] K. S. Chiang, Y. T. Chow, D. J. Richardson, D. Taverner, L. Dong, L. Reekie, and K. M. Lo. Experimental demonstration of intermodal dispersion in a two-core optical fibre. *Optics Communications*, 143:189–192, 1997.

[196] Nail Akhmediev and Adrian Ankiewicz. Novel soliton states and bifurcation phenomena in nonlinear fiber couplers. *Physics Review Letters*, 70:2395–2398, 1993.

[197] J. M. Soto-Crespo and Nail Akhmediev. Stability of the soliton states in a nonlinear fiber coupler. *Physics Review E*, 48:4710–4715, 1993.

[198] H. S. Eisenberg, Y. Silberberg, R. Morandotti, and J. S. Aitchison. Diffraction management. *Physical Review Letters*, 85:1863 – 1866, 2000.

[199] T. Pertsch, T. Zentgraf, U. Peschel1, A. Bruer, and F. Lederer. Anomalous refraction and diffraction in discrete optical systems. *Physical Review Letters*, 88:093901, 2002.

[200] D. Mandelik, R. Morandotti, J. S. Aitchison, and Y. Silberberg. Gap solitons in waveguide arrays. *Physical Review Letters*, 92:093904, 2004.

[201] A. V. Yulin, D. V. Skryabin, and A. G. Vladimirov. Modulational instability of discrete solitons in coupled waveguides with group velocity dispersion. *Optics Express*, 14(25):12347–12352, December 2006.

[202] S. Trillo, S. Wabnitz, G. I. Stegeman, and E. M. Wright. Parametric amplification and modulational instabilities in dispersive nonlinear directional couplers with relaxing nonlinearity. *Journal of the Optical Society of America B*, 6:889–900, 1989.

[203] B. Daino, G. Gregori, and S. Wabnitz. Stability analysis of nonlinear coherent coupling. *Journal of Applied Physics*, 58:4512, 1985.

[204] B. Daino, G. Gregori, and S. Wabnitz. New all-optical devices based on third-order nonlinearity of birefringent fibers. *Optics Letters*, 11:42–44, 1986.

[205] S. Jensen. The nonlinear coherent coupler. *IEEE Journal of Quantum Electronics*, 18:1580–1583, 1982.

[206] S. Trillo, S. Wabnitz, E. M. Wright, and G. I. Stegeman. Soliton switching in fiber nonlinear directional couplers. *Optics Letters*, 13:672–674, 1988.

[207] S. Wabnitz. Instabilities and all-optical phase-controlled switching in a nonlinear directional coherent coupler. *Applied Physics Letters*, 14:838–840, 1986.

[208] A. B. Aceves, C. De Angelis, Alexander M. Rubenchik, and Sergei K. Turitsyn. Multidimensional solitons in fiber arrays. *Optics Letters*, 19:329–331, 1994.

[209] A. V. Buryak and N. N. Akhmediev. Stationary pulse-propagation in n-core nonlinear fiber arrays. *IEEE Journal of Quantum Electronics*, 31(4):682–688, April 1995.

[210] Y. Lahini, E. Frumker, Y. Silberberg, S. Droulias, K. Hizanidis, R. Morandotti, and D. N. Christodoulides. Discrete x-wave formation in nonlinear waveguide arrays. *Physical Review Letters*, 98(2):023901, January 2007.

[211] C. J. Benton, A. V. Gorbach, and D. V. Skryabin. Spatiotemporal quasisolitons and resonant radiation in arrays of silicon-on-insulator photonic wires. *Physical Review A*, 78:033818, 2008.

[212] R. Morandotti, H. S. Eisenberg, and Y. Silberberg. Self-focusing and defocusing in waveguide arrays. *Physical Review Letters*, 86:3296–3299, 2001.

[213] Roberto Morandotti, Daniel Mandelik, Yaron Silberberg, J. Stewart Aitchison, Marc Sorel, Demetrios N. Christodoulides, Andrey A. Sukhorukov, and Yuri S. Kivshar. Observation of discrete gap solitons in binary waveguide arrays. *Optics Letters*, 29:2890–2892, 2004.

[214] Dmitry Skryabin. Stability of multi-parameter solitons: asymptotic approach. *Physica D*, 139:186–193, 2000.

[215] M.G. Vakhitov and A.A. Kolokolov. Stationary solutions of the wave equation in a medium with nonlinearity saturation. *Radiophysics and Quantum Electronics*, 16:783–789, 1973.

[216] D. V. Skryabin, F. Biancalana, D. M. Bird, and F. Benabid. Effective Kerr nonlinearity and two-color solitons in photonic band-gap fibers filled with a Raman active gas. *Physical Review Letters*, 93:143907, 2004.

[217] D. V. Skryabin and A. V. Yulin. Raman solitons with group velocity dispersion. *Physical Review E*, 74:046616, 2006.

[218] D. V. Skryabin, A. V. Yulin, and F. Biancalana. Nontopological Raman-Kerr self-induced transparency solitons in photonic crystal fibers. *Physical Review E*, 73:045603, 2006.

[219] M. Scalora, S. Singh, and C. M. Bowden. Anti-Stokes generation and soliton decay in stimulated Raman scattering. *Physical Review Letters*, 70:1248–1250, 1993.

[220] A. V. Sokolov and S.E. Harris. Ultrashort pulse generation by molecular modulation. *Journal of the Optical Society of America B*, 5:R1–R26, 2003.

[221] A. V. Sokolov, D. R. Walker, D. D. Yavuz, G. Y. Yin, and S. E. Harris. Raman generation by phased and antiphased molecular states. *Physical Review Letters*, 85:562–565, 2000.

[222] F. Benabid, J. C. Knight, G. Antonopoulos, and P. St. J. Russell. Stimulated Raman scattering in hydrogen-filled hollow-core photonic crystal fiber. *Science*, 298:399 – 402, 2002.

[223] A. E. Kaplan. Subfemtosecond pulses in mode-locked $2\pi$ solitons of the cascade stimulated raman scattering. *Physical Review Letters*, 73:1243–1246, 1994.

[224] A. E. Kaplan and P. L. Shkolnikov. Subfemtosecond pulses in the multicascade stimulated raman scattering. *Journal of the Optical Society of America B*, 13:347–354, 1996.

[225] The GNU Scientific Library, Free Software Foundation, Inc. (http://www.gnu.org/software/gsl/).

[226] Stephen Gasiorowicz. *Quantum Physics*. Wiley, 1993.

[227] Rick Trebino. *Frequency-Resolved Optical Gating*. Kluwer Academic Publishers, 2000.

[228] William H. Press, Brian P. Flannery, Saul A. Teukolsky, and William T. Vetterling. *Numerical Recipes in C*. Cambridge University Press, 1992.